The Hydrothermal Synthesis of Quantum and Carbon Dots

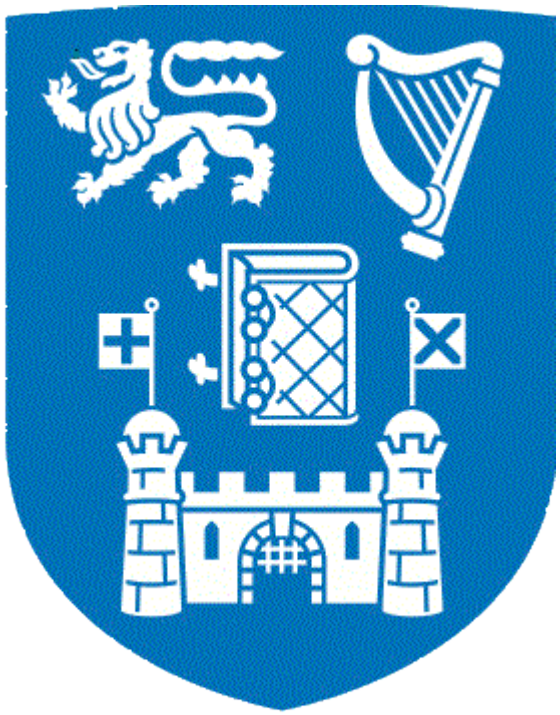

A thesis submitted to the School of Chemistry,

Trinity College Dublin,

For the degree of Doctor of Philosophy

By **Karlijn Hertsig**

2026

Supervisor: Prof. Peter W. Dunne

Declaration

I declare that this thesis has not been submitted as an exercise for a degree at this or any other university and it is entirely my own work.

I agree to deposit this thesis in the University's open access institutional repository or allow the Library to do so on my behalf, subject to Irish Copyright Legislation and Trinity College Library conditions of use and acknowledgement.

I consent to the examiner retaining a copy of the thesis beyond the examining period, should they so wish (EU GDPR May 2018).

_____

Karlijn Hertsig

Acknowledgements

I extend my deepest gratitude to my supervisor, Dr. Peter Dunne, who has been a solid rock of support and mentorship throughout my academic journey at Trinity College Dublin. His patience, insightful guidance, and constructive feedback have been essential in shaping this research. I am also thankful for the opportunities and freedom he provided, which allowed me to explore and research the topics about which I am most passionate.

My sincere thanks are also extended to the members of my thesis committee for their time and consideration to examine this work, I look forward to their feedback and unique perspectives on it. I am also grateful to the technical staff in the School of Chemistry, whose expertise and assistance were invaluable in the practical execution of experiments and characterisation. This research was made possible through the financial support through the Trinity College Dublin Provost Scholarship Programme whose commitment to advancing knowledge within the college is profoundly appreciated.

My sincere appreciation is extended to current and former group members, as well as the students with whom I had the privilege of collaborating. The mutual learning and support throughout our time in the laboratory together were invaluable.

A special note of appreciation goes to my office family for their support and kindness, and for creating a welcoming workspace. Your collective spirit and expertise have stayed with me, and I am excited to witness your future achievements and breakthroughs.

Finally, I want to say thank you from the bottom of my hearth to my partner and my family for their unconditional support, fierce encouragement, and their belief in my dreams. I could not have done it without you.

This thesis is not the end, it is the start of something new.

Abstract

In the context of the global energy transition, this thesis explores the hydrothermal synthesis of energy materials, specifically quantum dots and carbon dots, emphasising sustainable green chemistry approaches, as introduced in Chapter 1.

Chapter 2 details the hydrothermal synthesis of cadmium sulfide quantum dots (CdS QDs) using water as a solvent and reduced reaction temperatures. After systematic investigation of reactants, pH, molar ratio, and reaction time, excellent control over the optical properties and size of CdS QDs was achieved. Simplifying the reaction system to a cadmium source and a bifunctional ligand resulted in a 36% reduction in material input (in moles).

Chapters 3 and 4 address the synthesis of carbon dots (CDs) from seaweed and its derivatives as a sustainable alternative to metal-based quantum dots. Chapter 3 investigated the hydrothermal synthesis of blue emissive CDs from seaweed at 160 °C/4 h, identifying challenges in purification and stability due to aggregation and side product formation.

Consequently, Chapter 4 focused on optimising hydrothermal reaction parameters for six seaweed precursors using the Response Surface Method (RSM). This optimisation identified optimal reaction temperatures ranging from 180 °C to 210 °C and reaction times from 4 to 6 h. These optimised conditions significantly enhanced quantum yields (QYs) and photoluminescence compared to the standard conditions of 160 °C/4 h, with notable improvements observed for kelp and Irish moss when processed at 210 °C/4 h, with 139 and 114% respectively.

Overall, this work demonstrates the successful application of green chemistry principles, utilising water as a solvent, reducing reaction temperatures, and leveraging renewable biomass for the sustainable production of quantum and carbon dots. Using reaction optimisation method RSM for carbon dots synthesis is proposed to overcome isolation challenges and facilitate post-synthesis processing. This approach contributes to the development of eco-friendly nanomaterials crucial for advancements in renewable energy technologies.

Table of Contents

List of Figures

List of Tables

Chapter 1 Introduction

1.1 The Realm of Material Science

In an era defined by increasing technological complexity and a feverish pursuit of sustainable solutions, the study of materials and their properties became essential.[1] Materials science became a vital field of study, integrating knowledge from diverse disciplines to understand the fundamental principles governing material behaviour and to create innovative solutions for a broad range of every-day applications.[2] This interdisciplinary nature allows for the rational design and synthesis of novel materials with bespoke properties tailored for specific applications, innovation, and economic growth.[3, 4] The different disciplines contribute to materials science in distinct ways:

- Physics – provides insights into the atomic and molecular structures of materials, their interactions, and underlying physical phenomena.
- Chemistry – enables the exploration of chemical composition, reactions, and synthesis of materials.
- Engineering – expertise is crucial for designing and developing innovative applications and technologies using materials.
- Biology – offers perspectives on how natural materials and systems can inspire the development of new synthetic materials and biomaterials.

As materials science progressed, it evolved from an initial experimental stage, where materials were primarily developed through trial-and-error investigations, to theoretical and computational stages, enabling a more systematic, science-based approach to materials design.[5] The latest paradigm shift towards the data-intensive stage, fuelled by rapid advancements in artificial intelligence and machine learning, has opened new avenues for the efficient design and discovery of novel materials.[6]

1.2 Nanoscience

The emergence of nanoscience represented a significant milestone in the evolution of materials science.[7] Manipulating and controlling materials at the nanoscale has enabled the development of novel materials with unique properties distinct from their bulk counterparts. Nanoscience focuses on investigating phenomena that occur when materials are structured or patterned at scales generally smaller than 100 nm. This size regime includes the wavelength of light, the de Broglie wavelength of charge carriers, the dimensions where plasmonic resonance occurs, and the size of large biomolecules. Effective application of nanomaterials necessitates controlling nanostructure synthesis at the atomic level. This precise control over synthesis parameters is crucial, as the resulting size, shape, and composition of nanoparticles directly correlate with their physical, chemical, optical, catalytic, magnetic, and electrical properties, which are pivotal for their diverse applications in environmental, biotechnological, and biomedical fields.

Nanostructures possess a high surface-to-volume ratio, making their surface energy a priority for their properties and structure. This results in enhanced chemical reactivity, improved catalytic activity, and heightened sensitivity to external stimuli such as light, heat, and electromagnetic fields for these materials.[7, 8] The high surface area of nanomaterials provides more active sites for chemical reactions, leading to improved catalytic efficiency and enhanced sensitivity to environmental changes. Nanotechnology, drawing upon expertise from semiconductor physics, organic and inorganic chemistry, molecular biology, and

biotechnology, seeks to develop innovative solutions spanning modern electronics, industrial-scale catalysis, precision medicine, and quantum technology.

The confinement of electrons and photons within nanoscale dimensions can give rise to quantum size effects, which dramatically alter the optical and electronic properties of these materials.[9] This nanoscale confinement leads to the emergence of size-dependent band gaps, increased exciton binding energies, and enhanced light-matter interactions. In addition, the physical and mechanical properties of nanomaterials also exhibit significant size dependence. The reduced dimensions can lead to increased hardness, strength, and toughness, making them attractive for applications in structural materials, coatings, and protective devices.[10] Other material properties that are tuneable by the nanoscale include redox potentials and melting temperature.[11, 12] Regardless these distinct size-dependent properties, nanomaterials share commonalities with their bulk counterparts, such as fundamental atomic structure, and preserved chemical composition and crystal structure.

1.3 Energy levels in materials

First, this section delves into the fundamental principles governing the discrete energy states that electrons can occupy within various material systems. In an isolated atom, these energy levels are distinctly quantised, typically represented by orbitals such as 1s, 2s, and 2p, which electrons fill according to the Pauli exclusion principle starting from the lowest energy states.[1, 13] When atoms coalesce to form molecules or crystalline solids, their individual atomic orbitals overlap, leading to the splitting of discrete energy levels into a multitude of closely spaced molecular orbitals or continuous energy bands. This transformation from discrete atomic levels to continuous bands is a cornerstone of solid-state physics. This energy band concept is fundamental to understanding the electronic structure of crystalline materials, the dispersion of energy bands, the formation of bandgaps, and the origin of metallic, semiconducting, or insulating properties in bulk materials and directly dictates the electrical properties of materials, manifests in observable macroscopic properties including conductivity.

The energy band concept includes the valence band, which contains energy levels occupied by electrons that are typically bound to atoms and do not contribute to conduction. The conduction band is a range of electron energy levels that are high enough in energy that electrons in them can move freely through the material, enabling electrical conduction. In Figure 1.1 the three types of electron configurations in materials are displayed.

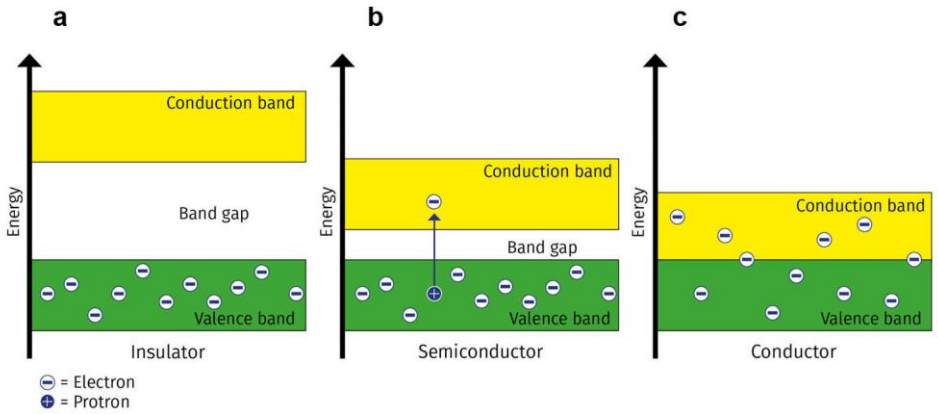

Figure 1.1, The electron configuration of an insulator, semiconductor, and conductor

In insulators, a large energy gap separates the valence band from the conduction band, preventing electron excitation into conductive states, whereas in metals, these bands overlap, facilitating electron movement and high conductivity. Semiconductors, however, possess a smaller bandgap, allowing for controllable conductivity through doping or thermal excitation, where the Fermi energy level lies between the valence and conduction bands. This bandgap represents the minimum energy required to excite an electron from the valence band to the conduction band.

The electrical conductivity of semiconductors can be substantially and predictably modified through the introduction of trace amounts of specific impurities. This process, known as doping, creates discrete energy levels within the semiconductor's bandgap. These introduced levels can either donate free electrons (n-type) or create holes (p-type). The interface formed by combining a p-type semiconductor with an n-type semiconductor constitutes a p-n junction, which serves as the fundamental building block for a wide array of electronic components, including diodes, transistors, and LEDs. Continuous refinement and control over these material properties, often involving detailed studies of defects to optimise performance, have been central to advancement of the electronics industry.

1.4 Quantum Dots: Properties, Discovery, and Applications

Semiconductor nanoparticles, known as quantum dots (QDs), form a unique class of materials distinct from their molecular and bulk forms. For these materials, precise control over their properties, particularly electronic structure and nanoscale effects, has become critically important in the field of material science. These nanomaterials exhibit unique optical and electronic characteristics due to quantum confinement, by emitting a light in a colour, based on their size, depicted in Figure 1.2. The discovery of quantum dots was a pivotal moment in nanoscience, inspiring extensive research into their distinctive properties, synthesis, and applications.

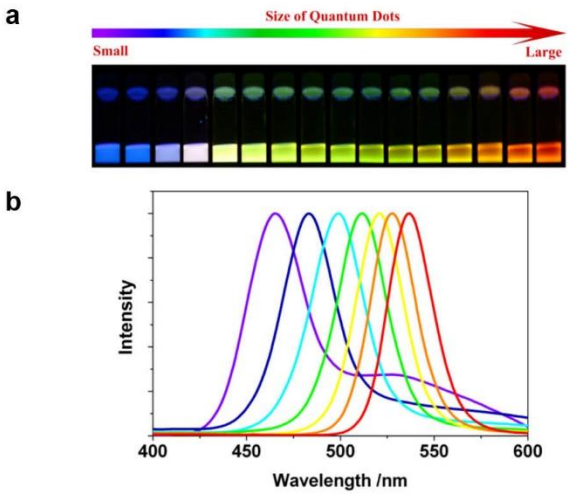

Figure 1.2, CdSe quantum dots, illustration of the controllable fluorescence properties of quantum dots, ranging the visible light spectrum, (a) under UV 365 nm from blue to green, and red and (b) photoluminescence emission plot 460 – 540 nm.[14]

The Laureates of The Nobel Prize in Chemistry 2023 played a pivotal role in establishing these capabilities for quantum dots, thereby sowing the seeds for the thriving field of nanoscience to flourish.[15]

While retaining the same structural and atomic composition as their bulk counterparts, their properties are dictated by particle size. Quantum dots exist on the nanoscale and are therefore governed by the quantum mechanical states of the material's charge carriers, leading to quantum size effects. When semiconductor materials are scaled down to the nanoscale, electrons become confined within the particle's dimensions, causing the quantisation of their energy levels. The energy of the excited state increases as particle size decreases, depending on the material's composition. This quantum confinement effect is the driving force behind the optical and electronic properties of semiconductor nanoparticles.

1.4.1 Particle-in-a-box model

The "particle-in-a-box" model is a fundamental concept in quantum mechanics that provides a simplified, yet powerful, analogy to understand how the confinement of electrons at the nanoscale leads to the quantum size effects observed in quantum dots, visualised in Figure 1.3.[16]

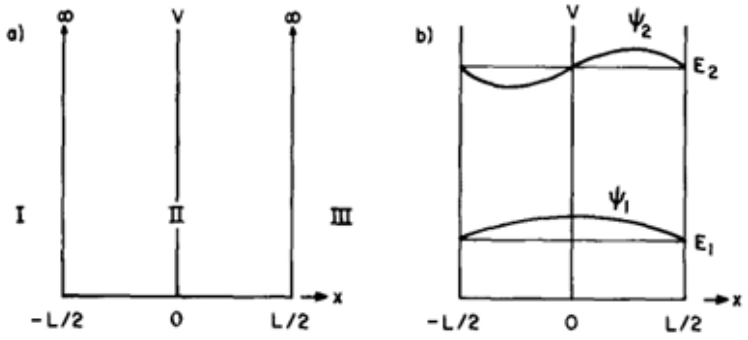

Figure 1.3, The box potential (a), and the first two levels and wave functions in the box (b).[16]

In quantum dots, electrons and holes (positive charge carriers) are confined within the nanoscale dimensions of the particle, acting like the "box." In this simplified model, the electron is free to move within the box but cannot escape it. According to classical physics, the electron could have any energy

within the box. However, quantum mechanics dictates a different reality. When a particle is confined to a small region, its energy levels become quantised, meaning only specific, discrete energy values are allowed. This is analogous to the harmonics of a vibrating string, which can only produce specific musical notes depending on its length and tension. The energy levels E_n for a particle in a one-dimensional box of length L are given by the equation:

$$E_n = \frac{n^2 h^2}{8mL^2} \tag{1.1}$$

Where:

- n is the principal quantum number ($n = 1, 2, 3, \ldots$)
- h is Planck's constant
- m is the mass of the particle (in our case, the electron)
- L is the length of the box (the size of the quantum dot)

The particle-in-a-box equation provides two key insights into the quantum size effect. First, the energy quantisation: The energy levels are discrete, and determined by the quantum number n. Second, the inverse square dependency on size whereby the energy levels are inversely proportional to the square of the box's length L.

This direct relationship between size and energy means smaller boxes (quantum dots) lead to larger energy spacing, while larger boxes lead to smaller energy spacing, approaching bulk material properties. This allows for the precise tuning of the quantum dot's optical properties, such as absorption and emission wavelengths, by controlling its size during synthesis. For example, the optical absorption and emission characteristics of CdSe quantum dots can be adjusted covering most of the visible light spectrum by controlling their energy bandgap, which ranges from 1.8 eV to 3 eV, as shown in Figure 1.4.[14, 17-19]

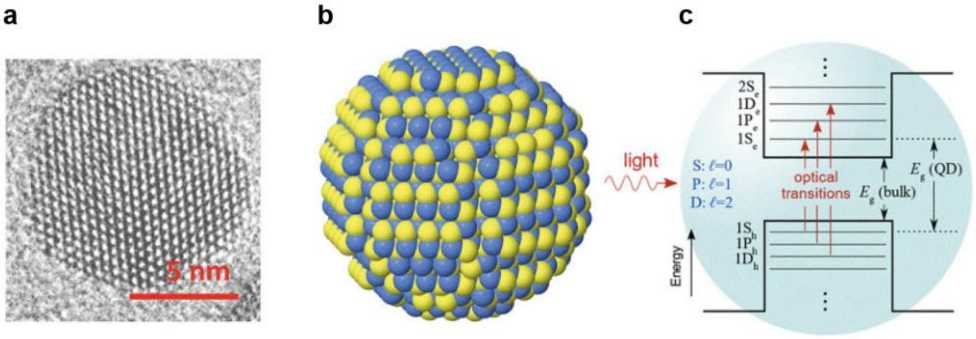

Figure 1.4, Illustration of quantum dots. Left: TEM image of a CdSe nanocrystal. Centre: Atomic structure of a nanocrystal. Right: Electronic states in a core-shell quantum dot, with the dot itself in the centre bracketed by a wide-bandgap shell.20

When comparing quantum dots to traditional fluorophores, several distinctions emerge: QDs demonstrate narrower emission spectra and notably lack the extended long-wavelength tail often observed in other fluorescent substances. This absence is particularly advantageous as it mitigates interference when employing multiple fluorophores in imaging or multi-analyte analyses. Furthermore, the emission spectra of quantum dots typically display a high degree of symmetry.[21]

Table 1.1, Spectral properties of conventional fluorophores and quantum dots

Properties	Fluorophores	Quantum Dots
Absorption	Narrow	Broad
Emission Spectrum	Asymmetric, with often a long-wavelength tail	Symmetric and Gaussian
Quantum yield	0.5 – 1.0	0.1 – 1
Lifetime	1 – 10 ns	Up to 2 µs
Thermal stability	Variable and dependent on dye class	High and depends on shell or ligand
Photochemical stability	Sufficient unless for high-light flux	High

The first observations of quantum size effects were made in the context of coloured glass.[15] Glassmakers historically understood that adding dopants like gold, silver, cadmium, sulfur, and selenium could alter the optical properties of glass. It was recognised that the glass properties were related to the inclusion of colloidal particles, but the precise mechanism was not yet understood.[22, 23]

In 1937, Herbert Fröhlich first suggested that a small particle's size could affect its material properties.[24] Subsequent theoretical studies predicted quantum size effects impacting metals and semiconductors,[25-30] later supported by experimental evidence from thin films and quantum wells.[31-38] This led to advancements like semiconductor heterostructures, for which Alferov and Kroemer received the Nobel Prize in Physics in 2000.[39-41]

1.4.2 Nobel Prize in Chemistry 2023

The Royal Swedish Academy of Sciences has awarded Moungi G. Bawendi, Louis E. Brus, and Aleksey Yekimov the Nobel Prize in Chemistry 2023, for the discovery and synthesis of quantum dots, pictured in Figure 1.5. The Nobel Prize in Chemistry acknowledged the groundbreaking discoveries and development of nanometre-scale semiconductor crystals.[15]

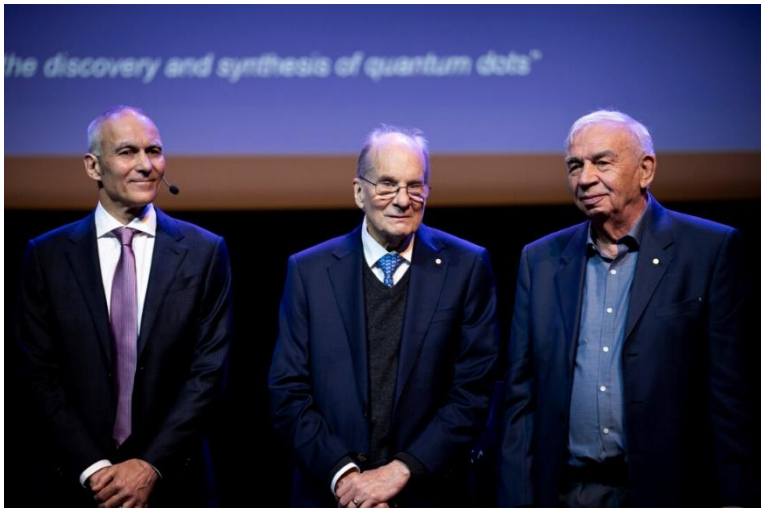

Figure 1.5, The three 2023 chemistry laureates after delivering their Nobel Prize lectures on 8 December 2023 at the Aula Magna, Stockholm University. From left: Moungi G. Bawendi, Louis E. Brus and Aleksey Yekimov. Nobel Prize Outreach.[15] Photo: Nanaka Adachi.

Aleksey Yekimov laid the foundation for understanding quantum confinement effects in semiconductor nanocrystals. His research group studied doped glasses, aiming to understand particle formation and

structure. Analysing silicate glasses with added Cu and Cl, they measured optical absorption spectra at 4.2 ˚K and observed exciton lines sensitive to heat treatment.[42] Consequently, the team concluded that a crystalline CuCl phase formed within the glass matrix through phase decomposition, and by adjusting the heating temperature and duration, they could control the crystal size. formed.[43] X-ray scattering confirmed crystal sizes ranging from nanometres to tens of nanometres and confirmed the narrow size distribution with the model for growth through recondensation.[44] Yekimov observed that the wavelength of CuCl exciton absorption lines shifted with nanocrystal size and presented with blue-shifting for smaller crystals.[45, 46] He attributed this to quantum size effects, an observation that aligned with the long-standing theoretical predictions where the absorption line position scaled inversely with the square of the average nanocrystal radius.

Yekimov's research demonstrated that quantum size effects could be observed in semiconductor quantum dots within a glass matrix, using traditional glass making methods. A limitation was that these quantum dots were embedded in glass and not amenable to further investigation or processing.

Once a method was developed to synthesise quantum dots as colloids using a sol-gel process, QDs became suitable for further processing. In 1983, Louis Brus and his colleagues investigated colloidal CdS nanoparticles, observing their quantum size effects. They synthesised small CdS particles in solution, stabilised to prevent aggregation.[47] The freshly prepared colloid had a narrow size distribution around 4.5 nm, but over time the particles dissolved and recrystallised into larger particles around 12.5 nm.[48, 49] Spectroscopic analysis presented a blue shift and broadening of the exciton line in smaller particles, attributed to quantum confinement. Brus developed a theoretical model to describe how particle size influences redox potentials and exciton energy, and later incorporated electron-hole interactions.[11, 50]

Research on colloidal nanocrystals was hindered by inconsistent quality and properties. The nanocrystals available in the late 1980s had low luminescence quantum yields, and showed variations in size, shape, crystallinity.[51-54] This limited the ability to utilise their quantum size effects for desired physical and chemical characteristics.

In 1993, Moungi Bawendi and colleagues developed the hot injection synthetic method for creating quantum dots with well-defined sizes and high optical quality. Sharp absorption spectra were observed at room temperature, shown in Figure 1.6.[55] This breakthrough facilitated the development of colloidal quantum dot applications. Bawendi and colleagues represented a flexible and reliable chemical technique for producing monodisperse nanoparticles across a diverse range of material systems. This breakthrough consequently enabled the advancement of large-scale quantum dot applications.

Finally, the particles can be purified and separated by size. The result is macroscopic amounts of nanoparticles with consistent core structure, shape, surface properties, and well-defined sizes determined by temperature control during growth. This produced relatively sharp optical absorption and emission spectra at room temperature, with luminescence quantum yields up to 10%. By sampling during growth, a range of particle sizes can be obtained in a single run.

The discovery of colloidal quantum dots led to significant efforts to improve their quality and explore their applications.[56] The development of core-shell quantum dots, with a wide-bandgap shell confining electrons and holes in the small-bandgap core, enhanced the optical quality.[57, 58] Modifications to the synthesis method enabled the addition of the extra shell layer,[59] resulting in CdSe/ZnS core-shell quantum dots with high luminescence quantum yield, better stability, and reduced bleaching compared to uncapped dots.

The development of water-soluble quantum dots with good optical properties allowed their integration with biological systems, overcoming the limitation of previous quantum dots synthesised in organic solvents. Methods like adding a silica layer or using bifunctional ligands enabled covalent attachment of biomolecules, preserving the quantum dots' optical advantages for biomolecular labelling and imaging.[60, 61]

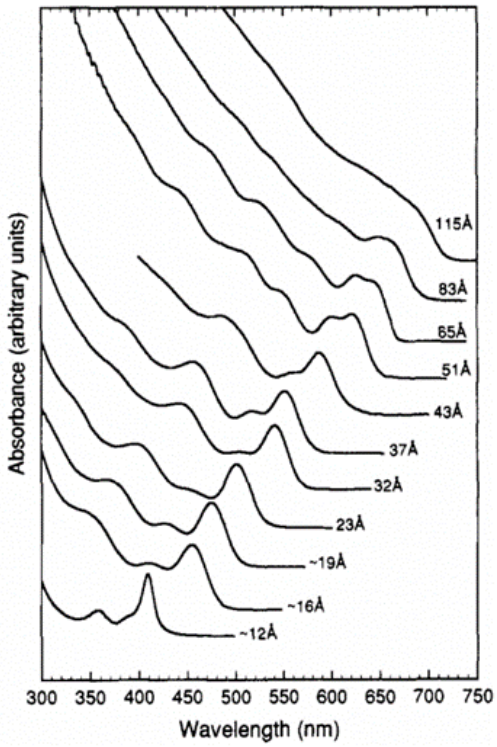

Figure 1.6 Room-temperature optical absorption spectra of CdSe nanocrystallites dispersed in hexane and ranging in size from ~12 to 115 Å.[55]

Subsequent research expanded the scope of quantum dots, leading to a better understanding of the growth mechanism of quantum dots, and therefore the development of different structures of nanomaterials, like elongated quantum rods and thin quantum platelets.[62-65] Their tuneable bandgap, efficient light absorption and emission, and ease of fabrication make them highly versatile.[66-70] For example, the global market size of quantum dots was estimated $4 billion in 2021 with application in lighting, display technologies, and biomedical imaging are at the forefront.[71, 72] Ongoing nanotechnology research explores their use in infrared photodetectors, solar energy conversion, light-emitting diodes, diagnostics, and photocatalysis.

1.4.3 Quantum Dot Applications

The first quantum dot technology commercialised, and of which I am a proud owner, is QLED (Quantum Dot Light-Emitting Diode) display technology. QLED displays utilise the precise emission characteristics of quantum dots to achieve superior colour accuracy and wider colour gamut compared to conventional LCDs (Liquid Crystal Displays).[73] QLED is a self-emissive technology, which integrates a thin-film transistor layer, a light source, and a light-emitting QD layer.[74] By combining red and green emitting QDs with a blue light

source, it provides superior colour accuracy and brightness. This technology offers a simpler and more efficient design than LCDs, eliminating the need for a backlight and resulting in thinner, lighter displays. QLED offers additional advantages including, uniform emission, improved contrast ratio, and reduced after imaging.

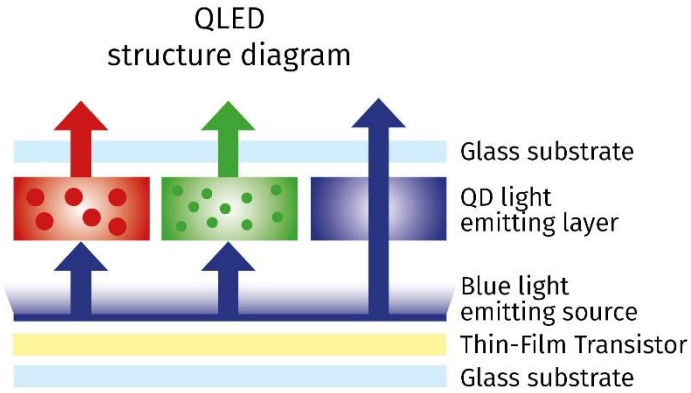

Figure 1.7 General structure of a QLED tv.

Quantum dot-sensitised solar cells (QDSSCs) have advanced photovoltaic technologies by building upon dye-sensitised solar cells, exploiting the quantum confinement effects of quantum dots to tune their bandgaps and enhance light absorption. Depicted in Figure 1.8, the mechanism of the QDSSC is as following: When light illuminates a quantum dot sensitised solar cell, the light-absorbing material releases electrons from its valence band to its conduction band within a specific visible light spectrum. These excited electrons move through a network of wide bandgap oxide materials (titanium oxide), to which the light absorbers are typically attached. Ultimately, these electrons reach the conducting substrate and then the external circuit, where they generate electricity for a load. Simultaneously, the oxidised light-absorbing material, now electron-deficient, receives supplementary electrons from the electrolyte system to regain stability. The electrons from the external circuit then return to the electrolyte system via the counter electrode, stabilising it. This process continues as long as there is light.[75]

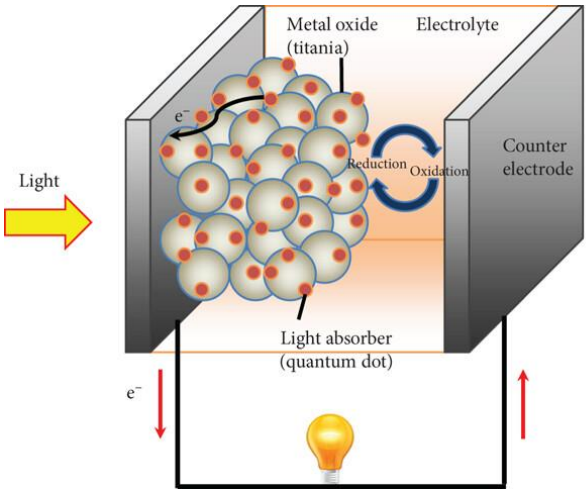

Figure 1.8, Mechanism of the quantum dot-sensitised solar cell.[75]

The efficiency gap between quantum dot sensitised solar cells and other emerging solar cell technologies, such as dye-sensitised and thin-film solar cells, is diminishing, with QDSSC efficiency exceeding 15% has been reported.[75] The reasons for this improvement include better performance of the sensitiser materials used, the application of doping agents, and an enhanced surface passivation strategy. QDSSCs offer advantages such as leak-proof construction and straightforward handling compared to traditional liquid-junction designs.[76] The size of QDs can be tuned to match the absorption spectra of organic dyes, thereby enhancing photovoltaic performance in hybrid solar cells.[77] This advancement in solar cell technology has triggered the development of tandem and multijunction cells, further improving solar cell efficiency. Additionally, the aesthetic integration of solar cells into building designs has transformed urban development which seamlessly combines energy generation with the built environment.[78] Beyond traditional photovoltaic applications, quantum dots are also being explored for their potential in next-generation solar concentrators and transparent solar cells, capitalising on their tuneable absorption and emission profiles.

In photocatalysis, QDs serve as efficient light harvesters and facilitate charge separation.[79-84] Their broad absorption spectrum, high extinction coefficients, photostability, and tuneable emission, coupled with reduced costs contribute to their effectiveness.[85] Quantum dot heterojunctions address key issues in energy conversion and environmental remediation by enhance photocatalytic efficiency and promote the advancement of sustainable technology.[86] The three main applications for photocatalysis of QD coupled heterojunctions include hydrogen production for the generation of a clean energy source, reduction reactions for conversion of CO_2 into solar fuels, and degradation of pollutants for environmental remediation technologies.

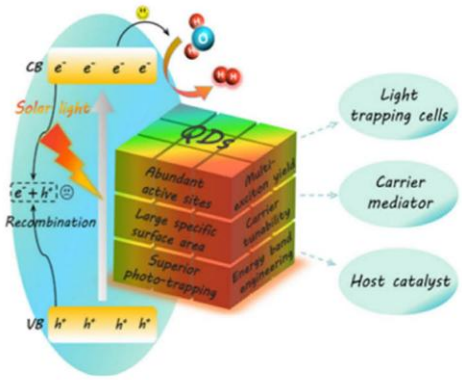

Figure 1.9, The role of quantum dots in QD-coupled heterojunction for photocatalysis[86]

QDs excel in photoluminescence sensing of chemical pollutants and biologically important species, cellular and in vivo imaging, and disease diagnosis and forensics, where the presence of an analyte can quench their luminescence.[87] Quantum dots are applied in technologies quantitative detection due to their effectiveness in facilitating redox reactions and charge-transfer phenomena. This allows for sensitive and selective detection of various analytes, including metal ions, organic contaminants, and biomolecules, crucial for environmental monitoring and biomedical applications, demonstrated in Figure 1.10.[88-103] They offer narrower emission spectra and superior optical characteristics compared to organic fluorophores, complemented by their high photostability and resistance to photobleaching.[89, 104] Modification of QDs has expanded the technology to detection of explosives, pharmaceuticals, hazardous compounds, and a wide range of metal ions. Despite

these many elegant investigations, some essential problems remain, hampering the commercialisation of QD sensors, including quantitative analyte detection, sensor standardisation and batch-to-batch reproducibility, and the prevalent toxicity of many heavy-metal-based quantum dots.[87]

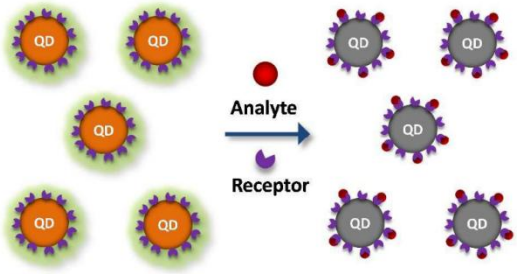

Figure 1.10, Detection of analyte using QDs[87]

Biomedical imaging is possible by conjugation of quantum dots with various biomolecules such as antibodies, DNA, proteins etc. for targeting them to various organelles.[105] QDs are brighter and more resilient to photobleaching when contrasted with conventional organic dyes and fluorescent proteins. Such properties are advantageous for dynamic imaging at the single-molecule level and for achieving ultra-high sensitivity in multiplexed biomedical diagnostics.[106] In Figure 1.11, an example of bioimaging of PbS QDs in the lymph nodes of a mouse is shown.

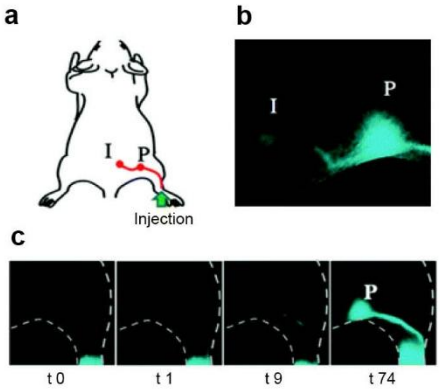

Figure 1.11, (a) Mouse lymph system. (b) Biological imaging of PbS QDs in lymph nodes. (c) Biological imaging of PbS QDs in lymph nodes with different time courses.[107]

Beyond these primary areas, QDs also find applications as magnetic materials through doping,[108, 109] as electrodes when deposited on conductive substrates,[110] Regarding health and environmental concerns researchers have extensively investigated the potential health impacts of quantum dots, particularly in the context of their medical and biological applications. Ongoing efforts are focused on developing less hazardous and more eco-friendly production methods for quantum dots. A key priority is to eliminate the use of heavy metals like cadmium, lead, and mercury in the fabrication of quantum dots, as these elements pose significant environmental and health risks. Alternative materials and synthesis techniques are being explored to create quantum dots that are inherently safer and more sustainable.

1.5 Carbon Dots: Sustainable Alternatives and their Impact

Carbon dots stand out as an environmentally sustainable material due to their synthesis from renewable biomass, their intrinsic eco-friendly properties such as low toxicity and excellent biocompatibility, and their versatile applications in environmental remediation, including pollutant detection and water treatment. Their production from diverse biological materials, including organic waste and side-products. Utilising such renewable precursors not only aligns with sustainable development goals, but also adds value to agricultural, marine, and forestry waste, mitigating environmental concerns.[111]

Carbon dots have emerged as a new class of carbon-based fluorescent nanomaterials. These nanoparticles typically measure less than 10 nanometres in diameter and are generally considered non-toxic and biocompatible. In 2004 carbon dots were discovered by Xu *et al*. as fluorescent nanoparticles during the purification of single-walled carbon nanotubes, illustrated in Figure 1.12.[112] Since then major advancements in surface functionalisation, solubility, and control in emission have improved the field of carbon dots.[112-118]

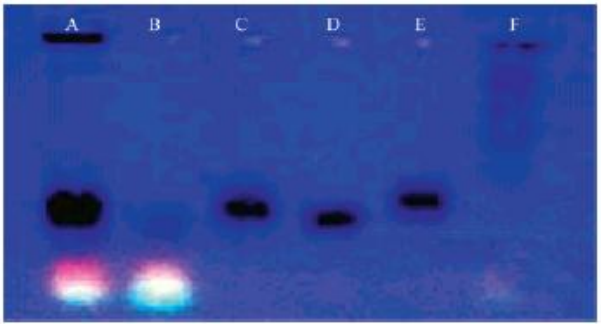

Figure 1.12, First report of carbon dots: Electrophoretic profile in 1% agarose gel under 365-nm UV light. (A) crude SWNTs suspension. (B) Fluorescent carbon. (C) Short tubular carbon. (D) and (E) Further separation of (C). (F) Cut SWNTs.[112]

Despite their quantum dot like optical properties and their similar size range of 2 – 10 nm, quantum dots and carbon dots possess significant underlying differences as provided in Table 1.2. While QDs emit light due to the precise confinement of electrons within their semiconductor structure, CDs' emitted light arises from a complex interplay of the carbon core's intrinsic optoelectronic properties and surface chemical functionalities.[113] This results in a bigger challenge to obtain control compared to the elegant size-dependent optical characteristics of quantum dots. Due to the complexity and ongoing research, terminology may vary across different studies.[119]

Table 1.2, Properties of quantum and carbon dots

	Quantum dots	**Carbon dots**
Material	Inorganic semiconductors	Carbon-rich
Band gap	Well-defined and tuneable	Complex and limited tuneability
Costs	High	Low
Hazard	Toxic	Non-toxic
Application	Displays, LED, photovoltaics, lasers, medical imaging and sensing	Bio-imaging, drug delivery, sensing, water treatment, environmental remediation

1.5.1 Carbon Dot Classification

In addition to the differences between quantum dots and carbon dots, carbon dots can also be divided into different types based on their distinct core structures and optical characteristics. These classifications are primarily driven by the precursor materials and synthetic methodologies employed, which dictate the atomic arrangement and resultant photophysical behaviours of the nanomaterials. Generally, carbon dots are categorised into graphene quantum dots (GQDs)[120], carbon quantum dots (CQDs), carbon nanodots (CNDs), and carbonised polymer dots (CPDs). In Table 1.3 an overview of the four types of carbon dots is given. The differences between the types of carbon dots are also illustrated in Figure 1.13.

Table 1.3, Carbon nanoparticles overview[113]

Type	Structure	Hybridisation	Precursors	Example	Preparation	PL mechanism
GQDs	Single-to-few-layer graphene Discoidal shaped graphene sheets	sp^2	Polymers or aromatic precursors	Graphene or graphite	Top-down	QCE or conjugated π domains
CQDs	Crystalline core Quasi-spherical,	sp^2	Small molecules	CA or carbohydrates	Top-down or bottom-up	QCE or conjugated π domains
CNDs	Amorphous Quasi spherical	sp^2 or sp^3	Small molecules or polymer precursors	Carbohydrate rich biomasses	Top-down or bottom-up	Defect states, molecular states, or crosslink-enhanced emission
CPDs	Amorphous or semi-crystalline Quasi spherical,	sp^3	Polymer precursors	polymers	Bottom-up	Molecular states or crosslink-enhanced emission

In this study, synthesis of carbon nanodots (CNDs) is attempted since the precursor of choice is seaweed, a carbohydrate rich biomass, and aimed at the introduction of defect states through the wide availability of functional groups and minerals present in the biomass.

1.5.2 Luminescence Mechanisms of Carbon Dots

The luminescent properties of carbon dots, including the mechanisms governing their fluorescence, are an active area of research. Proposed theories included in Table 1.3 are the quantum confinement effects, surface states and defects, molecular fluorescence, and crosslinked-enhanced emission.[119]

- Molecular (fluorophore) states – when the fluorescence is determined by molecules attached to the surface or embedded within the carbon dot. In which case, the carbon dot acts as a scaffold and the luminescence originating from the connected molecular species.
- Quantum confinement effects (QCEs) – due to the restricted dimensions of the conjugated π-domains at the nanoscale, the confinement of both electrons and holes within the nanoscale structures leads to discrete energy levels and the ability to tune their optical properties.
- Crosslink-enhanced emission states – the enhancement of fluorescence due to the crosslinking in carbon dots or the formation of fluorophore aggregates. The restricted molecular motion and increased rigidity in these structures contribute to enhanced radiative recombination and luminescence.

- Surface state and defects – stemming from functional groups attached to the surface, alongside intrinsic defects, serve as luminescence centres, influencing the overall emission. The strategic introduction of diverse functional groups (e.g., -OH, -COOH, $-NH_2$) significantly enhances their solubility, dispersibility, and facilitates specific surface modifications.

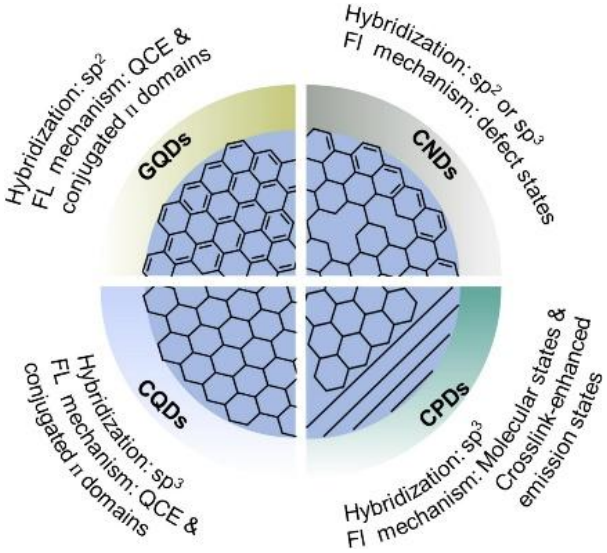

Figure 1.13, The four types of carbon dots structure and features illustrated[113]

1.5.3 Literature examples of understanding luminescence mechanism in carbon dots

Illustrated in Figure 1.14, Ding *et al*., found that the surface state, more specifically the degree of oxidation caused variation in photoluminescence emission between synthesised CDs.[121] The researchers used a hydrothermal method and silica column chromatography to create CDs that emit bright, stable light in a gradient of colours from blue to red under UV light. As the incorporation of oxygen species into the surface structure increases, the band gap decreases, resulting in a red shift in the emission peak.

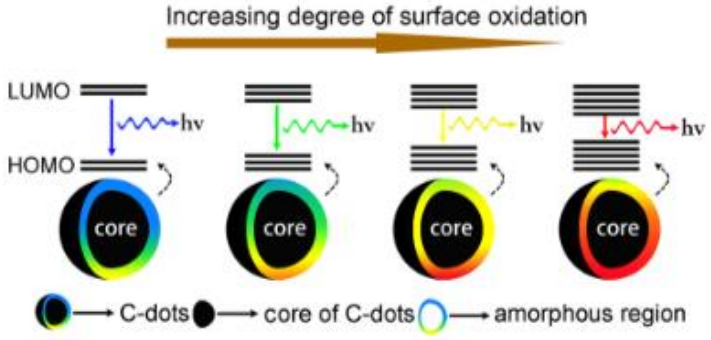

Figure 1.14, Model for the tuneable PL of CDs with different degrees of oxidation.[121]

Schneider *et al*., found that molecular fluorophores, specifically derivatives of citrazinic acid, contributed to the blue emission in CDs.[122] They synthesised three CD samples using citric acid with different nitrogen sources. By analysing nitrogen content, FTIR spectra, and optical spectra, they found that CDs synthesised with ethylenediamine, and hexamethylenetetramine exhibited molecular fluorophores that contributed to the blue emission.

Illustrated in Figure 1.15, quantum confinement effects – Ding *et al*. presented a second paper in which they manipulated reaction conditions (molar ratios, reaction time, temperature) to control the photoluminescent properties of CDs, achieving blue to red emission colours. They highlight the role of varying graphitisation

and nitrogen content leading to QCEs tuneability and narrowing the band gap produced a red shift.[123] Controlling deamination and dehydrogenation reactions allows modulation of these factors and fine-tuning of CD colour emission.

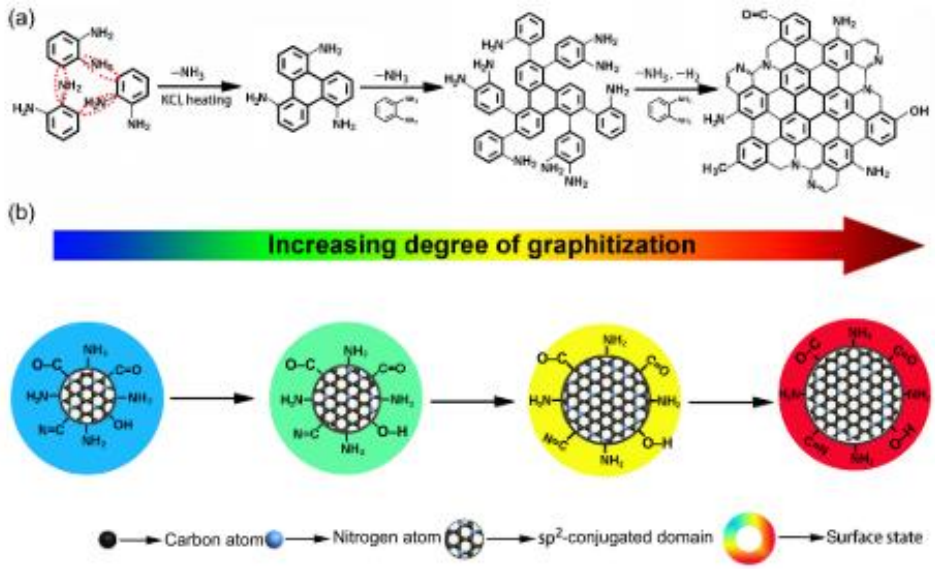

Figure 1.15, A formation mechanism (a) and PL mechanism (b) for CDs with tuneable PL emission.[123]

1.5.4 Strategies to Control Carbon Dot Properties

As seen in Table 1.3, carbon dot properties are closely tied to structure, precursor, and photoluminescence mechanism. When producing carbon dots, several considerations should be made: the intended application, the suitable photoluminescence mechanism for that application (which dictates the type of carbon dot), and the precursor and synthesis method that will yield the desired optical properties. A thorough understanding of the intricate relationship between synthetic conditions and resulting carbon dot characteristics is paramount for tailoring their performance to specific applications, as highlighted in the previous section. Key synthetic variables include reaction temperature, duration, pressure, and solvent. While some parameters are direct, others are influenced by multiple factors; for instance, reaction temperature and the ramp rate affect particle formation. Pressure within the reaction is determined by the fill fraction, temperature, and external system pressure.

Guo *et al.* demonstrated that the employment of a machine learning-based (ML), closed-loop strategy can be used to optimise the solvothermal synthesis of carbon quantum dots. This approach considered all variables including synthesis parameters such as reaction time, temperature, ramp rate, volume, and the selection of precursor, catalyst, and solvent. Desired properties, including photoluminescence wavelength and quantum yield, were achieved, producing full-colour fluorescent CQDs with high PLQY in just 20 iterations, shown in Figure 1.16.[124] However no true understanding of the photoluminescence emission was gained through this method.

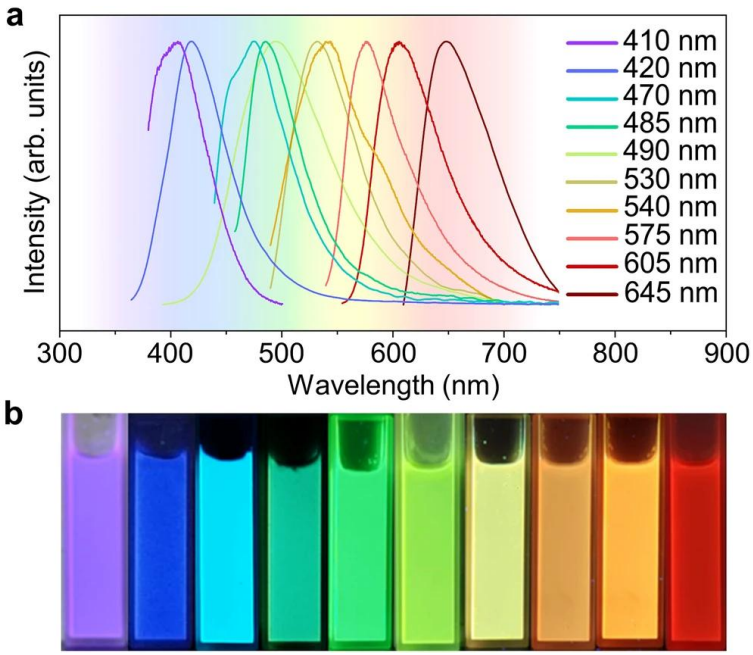

Figure 1.16, (a) Normalised photoluminescence spectrum of CDs, and (b) CQDs under 365 nm-UV light.[124]

1.6 Nucleation and Growth: Fundamental Mechanisms in Formation of Solid Materials

To gain true understanding of luminescence mechanisms, structure of (nano)materials and impact of synthesis parameters, the fundamental process of nucleation and growth should be considered. This process describes how atoms or molecules begin to cluster, lock in material properties, and dictate subsequent growth pathways.[125] This phase emergence from a homogeneous state is fundamentally governed by thermodynamics and kinetics, which dictate the composition, shape, and structure of resulting nanomaterials. Materials originate through nucleation, the formation of nuclei in solution or at interfaces. Growth follows, with both monomeric and oriented attachment, succeeded by phase transformation. Nucleation dictates the location and size of nuclei, while growth governs the size, shape, and aggregation of new nanoparticles, significantly influencing their functionalities, reactivities, porosities, and overall fate and transport. Mastering control over nucleation and growth during synthesis is therefore essential for tailoring material properties for targeted applications, particularly in nanotechnology.

Over the past decades, theoretical studies have tried to explain the complex processes of nucleation and growth. The Classic Nucleation Theory (CNT) explains nucleation as a process driven by thermodynamic variables that reduce the system's free energy.[126-129] A nucleus is modelled as a stable sphere with surface tension equivalent to a flat interface. This simplification, while offering a foundational understanding, often diverges from experimental observations, particularly for nanoscale systems where surface energy contributions become disproportionately significant.

The Rule of Stages is a sophisticated theory proposed by Ostwald in 1897 to accurately characterise intricate nucleation and growth phenomena.[130] Ostwald observed that material formation does not always proceed directly from solution to the final equilibrium state but can involve transitional intermediate states. The Rule

of Stages proposes that a system often passes through a series of metastable phases before reaching the most thermodynamically stable form.

The LaMer model, shown in Figure 1.17, was proposed in the 1950s and describes particle formation in solution-phase syntheses by separating nucleation and growth stages.[131] It explains how rapid monomer generation (I) leads to a supersaturation state, triggering a burst of nucleation (II). Subsequently, the monomer concentration drops below the critical level for new nucleation but remains sufficient for existing nuclei to grow through diffusion and Ostwald ripening (III), leading to monodisperse particle size distributions.

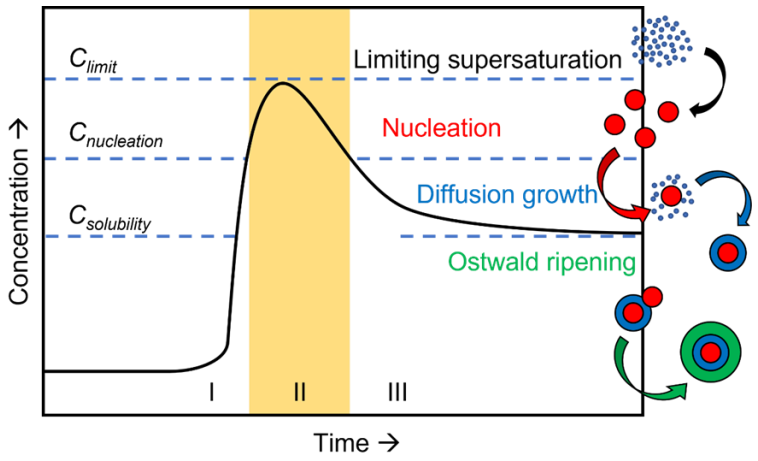

Figure 1.17, The three stages of particle formation in the LaMer model: (I) Increasing monomer concentration leading to supersaturation, (II) a rapid nucleation burst once a critical threshold is reached, and (III) particle growth via mechanisms like diffusion and Ostwald ripening, where smaller nuclei may redissolve and redeposit onto larger ones (focusing).

However, for many nanoscale systems, ordered phases involve non-classical nucleation and growth processes, which include multistep nucleation and intermediate-mediated self-assembly, influencing the ultimate product.[132-134] Such nonclassical pathways often involve the formation of dense liquid precursors or amorphous intermediates that subsequently transform into crystalline phases, challenging traditional views of direct solid-state crystallisation.[135] This complexity arises because the energy landscape for nucleation and growth at the nanoscale is often highly complex, with various pathways competing simultaneously.

To imagine this concept of nucleation and growth, an experiment of dancing peanuts in beer could be demonstrated.[136] Peanuts, denser than beer, exhibit a cyclical up-and-down movement. This peanut dance is shown in Figure 1.18. Heterogeneous bubble nucleation occurs on the peanut's surface. These attached bubbles increase its buoyancy, causing it to rise. Upon reaching the surface, the bubbles detach and burst, leading the peanut to lose buoyancy and sink. This cycle repeats as long as the beer remains supersaturated with gas.

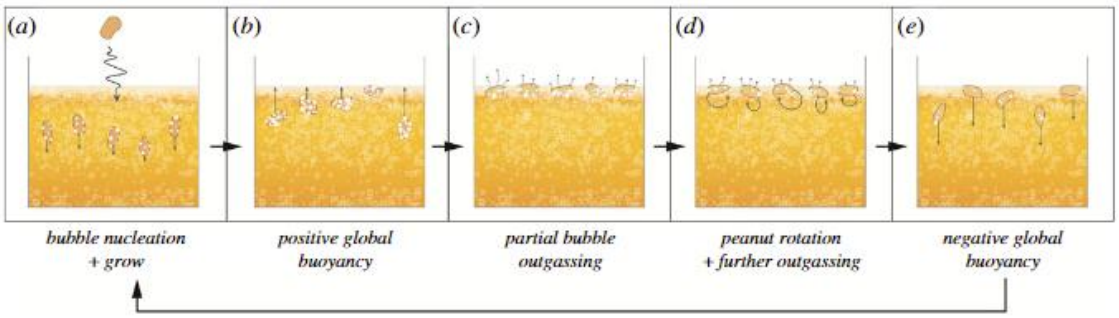

Figure 1.18, The peanut dance, analogue for nucleation and growth, (a) heterogeneous bubble nucleation occurs on the peanut surfaces, (b) attached bubbles increase the peanut's buoyancy, causing it to rise, (c) at the surface, bubbles detach and burst (d) reaching negative buoyancy of the peanut, (e) the peanut sinks, repeating the cycle if the beer remains supersaturated with gas.[136]

Having established the fundamental mechanisms of material formation, the next section will focus on synthesis methodologies employed for producing nanomaterials. These methods are carefully selected and optimised to yield specific material characteristics and morphologies.

1.7 General Approaches to Nanomaterial Synthesis

In Table 1.3 it was indicated carbon dots are either produced through bottom-up or top-down synthesis methods. This general division involves the following: Bottom-up methods include the assembly of nanostructures from atomic or molecular precursors, offering precise control over composition and structure. Conversely, top-down approaches involve the breakdown of bulk materials into nanoscale dimensions. A wide variety of physical, chemical, and biological methods are utilised for synthesising nanomaterials, with physical techniques typically falling under the top-down category, and chemical and biological methods aligning with bottom-up strategies. In the next sections, relevant methods for the synthesis of quantum and carbon dots are explained.

1.7.1 Top-down syntheses of photoluminescence nanomaterials

The top-down approach involves reducing the size of a larger, bulk material to create nanoscale structures, often through physical processes like lithography, milling, or etching. Relevant for the synthesis of quantum and carbon dots are the following methods:

- Pyrolysis – Thermal decomposition of organic material at elevated temperatures in the absence of oxygen, producing bio-oil, biochar, and syngas temperature, converting them into carbon-rich materials that form carbon dots
- Electrochemical exfoliation employs an applied electric field to exfoliate layered bulk materials, such as graphite rods, into individual sheets.[137, 138]
- The liquid-phase exfoliation method uses ultrasonication in organic solvents to exfoliate larger carbon precursors into graphene quantum dots.[139]

High-energy ball milling, physical vapor deposition, and laser ablation are also employed for nanoparticle synthesis, though they often require high energy input and specialised equipment.

1.7.2 Bottom-up syntheses of fluorescence nanomaterials

The golden crown in nanomaterial synthesis is the hot-injection method, a bottom-up technique, precisely controls nanoparticle size and monodispersity by rapidly introducing precursors into a hot coordinating solvent, ensuring a swift, uniform nucleation burst followed by controlled growth. This method developed by

Bawendi received the Nobel Prize in Chemistry in 2023, and depicted in Figure 1.19.[55] The control in particle size is practiced through the principle of temporally discrete nucleation followed by growth.
The hot injection method is broken down in three steps:

a. The injection of reactants causes instant supersaturation of the reagents and
b. triggers nucleation and the formation of small nanocrystals. However, the sudden temperature drop and precursor dilution, stop the particle growth.
c. Subsequent reheating allows a slow and controlled growth and annealing in the coordinating solvent, resulting in a colloidal dispersion.

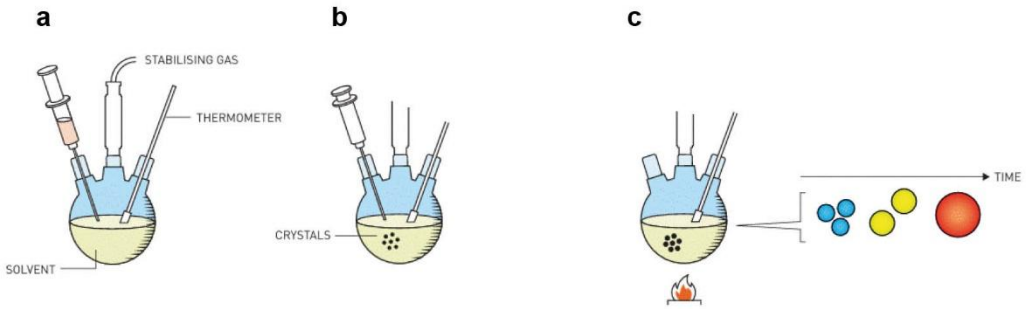

Figure 1.19, Bawendi's hot-injection synthesis explained[15, 55]

Hydrothermal/solvothermal synthesis involves chemical reactions in a sealed vessel using water (hydrothermal) or an organic solvent (solvothermal), above the solvent's boiling point, allowing for elevated pressures and temperatures that facilitate unique crystal growth and phase transformations due to the enhanced solubility and reactivity of precursors under supercritical conditions. Control is achieved through temperature, reaction time, pressure, and the choice of solvent, which critically influence the morphology, crystallinity, and size distribution of the resultant nanomaterials.[140]

Other bottom-up approaches for the synthesis of photoluminescence nanomaterials include:

- Microwave-assisted synthesis – Microwave radiation is used to rapidly and uniformly heat the reaction mixture, leading to quick synthesis of nanomaterials
- Electrochemical synthesis – Small organic molecules are oxidised and polymerised within an electrochemical cell containing two electrodes submerged in an electrolyte solution.

These bottom-up approaches, generally offer environmental friendliness, cost-effectiveness, and ease of operation, facilitating the synthesis of various nanomaterials like carbon dots from diverse precursors.[141]

1.7.3 Current Challenges in Nanomaterial Synthesis

Despite significant advancements in synthetic methodologies, several challenges persist, including achieving batch-to-batch reproducibility, and scaling up production while maintaining cost-effectiveness and environmental sustainability. These challenges necessitate continued innovation in synthetic routes, focusing on green chemistry principles and scalable manufacturing techniques to bridge the gap between laboratory-scale research and industrial applications. Considerations such as the choice of solvents, minimising waste, and utilising renewable resources are key considerations in developing sustainable nanomaterial synthesis protocols. Aqueous methods that utilise water as solvent for chemical reactions offer a promising avenue for addressing some of these issues.

1.8 Hydrothermal Synthesis: Principles, Mechanisms, and Green Chemistry Integration

Hydrothermal synthesis offers a sustainable and environmentally friendly approach to the production of a wide range of materials and compounds. Hydrothermal synthesis is a specific type of solvothermal synthesis, where water is selected as the solvent instead of other organic solvents. The elevated temperature and pressure conditions in hydrothermal synthesis facilitate the dissolution and crystallisation of precursor materials, enabling the production of high-quality nanoparticles with controlled morphology.

Water is renewable, non-toxic, and readily available. Utilising water as a solvent has gained increasing attention in recent years, particularly in the context of the growing demand for sustainable and environmentally friendly chemical processes. Advantages include reduced energy consumption and the elimination of the need for volatile organic compounds, which can pose significant environmental and health risks.

1.8.1 Basic Principles of Hydrothermal Synthesis

The hydrothermal process, depicted in Figure 1.21, occurs in a sealed reaction vessel where precursor materials undergo decomposition or chemical reactions in the presence of water at temperatures exceeding 100 °C.[140] The pressure within the vessel is autogenous, (self-generated) and will depend on the fill fraction of the autoclave or is externally imposed through compression of the reaction medium. Depending on the experimental conditions, the hydrothermal system may be heterogeneous or homogeneous and can operate in subcritical or supercritical regimes.

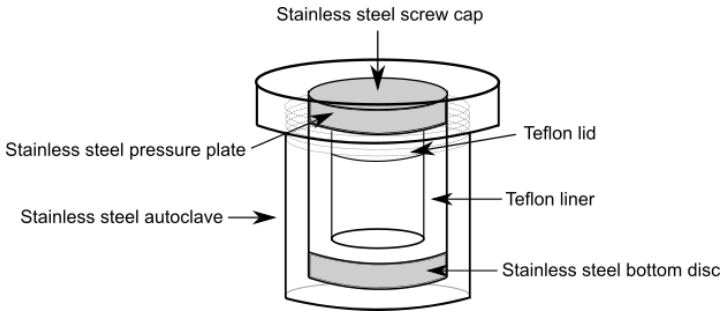

Figure 1.20, Illustration of a Teflon lined stainless-steel autoclave for hydrothermal synthesis

Under heterogeneous conditions, precursor materials may not fully dissolve in the solvent, leading to the coexistence of solid, liquid, and potentially gas phases within a sealed reaction vessel. While many nanomaterial syntheses rely on organic solvents due to water's limitations, such as its low boiling point and high polarity, these issues can be mitigated by using pressure to create superheated or supercritical water.[142, 143]

A key limitation of hydrothermal synthesis stems from safety considerations regarding the specific reactor design. This necessitates calculating anticipated pressures under isochoric conditions. Pressure values are estimated based on the reactor's fill fraction, utilizing binomial solutions derived from pressure-volume-temperature data, as reported by Kennedy.[144, 145]

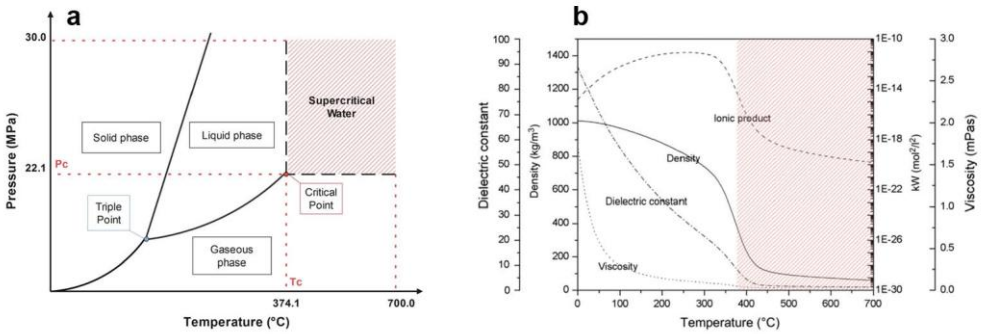

Figure 1.21, Phase diagram for pure water (a) and the properties of water as a function of temperature at 25 MPa (b).[146]

1.8.2 Advantages of Hydrothermal Synthesis and Green Chemistry Principles

The key scientific question for the chemical industry lies in designing a future-proof production system, It is not the question whether its products will be needed, but rather what the nature and production processes of the necessary synthetic chemicals for a sustainable society will be.[147] Chemistry has a long history of developing essential and beneficial products and processes, but this progress has often come at the cost of overlooking adverse consequences. Adhering to (inter)national goals and policies regarding energy consumption and greenhouse gas emissions, a critical consideration for the chemical sector involves sustaining and enhancing performance metrics while simultaneously mitigating or eradicating negative environmental consequences. Addressing this urgent challenge requires a systematic approach that goes beyond altering production conditions to changing the inherent nature of chemical products and processes. Redefining "performance" to be included with both function and sustainability, which can be achieved through thoughtful molecular design.

Over the past decade, green chemistry has made significant advancements in relevant research domains, such as catalysis, safer chemicals, and renewable feedstocks. The start can be dated back to 1962, when Rachel Carson published the mainstream, scientific book *Silent Spring,*[148] in which she highlighted the damaging effects of certain chemicals on local ecosystems, shown in Figure 1.22 (a). This served as a wake-up call that inspired the modern environmental movement. After this publication, the U.S. Congress passed the National Environmental Policy Act in 1969, which aimed to foster a productive harmony between humans and nature and established the Presidential Council on Environmental Quality. Later in 1998, the 12 principles of green chemistry were outlined in *Green Chemistry: Theory and Practice,*[149] by Paul Anastas and John Warner, shown in Figure 1.22 (b). The book laid out a philosophy that inspired academic and industrial scientists back then and still influences the green chemistry movement today. A firm definition of green chemistry was assigned: “the design of chemical products and processes that reduce or eliminate the use and generation of hazardous substances”.[150]

Figure 1.22, Covers of (a) Silent Spring by Rachel Carson and (b) Green Chemistry – Theory and Practice by Paul Anastas and John Warner

Today chemists are being educated to design sustainable products and processes, which underscores the potential for chemistry to address global environmental challenges. The principles of green chemistry chart a path toward environmental and economic prosperity. As green chemistry becomes the new norm, the need for a distinct label will diminish, though future obstacles remain unforeseeable.[151]

The 12 principles of green chemistry include:[149]

1. Waste Prevention
2. Atom Economy
3. Less Hazardous Chemical Synthesis.
4. Designing Safer Chemicals.
5. Safer Solvents and Auxiliaries.
6. Design for Energy Efficiency.
7. Use of Renewable Feedstocks.
8. Reduce Derivatives.
9. Catalysis.
10. Design for Degradation.
11. Real-time Analysis for Pollution Prevention.
12. Inherently Safer Chemistry for Accident Prevention.

The 12 principles of green chemistry were extended to the 12 principles of engineering at the Sandestin Declaration in 2003.[152, 153] The principles of green chemistry and engineering are here to address the environmental and health concerns associated with traditional chemical processes and products. The goal is to make chemical synthesis and engineering more sustainable, reduce the use of hazardous substances, minimise waste, and design chemicals and processes that are inherently safer. By following these guiding principles, chemists and engineers can work towards a future where chemistry benefits humanity and the environment, rather than causing harm.

Opting for hydrothermal synthesis in nanomaterial production aligns with green chemistry principles, emphasising judicious solvent selection, energy optimisation, and minimised waste generation.

1.9 Recent Advances and Future Trends

The energy transition is fundamentally a materials transition. Moving to clean energy will require more minerals and metals than the current fossil fuel energy systems.This profound shift, even with enhanced circularity, carries substantial implications for raw material extraction, environmental sustainability, and intense global competition for access to these vital resources.[154] Potential vulnerabilities and dependencies within these supply chains have been investigated and identified, particularly concerning critical raw materials that underpin emerging technologies like nanotechnology and semiconductors.[155]

Quantum dots, with their adjustable properties and growing commercial viability, present promising avenues for decreasing reliance on conventional materials across various energy applications, thereby alleviating some resource-related pressures.[15] Although quantum dots were discovered in the 1980s, their recent recognition, highlighted by the 2023 Nobel Prize in Chemistry has propelled them into widespread scientific and industrial exploration. This renewed focus aims to enhance the quantum yield and stability of QDs and to expand their commercial technological applications in energy, climate action, and healthcare. Additionally, the production of carbon-based materials, particularly carbon dots, represents a promising path for sustainable technological progress. This is due to their renewable nature, low toxicity, cost-effectiveness, biocompatibility, and wide-ranging potential for applications in bioimaging, drug delivery, and energy applications.[156]

Fundamentally, societal progress relies on molecular building blocks that form the basis of our products. The availability of chemicals and chemical products is integral to our quality of life, contributing to everything from essential pharmaceuticals to advanced materials. The central challenge, therefore, lies in supplying society with critical chemical products that are simultaneously economical, sustainable, and high performing. Current chemical manufacturing paradigms often prioritise productivity, efficiency, and cost, which frequently leads to processes that generate substantial waste and rely on non-renewable feedstocks. In contrast, Green Chemistry, by definition, involves the development of chemical products and processes that minimise or eliminate the use and generation of hazardous substances. The emphasis on development of environmentally friendly materials and synthesis has started to gain traction, with governmental funding channelled towards research initiatives focused on sustainable materials and renewable energy technologies. For example, the recently SEAI-funded project, "C-dots" in our research group, explores the development of photovoltaic applications using seaweed-derived carbon dots synthesised via hydrothermal methods, demonstrating a clear commitment to fostering eco-conscious innovation. This project, therefore, exemplifies the growing trend toward leveraging natural, abundant resources for advanced material synthesis, aligning with broader goals of circular economy and reduced environmental impact.[156] Such efforts underscore the potential for carbonaceous nanoparticles to serve as next-generation smart materials for a multitude of applications, including full-colour solid-state lighting, photovoltaics, and catalysis. [157]

A non-profit organisation known as Beyond Benign, was co-founded in 2007 by Dr Amy Cannon and Dr John Warner, (co-author of Green Chemistry: Theory and Practice[149]) committed to educating and supporting both teachers and students on green chemistry and sustainable science. Through these efforts, Beyond Benign aims to empower future scientists and the public with the knowledge necessary to create and choose products

that benefit human health and ecological well-being.[158] This inherently requires a paradigm shift from conventional chemical synthesis to one that prioritises the intrinsic properties of molecules from the earliest design stages, ensuring products are benign, renewable, and degradable rather than toxic, depleting, or persistent.

Therefore, future research will focus on the holistic approach of circular materials and the bio-based economy. Focus on resource impact and management, and sustainable alternatives such as renewable sources will come to the foreground against a much bigger movement of the nature-positive economy: one that not only reduces harm but actively restores ecosystems through forward-looking policy and business action, embodying a commitment to environmental stewardship beyond mere sustainability.[159] The interest from a capital market perspective in these enterprises is growing, driven by a recognition of the long-term value creation potential inherent in environmentally responsible business practices. This trend is further amplified by increasing regulatory pressures and consumer demand for eco-friendly products and services, making Nature Positive Enterprises attractive investment opportunities. The integration of quantum dot technology into Nature Positive Enterprises offers a compelling synergy, particularly in areas such as advanced environmental sensing, renewable energy solutions, and efficient photocatalysis for pollution remediation.

1.10 Research Aims

This study investigates the hydrothermal synthesis of quantum dots and carbon dots — a green, scalable route to fluorescent nanomaterials with broad applications in optoelectronics, sensing, and renewable energy generation — while optimising key parameters such as temperature, time, and precursor selection to achieve high quantum yields and monodispersity. Specifically, it employs systematic and statistical methods to evaluate the influence of diverse precursor materials, including metals and biomass-derived sources, on the optical properties and structural characteristics of the resulting nanomaterials, thereby advancing green chemistry principles and the bio-based economy.. The three main research aims are:

- Achieve control over optical properties and size of cadmium sulfide quantum dots by systematic investigation of the hydrothermal method by varying reaction conditions including reactants, pH, molar ratio, and reaction time.
- Investigate the hydrothermal synthesis of carbon dots using seaweed and seaweed derivatives as renewable precursor and compare this method to the hydrothermal synthesis of CdS QDs.
- Investigate the Response Surface Method as method to optimise the optical properties of carbon dots from seaweed and seaweed derivatives, and minimise the formation of by-products in the hydrothermal method by varying the reaction time and temperature.

1.11 References

1. R. Gillespie, *Chemistry*, Allyn and Bacon, the University of California, 2nd edn., 1988.
2. J. Shackelford, *Introduction to Materials Science for Engineers*, Pearson Education, 8th edn., 2015.
3. N. Jones, *Nat.*, 2018, **561**, 163-166.
4. J. Neugebauer and T. Hickel, *WIREs Comput Mol Sci.*, 2013, **3**, 438-448.
5. J. Lee, *Computational Materials Science: An Introduction*, CRC Press, Boca Raton, 2nd edn., 2016.
6. A. Agrawal and A. Choudhary, *APL Mater.*, 2016, **4**.
7. A. Edelstein and R. Cammaratra, *Nanomaterials Synthesis Properties and Applications*, CRC Press, Boca Raton, 2nd edn., 1996.
8. M. Pozzi, S. Jonak Dutta, M. Kuntze, J. Bading, J. S. Russbult, C. Fabig, M. Langfeldt, F. Schulz, P. Horcajada and W. J. Parak, *J. Chem. Educ.*, 2024, **101**, 3146-3155.
9. A. Ekimov, A. Efros and A. Onushchenko, *Solid State Commun.*, 1985, **56**, 921 - 924.
10. Q. Wu, W.-S. Miao, Y.-D. Zhang, H.-J. Gao and D. Hui, *Nanotechnol. Rev.*, 2020, **9**, 259-273.
11. L. Brus, *JCP*, 1983, **79**, 5566-5571.
12. A. Goldstein, C. Echer and A. Alivisatos, *Sci.*, 1992, **256**, 1425-1427.
13. M. Scroggie, *Principles of Semiconductors*, Iliffe Books Ltd, 1961.
14. D. Bera, in *Drug Delivery Nanoparticles Formulation and Characterization*, CRC Press, 2009, DOI: 10.3109/9781420078053-23, pp. 369-386.
15. Nobel Prize Outreach 2025, Quantum dots – seeds of nanoscience, The Nobel Prize in Chemistry 2023, <https://www.nobelprize.org/prizes/chemistry/2023/advanced-information/>, (accessed Wed. 20 Aug, 2025).
16. R. Shankar, *Principles of quantum mechanics*, Plenum Press, 2nd edn., 1994.
17. A. Sommerfeld, *Z. Phys.*, 1928, **47**, 1-32.
18. F. Bloch, *Z. Phys.*, 1929, **52**, 555-600.
19. R. De Kronig and W. Penney, *Proc. R. Soc. Lond. A Math. Phys. Sci.*, 1931, **130**, 499-513.
20. A. L. Efros and L. E. Brus, *ACS Nano*, 2021, **15**, 6192-6210.
21. J. Lakowicz, *Principles of Fluorescence Spectroscopy*, Springer Science + Business Media, 3rd edn., 2006.
22. N. Borrelli, in *Semiconductor Nanocrystals: From Basic Principles to Applications*, eds. A. Efros, D. Lockwood and L. Tsybeskov, Springer Science + Business Media, LLC, Nanostructure Science and Technology, 2003, ch. 1, pp. 1-51.
23. A. Efros and L. Brus, *ACS nano*, 2021, **15**, 6192-6210.
24. H. Fröhlich, *Physica*, 1937, **4**, 406-412.
25. L. Landau, *Z. Phys.*, 1930, **64**, 629-637.
26. W. De Haas and P. Van Alphen, 1930.
27. I. Lifshitz and A. Kosevich, *JETP*, 1956, **2**, 636-645.
28. R. Kubo, *Phys. Soc. Jpn.*, 1962, **17**, 975-986.
29. V. Sandomirskiĭ, *J. Exp. Theor. Phys.*, 1963, **16**, 1630.
30. V. Lutskii and L. Kulik., *JETP Lett.*, 1968, **8**.
31. Y. Ogrin, V. Lutskii and M. Elinson, *JETP Lett.*, 1966, **3**, 114.
32. A. Fowler, F. Fang, W. Howard and P. Stiles, *Phys. Rev. Lett.*, 1966, **16**, 901.
33. M. Elinson, V. Volkov, V. Lutskij and T. Pinsker, *Thin Solid Films*, 1972, **12**, 383-397.
34. A. Stasenko, *Sov. Phys. Solid State.*, 1968, **10**, 186-+.
35. R. Arthur, *J. Appl. Phys.*, 1968, **39**, 4032-4034.
36. R. Dingle, W. Wiegmann and C. Henry, *Phys. Rev. Lett.*, 1974, **33**, 827.
37. C. Weisbuch, R. Dingle, A. Gossard and W. Wiegmann, *Solid State Commun.*, 1981, **38**, 709-712.
38. T. Ando, A. Fowler and F. Stern, *RMP*, 1982, **54**, 437.
39. Nobel Prize Outreach 2025, Advanced information on the Nobel Prize in Physics 2000, https://www.nobelprize.org/prizes/physics/2000/advanced-information/, (accessed 14 Oct, 2025).
40. Z. Alferov, *Phys. Scr.*, 1996, **1996**, 32.
41. H. Kroemer, *Phys. Scr.*, 1996, **1996**, 10.
42. A. Ekimov, A. Onushchenko and V. Tsekhomskii, *Sov. Glass Phys. Chem*, 1980, **6**, 511-512.
43. V. Golubkov, A. Ekimov, A. Onushchenko and V. Tsekhomskii, *Fiz. Khim. Stekla*, 1981, **7**, 397-401.
44. I. Lifshitz and V. Slezov, *JETP*, 1959, **35**, 8.
45. A. Ekimov and A. Onushchenko, *JETP Lett.*, 1981, **34**, 345-349.
46. A. Ekimov and A. Onushchenko, *Sov. Phys. Semicond.*, 1982, **16**, 775-778.
47. K. Kalyanasundaram, E. Borgarello, D. Duonghong and M. Grätzel, *Angew. Chem. Int. Ed.*, 1981, **20**, 987-988.
48. R. Rossetti, S. Nakahara and L. Brus, *J. Chem. Phys.*, 1983, **79**, 1086-1088.
49. R. Rossetti, J. Ellison, J. Gibson and L. Brus, *J. Chem. Phys.*, 1984, **80**, 4464-4469.
50. L. Brus, *JCP*, 1984, **80**, 4403-4409.

51. L. Brus, *Appl. Phys. A: Solids Surf.*, 1991, **53**, 465-474.
52. A. Henglein, in *Electrochemistry II, Topics in Current Chemistry,*, Springer-Verlag, 1988, vol. 143, pp. 113-180.
53. Y. Wang and N. Herron, *J. Phys. Chem.*, 1991, **95**, 525-532.
54. T. Dannhauser, M. O'neil, K. Johansson, D. Whitten and G. McLendon, *J. Phys. Chem.*, 1986, **90**, 6074-6076.
55. C. Murray, D. Norris and M. Bawendi, *JACS*, 1993, **115**, 8706 - 8715.
56. V. Colvin, M. Schlamp and P. Alivisatos, *Nat.*, 1994, **370**, 354-357.
57. A. Eychmüller, A. Hässelbarth, L. Katsikas and H. Weller, *J. Lumin.*, 1991, **48**, 745-749.
58. M. Hines and P. Guyot-Sionnest, *J. Phys. Chem*, 1996, **100**, 468-471.
59. B. Katari, V. Colvin and P. Alivisatos, *J. Phys. Chem.*, 1994, **98**, 4109-4117.
60. M. Bruchez, M. Moronne, P. Gin, S. Weiss and P. Alivisatos, *Sci.*, 1998, **281**, 2013-2016.
61. W. Chan and S. Nie, *Sci.*, 1998, **281**, 2016-2018.
62. X. Peng, J. Wickham and P. Alivisatos, *JACS*, 1998, **120**, 5343-5344.
63. X. Peng, L. Manna, W. Yang, J. Wickham, E. Scher, A. Kadavanich and P. Alivisatos, *Nat.*, 2000, **404**, 59-61.
64. D. Milliron, S. Hughes, Y. Cui, L. Manna, J. Li, L.-W. Wang and Paul Alivisatos, *Nat.*, 2004, **430**, 190-195.
65. S. Ithurria, M. Tessier, B. Mahler, R. Lobo, B. Dubertret and A. L. Efros, *Nat. Mater.*, 2011, **10**, 936-941.
66. C. Luan, A. Vaneski, A. Susha, X. Xu, H. Wang, X. Chen, J. Xu, W. Zhang, C. Lee, A. Rogach and J. Zapien, *Nanoscale Res. Lett.*, 2011, **6**.
67. Z. Yang, L. Lu, C. Kiely, B. Berger and S. McIntosh, *Ind. Eng. Chem. Res.*, 2016, **55**, 11235-11244.
68. R. K. Kokal, A. R. C. Bredar, B. H. Farnum and M. Deepa, *ACS Appl. Nano Mater.*, 2019, **2**, 7880-7887.
69. S. Sfaelou, V. Dracopoulos and P. Lianos, *J. Adv. Oxid. Technol.*, 2014, **17**, 53-58.
70. N. Du, L. Ren, W. Sun, X. Jin, Q. Zhao, Y. Cheng, T. Wei and Q. Li, *J. Power Sources*, 2015, **284**, 162-169.
71. *Quantum Dot Market Size, Share, Industry Report 2030*, 2024.
72. A. Abdellatif, M. Younis, M. Alsharidah, O. Al Rugaie and H. Tawfeek, *Int. J. Nanomed.*, 2022, **17**, 1951-1970.
73. D. Quesada-González and A. Merkoçi, *Biosens. Bioelectron.*, 2025, **273**, 117180.
74. D. Haynes, Samsung, what is Quantum Dot display technology?, https://insights.samsung.com/2021/12/29/what-is-quantum-dot-display-technology/, (accessed 18/08/2025, 2025).
75. H. Jun and H. Tung, *J. Nanomater.*, 2022, **2022**, 1-7.
76. S. Sfaelou, A. Kontos, P. Falaras and P. Lianos, *J. Photochem. Photobiol., A Chem.*, 2014, **275**, 127-133.
77. M. Abdelbar, T. Fayed, T. Meaz, T. Subramani, N. Fukata and E. Ebeid, *J. Photochem. Photobiol., A Chem.*, 2019, **375**, 166-174.
78. A. Firoozi, A. Firoozi and M. Maghami, *Energy Convers. Manage.:X.*, 2025, **27**, 101058.
79. V. Rajendran, A. König, K. S. Rabe and C. M. Niemeyer, *Small*, 2010, **6**, 2035-2040.
80. Y. Guo, L. Jiang, L. Wang, X. Shi, Q. Fang, L. Yang, F. Dong and C. Shan, *Mater. Lett.*, 2012, **74**, 26-29.
81. D. Sagdeev, R. Shamilov and Y. Galyametdinov, *J. Appl. Spectrosc.*, 2021, **88**, 539-545.
82. A. Samadi-Maybodi and M. Sadeghi-Maleki, *J. Inorg. Organomet. Polym. Mater.*, 2018, **28**, 2620-2632.
83. Y. Fan, M. Deng, G. Chen, Q. Zhang, Y. Luo, D. Li and Q. Meng, *J. Alloys Compd.*, 2011, **509**, 1477-1481.
84. Y. Song, N. Li, D. Chen, Q. Xu, H. Li, J. He and J. Lu, *Appl. Catal. B-Environ.*, 2018, **238**, 255-262.
85. C. Baslak, E. Aslan, I. Patir, M. Kus and M. Ersoz, *Int. J. Hydrogen Energy.*, 2016, **41**, 20523-20528.
86. W. Yu, H. Chamkouri and L. Chen, *Chemosphere*, 2024, **357**, 141944.
87. L. Cui, X.-P. He and G.-R. Chen, *RSC Adv.*, 2015, **5**, 26644-26653.
88. H. Wang, C. Chen, Y. Liu, Y. Wu, Y. Yuan and Q. Zhou, *Talanta*, 2019, **198**, 242-248.
89. S. Narimani, S. Saadatmand and N. Samadi, *Anal. Bioanal. Chem. Res.*, 2023, **10**, 25-32.
90. M. Liu, L. Xu, W. Cheng, Y. Zeng and Z. Yan, *Spectrochim. Acta A.*, 2008, **70**, 1198-1202.
91. T. Noipa, T. Tuntulani and W. Ngeontae, *Talanta*, 2013, **105**, 320-326.
92. N. Butwong, T. Noipa, R. Burakham, S. Srijaranai and W. Ngeontae, *Talanta*, 2011, **85**, 1063-1069.
93. S. Wang, J. Yu, P. Zhao, S. Guo and S. Han, *ACS Omega*, 2021, **6**, 7139-7146.
94. J. L. Chen and C. Q. Zhu, *Anal. Chim. Acta*, 2005, **546**, 147-153.
95. C. Yao, T. Lin, Z. Lian, S. Liao, Z. Yan and S. Wu, *J. Fluoresc.*, 2020, **30**, 1601-1609.
96. S. Han, J. Liu, Z. Gan, J. Liang and S. Zhao, *J. Chin. Chem. Soc.*, 2008, **55**, 1069-1073.

97. K. Wang, E. Dong, M. Fang, W. Zhu and C. Li, *J. Fluoresc.*, 2022, **32**, 1099-1107.
98. M. Zhang, F. Wan, S. Ge and J. Yu, Univ Jinan, Jinan, Peoples R China, 2011.
99. A. Kumar and R. K. Dutta, *Anal. Sci.*, 2017, **33**, 565-571.
100. S. Akshya, P. Hariharan, V. Kumar and S. Anthony, *Spectrochim. Acta A.*, 2015, **135**, 335-341.
101. K. Ahmed, A. Pichikannu and A. Veerappan, *Sens. Actuators B Chem.*, 2015, **221**, 1055-1061.
102. Y. Zeng, X. Li, C. Tang, H. Huang, Y. Wang, Z. Su, H. Zhao, Y. Hu and J. Li, Macau, Peoples R China, 2011.
103. S. Ge, C. Zhang, Y. Zhu, J. Yu and S. Zhang, *Analyst*, 2010, **135**, 111-115.
104. K. Rafiq, I. Sadia, M. Z. Abid, M. Z. Waleed, A. Rauf and E. Hussain, *ACS Biomater. Sci. Eng.*, 2024, **10**, 7268-7313.
105. B. Santos, P. M. Farias, F. Menezes, A. Brasil, A. Fontes, L. Romao, J. Amaral, V. Moura-Neto, D. Tenório, C. Cesar, L. Barbosa and R. Ferreira, *Appl. Surf. Sci.*, 2008, **255**, 790-792.
106. B. A. Kairdolf, A. M. Smith, T. H. Stokes, M. D. Wang, A. N. Young and S. Nie, *Annu. Rev. Anal. Chem.*, 2013, **6**, 143-162.
107. W. Yang, X. Li, L. Fei, W. Liu, X. Liu, H. Xu and Y. Liu, *Green Chem.*, 2022, **24**, 675-700.
108. D. Sagdeev, R. Shamilov, V. Voronkova, A. Sukhanov and Y. Galyametdinov, *Russ. Chem. Bull.*, 2020, **69**, 1749-1754.
109. S. Chen, J. Zhang, S. Song, R. Feng, Y. Ju, C. Xiong and L. Dong, *Langmuir*, 2016, **32**, 611-618.
110. K. Tanno, M. Ashokkumar and P. Mulvaney, *Colloid Surf. A-Physicochem. Eng. Asp.*, 1999, **146**, 293-298.
111. S. Sanni, A. Bayode, H. Brink, N. Haneklaus, L. Fu, J. Shang and H.-J. Fan, *JoX*, 2025, **15**, 43.
112. X. Xu, R. Ray, Y. Gu, H. Ploehn, L. Gearheart, K. Raker and W. Scrivens, *JACS*, 2004, **126**, 12736-12737.
113. A. Rasal, T. Subrahmanya, S. Kizhepat, G. Getachew, A. Ghule, R. Devan, W.-S. Hung, M. Fahmi, A. Wibrianto and J.-Y. Chang, *Coord. Chem. Rev.*, 2025, **533**, 216510.
114. A. Bourlinos, A. Stassinopoulos, D. Anglos, R. Zboril, M. Karakassides and E. Giannelis, *Small*, 2008, **4**, 455-458.
115. H. Li, X. He, Z. Kang, H. Huang, Y. Liu, J. Liu, S. Lian, C. H. A. Tsang, X. Yang and S. T. Lee, *Angew. Chem. Int. Ed.*, 2010, **49**, 4430-4434.
116. F. Yuan, T. Yuan, L. Sui, Z. Wang, Z. Xi, Y. Li, X. Li, L. Fan, Z. A. Tan, A. Chen, M. Jin and S. Yang, *Nat. Commun.*, 2018, **9**.
117. L. Wang, W. Li, L. Yin, Y. Liu, H. Guo, J. Lai, Y. Han, G. Li, M. Li, J. Zhang, R. Vajtai, P. M. Ajayan and M. Wu, *Sci. Adv.*, 2020, **6**, eabb6772.
118. Y. Shi, Y. Zhang, Z. Wang, T. Yuan, T. Meng, Y. Li, X. Li, F. Yuan, Z. A. Tan and L. Fan, *Nat. Commun.*, 2024, **15**.
119. S. Zhu, Y. Song, X. Zhao, J. Shao, J. Zhang and B. Yang, *Nano Res.*, 2015, **8**, 355-381.
120. S. Chung, R. A. Revia and M. Zhang, *Journal*, 2021, **33**.
121. H. Ding, S.-B. Yu, J.-S. Wei and H.-M. Xiong, *ACS Nano*, 2016, **10**, 484-491.
122. J. Schneider, C. Reckmeier, Y. Xiong, M. von Seckendorff, A. Susha, P. Kasák and A. Rogach, *J. Phys. Chem. C.*, 2017, **121**, 2014-2022.
123. H. Ding, X.-X. Zhou, Z.-H. Zhang, Y.-P. Zhao, J.-S. Wei and H.-M. Xiong, *Nano Res.*, 2022, 1-8.
124. H. Guo, Y. Lu, Z. Lei, H. Bao, M. Zhang, Z. Wang, C. Guan, B. Tang, Z. Liu and L. Wang, *Nat. Commun.*, 2024, **15**.
125. Y.-S. Jun, Y. Zhu, Y. Wang, D. Ghim, X. Wu, D. Kim and H. Jung, *Annu. Rev. Anal. Chem.*, 2022, **73**, 453-477.
126. M. Volmer and A. Weber, *Z. phys. chem*, 1926, **119**, 277-301.
127. L. Farkas, *Z. Phys. Chem*, 1927, **125**, 236.
128. R. Becker and W. Döring, *Ann. Phys. (Berl.)*, 1935, **416**, 719-752.
129. Y. B. Zeldovich, *Acta Phys. Chim. URSS.*, 1943, **18**, 1.
130. W. Ostwald, *Z. Phys. Chem*, 1897, **22**, 289-330.
131. V. Lamer and R. Dinegar, *JACS*, 1950, **72**, 4847-4854.
132. S.-T. Yau and P. G. Vekilov, *Nat.*, 2000, **406**, 494-497.
133. S. Karthika, T. Radhakrishnan and P. Kalaichelvi, *Cryst. Growth Des.*, 2016, **16**, 6663-6681.
134. P. Smeets, A. Finney, W. Habraken, F. Nudelman, H. Friedrich, J. Laven, J. De Yoreo, P. M. Rodger and N. Sommerdijk, *PNAS.*, 2017, **114**, E7882-E7890.
135. D. Gebauer and H. Cölfen, *Nano Today*, 2011, **6**, 564-584.
136. L. Pereira, F. Wadsworth, J. Vasseur, M. Schmid, S. Thivet, R. Nuernberg and D. Dingwell, *R. Soc. Open Sci.*, 2023, **10**.
137. K. Parvez, Z.-S. Wu, R. Li, X. Liu, R. Graf, X. Feng and K. Müllen, *JACS*, 2014, **136**, 6083-6091.
138. K. Parvez, R. Li, S. R. Puniredd, Y. Hernandez, F. Hinkel, S. Wang, X. Feng and K. Müllen, *ACS Nano*, 2013, **7**, 3598-3606.
139. L. Lu, Y. Zhu, C. Shi and Y. T. Pei, *Carbon*, 2016, **109**, 373-383.
140. G. Demazeau, *Z. Naturforsch. B.*, 2010, **65**, 999 – 1006.

141. K. Hachem, M. Ansari, R. Saleh, H. Kzar, M. Al-Gazally, U. Altimari, S. Hussein, H. Mohammed, A. Hammid and E. Kianfar, *J. Bionanosci.*, 2022, **12**, 1032-1057.
142. E. H. Lester, P. W. Dunne, A. S. Munn, C. L. Starkey and T. A. Huddle, 2015, DOI: 10.1098/rsta.2015.0015.
143. Naoko Akiya and P. E. Savage, *Chem. Rev.*, 2002, **102**, 2725−2750.
144. G. C. Kennedy, *Am. J. Sci.*, 1950, **248**, 540–564.
145. U. S. S. o. C. o. b. o. t. U. S. o. America, Thermophysical Properties of Fluid Systems, https://webbook.nist.gov/chemistry/fluid/, (accessed 09/09, 2024).
146. G. De Souza, M. Pereira, L. Mourão, M. Dos Santos, J. De Oliveira, I. Garde, C. Alonso, V. Jegatheesan and L. Cardozo-Filho, *Rev. Environ. Sci. Bio/Technol.*, 2022, **21**, 75-104.
147. J. B. Zimmerman, P. T. Anastas, H. C. Erythropel and W. Leitner, *Sci.*, 2020, **367**, 397-400.
148. R. Carson, *Silent spring*, Houghton Mifflin, New York, 1962.
149. P. T. Anastas and J. C. Warner, *Green Chemistry: Theory and Practice*, Oxford University Press, 2000.
150. P. T. Anastas and M. M. Kirchhoff, *Acc. Chem. Res.*, 2002, **35**, 686-694.
151. P. Anastas, L. Heine and T. Williamson, in *Green Chemical Syntheses and Processes*, American Chemical Society, 2000, vol. 767, ch. 1, pp. 1-6.
152. M. Abraham and N. Nguyen, *Environ. Prog.*, 2003, **22**, 233-236.
153. P. T. Anastas and J. B. Zimmerman, *Journal*, 2003.
154. *Supply chain analysis and material demand forecast in strategic technologies and sectors in the EU – A foresight study*, Report ISBN: 978-92-68-00339-8, European Union, https://single-market-economy.ec.europa.eu/, 2023.
155. G. Li, A. Ascani and S. Iammarino, *Res. Policy*, 2024, **53**, 104914.
156. R. Das, R. Bandyopadhyay and P. Pramanik, *Mater. Today Chem.*, 2018, **8**, 96-109.
157. N. Ullal, R. Mehta and D. Sunil, *Anal.*, 2024, **149**, 1680-1700.
158. A. Cannon, J. Warner, J. Vidal, N. O'Neil, M. Nyansa, N. Obhi and J. Moir, *Green Chem.*, 2024, **26**, 6983-6993.
159. B. Kupilas, Cuevas, Natalia Burgos,Davis, McKenna,Elkina, Evgeniya,McDonald, Hugh, *Mapping policy and co-operate initiative landscapes for systemic change towards a nature-positive economy (Deliverable 1.3).*

Chapter 2 Hydrothermal synthesis of cadmium sulfide quantum dots

Quantum dots are nanoscale semiconductor particles exhibiting quantum mechanical phenomena due to their size, generally within the nanometre scale.[1, 2] They are present in multiple semiconductor categories and are composed of various elements, most commonly II – VI metal chalcogens. Quantum dots exhibit unique electronic and optical properties, such as tuneable band gaps and elevated photoluminescence quantum yields, primarily due to quantum confinement. This effect becomes apparent when the physical dimensions of the material are comparable to the exciton Bohr radius. The 2023 Nobel Prize in Chemistry recognised pioneering work in QDs, fostering the growth of nanoscience.[3] Semiconductor nanoparticles like QDs differ from their bulk forms due to quantum size effects, where electron confinement within nanoscale dimensions quantises energy levels.[4] This confinement, dependent on particle size and material composition, is the fundamental reason for their altered optical and electronic behaviours.

Cadmium sulfide, a II-VI semiconductor composed of a group twelve metal and a chalcogen, represents the specific quantum dots examined in this study. II-VI semiconductors feature direct bandgaps, facilitating the generation of electron-hole pairs. CdS crystallises in two forms: zinc blende (cubic) and wurtzite (hexagonal), which share notable similarities in their tetrahedral coordination and lattice parameters, often making their distinction challenging. Both crystal structures are composed of alternating close-packed layers, each containing sublayers of different ion types, resulting in the packing density of about 74%. Figure 2.1 illustrates that the cubic close-packed (CCP) structure (a, b, and c), also known as face-centred cubic, is characterised by a unit cell containing atoms at each corner and in the centre of each face of a cube is a highly efficient arrangement of atoms or spheres in a crystal. This structure is formed by stacking close-packed layers in an ABCABC sequence, contrasting with the ABABAB sequence of hexagonal close-packed (HCP) structures, of wurtzite (d, e, and f).

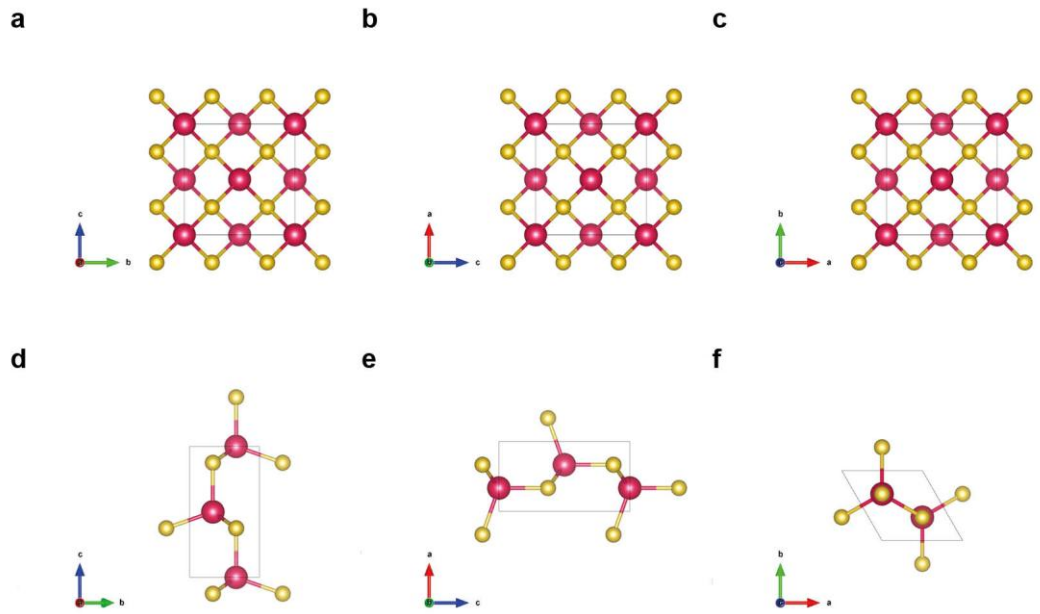

Figure 2.1, Cubic zinc blende of CdS, view along a axis (a), b axis (b) and c axis (c), hexagonal wurtzite structure of CdS, view along a axis (d), b axis (e) and c axis (f), created with vesta[5]

In this structure, the atoms form a hexagonal ring with an atom in the centre and a triangle of atoms in the middle of the structure. CdS consists of alternating planes of tetrahedrally coordinated S^{2-} and Cd^{2+} ions, stacked along the c-axis. The presence of oppositely charged ions results in a normal dipole moment and spontaneous polarization along the c-axis, leading to variations in surface energy.[6-9] Bulk CdS possesses a bandgap of 2.42 eV for the cubic zinc blende and 2.57 eV for the hexagonal wurtzite CdS. However, at nanoscale dimensions, these bulk properties are significantly altered due to quantum confinement effects, leading to size-dependent bandgap shifts and unique optical and electronic behaviours.[4]

2.1.1 Synthesis of CdS quantum dots

The hot injection technique, a method established by Bawendi for quantum dot synthesis, is recognised for its reliability, precision, and reproducibility, yielding desirable tunability in photoluminescence and high quantum yields.[10] This advancement facilitated industrial-scale production, leading to the integration of quantum dots into a wide array of devices and applications. However, drawbacks associated with quantum dots include their reliance on heavy metals, inherent toxicity, limited availability, and the environmental implications of metal extraction and synthesis.[11-13] Consequently, research has focused on developing alternative synthesis methodologies to achieve comparable material quality, with numerous published and optimised procedures available for the synthesis of CdS quantum dots.[14] These methods include, but are not limited to, the following:

- Thermolysis is a large-scale synthesis method. This process involves adding precursors to an organic medium and heating the solvent to facilitate colloidal nanocrystal growth until the solvent is cooled.[15] Initial heating can lead to partial nucleation, resulting in polydisperse material; thus, precursors should exhibit a reactivity transition at the target growth temperature.[16]
- The organometallic method is a particular thermolysis method, using thermolysis on an organometallic compound, which contain a bond between a metal atom and a carbon atom of an organic group. This method is recognised for yielding quantum dots of high quality, distinguished by notable crystallinity, elevated quantum yield, and a narrow size distribution that can be conveniently regulated by modifying the reaction temperature or duration.[17]
- Solvothermal synthesis involves combining precursors at a lower temperature in an organic solvent, followed by heating within a sealed autoclave to the designated reaction temperature to promote nanocrystal formation.[18] Studies using solvothermal synthesis of cadmium acetate and thioacetamide in ethylene glycol have successfully produced near-spherical cubic phase CdS quantum dots, with their properties confirmed through optical characterisation, transmission electron microscopy, and X-ray diffraction. The crystallite sizes, ranging from 4 to 9 nm, were observed to vary based on the quantity and molar ratio of the reactants employed.[19]

The solvothermal synthesis encompasses both aqueous and hydrothermal methods. The typical synthetic procedure for these nanocrystals involves dissolving a metal salt in water, with a thiol added as a stabilising agent, followed by the introduction of the chalcogen source. To initiate quantum dot synthesis, heating the reaction solution can promote particle growth and influence the size and morphology of the resulting quantum dots. Aqueous synthesis methods are both cost-effective and environmentally benign with water as a solvent. Hydrothermal synthesis is defined as a heterogeneous reaction occurring under high pressure and

temperature in the presence of aqueous solvents, facilitating the dissolution and recrystallisation of materials that are generally insoluble under ambient conditions.[20] This process involves combining precursors in water within a sealed autoclave and then raising the temperature to encourage nanocrystal formation, akin to solvothermal synthesis. The hydrothermal reactions are highly dependent on the solution's acidity or basicity, which leverages control to achieve monodisperse samples and specific photoluminescent properties.[21, 22] Other factors such as reaction temperature, duration, and precursor ratios all play a role in quantum dot formation.

2.1.2 Aqueous Solubility and Colloidal Stability of QDs

Quantum dots synthesised in organic solvents (orQDs), via methods such as hot-injection, thermolysis, or solvothermal synthesis, require a phase transfer process to achieve water solubility for numerous biological applications.[23] To enhance the hydrophilicity of orQDs, a hydrophilic shell is generally applied.[24] This transfer is often facilitated by a stabilising agent or ligand. Aqueous synthesis methods, on the other hand, eliminate the need for ligand exchange or encapsulation within amphiphilic polymers for biological uses. Consequently, water-dispersible QDs (aqQDs) exhibit inherent water dispersibility without requiring additional treatment, offering considerable benefits such as economic viability and the creation of water-dispersible QDs. The structural differences between orQDs and aqQDs are shown in Figure 2.2.

Typically, short thiol-based molecules are employed to substitute hydrophobic capping agents, thereby enabling control over the growth process at elevated temperatures. Ligands commonly used in aqueous synthesis are thiol- and carboxyl-modified short chain organic molecules, thiols including glutathione[25], 3-Mercaptopropionic acid (MPA)[26-33], thioglycolic acid (TGA)[34-39], mercapto-succinic acid,[40] and thioglycerol,[41] Among the mentioned stabilising agents, the thioalcohols (2-mercaptoethanol and1-thioglycerol) are effective size-regulating and stabilising agents for cadmium chalcogenide nanoparticles since cadmium exhibits a strong affinity for sulfur containing compounds acting as a soft Lewis acid and interacting readily with soft Lewis bases like sulfur.[17] Amino acids such as L-cysteine[25, 42-52] cysteamine,[53, 54] or methionine[55] have been used to improve water solubility, stability and biocompatibility as well. Polymers such as polyethyleneimine (PEI) [56-59] are also reported in literature as ligand.

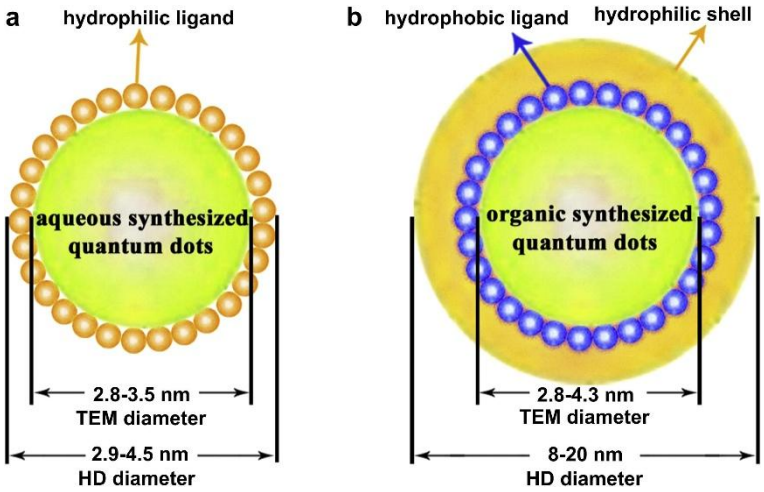

Figure 2.2, Schematic structures of (a) aqueous synthesised QDs and (b) organic synthesised QDs[24]

To fully realise the potential of nanotechnology, the development of synthetic methods that yield high-quality nanomaterials in a scalable, cost-effective, and environmentally conscious manner is crucial.[60] Aqueous and hydrothermal synthesis methods offer advantages: the low cost, environmental friendliness, and the use of safe reactants, aligning with the principles of green chemistry, which focuses on minimising or eliminating hazardous substances in chemical products and processes.[17, 61] A major advantage of aqueous synthesis techniques is the omission of post-synthesis procedures required to achieve water solubility for the quantum dots produced. This approach can potentially mitigate the deterioration of optical characteristics, including quantum yield and photostability.[23] Degradation pathways, such as photodamage to the material's surface or structural integrity, can lead to a reduction in light emission and overall performance. Such degradation in semiconducting nanomaterials is frequently instigated by exposure to ultraviolet radiation or other light sources. While aqueous synthesis offers advantages, the utilisation of water as a solvent may also induce surface defects that compromise the optical properties of quantum dots. This necessitates a careful balance of experimental conditions to fully leverage the benefits of aqueous synthesis while effectively mitigating its inherent drawbacks.

This project aims to address these challenges by employing green chemistry principles, specifically by utilising water as the solvent to avoid hazardous alternatives. Quantum dots produced via hydrothermal synthesis are advantageous for biological applications due to their inherent water dispersibility, which eliminates the need for post-synthesis treatments to achieve water solubility, thus preserving their optical characteristics and mitigating degradation.[62, 63] This method thus circumvents the typical issues associated with toxic reagents and extreme reaction conditions often found in conventional routes, while also enabling precise control over the nanoscale properties of the synthesised materials.[64] Therefore, this research aims to precisely control the optical characteristics of CdS quantum dots via hydrothermal synthesis. This approach enables a detailed examination of how properties like absorbance, emission, and bandgap energy correlate with reaction parameters such as pH and reaction time, and reactants.

2.1.3 Hydrothermal synthesis of quantum dots

The hydrothermal technique presents an accessible and economical approach for synthesising CdS quantum dots with precise control over their dimensions and morphology.[1] This process involves heating a precursor solution, which includes metal ions, a sulfur source, and ligands, within a sealed vessel under elevated pressure conditions. As both temperature and pressure rise, the solution reaches supersaturation, consequently promoting QD nucleation. The resultant size and shape of the QDs can be modulated by manipulating reaction parameters such as temperature, pressure, and duration. However, a notable challenge in hydrothermal synthesis is achieving highly uniform and monodisperse QDs. Despite this, the method remains comparatively cost-effective, requiring minimal precursors, an autoclave, and an oven. Contemporary advancements involve the introduction of novel precursors and surfactants to refine control over size and morphology, alongside investigations into alternative solvents like ionic liquids, supercritical fluids, and deep eutectic solvents.[1] These alternatives aim to improve precursor solubility and optimise reaction conditions for the production of high-quality QDs with narrow size distributions. For instance, researchers have successfully employed hydrothermal synthesis to fabricate uniform, monodisperse SnO_2 QDs by utilising hydrazine hydrate as both an alkaline agent and a ligand.[65]

2.1.4 Literature review on hydrothermal synthesis of II-VI quantum dots

The literature on the aqueous and hydrothermal synthesis of quantum dots reports two main types of studies: exploratory investigations where material properties are measured against reaction parameters, and those focusing on individual synthesis conditions. The former primarily focuses on controlling optical properties, which often leads to smaller nanoparticles but with broader size distributions. Conversely, the latter prioritises the formation of monodisperse particles over controlling optical properties, consequently yielding larger nanocrystals due to Ostwald ripening. This disparity highlights a significant challenge in achieving both precise optical tunability and narrow size distribution concurrently in quantum dot synthesis.

Table 2.1 provides examples of the first approach of synthesis of II-VI semiconductive quantum dots. As can be seen, reactions involve implementing either extended reaction times (7 – 16 h) or elevated reaction temperatures (150 – 190 ˚C) to ensure the formation of monodisperse particles. This often results in larger nanocrystals due to Ostwald ripening, where larger particles grow at the expense of smaller ones to minimise surface energy. In addition to the table, one more publication featured synthesised CuS/ZnS/SnS quantum dots hydrothermally, varying the reaction time from 6 to 48 h while keeping the reaction temperature at 180°C.[66] This method is particularly effective for controlling crystalline phase and particle morphology.

Table 2.1, Hydrothermal synthesis of II – VI semiconductor QDs

	Metal source	**Sulfur source**	**Ligand**	**Temp (˚C)**	**Time (h)**	**λ_{abs} (nm)**	**λ_{ex} (nm)**	**λ_{em} (nm)**	**Bandgap (eV)**	**Size (nm)**
ZnS[67]	Zinc acetate	Thiourea	-	190	12	295	-	-	3.82	2.4
ZnS[68]	Zinc acetate	Thiourea	3-aminopyridine	165	7	270	310	360	-	-
ZnS[69]	Zinc acetate	Sodium sulfide	Hexadecyltrimethyl-ammonium bromide	150	8	-	-	466 – 495	2.66 – 2.50	4.2 – 7.2
PbS[70]	Lead nitrate	Thiourea	-	150	16	250	-	-	5.04	21.0
CdS[71]	Cadmium nitrate	Sodium sulfide	-	180	8	490	-	-	2.2	-

In this research, the focus lies on the second synthetic approach, prioritising the modulation of optical properties and the production of smaller nanoparticles, acknowledging that this may lead to a broader size distribution. The objective of this category of reactions is to achieve control over the optical characteristics, quantum confinement, and size of the nanocrystals. The subsequent section will elaborate and give examples of studies that research the parameters influencing the properties of the synthesised materials. In aqueous and hydrothermal quantum dot synthesis, control can be exerted by adjusting reactant molar ratios, reaction pH, time, and temperature. For instance, specific ligand-to-metal ratios are critical for governing nucleation and growth rates, which in turn influence the final particle size and prevent aggregation. pH adjustments can modify precursor speciation and solubility, impacting the quantum dot's surface chemistry and stability. Furthermore, precise control over temperature and reaction time is essential for tuning particle growth kinetics, thereby affecting particle size and size distribution, which directly influences the quantum confinement effect and, consequently, the optical properties.

This was demonstrated by a study by Karimi *et al*. published on the hydrothermal synthesis of CdSe quantum dots using cadmium chloride and selenium oxide as starting materials, and 3-mercaptopropionic acid as a surface modifier.[72] The study investigated the influence of reaction temperature (80–180 °C) and time (30–90 min) on nucleation, growth, and Ostwald ripening processes during the hydrothermal synthesis of CdSe semiconductive nanomaterials, as depicted in Figure 2.3. Additionally, the research explored the impact of initial pH and surface modifier concentration on achieving quantum dots with maximum emission intensity in the visible spectrum.

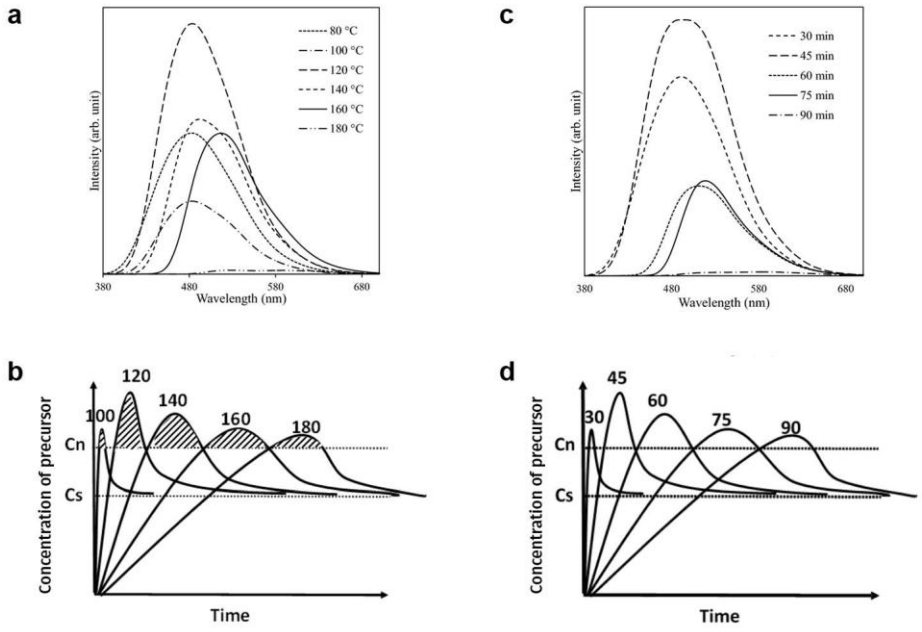

Figure 2.3, Emission differences for (a) varying reaction temperatures for 2 h and (c) varying reaction times at 140 ˚C, and Lamer diagram illustrating nucleation, growth and Ostwald ripening for (b) varying reaction temperatures for 2 h and (d) varying reaction times at 140 ˚C.[72]

In this investigation, it was observed that at lower temperatures during hydrothermal synthesis, an amorphous gel layer typically forms, which aids in crystal nucleation and subsequent growth. As the temperature increases, the formation of crystalline phases is enhanced, and the gel layer diminishes. Alternatively, particle nucleation and growth can occur within the solution, leading to product precipitation. Elevated temperatures tend to broaden the particle size distribution by allowing for more homogeneous nucleation and growth. Prolonged nucleus residence in this state leads to a bimodal particle distribution. This results in a decrease in photoluminescence peak intensity and a red shift, attributed to uncontrolled quantum dot growth and weakened quantum confinement. The sample synthesised at 100 °C displays lower PL intensity in the blue region due to an insufficient number of QD nuclei. Initially, PL intensity decreases as synthesis time increases from 30 to 45 min, suggesting the formation of a gel layer at 30 min, which subsequently reduces due to nucleation and crystalline particle formation at 45 min. Following this, emission intensities and peak wavelengths decrease over time as crystallites mature. Considering that the PL spectrum of particles synthesised for 1 hour falls within the QD emission range, a synthesis duration of 1 hour is deemed appropriate for subsequent experiments.

Control over optical properties of quantum dots through reaction time

Reaction time significantly influences the size of quantum dots; extended heating periods lead to the formation of larger QDs that exhibit emission at higher wavelengths. For instance, Cao *et al*. investigated the hydrothermal synthesis of CdTe QDs, systematically varying the reaction time between 45 and 85 min.[51]

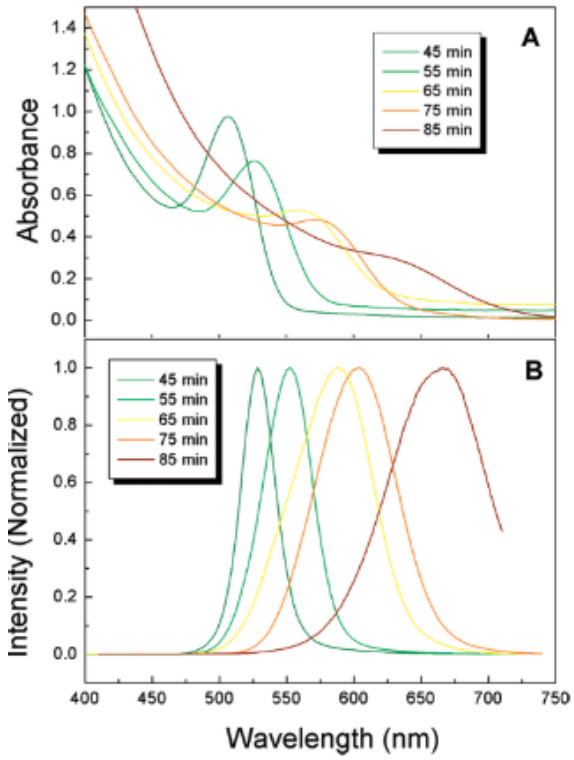

Figure 2.4, Absorption (a) and photoluminescence spectra (b) of L-cysteine-capped CdTe QDs grown at 180 °C for different times[51]

This variation resulted in a notable red shift in both absorbance and emission spectra, shown in Figure 2.4. In their methodology, cadmium chloride, trisodium citrate dihydrate, sodium telluride, sodium borohydride, and L-cysteine were combined in deionised water under vigorous stirring. The CdTe precursor solution was then placed in a Teflon-lined stainless-steel autoclave and heated at 180 °C for specified durations before being cooled to room temperature using flowing water. This process led to a red shift in the excitonic peak position in absorption from 507 to 633 nm, attributed to quantum confinement effects, and a corresponding shift in emission from 528 nm to 665 nm, indicating an increase in QD size from 2.5 to 4.1 nm.

Control over optical properties of quantum dots through temperature

Research by Li *et al*. demonstrates that the reaction temperature affects the behaviour of capping ligands and can be utilised to regulate the growth rate of CdSe QDs, consequently controlling the size of the final CdSe products.[73]

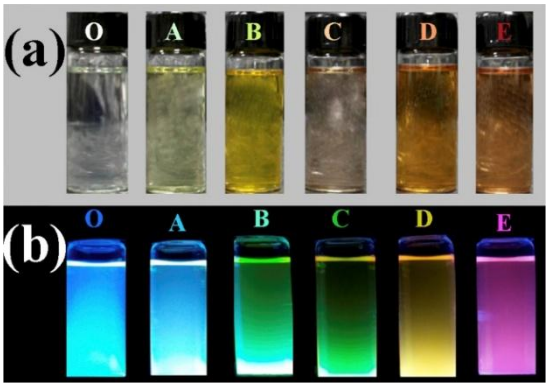

Figure 2.5, Digital photographs of the CdSe-QD solutions under the irradiation of (a) visible light and (b) UV light (l ¼ 365 nm) for: CdSe-O, CdSe-A, CdSe-B, CdSe-C, CdSe-D and CdSe-E (O: obtained by etching CdSe-A with H_2O_2, A at 60 ˚C, B at 90 ˚C, C at 120 ˚C, and D at 150˚C.[73]

In a study involving the hydrothermal reaction of cadmium acetate, sodium selenosulfate, and oleic acid, quantum dots of varying sizes were produced by adjusting the reaction temperatures, demonstrated in Figure 2.5. After mixing the reactants in water, the mixture transitioned from white to yellow and was subsequently transferred to a sealed, high-pressure autoclave and heated at different temperatures for 2 h. Lower reaction temperatures led to slower particle growth and smaller particle sizes. Smaller particles could also be achieved through an oxidative etching process using H_2O_2.[74] Experimental findings indicate that reaction temperature significantly influences nanoparticle growth rate and maximum size. With a deeper understanding of nanoparticle growth, control over emission colour and colour purity can be achieved to some extent, as these are strongly dependent on nanoparticle size and size distribution.

Control over optical properties of quantum dot through molar ratios

A study by Du *et al*. demonstrated the effect of reactant molar ratios on the hydrothermal synthesis of CdS QDs using cadmium chloride, a sodium sulfide, and glutathione as a stabilising agent.[75]

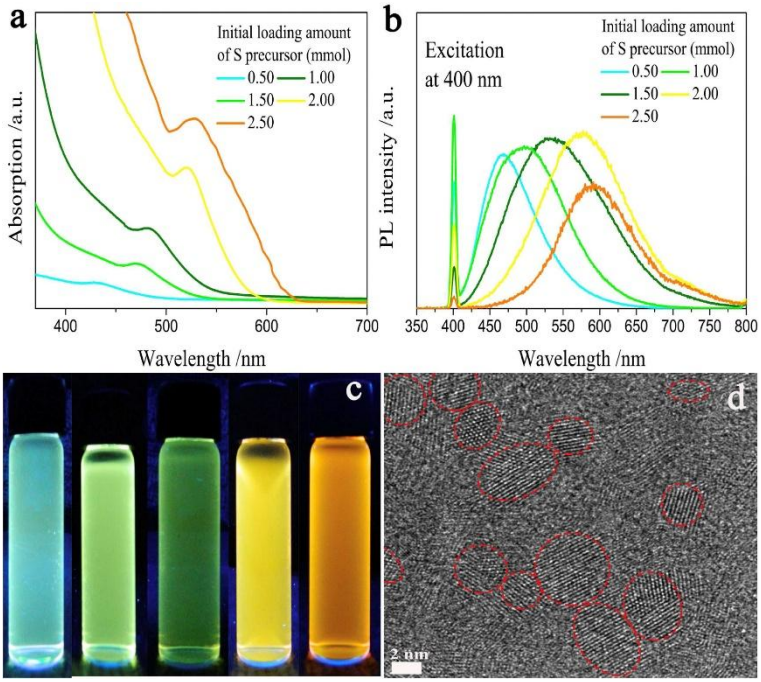

Figure 2.6, CdS colloidal QDs under different initial loading amounts of S precursors (from left to right are 0.5, 1.0, 1.5, 2.0–2.5 mmol): (a) UV–vis absorption spectra, (b) PL emission spectra, (c) digital photographs, and (d) HR-TEM image of optimised CdS QDs.[75]

Table 2.2, Tabulated results of the temperature/time experiment[75]

Molar ratio (Cd:S)	λ_{abs} (nm)	λ_{em} (nm) (for λ_{em} = 400 nm)
1.0:0.5	430	470
1.0:1.0	470	500
1.0:1.5	480	530
1.0:2.0	520	580
1.0:2.5	530	590

Their findings indicated that precise adjustments to the Cd-to-sulfur ratios were critical in influencing the resulting particle size, crystallinity, and luminescence properties of the CdS QDs, as illustrated in Figure 2.6 and summarised in Table 2.2. The molar ratios of the cadmium source to the sulfur source were varied between 1:0.5 and 1:2.5, allowing for nuanced control over stoichiometry, which is essential for modulating supersaturation conditions during nucleation and growth. Specifically, higher sulfur concentrations typically resulted in larger particles with red-shifted absorption and emission spectra.

Control of optical properties through reaction temperature, time and pH

Bu *et al.* investigated the influence of reaction temperature, time, and pH on the synthesis of mercaptoacetic acid -capped CdTe nanoparticles via hydrothermal methods.[76] The experiment used Cadmium Chloride as the Cd-source, NaHTe as the Te-source, and N-acetylcysteine (NAC) as the ligand, maintaining a molar ratio of Cd:Te:NAC of 1.0:0.2:1.2 at a concentration of 20 mM in water.

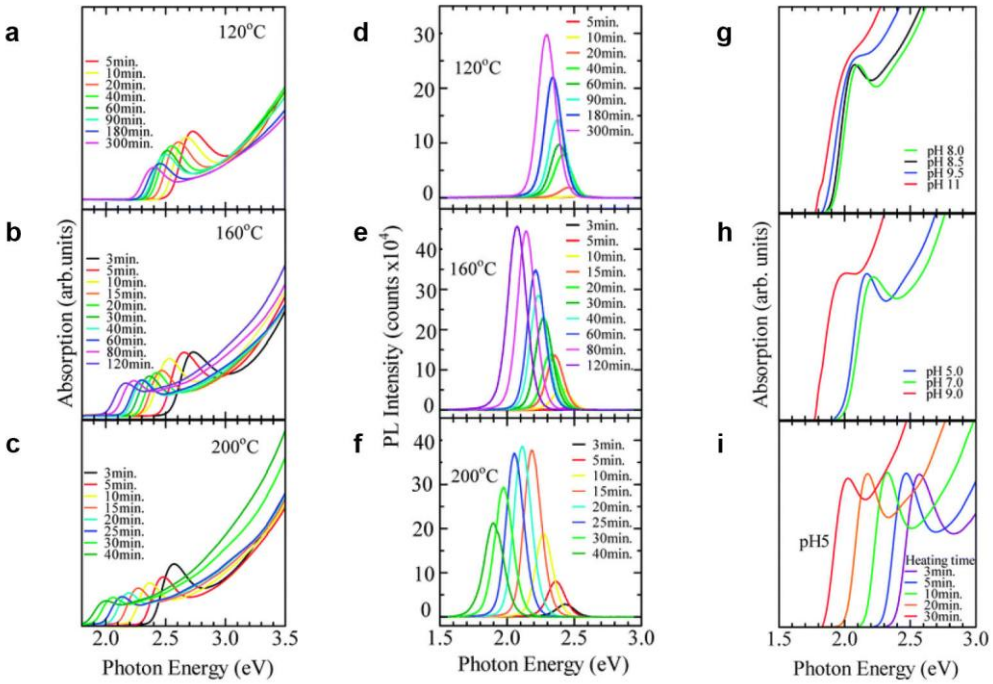

Figure 2.7, Temporal evaluation of absorbance spectra of as-prepared NAC-capped CdTe NPs during their growth in aqueous solution at pH 5.0 at reaction temperatures: (a) 120 °C, (b) 160 °C, and (c) 200 °C, and their photoluminescence spectra at reaction temperatures: (d) 120 °C, (e) 160 °C, and (f) 200 °C. UV-Vis absorbance of samples reacted at 200 ˚C at selected pH levels of (g) TGA-capped CdTe NPs recorded and (h) NAC-capped CdTe. Temporal evolution of absorbance spectra of NAC-capped CdTe NPs at pH level of 5 (i).[76]

Table 2.3, tabulated results of the temperature/time experiment[76]

Temperature (˚C)	Time (min)	λ_{abs} (eV)	λ_{em} (eV)	Size (nm)
120	5 – 300	2.75 – 2.40	2.45 – 2.30	2.1 – 2.6
160	3 – 120	2.75 – 2.15	2.35 – 2.10	2.3 – 3.3
200	3 – 40	2.60 – 1.95	2.45 – 1.90	2.5 – 4.3

To determine the effect of temperature, reactions were conducted over time intervals ranging from 5 to 300 min at temperatures of 120 °C, 160 °C, and 200 °C. The findings shown in Figure 2.7, and summarised in Table 2.4, indicated that increasing the reaction temperature accelerated the growth rate of CdTe QDs, resulting in larger nanoparticles with red-shifted emission and improved photoluminescence intensity, attributed to enhanced crystallinity and fewer surface defects. Similarly, varying the reaction time at a constant temperature allowed for precise control over particle growth; longer durations generally led to larger quantum dots and a shift in emission wavelengths. However, excessively high reaction temperatures could induce Ostwald ripening, diminishing emission intensity. Conversely, lower temperatures yielded smaller QDs but necessitated longer reaction times to achieve adequate crystallinity and optical properties.

The pH of the reaction mixture significantly impacted precursor solubility, reaction kinetics, and the efficacy of the capping agent, consequently affecting QD size, surface passivation, and luminescence efficiency. The study demonstrated that an optimal pH range exists, and increasing alkalinity tended to broaden the absorption peak. Precise pH control is vital for achieving high quantum yield and narrow size distribution, as deviations can promote aggregation and broaden emission spectra, aligning with observations in other chalcogenide quantum dot systems.

2.1.5 Research aims

This chapter outlines environmentally friendly hydrothermal techniques for synthesising conventional CdS quantum dots, emphasising a sustainable production pathway. This approach incorporates insights from the preceding literature review concerning the manipulation of quantum dot optical properties via reaction parameter optimisation, grounded in the fundamental processes of particle nucleation and growth. Within this chapter, two reaction systems are tested and optimised, including the hydrothermal synthesis of quantum dots in the conventional system involving autoclave and oven, as well as a system involving a heat block and Duran glass tubes. Key reaction parameters namely temperature, time, pH, cadmium source, sulfur source, and ligand, along with their respective molar ratios, are examined. Furthermore, the dual role of L-Cysteine as both a ligand and a sulfur source in the reaction is investigated. This novel methodology aims to harness the bifunctional characteristics of L-Cysteine to streamline the synthetic process while ensuring meticulous control over the resultant CdS quantum dot attributes. By carefully manipulating these parameters, it is aimed to achieve precise control over quantum dot size, morphology, and crystalline phase, which directly impacts their optical and electronic characteristics.

The implementation of green chemistry principles, such as utilising water as a solvent, offers significant advantages in the synthesis of nanomaterials like quantum dots, as it avoids the need for hazardous alternatives and contributes to safer, more energy-efficient, and less toxic production methods. For instance, in the context of quantum dot synthesis, employing water as a solvent is a direct application of green chemistry, leading to inherently water-dispersible quantum dots suitable for biological applications without requiring additional post-synthesis treatments. This approach, therefore, avoids the common challenges linked to hazardous chemicals and harsh reaction environments frequently encountered in traditional synthetic procedures, simultaneously allowing for meticulous regulation of the nanomaterials' characteristics at the nanoscale.

2.2 Materials and Methods

2.2.1 Materials

Cadmium nitrate tetrahydrate (98%), Cadmium Chloride (99%), cysteamine (98%), Thiourea (99%), Sodium Thiosulfate (98%), L-cysteine (97%), ammonium hydroxide (25%), and $Ru(bpy)_3 Cl_2$ were obtained from Sigma Aldrich, now Merck.

2.2.2 Hydrothermal synthesis of CdS quantum dots in conventional reaction system of autoclave and oven

This chapter begins with the exploration of the conventional hydrothermal synthesis of cadmium sulfide quantum dots based on previously published research by Aboulaich *et al*.[23] This article involved the hydrothermal synthesis of CdS@MPA, which provided a template for this experiment. The starting materials in the published study were cadmium chloride, thiourea, and 3-mercaptopropionic acid in the molar ratio Cd/Thiourea/MPA of 1/1.7/2.3. The reaction solution was transferred to the autoclave and maintained at 100 ˚C for a designated time between 45 min and 3 h, after which the autoclave was cooled to room temperature.

Guided by this paper, a molar ratio of Cd/S/ligand of 1/1.8/2.2 was chosen for the experiment in this study. In the lab, the initial experiments involved preparing stock solutions of cadmium nitrate, thiourea, and L-cysteine at 0.1, 0.18, and 0.22 M, respectively. Subsequently, 4 mL of each stock solution was added to a Teflon-lined stainless-steel autoclave and stirred until a homogeneous solution with a pH of 2.56 was formed. The autoclave was placed in a preheated, conventional, non-fan-assisted oven. This heating system permits variation in reaction time and temperature, as well as flexibility in reactant choices. In the initial experiments, reaction time was varied between 1 and 4 h, and reaction temperature between 100 and 200 °C, to form CdS QDs and control their optical characteristics. Upon completion, the autoclave was cooled to room temperature. The outcome of the reactions was initially evaluated by recording the photoluminescence colour emitted under UV 365 and observing whether the reaction solution contained only soluble or precipitated particles.

To assess the impact of the ligand on the reaction, L-cysteine was substituted with 0.22 M cysteamine. Similarly, to evaluate the influence of the pH on the reaction system, the reaction mixture was titrated to a pH of 10 with 25 % ammonium hydroxide with use of a Mettler Toledo pH meter and pH Sensor InLab Versatile Pro probe. The autoclave with Teflon liner was filled with 12 mL of the resulting reaction mixture, then treated as outline before.

2.2.3 Hydrothermal reaction of CdS quantum dots in Duran tubes and heat block

For reactions conducted using a heat block, a modified procedure was employed. Initially, the heat block was set to 130 °C and allowed to stabilise for one hour. Concurrently, approximately 80 mL of distilled water was stirred in a 250 mL beaker using a magnetic stirrer. For the standard reaction involving the Cd/S/ligand molar ratio, 73 mmol (0.88 g) of L-cysteine were weighed and added to the beaker, forming a suspension. Ammonium hydroxide was then added dropwise to adjust the pH to 7, ensuring the cysteine in a soluble state. Subsequently, 33 mmol (1.02 g) of Cadmium Nitrate were introduced, followed by 60 mmol (1.48 g) of

Sodium Thiosulfate, and the pH was adjusted again. The reaction mixture achieves solubility in the pH range of 6.5–7. The pH was further elevated to the desired level using ammonium hydroxide and allowed to stir until stable for over one minute. Following this, the reaction mixture was transferred to a 100 mL volumetric flask and diluted to volume with distilled water to maintain consistent reactant concentrations across all experiments. The pH of the 100 mL reaction mixture was remeasured. Subsequently, 18 mL of the reaction mixture was transferred into a Duran tube, corresponding to 52% fill fraction, the same compared to the autoclave reaction. The Duran tube was sealed with a pressure-resistant cap. Four additional Duran tubes were prepared in the same manner for a time-series reaction study, with durations of 5, 10, 20, 30, and 40 min. The heat block's temperature was verified to have stabilised at 130 °C. Upon confirmation, all Duran tubes were simultaneously placed within the heat block, and timers for each reaction duration were initiated. As each timer expired, one Duran tube was retrieved from the heat block and placed in a tube rack to cool to room temperature. This process was repeated until all reactions have been removed from the heat block, after which the heat block was turned off. One hour after the final tube was removed, the tubes have reached room temperature and were subsequently opened.

2.2.4 Systematic assessment of successful synthesis, material's quality, and performance of reaction system

Initially, post reaction pH was measured with use of a Mettler Toledo pH meter and pH Sensor InLab Versatile Pro probe and a qualitative fluorescence assessment by eye under a UV 365 nm lamp determined if the reaction yielded a fluorescent sample; non-fluorescent samples were excluded from further analysis. If fluorescence was observed, the presence of precipitate was noted. A precipitate indicated reduced conversion yield and directed the analysis toward solid-phase characterisation. Samples without precipitate proceeded directly to supernatant optical characterisation. For samples with precipitate, the supernatant and precipitate were separated via centrifugation. The supernatant was retained for optical characterisation, while the isolated precipitate was sequentially washed with water, ethanol, and toluene, involving redispersion in each solvent, followed by centrifugation and decantation to remove residual solvent. The washed solids were dried overnight at 40 °C and then ground into a powder using a pestle and mortar for XRD analysis. The XRD patterns identified the species, typically revealing either crystalline CdS, suggesting overly harsh reaction conditions or insufficient ligand interaction, or an L-cysteine complex, indicating either an excess of the ligand or competitive formation of quantum dots and the L-cysteine complex. Subsequently, the fluorescent solution was characterised using UV-vis absorption, photoluminescence excitation and emission, and dynamic light scattering. In an ideal scenario, optical characterisation of the reaction system shows quantum dot samples exhibiting a time-dependent red shift in both absorption and emission spectra, alongside a dynamic light scattering-measured polydispersity index below 0.2, with - 20 > zeta potential > + 20 mV.Finally, the most effective products from the experimental set were replicated in quintuplicate to ensure enough soluble quantum dots were obtained post-reaction.

2.2.5 Isolation and purification of precipitate from reaction

Following centrifugation at 6800 rpm for 20 min, the solid precipitates are separated from the supernatant. The supernatant is then retained for subsequent optical and photoluminescence analysis. The isolated solids undergo a washing procedure involving sonication with 30 mL of water, followed by centrifugation at 6800

rpm for 20 min, with the supernatant being decanted. This washing sequence is replicated using ethanol and toluene to effectively eliminate all soluble impurities from the solids. After the final centrifugation and decantation of toluene, the solids are thoroughly dried overnight in a drying oven maintained at 40 °C. If completely dry, the samples are subjected to grinding using a pestle and mortar to yield a fine powder.

2.2.6 Quantum dot isolation and purification

For isolation and purification of soluble quantum dots, the optimised synthesis parameters were chosen, the reaction was reproduced several times using the methodology detailed in section 2.2.3. In this adapted procedure, five Duran tubes were placed into and retrieved from the heat block concurrently at specific time points, resulting in a total sample volume of 90 ml. One millilitre of the separated supernatant was reserved for optical characterisation. The remaining sample was transferred to a 500 mL round-bottom flask and subjected to rotary evaporation. The water bath was maintained at 50 °C, rotation at 20 rpm, and vacuum at 60 mbar. Water evaporation from the combined sample occurred over several h, leading to the precipitation of quantum dots from the solution due to oversaturation. Once precipitation occurred, the process was terminated, and the suspension was transferred to a centrifuge tube. To ensure complete recovery of the quantum dots from the flask and further induce precipitation, acetone was used to rinse the glassware, collecting all quantum dots. The acetone and solid quantum dots were combined in the centrifuge tube and centrifuged at 6500 rpm for 15 min. The resulting water-acetone solvent mixture was decanted, and the isolated quantum dots were dried overnight at 40 °C. Upon complete drying, the quantum dot sample was ground into a powder, and its mass was recorded. The colour of the powder and its luminescence under UV365 nm were documented. The powder was then stored for subsequent optical and structural characterisation.

2.2.7 Characterisation of quantum dots

Optical characterisation of the quantum dots in solution includes UV-vis absorbance, photoluminescence spectroscopy (PL), and dynamic light scattering (DLS). Structural characterisation includes X-Ray Diffraction and Transmission Electron Microscopy.

UV-vis absorbance

UV-Vis spectra were acquired utilising a Varian CARY50 UV-Vis spectrophotometer and four-sides quarts cuvettes. Measurements were conducted across a wavelength range of 250 to 800 nm, with a data interval of 1 nm, a slit width of 1 nm, and a scan speed of 240 nm/min. The lamp was switched at 326 nm, and a 10 mm quartz cuvette with four usable sides was employed. Sample concentration was adjusted to achieve an absorbance of approximately 0.1 A at a wavelength of around 395 nm; solutions with absorbance greater than 0.1 A were diluted.

Band gap energies were determined from the UV-Vis spectra using a Tauc plot analysis. Since cadmium sulfide functions as a direct bandgap semiconductor, exhibiting both zinc blende and wurtzite crystal structures.

The Beer-Lambert Law states

$$A = \varepsilon cl = \log\frac{I_0}{I} \tag{2.1}$$

Where A is absorbance,

ε is molar absorption,

c is concentration,

l is the path length,

I_0 is the incident light, and

I is the transmitted light.

The absorption coefficient α is expressed as the combination of the molar absorption (ε) and the concentration (c). can be condensed to the absorption coefficient.

$$\alpha = \varepsilon c \tag{2.2}$$

The absorption coefficient can be expressed as a function of the absorbance through the following derivation:

$$\alpha l = \log\frac{I_0}{I} \tag{2.3}$$

$$e^{\alpha l} = \frac{I_0}{I} \tag{2.4}$$

$$e^{-\alpha l} = \frac{I}{I_0} \tag{2.5}$$

$$A = \log\frac{I_0}{I} = -\log\frac{I}{I_0} = \alpha l * 0.434 \tag{2.7}$$

$$A = \alpha l * 0.434 \tag{2.8}$$

$$\alpha = \frac{A}{l * 0.434} = 2.303\frac{A}{l} \tag{2.9}$$

$$\alpha = 2.302\ A\ cm^{-1} \tag{2.10}$$

The Tauc equation provides:

$$(\alpha h\upsilon)^{\gamma} = A\left(h\upsilon - E_g\right) \tag{2.11}$$

Where h is the Planck's constant, $= 6.626 * 10^{-34}\ Js$,

υ is the photon frequency,

E_g is the bandgap energy, and

γ is the nature of the electronic transition, $= 2$, for direct allowed transitions

The bandgap energy is determined by extrapolating the linear region of the Tauc plot to the x-axis. The intersection point with the x-axis, representing the x-intercept (where the y-axis value is zero), yields the bandgap energy.

$$y = m(x) \tag{2.12}$$

Where m is the slope. This gives:

$$0 = A\left(h\upsilon - E_g\right) \tag{2.13}$$

$$h\upsilon = E_g \tag{2.14}$$

This formula can be derived with the incident light to be expressed as function of the wavelength:

$$E = h\upsilon = \frac{hc}{\lambda} = \frac{6.626 * 10^{-34}(Js) * 2.998 * 10^{8}\left(\frac{m}{s}\right)}{\lambda(m)} \tag{2.15}$$

$$1\ eV = 1.602 * 10^{-19} J \tag{2.16}$$

$$E = \frac{1.986 * 10^{-25}\ (eVm)}{\lambda\ (m) * 1.602 * 10^{-19}} = \frac{1.240 * 10^{-6}\ (eVm)}{\lambda(m)} \tag{2.17}$$

Since the experimental data is measured in nanometres, the units are converted to accommodate this:

$$E = \frac{1240 * 10^{-9}(eVm)}{\lambda(m)} = \frac{1240\ (eV\ nm)}{\lambda(nm)} = \frac{1240}{\lambda} eV \tag{2.18}$$

Where E is the incident energy,

c is the speed of light $= 2.998 * 10^{8}\ ms^{-1}$, and

λ is the wavelength in m.

From this formula the incident energy is expressed as:

$$E = \frac{1240}{\lambda} eV \tag{2.19}$$

Once α and E are established$(\alpha hv)^2$ in $(eV\ cm^{-1})^2$ can be plotted against the E in (eV), and the band gap energy read from the x-intercept value.

Photoluminescence

Photoluminescence spectra were acquired using a HORIBA FluoroMax benchtop spectrometer, with excitation wavelengths scanned from 300 to 600 nm. Specifically, excitation occurred within the 300-400 nm range, and slit widths were adjusted to achieve a reliable signal magnitude of 10^6. Measurements were performed using a 10 mm four-sided QS High Precision Cell from Hellma Analytics.

Quantum Yield Measurements

Emission quantum yields were determined using the optically dilute method.[77, 78] Stock solutions of absorbance values of *ca.* 0.3 at λ_{ex} = 395 nm were prepared and diluted to yield solutions with absorbances of *ca.* 0.1, 0.075, 0.05 and 0.025. The Beer-Lambert Law was found to be linear at these concentrations. Emission spectra were obtained in aerated conditions. Linear regression analysis between the absorption and emission intensity verified the relationship with R^2 values surpassing 0.99 in all cases. Individual relative quantum yield values were calculated for each solution and reported values represent the slope value:

$$\varphi_s = \varphi_r \left(\frac{A_r}{A_s}\right)\left(\frac{I_s}{I_r}\right)\left(\frac{n_s}{n_r}\right)^2 \tag{2.20}$$

φ_r is the absolute quantum yield of the reference

n is the refractive index of the solvent and assumes $n \approx 1.33$ for water.

A and *I* describe the absorbance values at the excitation wavelength and integrated area under the emission curves, respectively,

while *r* and *s* subscripts denote the reference and sample values, respectively

A solution of $Ru(bpy)_3\ Cl_2$ in water (φ_r = 4.0%) was used as the external reference.[79,80]

Dynamic light scattering

DLS measurements were carried out on the Malvern Zetasizer Nano-ZS with Zetasizer Software. Measurements were performed at 25 °C and in aqueous solution in a four-sided plastic cuvette for the size measurements and syringed into cuvettes specialised for zeta potential measurements. All samples were subjected to three rounds of size and Zeta potential measurements, performing automated cycles to measure

the size, providing statistically accurate data. Temperature-dependent DLS studies on the aqueous solution of nanoparticles may provide information that the aggregation is essentially driven by noncovalent interactions between thiol-stabilised QDs.[81]

X-ray diffraction

X-ray diffraction (XRD) patterns were recorded on a Bruker D8 advance diffractometer using Cu Kα radiation from 5 to 85° 2θ with step–size 0.01 at 0.5 s/step using a zero–background Si sample holder. An average particle size of QDs estimated from the Scherrer's formula:

$$D = \frac{K\,\lambda}{B\cos\theta} \tag{2.21}$$

Where D is particle size (diameter in nm),
K is particle shape factor ~ 0.9,
λ is the X-ray wavelength, 1.5418 Å,
B is full weight at half maximum (in radians), and
θ is diffraction angle.

Transmission electron microscopy

Transmission electron microscopy (TEM) micrographs were obtained on the JEOL 2100 LaB TEM microscope, fitted with an AMT XR50, 5k CCD, bottom mount camera, operating at 200 kV. Samples were prepared by dispersion in IPA, sonicated for 15 min. The quantum dots were deposited on carbon film on copper grids and dried overnight.

2.3 Results and discussion

2.3.1 Exploration of conventional reaction system for CdS QDs – autoclave and oven

The initial variation of reaction temperature and time yielded mostly blue emitting samples, suggesting minimal influence in optical properties. One reaction with parameters set to 150 ˚C and 2 h, resulted in observed red emission, indicative of quantum dot formation. The results of the experiment are presented in Table 2.4. A distinction was made between reactions with precipitate formation and without.

Table 2.4, Results of the hydrothermal reaction of cadmium nitrate, thiourea, L-cysteine in conventional oven, no pH adjustments.

Reaction time	Reaction temperature								
	100 ˚C			150 ˚C			200 ˚C		
	PL	Precipitate formation	λ_{abs} (nm)	PL	Precipitate formation	λ_{abs} (nm)	PL	Precipitate formation	λ_{abs} (nm)
1 hour	Blue	No	298	Blue	No	301	Blue	Yes	310
2 h	Blue	No	301	Red	No	298	Blue	Yes	310
3 h	Blue	No	301	Blue	No	310	Blue	Yes	308
4 h	Blue	No	301	Blue	Yes	310	Blue	Yes	304

Typically, harsher reaction conditions, of 150 °C and 4 h, as well as 200 °C and 1 – 4 h reaction yielded solids. The absorption spectra of this set of reactions are shown in Figure 2.8, revealing λ_{abs} of 298 – 301 nm for all reaction times at 100 °C (a), and 1 – 2 h reaction at 150 °C (b). Additionally, the 2 hour 150 °C showed a second absorption maximum near 410 nm. This was calculated as a direct bandgap of 2.78 eV and particle size of 5.3 nm with the Tauc plot depicted in Figure 2.8 (d). Reactions at 150 ˚C and 3 – 4 h produced λ_{abs} 310. The same wavelength was measured for the reactions at 200 ˚C and 1 – 2 h (d) together with observed increase in the slope of the curve into the visible light spectrum, which continued at longer reaction times of 3 and 4 h as well, reducing the peak at λ_{abs} 310 nm into a shoulder and slightly blue shifted. This increase in slope is associated with the formation of precipitate in reaction and was further investigated.

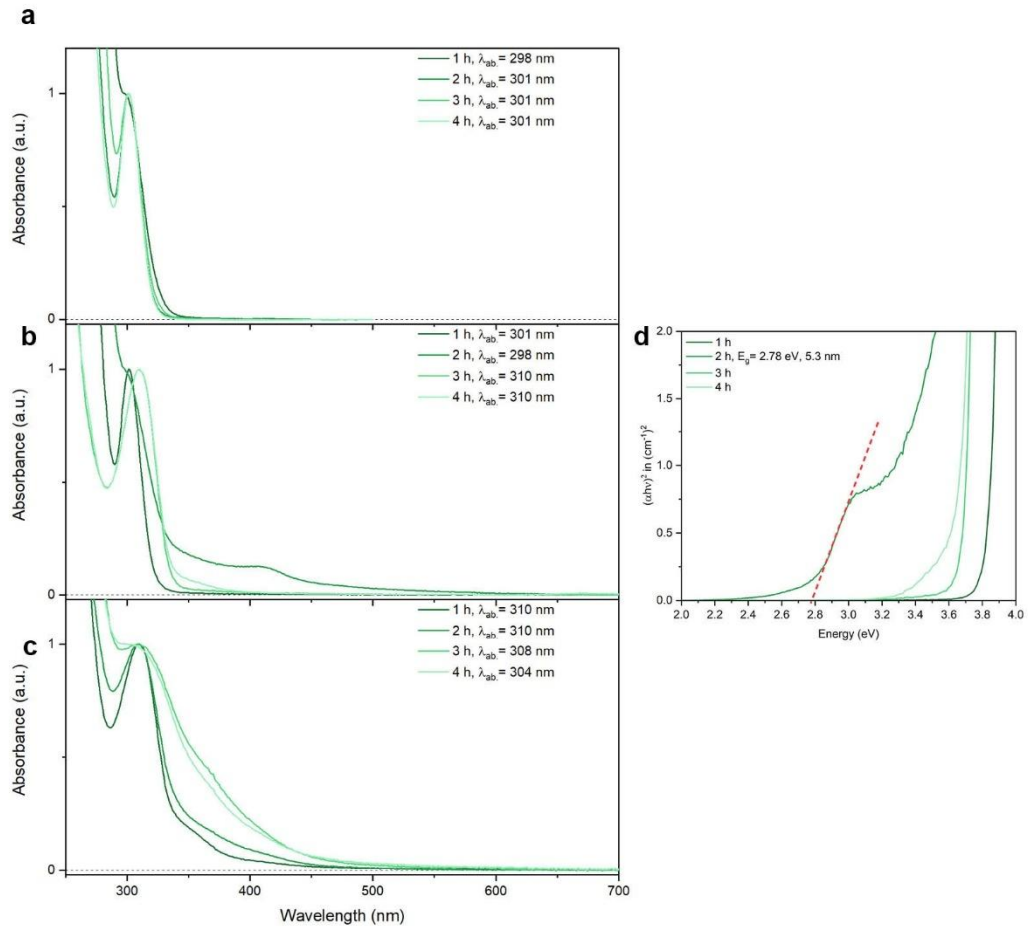

Figure 2.8, Normalised absorbance and photoluminescence emission of the hydrothermal reaction of cadmium nitrate, thiourea, L-cysteine in conventional oven, no pH adjustments, 1 – 4 h, at 100 °C (a), 150 °C (b), and 200 °C (c), additionally the Tauc plot of the 150 °C reactions (d).

Samples that formed a precipitate underwent post-reaction treatment as described in the methods section. The isolated solids were characterised using XRD, and a representative pattern of the precipitate is shown in Figure 2.9. The hexagonal packing (in green) has a set of peaks at angles 24.77, 28.14, 43.62, 47.76, and 51.74˚, this set of reflections corresponds to diffraction from (100), (002), (101), (102), and (110) lattice planes respectively.[7] The lack of a peak at 31˚ (in red), indicative of the (200) lattice plane of the cubic phase, confirms a mostly hexagonal phased sample. The XRD pattern of nanomaterials exhibit broad reflexes,

indicating a pronounced size effect, while bulk material exhibits sharp, well-defined reflections indicative of larger crystallites, as is seen here in the CdS diffraction pattern.

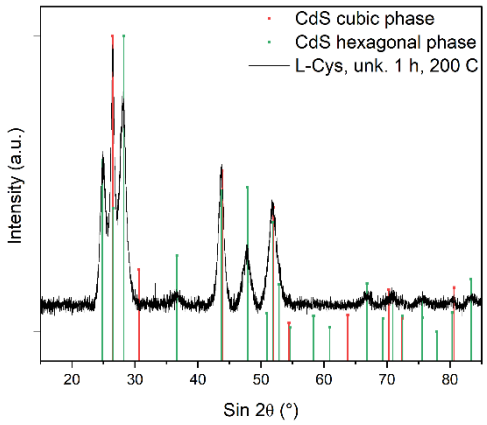

Figure 2.9, XRD pattern of the solids collected from the hydrothermal reaction of cadmium nitrate, thiourea, L-cysteine in conventional oven, no pH adjustments, 1 h, 200 ˚C.

Overall, by increasing reaction time and/or temperature, a certain energy barrier was overcome, resulting in the formation of larger CdS particles. This indicates a system boundary beyond which further temperature or time extensions will promote the formation of bulk CdS, as reflected by sharper peaks in XRD patterns and reduced photoluminescence properties.

2.3.2 Equilibrium shift through pH

Following the methodology of Aboulaich *et al.*[23], the experiment was re-conducted under basic conditions to shift the reaction's equilibrium and enhance ligand reactivity, aimed at inducing reactivity at the thiol group of L-cysteine. The reaction mixture was adjusted to pH 10 using ammonium hydroxide prior to its placement in a conventional oven, yielding the subsequent observations.

Table 2.5, Results of the hydrothermal reaction of cadmium nitrate, thiourea, L-cysteine in conventional oven, pH 10.

Reaction time	Reaction temperature											
	100 ˚C				150 ˚C				200 ˚C			
	PL	Ppt.	λ_{abs} (nm)	λ_{em} (nm)	PL	Ppt.	λ_{abs} (nm)	λ_{em} (nm)	PL	Ppt	λ_{abs} (nm)	λ_{em} (nm)
1 h	Blue	No	299	419	Yellow	No	370	509	Orange	Yes	406	607
2 h	Green	No	370/475	507	Red	No	412	>700	Blue	Yes	295	391
3 h	Orange	No	392	615	Blue	Yes	291	383	Blue	Yes	295	422
4 h	Red	No	404	698	Blue	Yes	290	391	Blue	Yes	312	458

Under basic conditions, the photophysical properties of the resulting samples exhibit a more pronounced dependence on reaction time and temperature. Varying these parameters led to luminescence spanning from blue to green, yellow, orange, and red. Specifically, increasing the reaction time resulted in a red shift in luminescence (blue, green, orange, red) at 100 °C. Additionally increasing the temperature also induced a red shift (blue, yellow, orange) for reactions conducted for 1 hour. This suggests a relationship between the modulation of optical characteristics and the acceleration of reaction kinetics via temperature. Increasing reaction time will not enhance reaction kinetics but instead, prolonged heating primarily permits further

growth of existing nanocrystals, resulting in larger CdS particles and a red-shift of the emission peak, as well as the formation of precipitate in reaction.

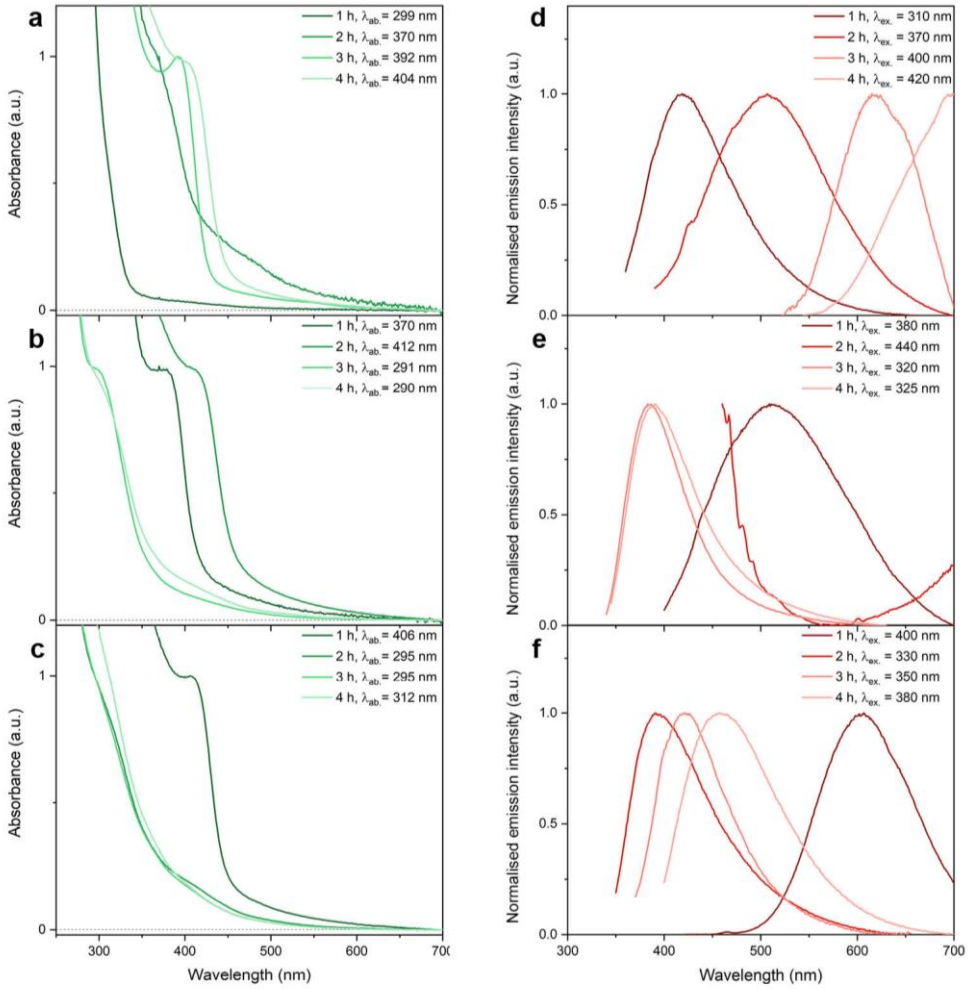

Figure 2.10, Normalised absorbance and photoluminescence emission of the hydrothermal reaction of cadmium nitrate, thiourea, L-cysteine in conventional oven, pH 10, 1 – 4 h.

Optical characterisation of the synthesised samples was performed using UV-vis absorption and photoluminescence spectroscopy. At 100 °C, the UV-vis spectra, shown in Figure 2.10 (a) did not reveal a distinct absorption maximum for the 1-hour reaction time. However, extending the reaction duration to 2, 3, and 4 h resulted in a bathochromic shift, with absorption maxima increasing to 370, 392, and 404 nm, respectively. This also translated to the photoluminescence spectra, shown in (b), which produced a red shift from 419 to 698 nm for the time series. Notably, the 2-hour reaction exhibited an intensified tail into the visible spectrum, characterised by a shoulder at 475 nm.

At 150 °C, the absorption spectra (b) further shifted into the visible region, displaying absorption shoulders at 370 nm and 412 nm for 1-hour and 2-hour reaction times, respectively. Conversely, for reaction times of 3 and 4 h at 150 °C, the absorption shoulder decreased to 290 nm, coinciding with the formation of a precipitate. This observation suggests that prolonged reaction times may lead to particle overgrowth beyond the nanoscale, forming bulk, non-emissive CdS. The persistence of favourable reaction dynamics under these conditions could also promote the formation of new, smaller, blue-emitting particles, which would be detected at lower wavelengths. The photoluminescence spectra (e) support this theory, by bathochromic shift

from 507 to over 700 nm, between 1 and 2 h, then hypsochromic shifting to 383 – 391 nm for the 3- and 4-hour reactions.

At 200 °C, a similar trend was observed, with the 1-hour reaction yielding an absorption and photoluminescence maximum at 406 and 607 nm, respectively. While longer reaction times resulted in hypsochoromic shift to λ_{abs} at 300 nm, shown in (c). The photoluminescence spectra (f) demonstrated a progressive red shift between the 2-, 3- and 4-hour reactions.

At 100 °C, the initial sample of 1 hour reaction time emitted in the blue-green region, whereas extended, higher-temperature reactions exhibited dominant yellow to red emission bands. This shift towards longer wavelengths aligns with observations at 150 °C and 200 °C, where the formation of precipitation further influences the photoluminescence wavelength. Precipitated solids from the reactions were isolated via centrifugation, subsequently washed with water, ethanol, and toluene, and then dried for characterisation by XRD, confirming their composition as bulk CdS material, shown in Figure 2.11.

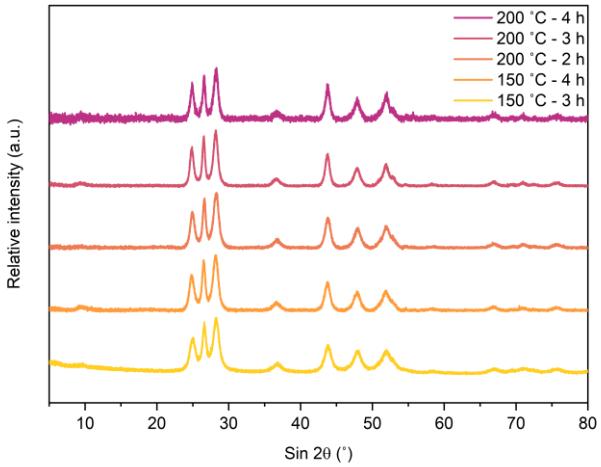

Figure 2.11, XRD patterns of precipitate of hydrothermal reactions of cadmium nitrate, thiourea, L-cysteine in conventional oven, pH 10, varying reaction time and temperature.

The combined data from both experimental sets indicates that the formation and luminescence characteristics of the particles are contingent upon time, temperature, and pH. A plausible hypothesis suggests that optimal control resides within a parameter window of 100–150 °C, reaction times of 1–3 h, and basic pH conditions. This hypothesis may also propose that blue emission represents a baseline rather than a specific control outcome, as it appears at both extremes of the parameter variance. Furthermore, basic conditions were found favourable as the ligand's reactivity is enhanced, leading to improved particle stabilisation and red-shifted emission, thereby enabling control over particle growth and bandgap narrowing. Consequently, ligand attachment effectively inhibits aggregation, ensuring the dispersion of quantum dots in solution even during prolonged reaction periods.

2.3.3 Further exploration of conventional reaction system for CdS QDs with alternative ligand – Cysteamine

Following an evaluation of the initial reaction system, a second ligand, Cysteamine, was examined. Cysteamine, an organosulfur compound, is soluble in water and possesses both amine and thiol functional groups. These characteristics suggest its suitability for binding to Cadmium, thus qualifying it as a ligand for this research. Table 2.6 provides a comparison of the properties of L-cysteine and cysteamine. Figure 2.12 indicates that at pH values exceeding 8, cysteamine undergoes deprotonation, leading to increased reactivity and dimerization into cysteamine. This process renders it an ineffective ligand for thiol-mediated attachment due to disulfide bond formation. Therefore, cysteamine is only investigated at neutral or acidic conditions.

Table 2.6, Ligand properties of L-cysteine and cysteamine[82]

Ligand	Abbreviation	Structure	MW (g/mol)	pKa (25 °C)			pI(25°C)
				$-CO_2H$	$-NH_2$	-SH	
L-Cysteine	L-Cys	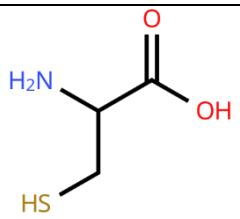	121.16	1.7	8.3	10.8	5.1
Cysteamine	CysA	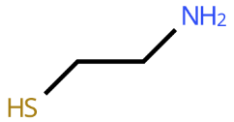	77.15	-	10.8	8.2	10.4

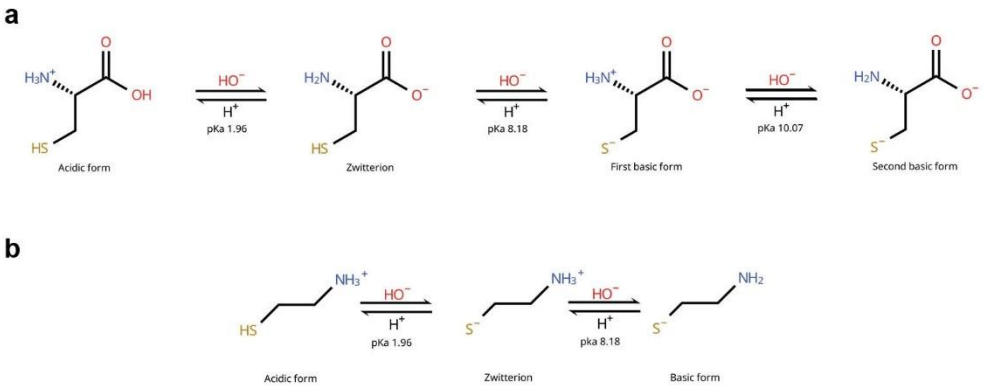

Figure 2.12, pH dependent forms of L-cysteine and Cysteamine[83, 84]

A stock solution of 0.22 M Cysteamine in water was prepared and utilised in a manner consistent with the methodology of the first experiment in this chapter. The resultant reaction mixture yielded a homogeneous solution at a pH of 5.6. Subsequent testing of identical reaction parameters for time and temperature produced the following outcomes, summarised in Table 2.7.

Table 2.7, Results of the hydrothermal reaction of cadmium nitrate, thiourea, cysteamine in conventional oven, pH 5.6.

Reaction time	Reaction temperature											
	100 ˚C				150 ˚C				200 ˚C			
	PL	Ppt	λ_{abs} (nm)	λ_{em} (nm)	PL	Ppt	λ_{abs} (nm)	λ_{em} (nm)	PL	Ppt	λ_{abs} (nm)	λ_{em} (nm)
1 h	Blue	No	-	426	Blue	No	-	448	Red	No	403	652
2 h	Blue	No	-	436	Red	No	410	651	Orange	Yes	294	422
3 h	Red	No	390	607	Red	Yes	432	463	Blue	Yes	297	426
4 h	Red	No	395	619	Blue	Yes	420	425	Blue	Yes	297	419

Under low-temperature conditions (100 ˚C), the synthesised samples exhibited blue emission at shorter reaction durations (1 – 2 h) and shifted to red emission with prolonged reaction times (3 – 4 h), shown in Figure 2.13 (a, d). No precipitation occurred across all tested reaction times at low temperatures. This observation suggests that either the deprotonated ligand or the low concentration of H^+ ions facilitated formation of the product more readily at low temperatures compared to reactions with L-cysteine at neutral conditions.

At 150 °C (b, e), the observed pattern of blue-red-blue emission resembled that of the L-cysteine experiments. Whereby both ends of the reaction time range resulted in blue emission, and the reaction times between in red emission. Solid formation was again observed at the 150 °C/3 h condition, establishing a consistent boundary between soluble and insoluble particles across all experiments.

At elevated temperatures (200 °C) the spectra depicted in (c, f), and brief reaction duration (1 hour), red emission was observed, suggesting that cysteamine, acting as a ligand, and the reaction solution's pH contribute to controlled particle growth. The two-hour reaction yielded orange emission, which, being blue-shifted relative to the one-hour reaction, deviates from the typical trend of red-shifted emission with extended reaction times. This deviation is likely attributable to the precipitation of the largest particles into non-emissive bulk material, thereby revealing the soluble, emissive nanomaterials remaining in solution.

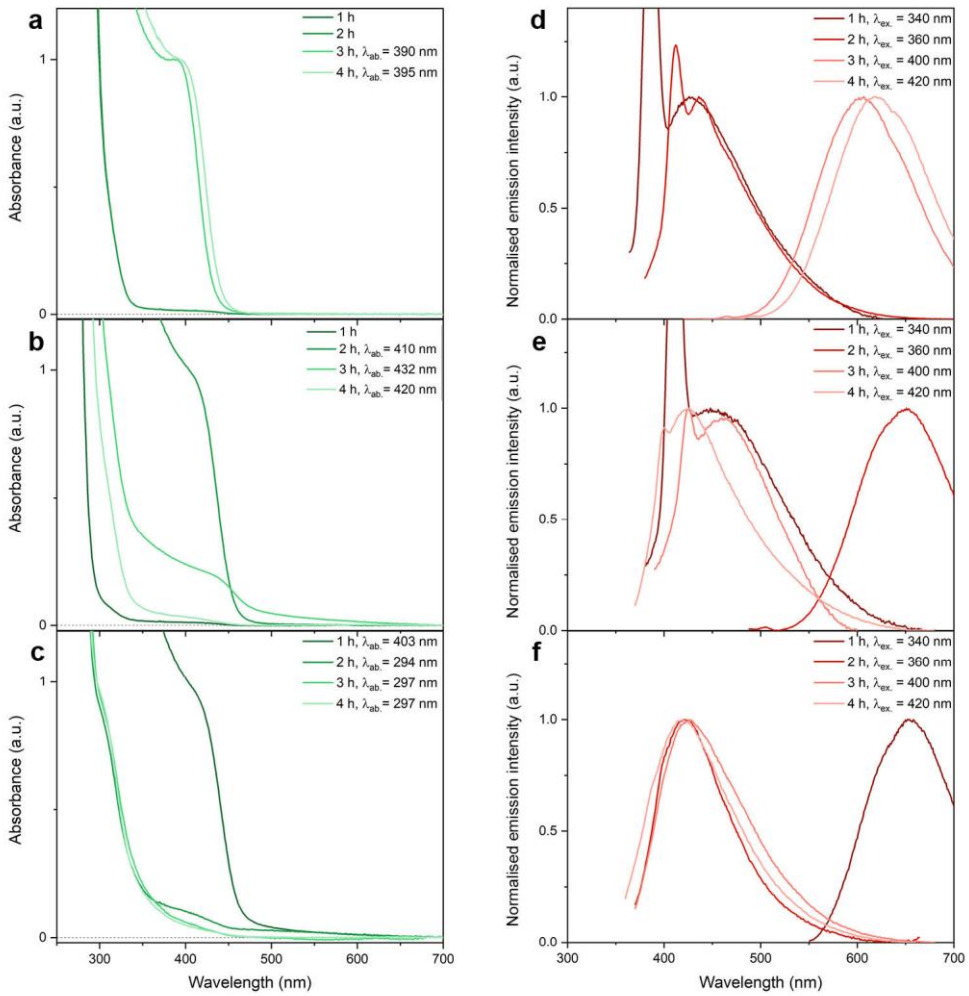

Figure 2.13, Normalised absorbance and photoluminescence emission of the hydrothermal reaction of cadmium nitrate, thiourea, cysteamine in conventional oven, pH 5.6, 1 – 4 h, 100 – 200 ˚C

A comparative analysis suggested that L-cysteine and Cysteamine can serve as an effective ligand for the formation of CdS quantum dots in hydrothermal synthesis, whereby L-cysteine performs better in alkaline environments, while cysteamine performs well in mildly acidic conditions. The zwitterionic character of both cysteine and cysteamine likely contributes to their preference for neutral or alkaline conditions. Cysteine exhibits a neutral dipole moment at pH 7 and becomes negatively charged at pH 10 due to the deprotonation of its thiol group, facilitating interaction with Cd^{2+} ions. While cysteamine also experiences thiol group deprotonation under basic conditions, this leads to dimerization and formation of disulfide bond, therefore preferring a lower pH.

2.3.4 Optimised reaction system for hydrothermal synthesis of CdS QDs

Previous experiments delineated the operational parameters for quantum dot synthesis in the conventional reaction system of autoclave and oven using the ligands L-cysteine and cysteamine. Each system was optimised to produce a broad range of emission wavelength, by altering the reaction conditions within the observed systems. Preliminary investigations at a reaction temperature of 150 °C, with reaction times ranging from 1 to 2 h at 20-minute intervals, demonstrated limited control, characterised by a rapid transition from no luminescence to red emission and from the absence of solid formation to precipitation accompanied by red

luminescence. Therefore, a reaction temperature of 130 °C was proposed to modulate the reaction kinetics, thereby enabling control over particle growth while still supplying adequate energy for reaction initiation. Lowering the reaction temperature to 130 °C successfully provided sufficient thermal energy for nucleation while enhancing control over particle size and optical characteristics.

Hydrothermal synthesis of cadmium nitrate, thiourea and L-cysteine at pH 7 resulted in the following. In Figure 2.14 (a) a picture of the produced samples under UV 365 light is given, supplemented with the optical characterisation of UV-vis absorbance (b), and photoluminescence spectroscopy (c).

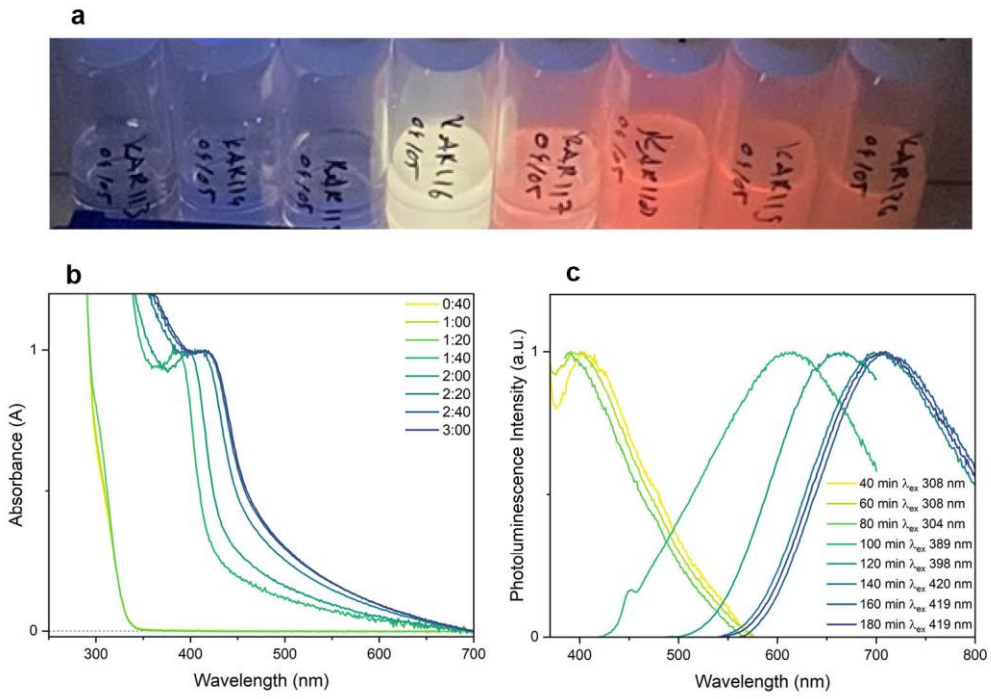

Figure 2.14, Picture of the supernatant produced under UV 365 nm and normalised absorbance and emission spectra of the hydrothermal synthesis of cadmium nitrate, thiourea, L-cysteine in conventional oven, 40 min to 3 h at 130 ˚C

During initial reaction periods (40 – 80 min), a minor absorbance shoulder was observed at 300 nm. Subsequently, at extended reaction times (100–180 min), the absorbance increased significantly to 383 nm and further shifted to 415 nm. Photoluminescence analysis mirrored these absorption trends, with reaction times up to 80 min yielding blue emission around 400 nm. Beyond 100 min, a transition to red emission occurred, shifting from 616 nm to 709 nm with increasing reaction duration. The final reaction times (160–180 min) showed consistent absorbance and emission wavelengths, suggesting the system's upper limit had been reached.

The hydrothermal synthesis of cadmium nitrate, thiourea, and cysteamine at pH 5.6, provided with the following results, shown in Figure 2.15 (b).It was observed that even the shortest reaction times yielded an absorbance peak, in contrast to the L-cysteine reactions. A distinct shift in absorbance from 347 nm to 393 nm occurred between the 40- and 180-minute reaction intervals. Concurrently, the emission spectrum exhibited a corresponding shift from 506 nm to 701 nm depicted in (c), accompanied by a loss of

luminescence intensity. The reaction times of 160 and 180 min demonstrated the same absorbance and emission wavelengths, suggesting the system had reached its upper limit, like the L-cysteine reaction system.

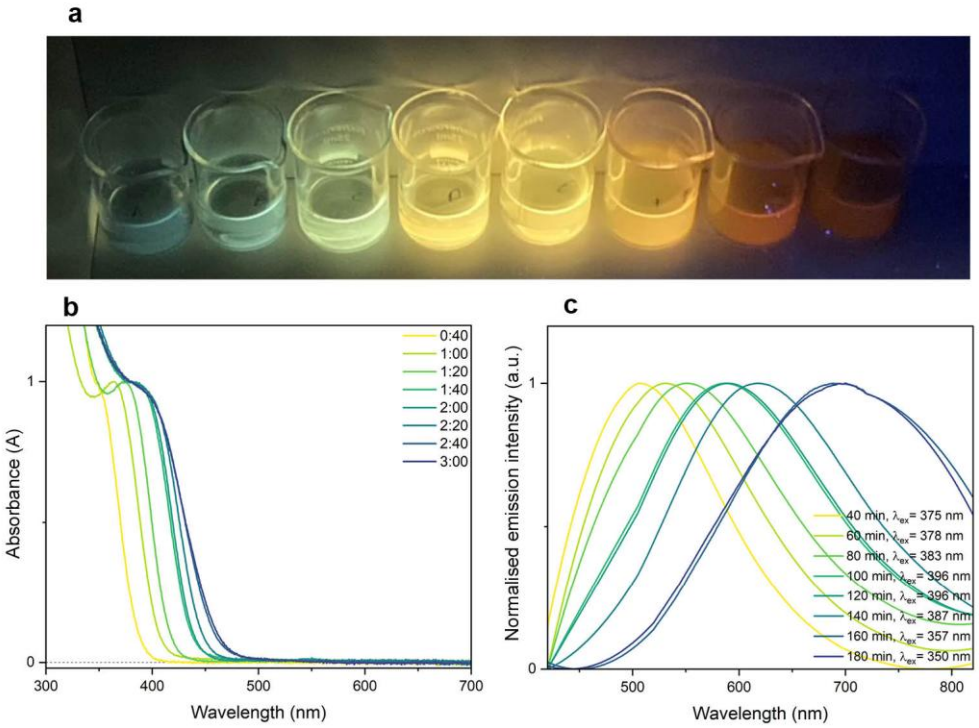

Figure 2.15, Picture of the samples produced under UV 365 nm and normalised absorbance, excitation, smoothed, and relative emission spectra of hydrothermal synthesis of cadmium nitrate, thiourea, cysteamine in conventional oven, 40 min to 3 h at 130 ˚C

In Table 2.8, the results of both systems are tabulated. This research demonstrates the production of tuneable bandgap emission ranging from blue to red CdS quantum dots through hydrothermal synthesis by modulating reaction time, the appropriate temperature, applicable to two systems which differ in ligand selection and pH align with previously reported hydrothermal syntheses where extended reaction times produce red-shifted photoluminescence and larger CdS nanocrystals, corroborating the time and temperature dependent bandgap tuning documented in the literature. Optimised reaction for L-cysteine shows no luminescence properties for shorter reaction times of 30 min and under, while Cysteamine shows blue-green luminescence for these reaction times. It suggests L-cysteine must overcome a bigger energy barrier than Cysteamine to react.

Table 2.8, Results of the optimised conventional hydrothermal reaction system at 130 ˚C of cadmium nitrate, thiourea, varying ligands L-cysteine at pH 7, and cysteamine at pH 5.6, and reaction time from 40 min to 3 h.

Reaction time	L-cysteine				Cysteamine			
	PL	Ppt	λ_{abs} (nm)	λ_{em} (nm)	PL	Ppt	λ_{abs} (nm)	λ_{em} (nm)
40 min	Blue	Yes	300	404	Blue	No	352	506
60 min	Blue	Yes	300	401	Turquoise	No	364	531
80 min	Blue	Yes	300	391	Green	No	371	551
100 min	Yellow	Yes	387	616	Yellow	No	377	586
120 min	Red (low intensity)	Yes	397	667	Yellow	No	381	590
140 min	Red	Yes	410	704	Yellow/Orange	No	381	619
160 min	Red	Yes	416	709	Orange/Red	No	378	689
180 min	Red	Yes	415	704	Red	No	378	701

2.4 Heat block reactions: introducing an alternative system for hydrothermal synthesis of CdS quantum dots

The formation of solids, which enables photoluminescent nanomaterials to consolidate into bulk material, provides significant insights into the limitations and control mechanisms inherent in reaction systems for semiconductive nanomaterial synthesis. Nucleation is an energetically demanding process involving the overcoming of a free energy barrier to form a stable cluster. In contrast, growth is a less energy-intensive process where the nucleus expands through the accretion of additional monomers. While the batch hydrothermal process operates as a closed system, its opacity limits understanding to the initial materials, final products, and reaction parameters, without revealing internal dynamics; furthermore, the mechanisms and progression of convection remain elusive.[85] Comprehending heat and mass transfer is essential for refining control over batch hydrothermal synthesis; however, direct investigation of internal processes is challenging due to the elevated temperatures and pressures within the reaction vessels.

To better understand the reaction and solid formation, an alternative heating system was employed that allows for real-time observation and improved control over the reaction. This system, which includes a heat block, offers advantages such as controlled temperature, shorter reactions, and increased reproducibility. The later was achieved because the setup could hold eight vials at once, improving the uniformity of reaction conditions and samples. Reactions were performed in Duran glass vials with pressure caps for sealing and pressure management, and these vials allowed for real-time monitoring. Implementation of this system was possible because the earlier investigation identified the reduced reaction temperature of 130 ˚C as sufficient to induce the formation of photoluminescence materials. This came with the additional advantage of improved heating time, which was massively reduced, to reaction times under 1 hour. The results of these experiments will be presented next. For brevity, reaction times will be denoted using a shorthand notation: t5 represents a reaction time of 5 min, t10 represents 10 min, and so on.

2.4.1 Reaction system Cadmium Nitrate, Thiourea, and L-cysteine

The investigation into the hydrothermal synthesis of quantum dots followed a systematic methodology, initiating with a reaction analogous to that described previously, the equivalent of conventional oven/autoclave reaction with heat block/Duran tubes. This involved employing Cadmium Nitrate, Thiourea, and L-cysteine as reactants in solution, while systematically altering the reaction parameters of pH and time. The specific variations tested are shown in Figure 2.16.

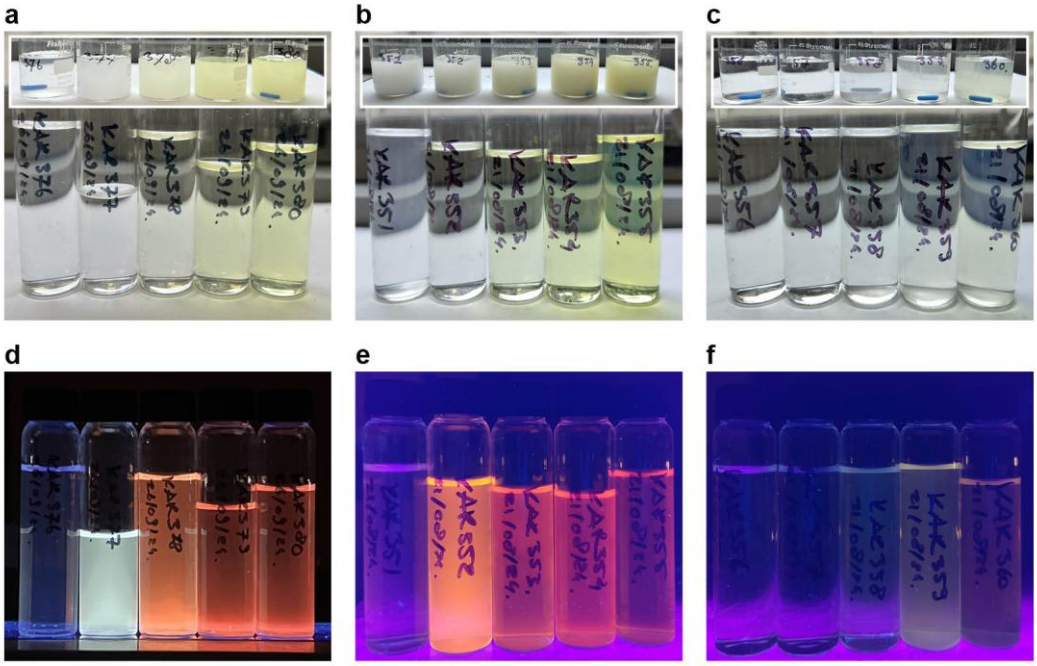

Figure 2.16, Pictures of reaction samples of the hydrothermal synthesis of CdS quantum dots from Cadmium Nitrate, Thiourea, and L-Cysteine, for reaction times 5, 10, 20 30 and 40 min from left to right, sample (inset) and supernatant in daylight, of reactions at pH 7 (a), 8.5 (b), and 10 (c), and the supernatant under UV 365 of reaction at pH 7 (d), 8.5 (e), and 10 (f).

The synthesis of cadmium sulfide quantum dots at neutral pH, depicted in Figure 2.16 (a) produced a t5 clear and colourless solution with minimal formation of solids as predicted. Reaction at t10 produced a white suspension with a gradual change to pale yellow for t40. The collected supernatant was clear, t5 colourless and gradually changing to clear and yellow. When regarding the supernatants under UV, shown in (d) t5 produced no luminescence, t10 a bleak green/yellow, t20 vibrant orange and t30-40 a reduced red.

At pH 8.5, visibly more solids were formed in reaction, depicted in Figure 2.16 (b). Reaction t5 produced white solids which gradually turned to pale yellow for t40 or could be a mix of white and yellow solids simultaneous produced. The supernatant and solids were isolated with centrifugation. The supernatants collected were transparent but different colours were observed, t5 white, t10 colourless, and t20-40 pale yellow to yellow. Under UV-light, shown in (e) t5 produced no luminescence, t10 yellow, t20 orange and t40 red, however t40 showed a muted colour red.

The samples from the reaction at pH 10 produced clear and colourless samples for t5 – t10, white suspension for t20 developing towards pale yellow at t40, however significantly less solids were produced, as can be seen in Figure 2.16 (c). The supernatants t5 – t30 were transparent and colourless and t40 was transparent and pale yellow. Under UV 365 (f) t5 – t10 produced no luminescence, t20 blue, t30 yellow, and t40 red, however all at significant low intensity, compared to the reactions at pH 7 and 8.5.

Optical characterisation of the supernatant of the hydrothermal synthesis of CdS quantum dots from Cadmium Nitrate, Thiourea, and L-Cysteine at pH 7 showed absorption shift from t10 365 to t40 403 nm, in Figure 2.17 (a). The longer reaction times from t20 show a second shoulder around 315 nm, however λ_{ex} optimal was found from the bathochromic shifted λ_{abs}.

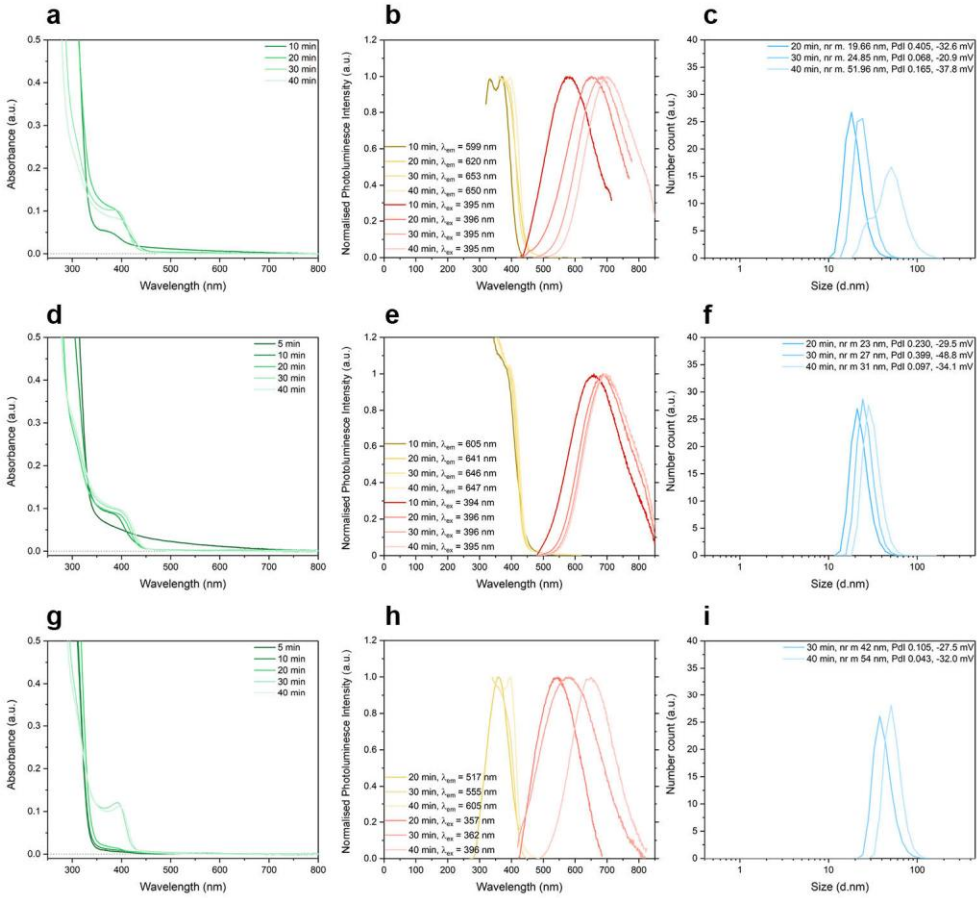

Figure 2.17, Optical characterisation of the supernatant of the hydrothermal synthesis of CdS quantum dots from Cadmium Nitrate, Thiourea, and L-Cysteine at pH 7, for reaction times 5, 10, 20 30 and 40 min at pH 7 absorption (a) photoluminescence (b), and dynamic light scattering spectra (c), at pH 8.5 absorption (d) photoluminescence (e), and dynamic light scattering spectra (f),and at pH 10 , absorption (g) photoluminescence (h), and dynamic light scattering spectra (i).

Table 2.9, Overview optical properties CdS QDs from Cadmium Nitrate, Thiourea, and L-Cysteine, varying pH and reaction time,* measured in triplets and averaged.

pH	Time (min)	λ_{abs} (nm)	λ_{ex} (nm)	λ_{em} (nm)	Bandgap (eV)	Tauc size (nm)	DLS size (nm)*	PdI*	Zeta-pot. (mV)*
7	5	365	365	575	2.99	4.2	-	-	-
7	10	385	395	653	2.95	4.4	-	-	-
7	20	399	396	686	2.96	4.3	19.66	0.405	- 32.6
7	30	405	395	698	2.88	4.7	24.85	0.068	- 20.9
7	40	415	395	722	2.80	5.1	51.96	0.165	- 37.8
8.5	5	-	-	-	-	-	-	-	-
8.5	10	389	394	659	3.00	4.2	-	-	-
8.5	20	396	396	687	2.94	4.4	22.95	0.230	- 29.5
8.5	30	400	396	696	2.89	4.6	26.53	0.399	- 48.8
8.5	40	403	395	700	2.88	4.7	31.46	0.097	- 34.1
10	5	-	-	-	-	-	-	-	-
10	10	-	-	-	-	-	-	-	-
10	20	394	357	547	3.68	2.8	-	-	-
10	30	391	362	573	2.98	4.2	42.14	0.105	- 27.5
10	40	394	396	649	2.96	4.3	54.35	0.043	- 32.0

The emission spectra shown in (b), present a periodic red shift in $\lambda_{em\ max}$ shifting from t10 to t40, from 575 to 722 nm respectively. Dynamic Light Scattering (c) analysis showed PdI > 0.3 for t10 and t20 indicating polydispersity and rendering the size data unreliable for calculating an average size. Particle growth from t20 to t30 and t40 is recorded from 20 to 25 to 52 nm, together with good zeta potential < - 20 mV. However, the sizes measured cannot be accepted as the true particle size. As DLS measures the hydrodynamic particle size including the core particle and any material bound to its surface in solution. Consequently, the observed sizes did not align with the expected <10 nm range. Nevertheless, the trend of increasing particle size with reaction time suggests particle growth or agglomeration of the samples. Alternatively, the calculated size and band gap energy, retrieved from the Tauc plot, provide a better estimation of the particle size presented in Table 2.9. The band gap energy was calculated to reduce from 2.99 to 2.80 eV, and the size to increase from 4.2 to 5.1 nm, between t5 and t 40.
Since the DLS data provides valuable information on the stability and uniformity of the material producedit was included in the findings.

UV-vis absorbance of samples from reactions at pH 8.5, presented in Figure 2.17(d), showed the presents of solids in supernatant t5 resulting in a background signal. Only a small shift from 389 to 403 nm was recorded between t10 and t40. Reaction t20 – 40 produced a second shoulder starting to form at 305 nm. Photoluminescence characterisation (e) showed no shift in λ_{ex}, for all around 396 nm. $\lambda_{em,max}$ shifts from t10 to t40 from 659 to 700 nm. The band gap energy was calculated to range between 2.88 and 3.00 eV and a size of 4.2 – 4.7 nm. DLS showed t5 – t10 is polydisperse, while t20 – t40 shows good PdI, good zeta potential.

At pH 10 the absorption plot of the supernatant, Figure 2.17 (g), showed no observed absorbance for t5 and slight absorbance for t10 and t20. Reaction t30 produced a shoulder at 390 nm, and t40 at 395 nm, indicating a small shift. No photoluminescence data was observed for t5-10, but t20 to t40 showed an emission shift from 547 to 649 nm, shown in (h). This covers a broad range on the visible wavelength range but reduced emission intensity, calculated band gap energy of 2.96 – 3.68 mV, and size 2.8 – 4.3 nm. DLS showed t5 to t20 was polydisperse with good zeta potential around -30 mV.

A comprehensive analysis of all reactions revealed that the t5 reactions were consistently insufficient in duration to facilitate the formation of luminescent materials across all experimental systems. A consistent colour progression from colourless to white to yellow was observed in both the precipitate and their respective supernatants. This colour change correlated with a red shift over reaction time, suggesting particle growth, which was characterised by UV-Vis and photoluminescence analysis. This observation aligns with previous studies where increased reaction time leads to larger nanoparticles and a corresponding red-shifted emission, indicating a growth in particle size.[51, 72, 76] DLS measurements further validated this trend, showing a progressive increase in hydrodynamic diameter with prolonged reaction durations, and general trend in declining PdI with reaction time.

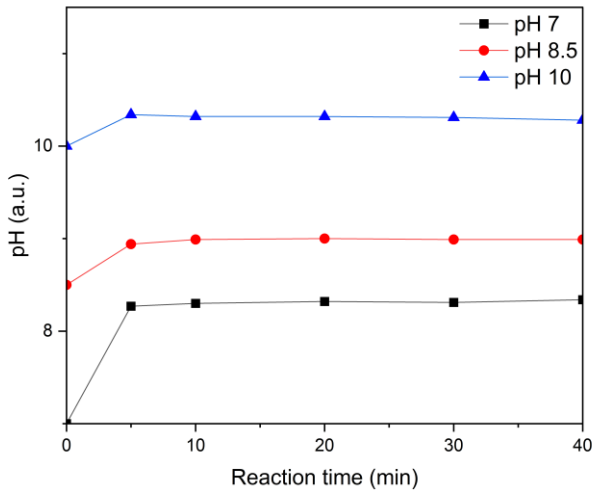

Figure 2.18, pH development of the hydrothermal synthesis of CdS quantum dots from Cadmium Nitrate, Thiourea, and L-Cysteine at pH 7, 8.5, and 10, for reaction times 5, 10, 20 30 and 40 min

Investigating the pH development between t0 and t40 revealed that in the first five min of the reaction the pH increased, depicted in Figure 2.18. After t5 the pH remains stable at pH 8.3, 9.0 and 10.3 for starting pH 7, 8.5 and 10 respectively. Together with the previous observation that t5 does not yield photoluminescence samples, it is deducted that in the first stages of the reaction, the reactants are broken down and the concentration of H^+ reduced before a new material is formed. Additionally, it was revealed that reactions initiated within the pH range of 7 to 8.5 consistently produced a quantity of solids. Conversely, the reaction conducted at pH 10 resulted in a substantially lower yield of solids, implying that L-Cysteine largely persisted in solution under these conditions. Nevertheless, the resultant low emission intensity indicates a restricted formation of luminescent particles. While this pH condition favours the dissolution of the ligand, it simultaneously impedes the optical properties of the material produced. XRD characterisation revealed that the solids formed at pH 8.5 in this reaction consisted of a cysteine complex, shown in Figure 2.19.[86] This materials showed consistent peak positions and widths over time, with no new peaks emerging with reaction time.

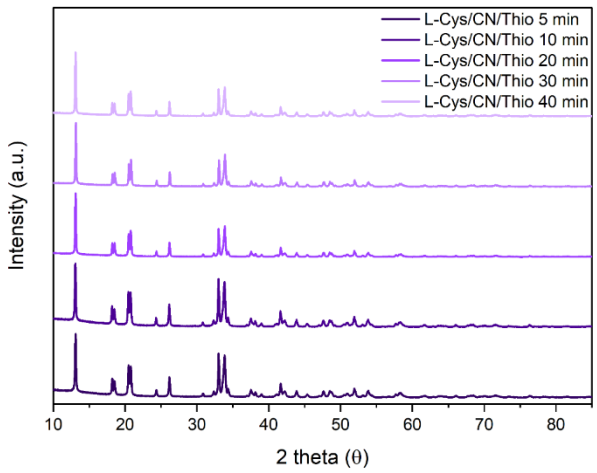

Figure 2.19, XRD patterns of the precipitates from the hydrothermal synthesis of CdS quantum dots from Cadmium Nitrate, Thiourea, and L-Cysteine at pH 8.5, for reaction times 5, 10, 20 30 and 40 min

2.4.2 Reaction system Cadmium Nitrate, Thiourea, Cysteamine

Subsequently, the heat block system was used to synthesise CdS quantum dots with Cysteamine as the ligand, replacing L-Cysteine. Previous studies using autoclave systems indicated that Cysteamine reactions with thiourea and cadmium nitrate were effective under acidic conditions at pH 5.6, establishing a blue print for the heat block system. Autoclave-based hydrothermal synthesis demonstrated that Cysteamine reactions could yield full spectrum emitting species. To capture the spectral range, reaction times were extended up to 90 min, examining the resultant optical properties. The reaction times investigated were 10, 20, 30, 40, 50, 60, and 90 min. Notably, the t10 experiment did not produce photoluminescent species, establishing a lower system boundary. Throughout the reaction, the pH increased from 5.6 to 6.4 over time. No precipitate formation was observed across all reaction times, and the samples were transparent, with a colour gradient from colourless to yellow, shown in Figure 2.20 (a), consistent with the conventional hydrothermal system. Under luminescence light, shown in (b), a red shift was observed: blue/green emission at t20, transitioning to yellow at t30, orange at t40 and t50, and finally orange/red at t60 to t90. The highest luminescence intensity, observed visually, was produced by samples from t20 and t30. The results of this reaction series are summarised in Table 2.10.

Table 2.10, Overview optical properties CdS QDs from Cadmium Nitrate, Thiourea, and Cysteamine at pH 5.6, varying reaction time, * measured in triplets and averaged.

Time (min)	λ_{abs} (nm)	λ_{ex} (nm)	λ_{em} (nm)	Bandgap (eV)	Tauc Size (nm)	DLS size (nm)*	PdI*	Zeta-pot. (mV)*
10	-	-	-	-	-	-	-	-
20	368	373	587	3.11	3.8	-	-	-
30	376	381	615	3.00	4.2	-	-	-
40	382	393	635	2.96	4.3	9.223	0.220	36.3
50	387	395	659	2.92	4.5	10.27	0.147	12.8
60	395	398	659	2.89	4.6	17.9	0.151	19.5
90	400	400	682	2.86	4.8	19.64	0.180	24.1

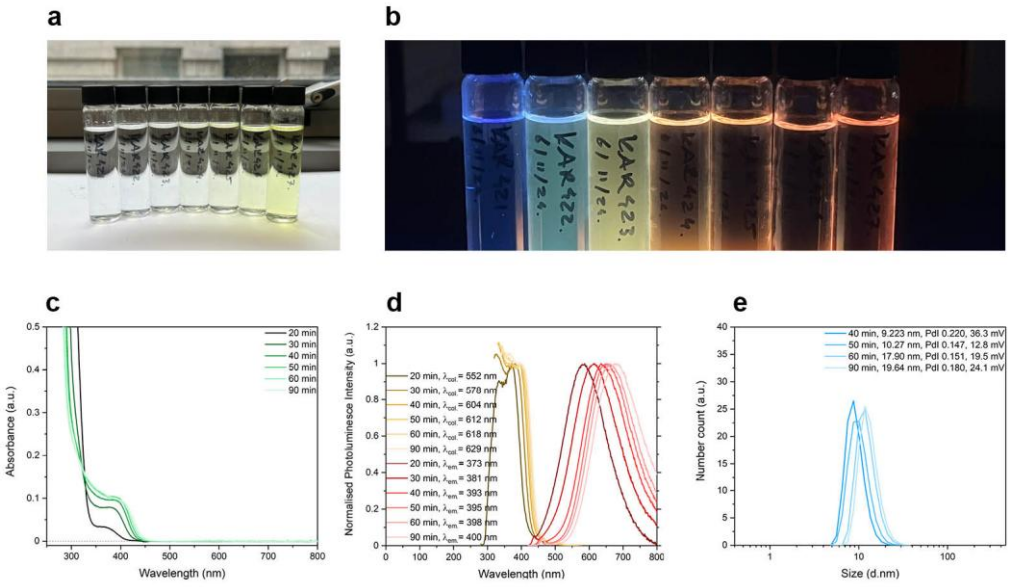

Figure 2.20, crude sample in daylight (left) and UV 365 (right) ,Absorbance (a), photoluminescence (b), and DLS (c) plot for the supernatant of the repeated hydrothermal synthesis of CdS quantum dots from Cadmium Nitrate, Thiourea and Cysteamine at pH 5.6, for reaction time of 20, 30, 40, 50, 60, and 90 min

Characterisation revealed no discernible absorbance or luminescence spectra for the t10 sample. Depicted in Figure 2.20 (c) a red shift in absorbance was observed, ranging from 368 to 400 nm for t20 to t90, corresponding to calculated bandgap energies between 2.86 and 3.11 eV and particle sizes between 3.8 and 4.8 nm. The maximum excitation wavelength consistently increased from 371 to 396 nm, while the maximum emission wavelength shifted from 587 to 682 nm, depicted in (d) indicating reliable control over the particles' optical properties. Dynamic Light Scattering analysis showed a decrease in the PdI with increasing reaction time and acceptable PdI values were achieved from t40 onwards. Zeta potentials showed an inverse relation with the PdI, ranging between 12.8 – 36.3 mV.

Additionally, the influence of pH adjustments was tested by varying the pH: 7, 8.5, and 10 for reaction times 5, 10, 20, 30, and 40 min, consistent with the L-cysteine experiments. In Figure 2.21 the reaction samples under daylight and UV 365 are shown in (a, b, c) for respectively, pH 7, 8.5 and 10. All samples produced showed colourless and transparent samples, without the formation of precipitate. Only one sample at pH 7, 40 min. shown in (d), produced luminescence, in yellow, characterised with λ_{abs} 388 nm and fluorescence characterisation resulted in $\lambda_{em\ max}$ 607 nm, indicating delayed formation, and therefore availability of cysteamine in reaction. This could be connected to the deprotonation of the zwitterion of cysteamine into its basic form at pKa of 8.18.

Between these observations of no yellow colour of the supernatant under normal light, no precipitate formation, and the temporal photoluminescence shift at pH 5.6, it is theorised that at elevated pH, formation of CdS is not possible. It is suspected that the reaction mixture does not support the generation of sulfide fir the formation of the particles. This brings our attention to thiourea, and its function in this reaction. Additionally, this raises the question, what is the sulfide generated from at reduced pH of 5.6?

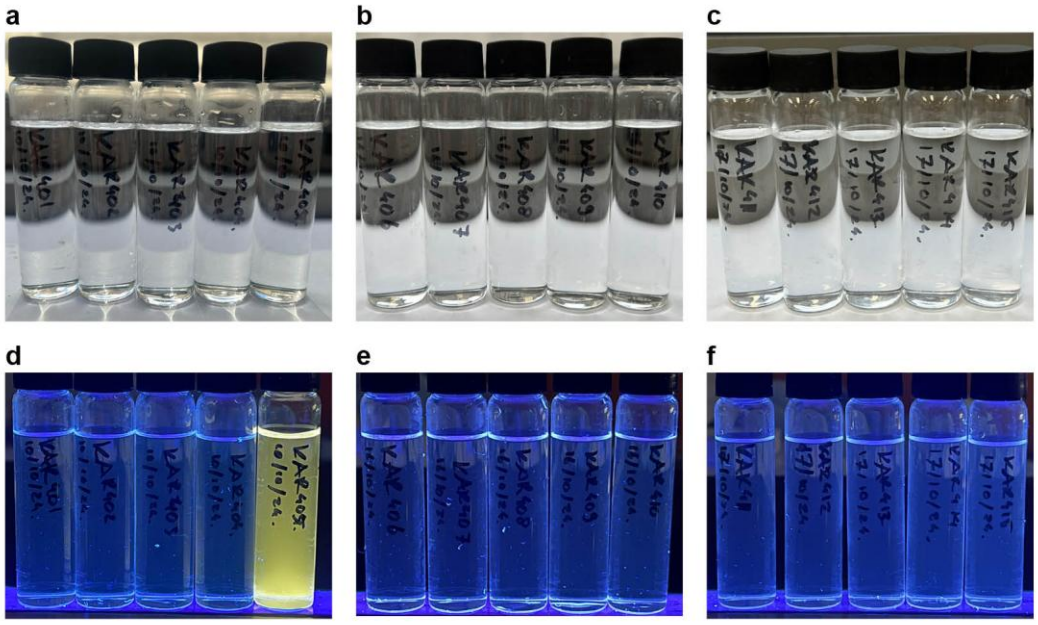

Figure 2.21, Pictures of reaction samples of the hydrothermal synthesis of CdS quantum dots from Cadmium Nitrate, Thiourea, and Cysteamine, for reaction times 5, 10, 20 30 and 40 min from left to right, sample in daylight, of reactions at pH 7 (a), 8.5 (b), and 10 (c), and under UV 365 of reaction at pH 7 (d), 8.5 (e), and 10 (f).

Table 2.11, Optical properties of CdS QDs from cadmium nitrate, thiourea, and cysteamine at pH 7, reaction time 40 min.

pH	Time (min)	λ_{abs} (nm)	λ_{ex} (nm)	λ_{em} (nm)	Bandgap (eV)	Size (nm)
7	40	388	388	600	2.95	4.4

2.4.3 Evaluation of the proposed reaction system with Duran tubes and heat block

The hydrothermal reaction system utilising a heat block and Duran tubes, with modifications, effectively replicates the autoclave and oven setup. Cadmium nitrate and thiourea react with the chosen ligand to form materials with tuneable optical properties. Investigations into the influence of pH on ligand performance indicated that L-cysteine yields favourable control within pH ranges of 7 and 8.5 across reaction times from 10 to 40 min. In contrast, cysteamine performs best under acidic conditions (pH 5.6) with extended reaction times ranging from 20 to 90 min. Furthermore, cysteamine exhibits greater stability in solution upon heating, whereas L-cysteine tends to precipitate readily. In Table 2.12. the impact of these ligands on the proposed reaction system are summarised.

Table 2.12, Ligand effects of L-cysteine or Cysteamine in hydrothermal reaction with Cadmium nitrate and Thiourea

	L-Cysteine	**Cysteamine**
Tuneable optical properties (λ_{abs}, nm):	365 – 415	368 – 400
Tuneable optical properties (λ_{em}, nm):	547 – 722	587 – 682
Band gap (eV)	2.80 – 3.68	2.86 – 3.11
Size (nm)	2.8 – 5.1	3.8 – 4.8
Time (min)	10 – 40	20 – 90
pH	7 – 10	5.6
Formation of precipitation	L-cysteine complex	No

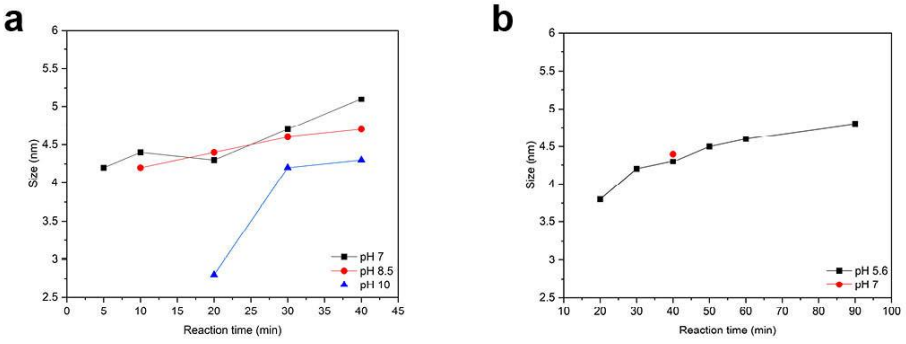

Figure 2.22, Sizes of CdS quantum dots produced in hydrothermal synthesis of cadmium nitrate, thiourea and L-cysteine (a), and cysteamine (b).

2.5 Reaction system with alternative sulfur source

Since the findings in 2.4.2 raised questions about the generation of sulfide and the formation of CdS in the proposed reaction system, the influence of the sulfur precursors is investigated more deeply here. To ascertain the influence of the sulfur precursor on the reaction mechanism, thiourea was substituted with sodium thiosulfate. This alternative sulfur source exhibits a lower decomposition temperature compared to thiourea,

which correlates directly with the activation energy required for decomposition. Consequently, sodium thiosulfate is anticipated to participate in the reaction at an earlier stage, thereby decreasing the reaction duration, energy consumption, and overall operational expenses.

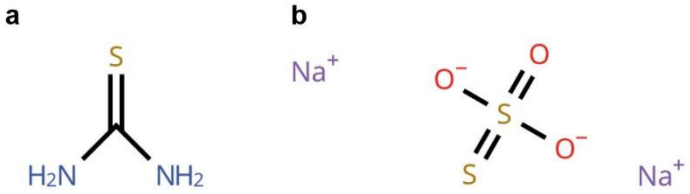

Figure 2.23, Molecular structure of thiourea and sodium thiosulfate[82]

2.5.1 Reaction system with Cadmium Nitrate, Sodium Thiosulfate, and L-Cysteine

The initial phase involved the hydrothermal synthesis of cadmium sulfide quantum dots using cadmium Nitrate, Sodium Thiosulfate, and L-Cysteine, reacting at a pH of 7. Observations from Figure 2.24 (a) indicate that the reaction produced a suspension across all tested reaction times, presenting as white at the 5-minute mark (t5) and yellow from 10 to 40 min. Following centrifugation, the supernatant was found to be colourless for t5 and yellow for t10 – t40. Under UV irradiation shown in (d), the emitted light ranged from blue/green at t5, shifting to orange at t10, and red at t40, although the emission intensity for t20 – t40 was reduced compared to the t5 – t10 reactions. These observations suggest that the earlier release of sulfide ions from sodium thiosulfate accelerates nucleation, yielding smaller nanocrystals and consequently diminished photoluminescence at longer reaction times.

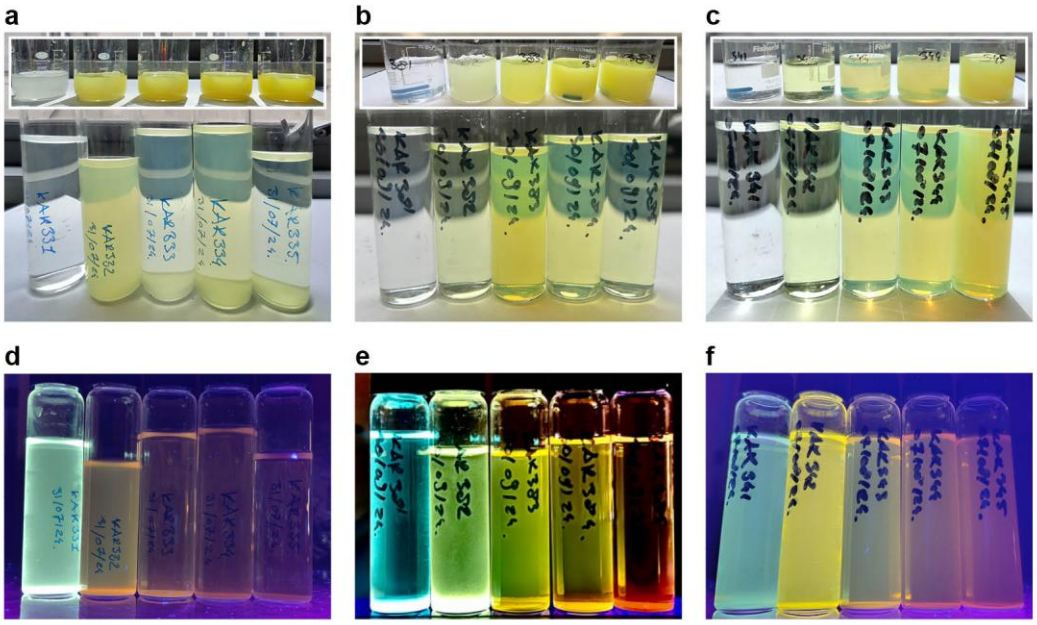

Figure 2.24, Pictures of reaction samples of the hydrothermal synthesis of CdS quantum dots from Cadmium Nitrate, Sodium Thiosulfate, and L-Cysteine, for reaction times 5, 10, 20 30 and 40 min from left to right, sample (inset) and supernatant in daylight, of reactions at pH 7 (a), 8.5 (b), and 10 (c), and the supernatant under UV 365 of reaction at pH 7 (d), 8.5 (e), and 10 (f).

The reaction series at pH 8.5 shown in Figure 2.24 (b), yielded a clear, colourless solution at t5, whereas the suspensions formed at t10 were white, and at t20-40 were yellow. This result parallels the trend seen in the pH 7 reaction series, though with less dramatic changes over the same period. The supernatants were initially transparent and colourless at the 5-minute mark, gradually increasing and then decreasing in yellow colour intensity. This resulted in the highest concentration of cadmium in solution at t20. Either caused by an increase in particle size or a higher concentration of synthesised material. The decrease in colour intensity after 20 min suggests that the particles may have exceeded their precipitation threshold, leading to sedimentation from the solution. Under UV excitation at 365 nm in (e) the photoluminescence exhibited a spectral shift from blue at t5, to green at t10, yellow at t20, orange at t30, and finally red at t40. A significant reduction in emission intensity was noted by eye at t40.

At pH 10 depicted in Figure 2.24 (c), no visible solids were observed in the reaction series. Nonetheless, a progression from a clear, colourless solution at t5 to a clear, pale-yellow solution at t10, culminating in an opaque, yellow suspension at t40, indicated the formation of cadmium sulfide materials with increasing size or concentration. Centrifugation of the t40 sample successfully isolated precipitate. The elevated solubility of L-cysteine under basic pH conditions accounts for the prevention of ligand precipitation. The supernatant displayed an increasing intensity of yellow coloration and opacity. Under UV excitation at 365 nm shown in (f), discernible blue and yellow emissions were noted, alongside muted orange and red hues; the t40 sample additionally produced a red emission, albeit with significantly reduced intensity.

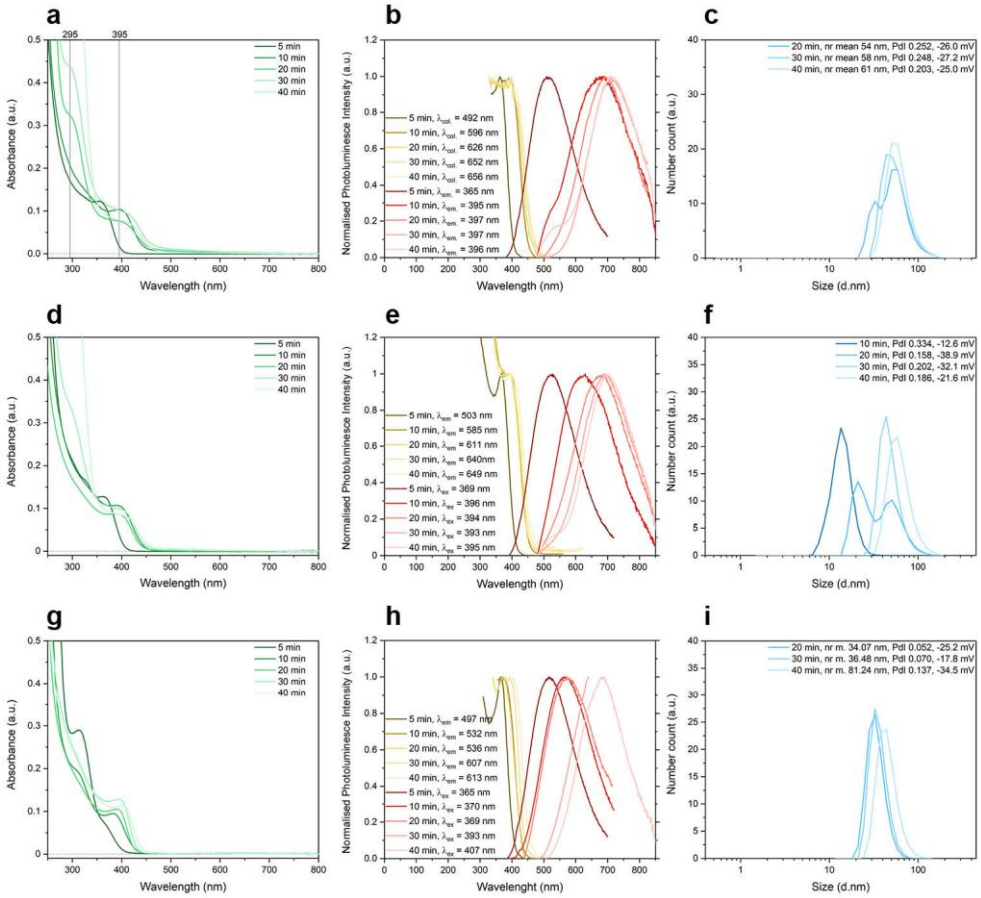

Figure 2.25, Optical characterisation of the supernatant of the hydrothermal synthesis of CdS quantum dots from Cadmium Nitrate, Sodium Thiosulfate, and L-Cysteine at pH 7, for reaction times 5, 10, 20 30 and 40 min at pH 7 absorption (a) photoluminescence (b), and dynamic light scattering

spectra (c), at pH 8.5 absorption (d) photoluminescence (e), and dynamic light scattering spectra (f),and at pH 10 , absorption (g) photoluminescence (h), and dynamic light scattering spectra (i).

Table 2.13, Overview optical properties CdS QDs from cadmium nitrate, sodium thiosulfate, and L-cysteine, varying pH and reaction time, * measured in triplets and averaged.

pH	Time (min)	λ_{abs} (nm)	λ_{ex} (nm)	λ_{em} (nm)	Bandgap (eV)	Tauc size (nm)	DLS size (nm)*	PdI*	Zeta-pot. (mV)*
7	5	353	365	509	3.19	3.6	-	0.30	-27.2
7	10	395	395	688	2.87	4.7	-	0.42	-29.4
7	20	395	395	691	2.81	5.1	54.09	0.25	-26
7	30	397	397	710	2.76	5.4	57.74	0.25	-27.2
7	40	396	396	706	2.77	5.4	61.29	0.20	-25
8.5	5	362	367	527	3.14	3.7	-	-	-
8.5	10	391	394	630	2.87	4.7	13.54	0.334	-12.6
8.5	20	395	394	687	2.90	4.6	32.67	0.158	-38.9
8.5	30	399	396	693	2.85	4.8	43.82	0.202	-32.1
8.5	40	407	395	699	2.81	5.1	58.77	0.1861	-21.6
10	5	365	365	517	3.19	3.6	101.59	0.29	-28.6
10	10	381	370	570	2.99	4.2	17.85	0.40	-21.6
10	20	391	369	571	2.98	4.2	34.07	0.05	-25.2
10	30	395	393	633	2.94	4.4	36.48	0.07	-17.8
10	40	403	399	687	2.88	4.7	81.24	0.14	-34.5

Optical characterisation via UV-vis absorbance revealed the presence of two distinct shoulder peaks at varying intensities across different reaction times, identified at 295 nm and 395 nm, indicated in Figure 2.25 (a). The t5 reaction showed a clear peak at 353 nm, alongside the 295 nm shoulder. Maximum photoluminescence spectra were obtained by exciting at the absorbance peak wavelengths, shown in (b). For t5, excitation at 365 nm yielded a maximum emission peak at 509 nm, while excitation at 395 nm for t10 to t40 reactions resulted in emission peaks ranging from 688 to 706 nm. Analysis of the Tauc plot indicated a shift in bandgap energy from 3.19 eV to 2.77 eV as reaction times progressed from 5 to 40 min, corresponding to a change in nanoparticle diameter from 3.6 nm to 5.4 nm. Dynamic Light Scattering analysis showed PdI > 0.3 for t5 and t10 indicating polydispersity and rendering the size data unreliable for calculating an average. Zeta-potential measurements ranged from -25 to -30 mV, suggesting favourable particle surface charge.

Optical characterisation of the samples from the time series at pH 8.5 confirmed the presence of a shoulder peak at 320 nm, shown in Figure 2.25 (d). The λ_{ex} shifted from 362 nm at t5 to 398 nm at t30 – t40, resulting in a corresponding emission wavelength shift from λ_{em} 510 nm at t5 to 693 nm at t40, spanning a broad spectral range, depicted in (e). The Tauc plot analysis revealed a decrease in bandgap energy from 3.22 eV to 2.82 eV, correlating with an increase in nanoparticle diameter from 3.6 nm to 5.0 nm. Dynamic Light Scattering results indicated polydispersity for samples at t5 and t10. At t20, a low PdI of 0.052 was observed, but it yielded two distinct particle sizes (3.6 nm and 6.5 nm). The sample at t30 showed a PdI of 0.007, indicating monodisperse particles, though with a suboptimal zeta potential of -17.8 mV. Finally, the sample at t40 an acceptable PdI of 0.137 and a favourable zeta potential of -34.5 mV. These trends are comparable to those observed in the samples and pH measurements, where smaller variations were noted over the same time

frame compared to the pH 7 reaction series. Reliable DLS data for particle growth was only apparent from t30, in contrast to t20 for the pH 7 series. This delay in acquiring reliable DLS data likely stems from the later emergence of sufficiently large particles detectable by hydrodynamic sizing.

The UV-vis absorbance spectra for pH 10 shown in Figure 2.25 (g), revealed absorption bands at 315 and 365 nm for t, the latter shifted to 407 nm by t40, while the former remained constant. The recorded spectra demonstrated a periodic increase in excitation wavelength (λ_{ex}), this trend was mirrored in the emission spectra, showing a red shift from 517 to 687 nm between t5 and t40 depicted in (h). The bandgap energy exhibited a change from 2.88 to 3.19 eV, corresponding to nanoparticle sizes of 3.6 – 4.7 nm over the 10–40 min reaction period. These findings suggest that alkaline conditions promote the formation of larger, less aggregated CdS nanocrystals, consequently shifting optical properties towards longer wavelengths. Dynamic Light Scattering analysis indicated acceptable PdI samples from 20 to 40 min, whereas samples at 5 and 10 min exhibited polydispersity. accompanied by fluctuating zeta potential values ranging from – 35 to – 18 mV, with no discernible correlation.

Observations regarding reaction duration when utilising sodium thiosulfate reveal a consistent progression in solid formation, a colour evolution in both samples and supernatants from colourless to white to yellow, and a red shift in all supernatants under 365 nm UV excitation as reaction time extends. Photoluminescence characterisation further demonstrates shifts in both excitation and emission wavelengths. DLS analysis suggests an increase in particle size with prolonged reaction durations. These findings align with previously documented hydrothermal CdS quantum dot syntheses that employed thiourea. The primary distinction between these two sulfur sources resides in the decomposition energy required; sodium thiosulfate necessitates lower energy, leading to faster nucleation, smaller initial nanocrystals, and a more pronounced redshift in optical spectra, evidenced by blue-green emission in 5-minute reactions.

As alkalinity increased from pH 7 to 8.5 and 10, the quantity of solids produced in the reaction samples decreased. This phenomenon is attributed to the enhanced solubility of L-cysteine at elevated pH levels, which in turn suppresses ligand precipitation and promotes the formation of dispersed nanocrystals, thereby mitigating aggregation. Moreover, an increase in alkalinity leads to a reduction in reaction kinetics, resulting in consistently spaced variations between reaction intervals. This trend is further supported by observations in collected supernatants under UV 365 nm excitation, where more alkaline conditions yielded a broader emission spectrum and enhanced intensity.

Precipitates obtained from the reaction at pH 8.5 were isolated and washed and subsequently characterised using X-ray diffraction. The resulting XRD patterns, shown in Figure 2.26, confirmed the presence of a cysteine complex across all reaction times. Subsequently, broad peaks consistent with the calculated pattern for CdS were observed at t30 and t40, with their intensity increasing proportionally to the reaction duration. However, the persistent presence of cysteine complex peaks indicated that it was not directly attached to the CdS.

Overall, adjusting the reaction pH offers a straightforward method for modulating the properties of CdS quantum dots and their emission wavelength. Furthermore, the substitution of thiourea with sodium

thiosulfate accelerates the nucleation process, leading to the formation of smaller nanocrystals and a distinct blue-green emission at early reaction times, thus providing an additional means for spectral tuning.

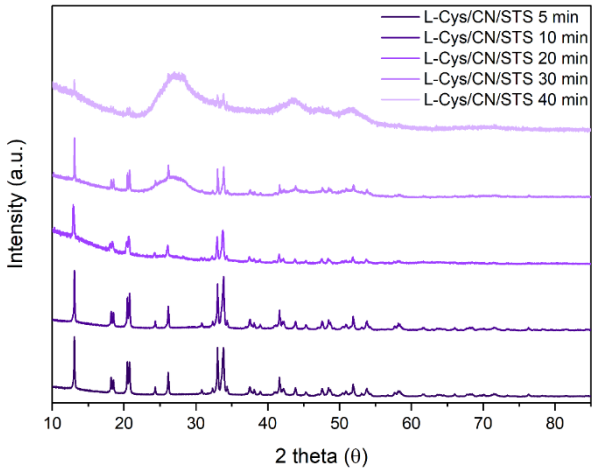

Figure 2.26, Normalised XRD patterns of solids from the hydrothermal synthesis of CdS quantum dots from Cadmium Nitrate, Sodium Thiosulfate, and L-Cysteine at pH 8.5, for reaction times 5, 10, 20 30 and 40 min

2.5.2 Reaction system with Cadmium Nitrate, Sodium Thiosulfate, and Cysteamine

The reaction system employing thiosulfate as the sulfur source was further investigated using cysteamine as the ligand. Initial pH measurements of the reaction mixture containing cysteamine, cadmium nitrate, and sodium thiosulfate in water were recorded at 7.6. Adjustments were made using hydrochloric acid to achieve neutral and acidic pH levels of 5.6, and ammonium hydroxide to reach pH 8.5 and 10. Throughout the reactions, the pH values stabilised within the first 10 min, reaching 7.7, 8.4, 9.1, and 10 for initial pH values of 5.6, 7, 8.5, and 10, respectively. In contrast to reactions involving thiourea, all reactions utilising cysteamine and thiosulfate produced precipitates. The sample colour transitioned from white at 5 min to yellow by 40 min, shown in Figure 2.28 (a, d, g, j). Post-centrifugation, the supernatants were clear, shifting from colourless at 5 min to a pale yellow at 40 min. Under UV 365 nm excitation, the supernatant exhibited blue emission at 5 min, demonstrated in (b, e, h, k), however the longer reactions did not show any luminescence.

Table 2.14, Overview optical properties CdS QDs from cadmium nitrate, sodium thiosulfate, and cysteamine, varying pH and reaction time is five min.

pH	Time (min)	λ_{abs} (nm)	λ_{ex} (nm)	λ_{em} (nm)	Bandgap (eV)	Tauc size (nm)
5.6	5	306/333	323	410	3.55	3.0
7	5	355	369	467	3.35	3.3
8.5	5	300	344	481	3.88	2.6
10	5	341	351	489	3.40	3.2

The findings of the optical characterisation were summarised in Table 2.14. The DLS data revealed polydisperse samples, > 0.3 PdI for all reaction times.The 5-minute reactions across pH levels 5.6, 7, 8.5, and 10 identified one or two distinct absorbance regions, located at 306 nm and 333 nm for pH 5.6. The latter was used to calculate the band gap energy of 3.55 eV and particle diameter of 3.0 nm. Photoluminescence

analysis indicated optimised emission spectra, with maximum emission wavelengths between 410 and 498 nm. DLS analysis revealed low zeta potential and polydispersity across all samples. This was supported by the luminescence precipitates under UV light, shown in (c, f, i, l), indicative of poor solubility and low surface tension of the material, resulting in precipitation of cadmium sulfide. To confirm this, the precipitates were subjected to XRD characterisation, depicted in Figure 2.27.

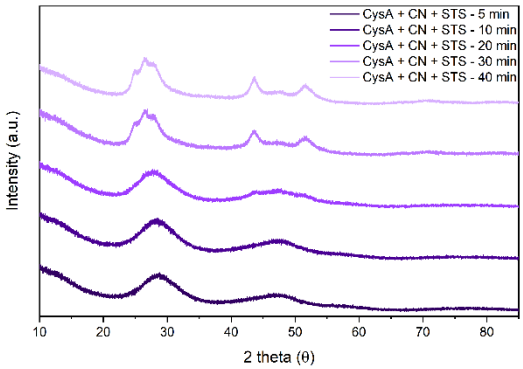

Figure 2.27, XRD plots of the precipitate isolated from the hydrothermal synthesis of CdS quantum dots from Cadmium Nitrate, Sodium Thiosulfate and Cysteamine, at pH 7.

X-ray diffraction patterns confirmed the presence of nanoscale cadmium sulfide, with peak sharpness increasing with increased reaction duration. No ligand-related features were observed in any reactions, suggesting that cysteamine maintained its solubility. While the interaction of cadmium nitrate, sodium thiosulfate, and cysteamine did yield luminescent CdS, its inadequate solution stability resulted in

precipitated CdS that retained some luminescent properties. Consequently, this reaction mixture was not subjected to further investigation.

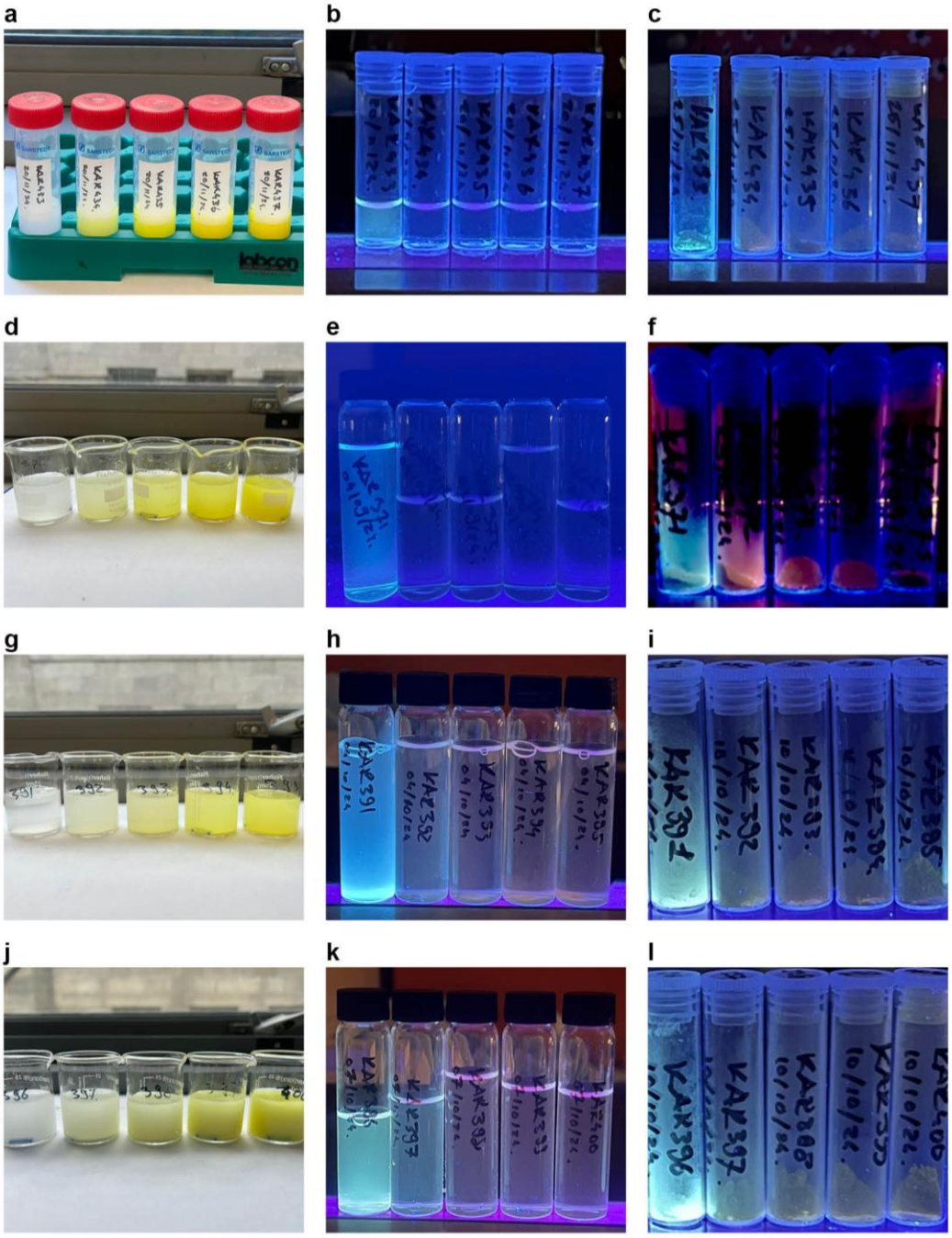

Figure 2.28, Pictures of reaction samples of the hydrothermal synthesis of CdS quantum dots from Cadmium Nitrate, Sodium Thiosulfate, and Cysteamine, for reaction times 5, 10, 20 30 and 40 min from left to right. Samples from reaction at pH 5.6, (a) sample in day light, (b) supernatant and (c) precipitate under UV 365, pH 7, (d) sample in day light, (e) supernatant and (f) precipitate under UV 365, pH 8.5, (g) sample in day light, (h) supernatant and (i) precipitate under UV 365, and pH 10 (j) sample in day light, (k) supernatant and (l) precipitate under UV 365

2.5.3 Evaluation of the proposed reaction system with the alternative sulfur source

Using precursor sodium thiosulfate in the hydrothermal reaction with cadmium nitrate and either ligand resulted in the following. Photoluminescence was observed as early as 5-minute reactions, luminating a blue colour, not observed in the thiourea reaction system. Temporal control was observed for the L-cysteine ligand and were favourable in the pH range of 7 and 8.5 across reaction times, extending reaction times from 5 to 40 min. In contrast, cysteamine did not show temporal control over the optical properties, resulting in blue luminescence at 5 min for all pH conditions, but no luminescence at longer reaction times. XRD characterisation confirmed the formation of precipitate of a L-cysteine complex in the L-cysteine reaction, and over time the formation of CdS on the nanoscale. The cysteamine reaction formed precipitate of nanoscale CdS only, for all reaction times, unlike the thiourea equivalent reaction. In Table 2.15. the impact of these ligands on the proposed reaction system are summarised.

Table 2.15, Ligand effects of L-cysteine or Cysteamine in hydrothermal reaction with Cadmium nitrate and Sodium Thiosulfate

	L-Cysteine	Cysteamine
Tuneable optical properties (λ_{abs}, nm)	353 – 407	300 – 355
Tuneable optical properties (λ_{em}, nm)	509 – 710	410 – 489
Band gap (eV)	2.76 – 3.19	3.35 – 3.88
Size (nm)	3.6 – 5.4	2.6 – 3.3
Time (min)	5 – 40	5
pH	7 – 10	5.6 - 10
Formation of precipitation	L-cysteine complex/CdS	CdS

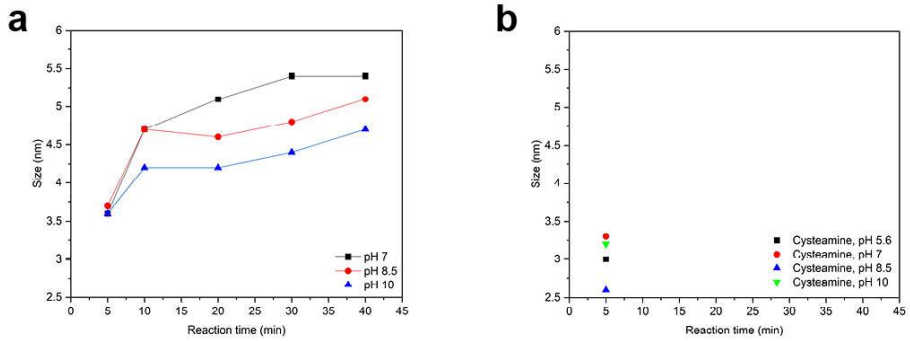

Figure 2.29, sizes of CdS quantum dots produced in hydrothermal synthesis of cadmium nitrate, thiourea and L-cysteine (a), and cysteamine (b).

2.5.4 Overall findings on the effect of ligand and sulfur choice in the heat block reaction system

A comparative analysis of ligands in the reaction system highlights differences in solid formation. Reactions employing L-cysteine with thiourea generated significant solid precipitates, identified by XRD analysis as a cysteine complex shown in Figure 2.30 (a).[86] In contrast, reactions using cysteamine with thiourea did not produce solids, suggesting cysteamine's greater solubility and a more favourable outcome in this context.

When L-cysteine was used with sodium thiosulfate, XRD analysis again identified the cysteine complex, depicted in Figure 2.30 (b). Notably, extended reaction times (t30 – t40) showed the development of nanoscale CdS peaks, indicating co-precipitation of both the cysteine complex and CdS. Reactions with cysteamine and sodium thiosulfate did yield solids presented in (c), with XRD revealing sharper CdS nanomaterial peaks over time, indicative of crystalline CdS formation and growth.

Evaluating the optical characteristics, the combination of thiourea and cysteamine provided good control absorption and emission properties with reaction time at pH 5.6. Neutral and basic conditions showed delayed luminescence particle formation and even cessation at pH 10. The utilisation of sodium thiosulfate as an alternative sulfur source consistently yielded blue luminescent samples at the initial t5 time point across all tested pH conditions. However, elongating these reactions resulted in non-emissive, and precipitated nano cadmium sulfide.

In conclusion, cysteamine can serve as a ligand for CdS quantum dot formation, offering good control over optical properties with reaction time variations. However, its efficacy is highly dependent on the specific reaction system, pH, and sulfur source. L-cysteine, while involving a competitive formation between a L-cysteine complex and CdS quantum dots, offers luminescence across a range of pH conditions (neutral to basic) with both sulfur sources, and provides a broader emission spectrum with reasonable control over optical properties via reaction time. Consequently, the L-cysteine system is deemed more versatile despite the competitive precipitation.

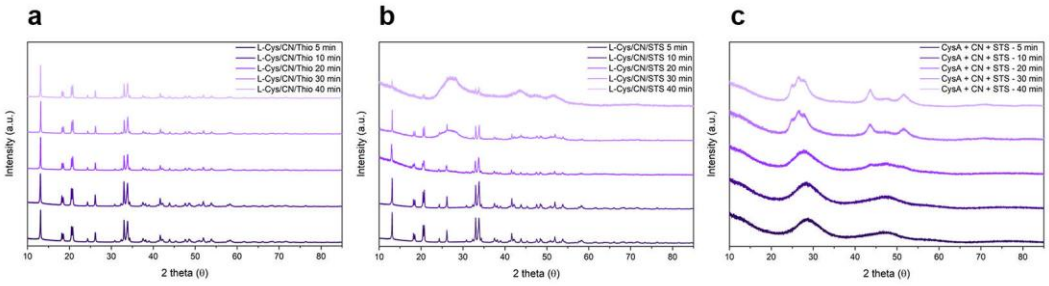

Figure 2.30, XRD patterns of the solids produced in hydrothermal reaction of (a) Cadmium Nitrate, Thiourea and L-cysteine at pH 8.5, (b) Cadmium Nitrate, Sodium Thiosulfate and L-Cysteine at pH 8.5, and (c) Cadmium Nitrate, Sodium Thiosulfate and Cysteamine at pH 5.6.

2.6 Reaction system with alternative cadmium source

To assess the adaptability of the proposed reaction system, the cadmium source was investigated. The optimal reaction parameters previously determined considering pH, ligand and sulfur source were employed, with the substitution of Cadmium Nitrate by Cadmium Chloride. Three reaction time series were conducted: Initially, the combination of Cadmium Chloride with Thiourea and L-Cysteine was examined at pH 7, yielding some precipitate, though significantly less than under more alkaline conditions. This mixture demonstrated favourable performance with Cadmium Nitrate, and at pH 10, minimal precipitate formation was observed, indicating a preference for this condition over more neutral pH levels. Subsequently, the combination of Cadmium Chloride with Sodium Thiosulfate and L-Cysteine was evaluated at pH 10. Lastly, Cadmium Chloride with Thiourea and Cysteamine was tested at pH 5.6, a condition where no precipitate was formed with Cadmium Nitrate.

2.6.1 Reaction system L-Cysteine, Cadmium Chloride and Thiourea, pH 7

Upon evaluating the reaction involving thiourea and cysteine at pH 7, several observations were made shown in Figure 2.31 (a). Precipitation was visible from the 10-minute mark, accompanied by a colour transition from white to yellow by t40 as the reaction progressed. XRD analysis (f) of the precipitate confirmed them to be the L-cysteine complex, aligning with prior L-cysteine reactions. The supernatant transformed from a transparent and colourless sample at t5 to a transparent yellow sample by t40. Under UV light shown in (d), a redshift was noted, progressing from green at t10 to orange at t20 and red at t30 and t40. The pH of the reaction mixture raised from 7 to 8.3 between t10 and t20, and then slightly declining to 8.1 at t30. This delayed pH shift is consistent with the elevated thermal decomposition of cadmium chloride compared to cadmium nitrate.

Optical characterisation in Figure 2.31 (b) revealed λ_{abs} shift from 399 to 407 nm for t20 to t40, respectively. Excitation and emission spectra (c) indicated a slight shift as well, measured at λ_{ex} 396 to 399 nm, and λ_{em} 720 to 724 nm, respectively. The undiluted supernatant from t10 did not exhibit absorption during characterisation, which is attributed to a delay in characterisation after synthesis. Despite the visual appearance of the samples, characterisation data suggests limited control over the optical properties. The Tauc plot analysis for the 20-, 30-, and 40-minute samples indicated a decrease in bandgap energy from 2.96 eV to 2.88 eV, corresponding to particle sizes of 4.3 to 4.7 nm, respectively.

Dynamic Light Scattering measurements showed a decrease in the polydispersity index from 0.40 to 0.16 with reaction time, and a stable zeta potential ranging between -42 mV and -30 mV, shown in (e). The reaction conditions employed resulted in the formation of luminescent CdS from t10, which is attributed to the decomposition of cadmium chloride, supported through the observed pH increase from pH 7 to 8.3 between t10 and t20. The delay in nucleation, led to a reduced control over the optical properties with extended reaction times. Although particle growth is evident through absorbance and DLS measurements, this suggests delayed nucleation resulting in similar results for all reaction times in this reaction system.

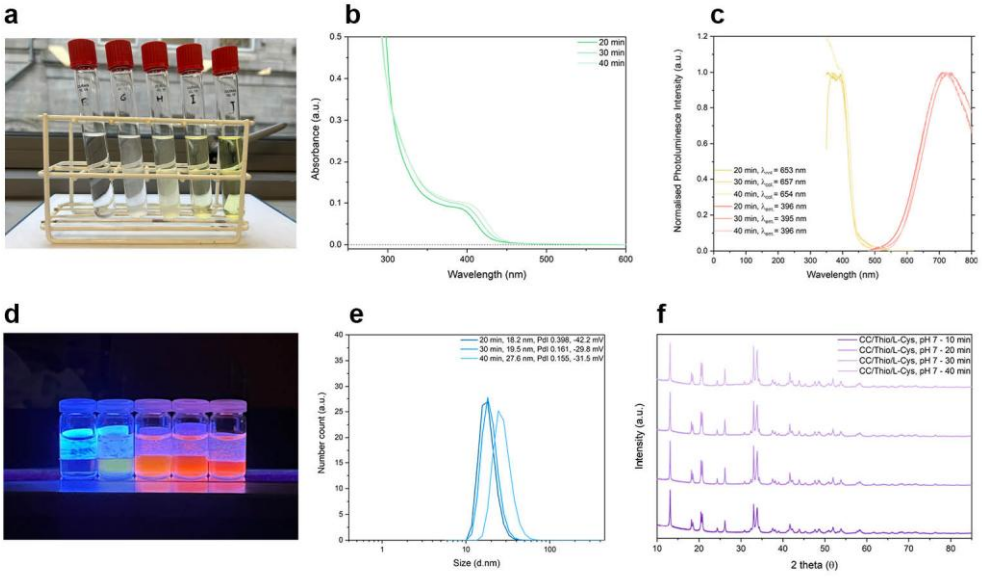

Figure 2.31, Crude sample in day light (a), supernatant under UV 365 light (d), of the hydrothermal synthesis of quantum dots from L-Cysteine, Cadmium Chloride and Thiourea, pH 7, reaction times 5,

10, 20, 30, and 40 min (left to right). Spectra of supernatant: absorbance (b), photoluminescence (c), DLS (e), and XRD pattern (f).

Table 2.16, Overview optical properties CdS QDs from cadmium chloride, thiourea, and L-cysteine, pH 7 and varying reaction time, * measured in triplets and averaged.

pH	Time (min)	λ_{abs} (nm)	λ_{ex} (nm)	λ_{em} (nm)	Bandgap (eV)	Tauc size (nm)	DLS size (nm)*	PdI*	Zeta-pot. (mV)*
7	5	-	-	-	-	-	-	-	-
7	10	-	-	-	-	-	28.48	0.335	-34.3
7	20	386	396	720	2.96	4.3	18.24	0.398	-42.2
7	30	385	399	738	2.91	4.5	19.53	0.161	-29.8
7	40	395	400	724	2.88	4.7	27.63	0.155	-31.5

2.6.2 Reaction system L-Cysteine, Cadmium Chloride and Sodium Thiosulfate, pH 10

This reaction produced only a small amount of solids after 40 min. The pH decreased minimally from 10 to 9.8 between the 5- and 40-minute marks. The supernatant transitioned from transparent and colourless at 5 min to transparent and yellow at 10 min, subsequently becoming opaque and yellow with increasing opacity from 20 to 40 min, shown in Figure 2.32 (a). When subjected to UV 365 nm irradiation, a diverse array of colours was observed, progressing from bright cyan at 5 min, bright yellow at 10 min, bright orange at 20 min, orange/red at 30 min, and finally red at 40 min, depicted in (b). The two reactions with the longest durations displayed strong luminescence, albeit diminished in comparison to the 5- and 10-minute reaction times. The optical properties were summarised in Table 2.17.

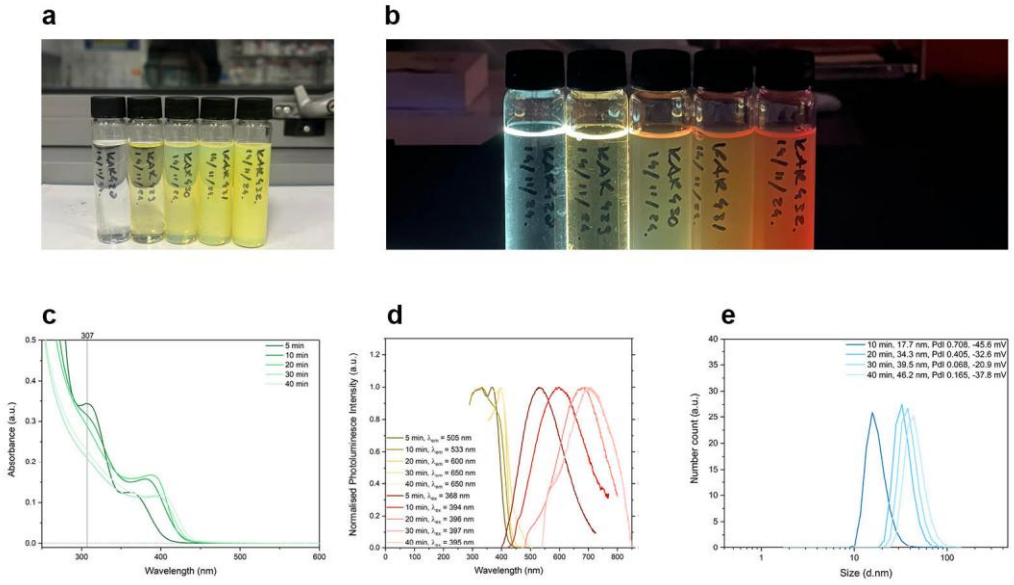

Figure 2.32, Crude sample in daylight (a) and UV 365 (b), absorbance (c), photoluminescence (d), and DLS (e) plot for the supernatant of the hydrothermal synthesis of CdS quantum dots from Cadmium Chloride, Sodium Thiosulfate and L-Cysteine at pH 10, for reaction time of 5, 10, 20, 30, and 40 min

Table 2.17, Overview optical properties CdS QDs from cadmium chloride, sodium thiosulfate, and L-cysteine, pH 10 and varying reaction time, * measured in triplets and averaged.

pH	Time (min)	λ_{abs} (nm)	λ_{ex} (nm)	λ_{em} (nm)	Bandgap (eV)	Tauc size (nm)	DLS size (nm)*	PdI*	Zeta-pot. (mV)*
10	5	307/363	368	527	3.15	3.7	-	-	-
10	10	380	394	597	3.02	4.1	17.68	0.277	-37.2

10	20	389	396	688	2.99	4.2	34.28	0.051	-22.5
10	30	395	397	695	2.95	4.4	39.49	0.059	-37.8
10	40	400	395	701	2.91	4.5	46.15	0.092	-33.9

Absorbance spectroscopy shown in Figure 2.32 (c) revealed a shoulder at 307 nm in all samples, with a secondary shoulder exhibiting a red shift from 365 to 404 nm between t5 and t40. The photoluminescence spectra in (d) showed the excitation maximum shifted progressively from 368 to 396 nm from t5 to t20, remaining constant thereafter. The emission maximum showed a significant red shift from 527 to 701 nm from t5 to t30, though this trend did not extend to t40, indicating a system boundary. Tauc plot analysis indicated a band gap energy ranging from 2.91 to 3.15 eV, corresponding to particle sizes of 3.7 to 4.5 nm. DLS measurements identified polydispersity in samples from t5 to t20, yet all samples displayed a favourable zeta potential of -30 mV, depicted in (e).

Overall, this experimental series consistently produced favourable results, evidenced by negligible solid formation, a wide and tuneable spectrum of optical properties as determined through absorbance and photoluminescence spectroscopy, and recorded zeta potentials surpassing the cadmium nitrate counterpart, implying superior particle stability.

2.6.3 CdS Quantum dots from Cysteamine, Cadmium Chloride and Thiourea, pH 5.6

Lastly, the reaction system involving cadmium chloride, thiourea with cysteamine was tested at pH 5.6. The synthesis yielded transparent solutions that ranged from colourless to slightly yellow, shown in Figure 2.33 (a). Comparable to the reactions involving cysteamine with thiourea and cadmium nitrate, no solid precipitates were formed. While no luminescence was detected at t5, it was observed to be orange/red to red from t10 to t40 under UV 365 nm irradiation (b) consistent with other reactions employing thiourea as the sulfur source. The pH remained stable at 5.5 throughout the process. Optical characterisation indicated a slight shift in absorption maxima from 398 to 402 nm from t5 to t40, (c). Excitation spectra showed shifts in λ_{ex} from 391to 410 nm, accompanied by a small, steady increase in $\lambda_{em\ max}$ from 634 to 702 nm, depicted in (d). Tauc plot analysis of reactions from t10 to t40 revealed a decrease in bandgap energy from 2.96 eV to 2.84 eV, with a corresponding increase in number mean particle size from 4.3 nm to 4.9 nm. DLS indicated favourable zeta potentials for all samples, ranging from 20 to 32 mV. However, samples from t5-t20 exhibited polydispersity (PdI > 0.3), while samples from t30-t40 showed acceptable PdI values of 0.2 and

0.3, with number mean particle sizes of 21 nm, 22 nm, and 22 nm at t20, t30, and t40, respectively. The findings were summarised in Table 2.18.

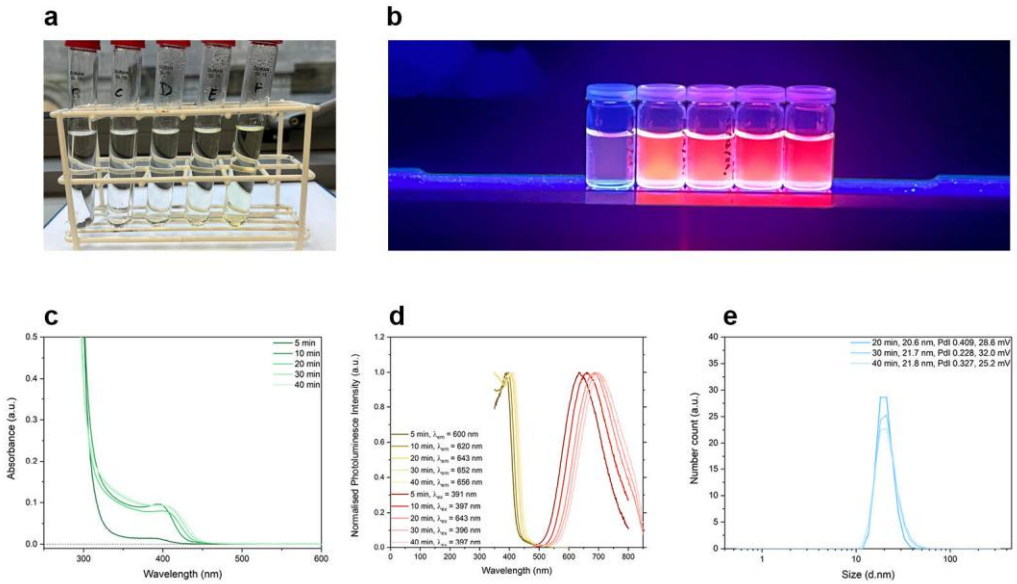

Figure 2.33, crude samples in daylight (a) and under UV 365 nm (b) Absorbance (c), photoluminescence (d), and DLS (e) plot for the sample of the hydrothermal synthesis of CdS quantum dots from Cysteamine, Cadmium Chloride and Thiourea, pH 5.6, reaction times 5-, 10-, 20-, 30-, and 40-min.

Table 2.18, Overview optical properties CdS QDs from cadmium chloride, thiourea, and cysteamine, pH 5.6 and varying reaction time, * measured in triplets and averaged.

pH	Time (min)	λ_{abs} (nm)	λ_{ex} (nm)	λ_{em} (nm)	Bandgap (eV)	Size (nm)	DLS size (nm)*	PdI*	Zeta-pot. (mV)*
5.6	5	383	391	634	-	-	-	-	-
5.6	10	393	397	663	2.96	4.3	-	-	-
5.6	20	400	407	684	2.9	4.6	18.24	0.398	-42.2
5.6	30	400	405	695	2.86	4.8	19.53	0.161	-29.8
5.6	40	400	410	702	2.84	4.9	27.63	0.155	-31.5

The cysteamine reaction yielded luminescent quantum dots, all exhibiting emissions at the far-red end of the visible spectrum. This uniformity suggests a constrained ability to manipulate optical properties by merely adjusting reaction time. Although discernible shifts were noted in absorbance, photoluminescence, and DLS data, only minor variations correlated with reaction time. This could be attributed to an elevated concentration of non-emissive CdS, as evidenced by the supernatant's colour transition from colourless to yellow.

When considering the collective findings from all three cadmium chloride reactions, it implies that cadmium chloride demonstrates less compatibility with thiourea as a sulfur source compared to sodium thiosulfate. The heightened decomposition energies associated with both cadmium chloride and thiourea, in contrast to cadmium nitrate and sodium thiosulfate respectively, may explain the reduced controllability afforded by reaction time. The necessity for extended reaction times to overcome the energy barrier for nucleation effectively narrows the window of control at shorter reaction durations, thereby leading to a decrease in the observed variations in optical properties.

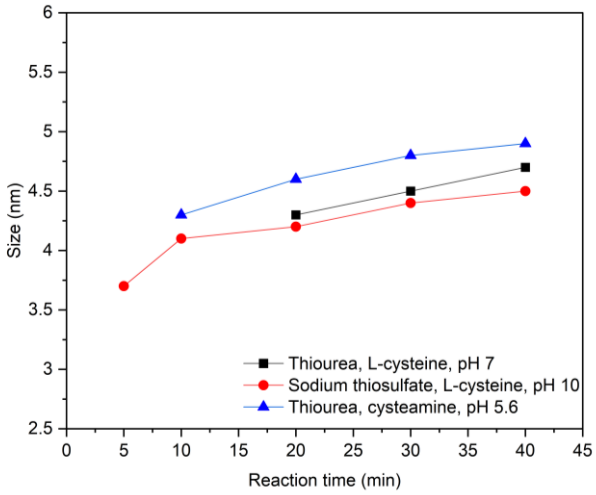

Figure 2.34, The calculated sizes of the CdS quantum dots from hydrothermal reaction with cadmium chloride, and selected sulfur source, ligand, and pH.

2.7 Reaction system validation

The ambiguity surrounding the reactant responsible for sulfide generation in section 2.4.2 comprising the reaction system Cadmium Nitrate, Thiourea, and Cysteamine under varying pH conditions, coupled with the absence of conclusive findings regarding alternative sulfur sources in prior investigations in section 2.5, necessitated a rigorous set of control experiments. These experiments were designed to unequivocally validate and reinforce the groundbreaking discoveries presented in this study. Specifically, a series of experimental iterations meticulously investigated the individual contributions of each component by removing them sequentially from the reaction mixture, thereby elucidating their precise roles in the formation of CdS QDs.After questions were raised in section 2.4.2, on the reactant responsible for the sulfide generation in the reaction system with Cadmium Nitrate, Thiourea, and Cysteamine at acidic and basic conditions, and no conclusive findings in the alternative sulfur source, the outcomes of this study were validated and reinforced by carrying out a set of control reactions.

To resolve this, the most advantageous reaction conditions, also employed for the alternative cadmium source reactions (section 2.6), were explored by omitting either the sulfur source or the ligand, given in Table 2.19. All reactions were conducted at 130 ˚C for a duration of 30 min. This methodical elimination process facilitated the separation of the individual impacts of each component on the reaction's results, thereby guaranteeing that the observed effects could be attributed to the targeted variables and not to synergistic or confounding influences.

Table 2.19, Overview reaction conditions (30 min) and observations of the control reactions

Cd-source	S-source	Ligand	pH	Ppt	PL
Cadmium Nitrate	Sodium Thiosulfate	-	10	Yellow	No
Cadmium Nitrate	Thiourea	-	8.5	Minimal/orange	No
Cadmium Nitrate	-	L-Cysteine	7	White	Red
Cadmium Nitrate	-	L-Cysteine	10	White	Yellow
Cadmium Nitrate	-	Cysteamine	5.75	No	blue

Luminescence was observed in reactions containing a Cd-source and ligand only, without an additional S-source of thiourea or sodium thiosulfate. It was hypothesised that L-Cysteine acts as both a sulfur source and a ligand in the hydrothermal reaction of cadmium nitrate and L-cysteine. The luminescence in the absence of an explicit sulfur source indicates complex pathways involving L-Cysteine degradation for CdS formation.

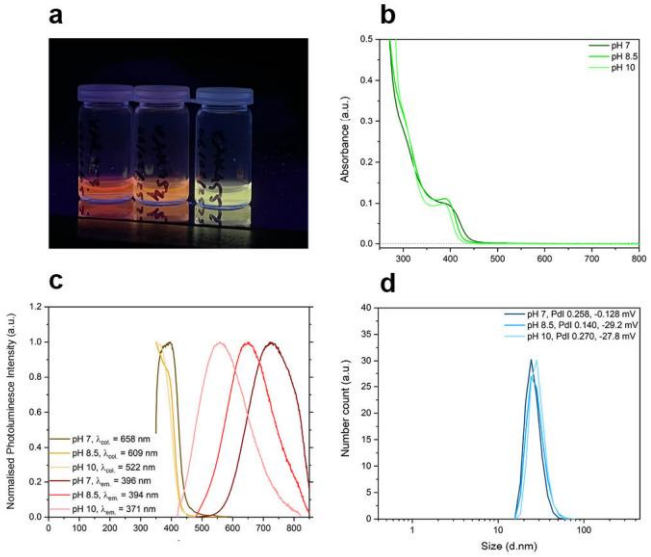

Figure 2.35, Supernatant under UV 365 nm (a), absorbance (b), photoluminescence (c), and DLS (d) spectra for the supernatant of the hydrothermal synthesis of CdS quantum dots from Cadmium Nitrate and L-Cysteine at 130 ˚C for 30 min and pH 7, 8.5 and 10.

Table 2.20, Overview optical properties CdS QDs from cadmium nitrate and L-cysteine, varying pH and reaction time of 30 min.

pH	Time (min)	λ_{abs} (nm)	λ_{ex} (nm)	λ_{em} (nm)	Bandgap (eV)	Size (nm)
7	30	394	396	722	3.03	4.1
8.5	30	390	394	653	2.98	4.2
10	30	386	371	556	2.90	4.6

To confirm this finding, the reaction of L-cysteine and cadmium nitrate was repeated at pH 7, 8.5 and 10. Observation the reaction products at varying pH levels revealed tuneable CdS quantum dots with hypsochromic shift from red, to orange, and yellow emissions corresponding to increasing pH, shown in Figure 2.35 (a). Absorption in (b) and excitation and emission wavelengths in (c) showed a blue shift, indicating pH-dependent control over optical properties. DLS suggested no particle growth with increasing pH. However, the Tauc plot calculated a size increase from 4.1 to 4.6 nm, and band gap of 3.03 to 2.90 eV. This reaction system offers excellent control compared to reactions with added sulfur sources and warrants comprehensive evaluation, suggesting that pH variations influence surface passivation or particle size, thus modulating optical characteristics, previously seen by Bu *et al.*[76] This supports the notion that pH is crucial for governing quantum dot optical properties. More importantly, this study provides a new insight into the hydrothermal formation of CdS quantum dots, in which, unlike the literature of Aboulaich *et al.*[23], only two components, a Cd-source, and a S-source which acts as core material and ligand, are needed to produce CdS quantum dots with control over optical properties by varying the reaction time and pH.

The study was extended with an additional time-series investigation of reaction of Cadmium Nitrate and Cysteamine, pH 5.9, 130 °C. This system showed no solid precipitation, depicted in Figure 2.36 (a) but

increasing intensity of blue-green luminescence with reaction time (b). This observation indicates that the concentration of QDs increases, rather than the size of the particles.

Figure 2.36, Crude samples (a) and supernatant under UV light (b) of Cysteamine and Cadmium nitrate at pH 5.9 for reaction times 10, 20, 30, 40, 50,60 and 90 min.

2.8 Investigation into the dual role of L-Cysteine during the hydrothermal synthesis at pH levels of 7, 8.5, and 10.

To further investigated this alternative reaction system, a time-series experiment at pH 7, 8.5 and 10 was conducted with two reactants cadmium nitrate and L-cysteine for quantum dot formation, omitting a conventional sulfur source. This simplified approach involved reacting L-Cysteine and Cadmium Nitrate at a 2.2:1 molar ratio. Samples were collected at intervals of 5, 10, 20, 30, and 40 min, consistent with previous experimental timelines.

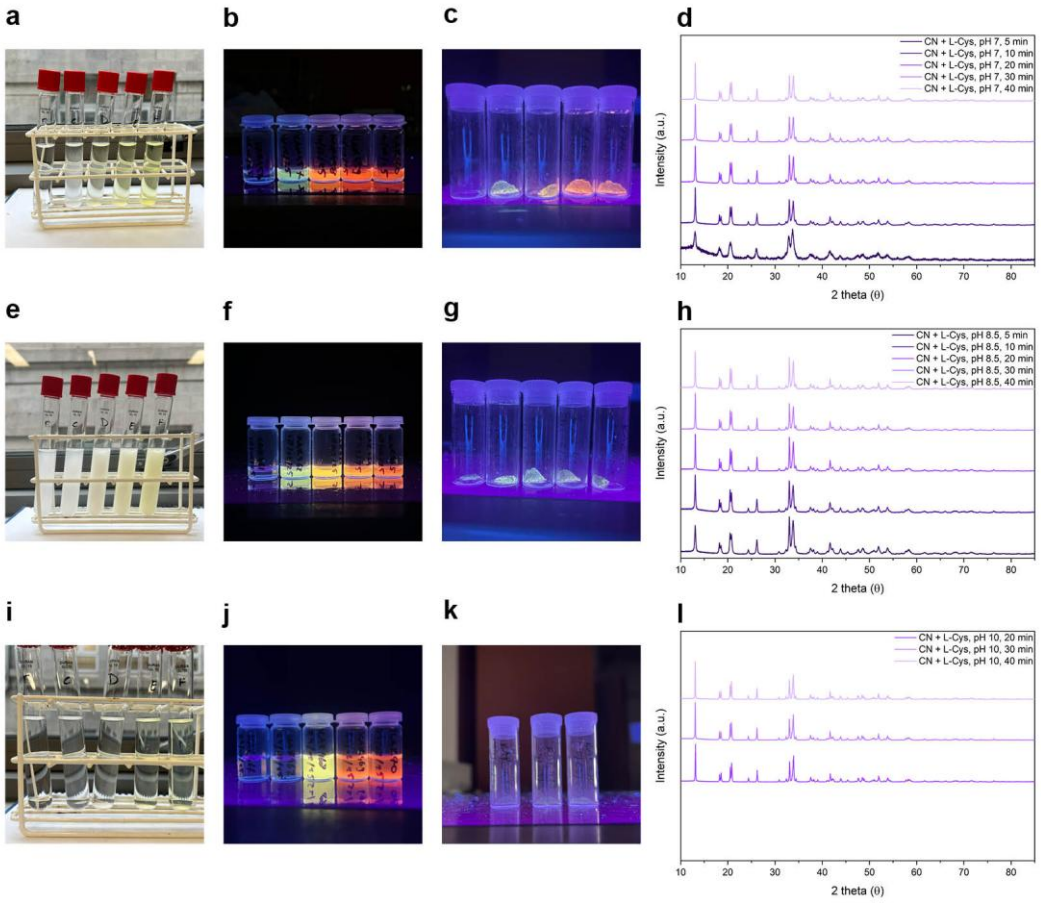

Figure 2.37, Crude sample (a), supernatant (b), solids (c), and XRD pattern of the solids collected (d) from hydrothermal reaction of L-Cysteine and Cadmium nitrate at pH 7. Crude sample (e), supernatant (f), solids (g), and XRD pattern of the solids collected (h) from hydrothermal reaction of

L-Cysteine and Cadmium nitrate at pH 8.5. Crude sample (i), supernatant (j), solids (k), and XRD pattern of the solids collected (l) from hydrothermal reaction of L-Cysteine and Cadmium nitrate at pH 10. (top), 8.5 (middle) and 10 (bottom) for reaction times 5, 10, 20, 30 and 40 min.

Samples were collected at 5, 10, 20, 30, and 40 min for the neutral reaction system, depicted in Figure 2.37 (a), with the initial sample (t5) being colourless and transparent with minimal solid formation. At t10, a white suspension and solids were observed, transitioning to a less suspended state with precipitate ranging from pale yellow to yellow between t20 and t40. Over 80 mg of solids were collected for the samples from t10 to t40. While the t5 sample did not produce luminescent quantum dots, samples from t10 to t40 exhibited luminescence in green to red hues under UV light shown in (b). Notably, the precipitates displayed the same luminescence under UV 365 given in (c). X-ray Diffraction analysis indicated that the precipitate consisted of the L-Cysteine complex. Examination of the reaction's pH development, shown in Figure 2.38, revealed that the pH began to increase only after t5, suggesting that sulfur became available for reaction after this point through the degradation of L-Cysteine, which explains the absence of synthesised luminescent species at t5.

At the pH of 8.5, similar results compared to pH 7 were produced, shown in Figure 2.37 (e – h). A comparable quantity of precipitate were collected; however, all samples exhibited white luminescence under UV 365 excitation. The supernatant displayed enhanced control contingent upon reaction duration, with supernatants emitting green at 10 min, yellow at 20 min, orange at 30 min, and red at 40 min.
At a pH of 10, the formation of the L-Cysteine complex was significantly diminished, as was seen in section 2.4.1 and was attributed to enhanced solubility of the compound L-cysteine. The alkaline conditions also retarded the generation of luminescent species, yielding samples that emitted yellow at t20, orange at t30, and red at t40. While the pH development showed only a minor alteration, this delay coincided with the onset of non-emissive precipitation from t20 onwards.

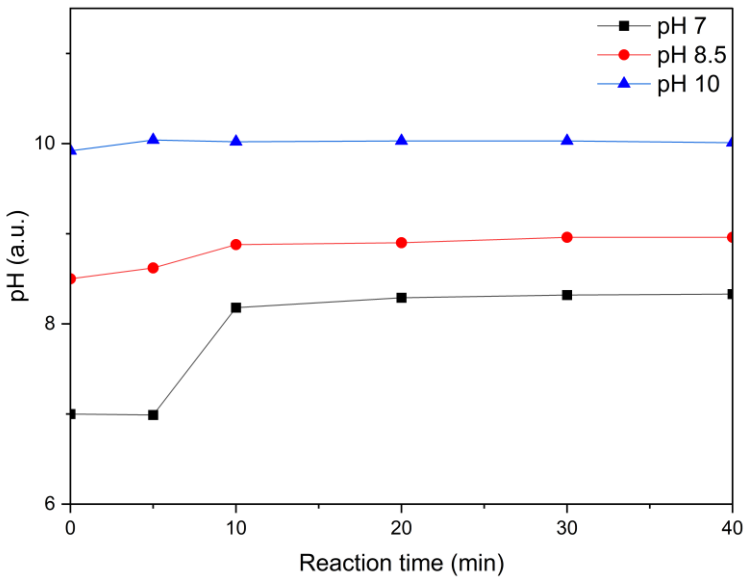

Figure 2.38, pH development of hydrothermal synthesis of hydrothermal reaction of cadmium nitrate and L-cysteine at pH 7, 8.5, and 10, at reaction times 5, 10, 20, 30, and 40 min.

Although absorbance and emission exhibit bathochromic shift with reaction time, a hypsochromic shift was observed with increasing reaction pH. Additionally, at pH 10 the delayed formation of luminescent materials prevents the observation of the initial luminescence species. Luminescence materials were produced from t20, with absorption at 380 nm, excitation at 367 nm, and emission at 576 nm. The precipitates formed at pH 7 exhibit luminescence consistent with that of the supernatant, indicating poor colloidal stability owing to co-

precipitation with the cysteine complex. At pH 8.5 this has changed to emissive precipitate but white (all colours simultaneously), and to non-emissive at pH 10, indicating improved surface properties, and better separation, at basic reaction conditions.

The optical characterisation, shown in Figure 2.39, indicated that the time series performed at pH 8.5 demonstrated the most favourable outcomes, evidenced by the sharpest absorbance peaks (c) and superior range of photoluminescence (d) as a function of reaction time. This suggests that the chosen pH optimises the kinetics of quantum dot formation and growth, allowing for precise manipulation of their optical properties through reaction duration. Specifically, the ability to obtain distinct green, yellow, orange, and red emissions by varying reaction time at pH 8.5 underscores the potential for fine-tuning QD spectral output for various applications.

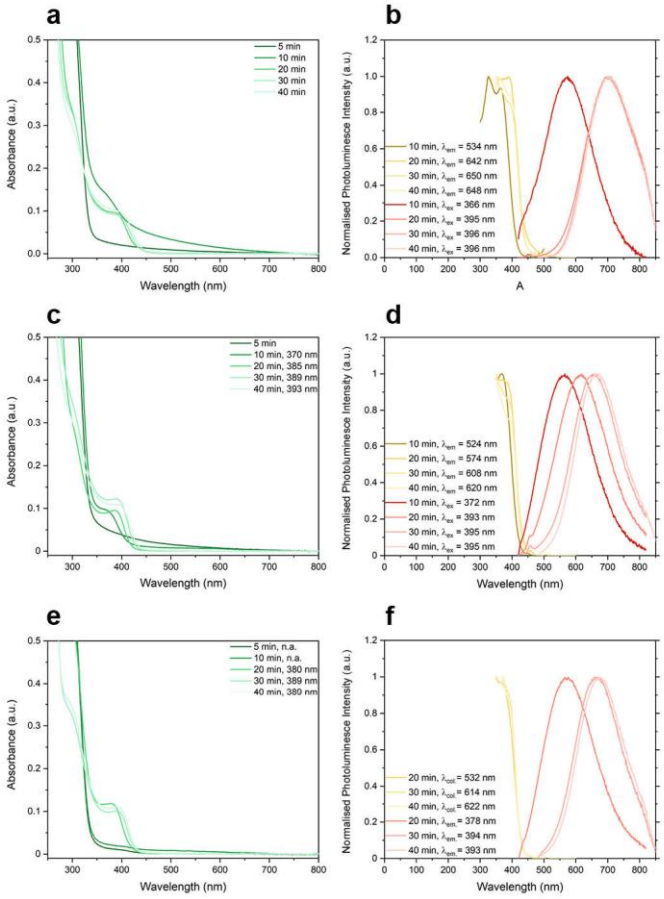

Figure 2.39, Compiled data of absorbance (a) and photoluminescence (b) spectra of hydrothermal reactions of L-Cysteine and Cadmium Nitrate at pH 7, 8.5 and 10 for 5, 10, 20, 30 and 40 min

Table 2.21, Overview optical properties CdS QDs from cadmium nitrate and L-cysteine, varying pH and reaction time.

pH	Time (min)	λ_{abs} (nm)	λ_{ex} (nm)	λ_{em} (nm)	Bandgap (eV)	Size (nm)
7	5	-	-	-	-	-
7	10	362	366	575	-	-
7	20	379	395	705	2.97	4.4
7	30	383	396	702	2.93	4.4
7	40	394	396	706	2.9	4.6
8.5	5	-	-	-	-	-
8.5	10	370	372	566	3.08	3.9
8.5	20	385	393	618	3.02	4.1

8.5	30	389	395	660	2.96	4.3
8.5	40	393	395	667	2.93	4.4
10	5	-	-	-	-	-
10	10	-	-	-	-	-
10	20	380	378	576	3.04	4.0
10	30	389	394	663	2.97	4.3
10	40	389	393	677	2.96	4.3

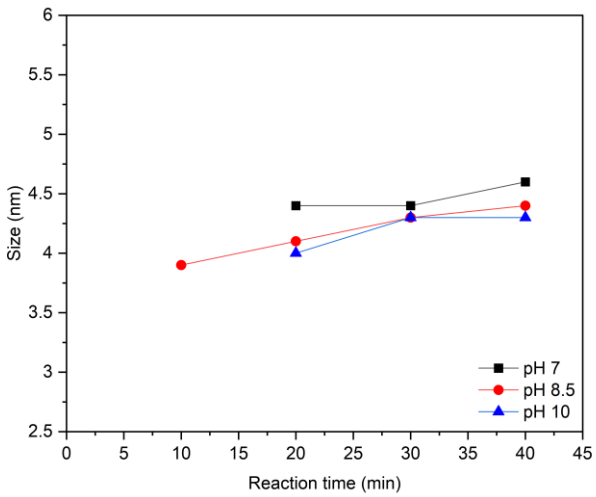

Figure 2.40, The calculated sizes of the CdS quantum dots from hydrothermal reaction of cadmium nitrate and L-cysteine, at pH 7, 8.5 and 10, reaction time 10 – 40 min.

2.9 Varying molar ratios between cadmium nitrate and L-cysteine

While literature suggests a 1:2.2 molar ratio for Cadmium Nitrate and L-Cysteine to form CdS quantum dots in solution,[23] this ratio is based on a broader Cd:S:ligand ratio of 1:1.8:2.2 and warrants re-examination. This study investigates the impact of varying molar ratios of cadmium and sulfur precursors on quantum dot characteristics, including size, stability, and luminescence. The experiments were conducted under specific hydrothermal conditions: 130 °C, reaction times of 5, 10, 20, 30, and 40 min, and a pH of 8.5, without an

additional sulfur source. Three molar ratios were investigated and compared to the original molar ratio of 1:2.2 used in section 2.8. The molar ratios investigated included (1:1.5), (1:2), and (1:4).

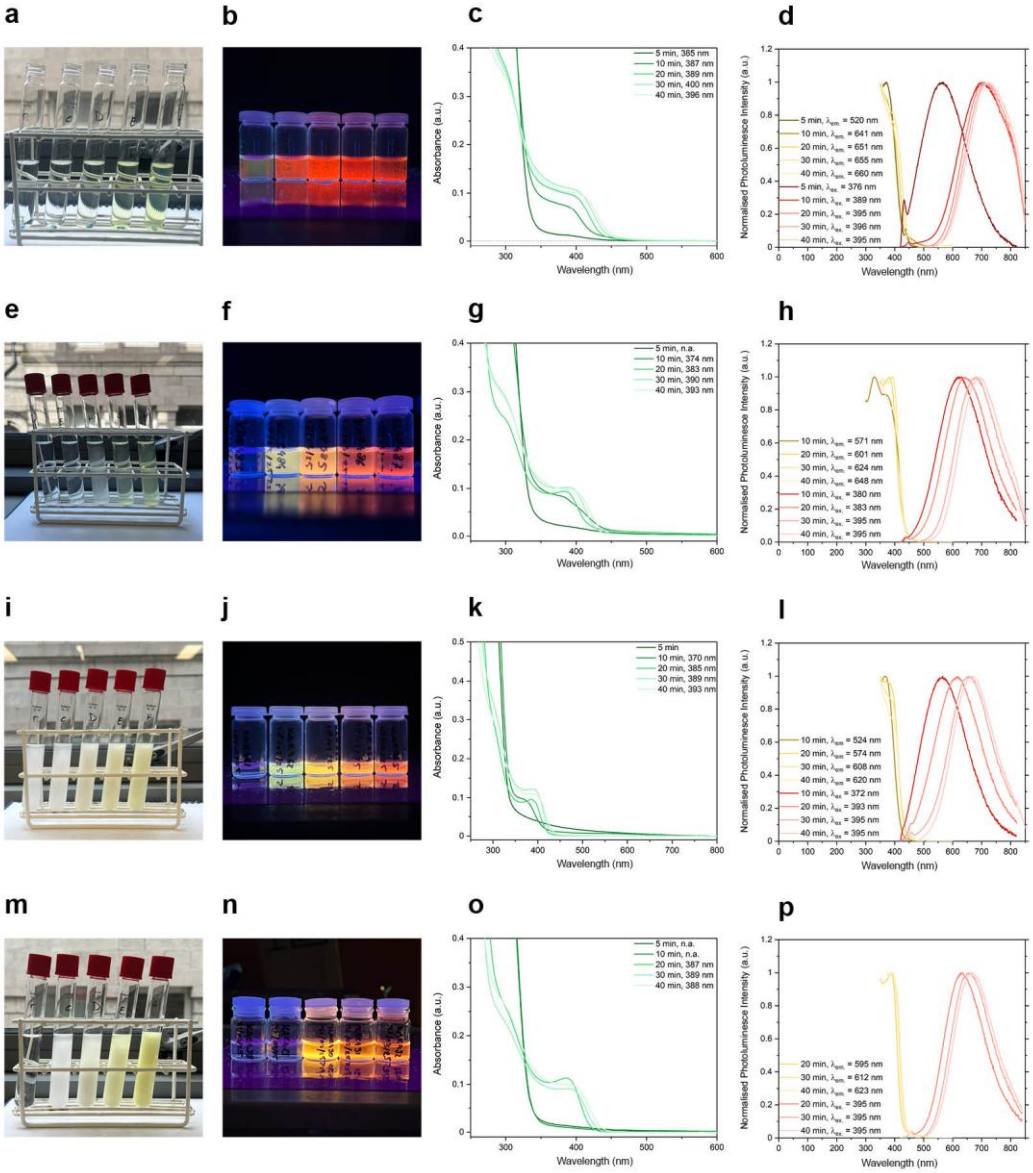

Figure 2.41, Reaction sample in daylight (a), supernatants under UV 365 (b), absorbance spectrum (c), and photoluminescence spectrum (d) of hydrothermal synthesis of CdS quantum dots from Cadmium Nitrate and L-cysteine at pH 8.5 molar ratio 1 : 1.5. Reaction sample in daylight (e), supernatants under UV 365 (f), absorbance spectrum (g), and photoluminescence spectrum (h) of hydrothermal synthesis of CdS quantum dots from Cadmium Nitrate and L-cysteine at pH 8.5 molar ratio 1 : 2. Reaction sample in daylight (i), supernatants under UV 365 (j), absorbance spectrum (k), and photoluminescence spectrum (l) of hydrothermal synthesis of CdS quantum dots from Cadmium Nitrate and L-cysteine at pH 8.5 molar ratio 1 : 2.2. Reaction sample in daylight (m), supernatants under UV 365 (n), absorbance spectrum (o), and photoluminescence spectrum (p) of hydrothermal synthesis of CdS quantum dots from Cadmium Nitrate and L-cysteine at pH 8.5 molar ratio 1 : 4.

Initially, a molar ratio of 1:1 was assessed, but this mixture proved insoluble at pH 8.5. Subsequently, a molar ratio of 1:1.5 was used and this produced a soluble reaction mixture at the desired pH. The resulting reaction produced a suspension containing a minimal amount of white precipitate, with a supernatant that ranged from colourless to yellow, and this colouration intensified with increasing reaction time, shown in Figure 2.41 (a). Thirdly, a molar ratio of 1:2 was prepared, which mirrors the ratio between Cadmium Nitrate and the sulfur source as utilised in hydrothermal reactions involving a Cd source, S source, and ligand. The samples

generated by the 1:2 ratio were similar to the 1:1.5 ratio, with a greater amount of white precipitate observed (e). This trend persisted upon increasing the ratio to 1:2.2 (i) and 1:4 (m), yielding more solids as the L-cysteine concentration increased, which is indicative of an excess of the ligand.

Table 2.22, Overview optical properties CdS QDs from cadmium nitrate and L-cysteine, varying molar ratios and reaction time, at ph 8.5.

Molar ratio	Time (min)	λ_{abs} (nm)	λ_{ex} (nm)	λ_{em} (nm)	Bandgap (eV)	Size (nm)
1:1.5	5	385	376	566	-	-
1:1.5	10	387	389	701	2.98	4.2
1:1.5	20	389	395	708	2.91	4.5
1:1.5	30	400	396	713	2.88	4.7
1:1.5	40	396	395	725	2.84	4.9
1:2	5	-	-	-	-	-
1:2	10	374	380	619	-	-
1:2	20	383	383	644	3.03	4.1
1:2	30	390	395	680	2.96	4.3
1:2	40	393	395	688	2.90	4.6
1:2.2	5	-	-	-	-	-
1:2.2	10	370	372	566	3.08	3.9
1:2.2	20	385	393	618	3.02	4.1
1:2.2	30	389	395	660	2.96	4.3
1:2.2	40	393	395	667	2.93	4.4
1:4	5	-	-	-	-	-
1:4	10	-	-	-	-	-
1:4	20	387	395	634	3.02	4.1
1:4	30	389	395	660	2.95	4.4
1:4	40	388	395	661	2.92	4.5

Under UV 365 excitation, the supernatant from the 1:2 molar ratio reaction exhibited a colour spectrum ranging from green to yellow to red for time points of 10-40 min, with no luminescence observed at 5 min, shown in Figure 2.41 (f). In contrast, the reduced 1:1.5 molar ratio (b) reaction showed a slight green hue at 5 min, and red colouration for time points of 10-40 min. This red colouration is attributed to incomplete coverage of the formed CdS and particle overgrowth, which compromises control over optical properties and suggests a lower boundary for the Cd:ligand ratio. Conversely, the 1:4 molar ratio (n) reaction series displayed a gradual colour shift from yellow to orange between 20-40 min, indicating slow growth potentially due to excess ligand. This excess also delays CdS formation as sulfur becomes available through L-cysteine degradation. This Cd:ligand ratio limits and reduces the range and control over optical properties and particle size. These findings are corroborated by the optical characterisation of the samples,

characteristics given in Table 2.22 leading to the conclusion that the 1:2 or 1:2.2 molar ratios offer an optimal balance between the Cd source and the ligand, as suggested by Aboulaich *et al*.[23]

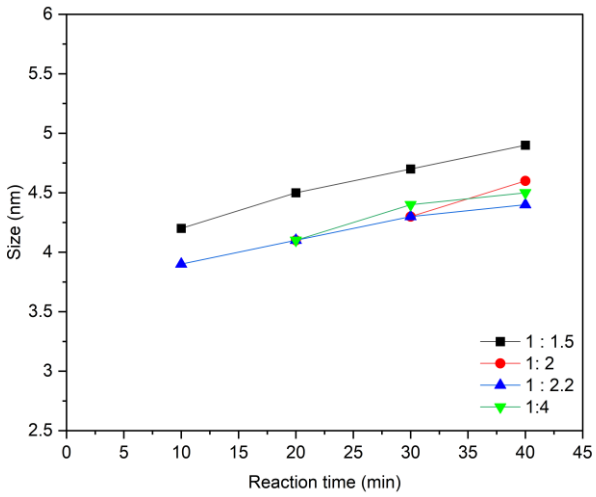

Figure 2.42, The calculated sizes of the CdS quantum dots from hydrothermal reaction of cadmium nitrate and L-cysteine, at pH 8.5, varying the molar ratio (1:1.5) – (1:4), and reaction time 10 – 40 min.

2.10 Characterisation of isolated CdS quantum dots

Following the identification of an optimal reaction system at 130 ˚C and pH 8.5, using Cadmium Nitrate and L-Cysteine in a 1:2.2 ratio with reaction times of 10, 20, 30, and 40 min, these conditions were replicated five-fold to isolate the quantum dots from the resulting supernatant. The Optical characterisation was summarised in of the supernatant revealed absorption maxima (λ_{abs}) between 387 and 399 nm, λ_{ex} from 376 to 398 nm, and λ_{em} ranging from 690 to 708 nm. This was converted to band gaps from 2.99 to 2.87 eV and sizes 4.2 and 4.7 nm. The observed wavelength range is narrower than anticipated, potentially due to increased variability arising from the multi-stage reaction process. Quantum yields were determined using $Ru(bpy)_3$ as a standard, with an excitation wavelength of 395 nm, yielding QYs of 4.5%, 2.9%, 1.7%, and 1.5% for reaction times of 10, 20, 30, and 40 min, respectively.[87] These measured quantum yields are relatively low compared to the maximum QY of 17, 20, and up to 50% of aqueous cadmium sulfide nanoparticles reported in literature.[23, 88, 89] An explanation for this would be the reactant degradation in storage as L-cysteine is vulnerable to oxidation. Due to time constraints this experiment could not be repeated with a newly acquired ligand. Additionally, the observed decline in quantum yield with prolonged reaction times suggests either growth of the quantum dots beyond their optimal size for efficient luminescence or an increase in surface defects that promote non-radiative recombination pathways.

Table 2.23, Overview optical properties CdS QDs from cadmium nitrate and L-cysteine molar ration (1:2.2), pH 8.5, and varying reaction times of 10, 20, 30, and 40 min.

Time (min)	λ_{abs} (nm)	λ_{ex} (nm)	λ_{em} (nm)	Bandgap (eV)	Size (nm)	QY (%)
10	387	376	690	2.99	4.2	4.5
20	394	394	676	2.95	4.4	2.9
30	397	395	699	2.90	4.6	1.7
40	399	398	708	2.87	4.7	1.5

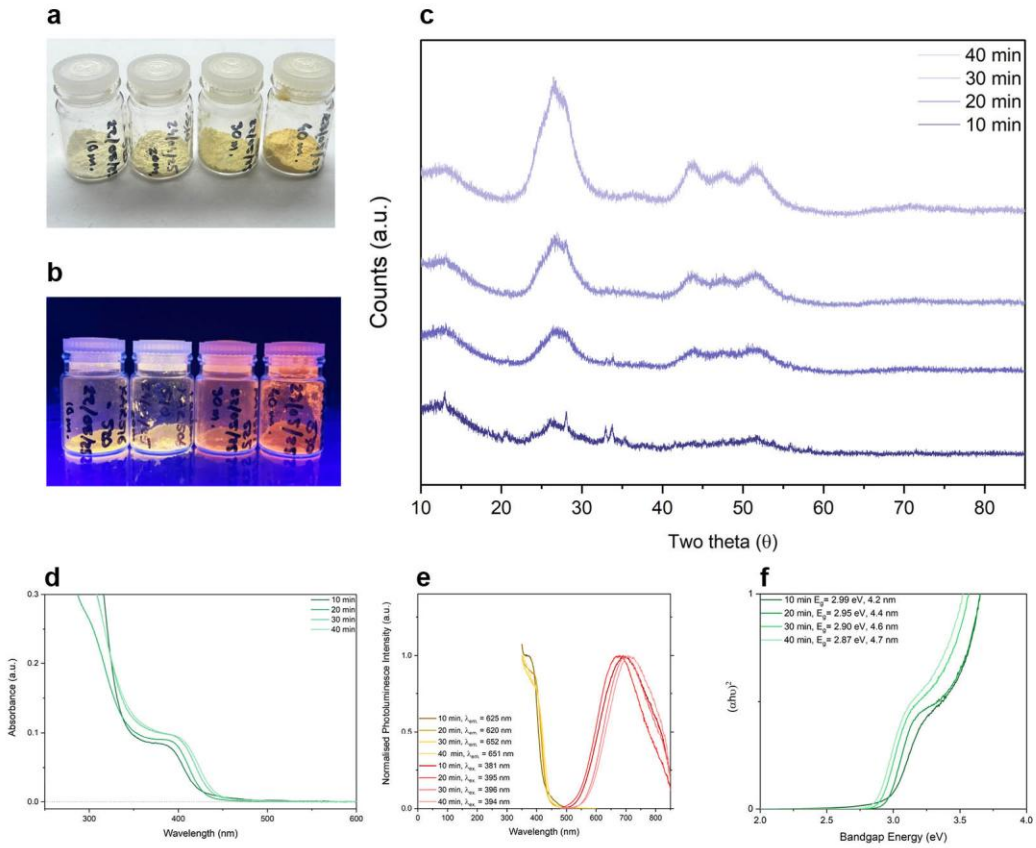

Figure 2.43, CdS quantum dots in daylight (a) and under UV 365 nm (b) and XRD patterns of the quantum dots (c) from the hydrothermal synthesis of Cadmium Nitrate and L-Cysteine in ratio 1:2.2, pH 8.5, time series 10-, 20-, 30-, and 40-min

The quantum dots were precipitated from the supernatant and dried overnight. The isolated quantum dots, obtained in powder form, exhibited a colour transition from pale yellow to yellow under ambient daylight, shown in Figure 2.43 (a). Upon excitation with UV light at 365 nm, they emitted yellow and orange/red luminescence (b). X-ray diffraction analysis was performed on these samples, revealed in (c). The characteristic pattern of hexagonal CdS on the nanoscale is visible with significantly broadened peaks and improved definition observed for the samples corresponding to longer reaction times of 30 and 40 min. The short reaction times of 10 and 20 min show a few sharper peaks associated with the L-cysteine used in reaction. The reduction of these sharp peaks with reaction time suggest that the L-cysteine is bound to the CdS nanomaterial.

Transmission electron microscopy images of the four samples are shown in Figure 2.44, each on two different scales. All images show aggregated nanoparticles under 5 nm, consistent with the sizes calculated with the Brus equation and Tauc plot. In figure (a) and (c) the quantum dots are embedded in an amorphous layer, whereby the particles in (e) and (g) seem less so, providing defined separation between aggregate and the environment. In the zoomed-in pictures the emergence of crystal lattices between 10 (b) and 20 min (d), and continuation at t30 and t40 (f and h) supports this, together with the XRD patterns produced. However, from these images it was not possible to find the size distribution of the particles and compare these between reaction times. Nevertheless, these images provide visual confirmation of the synthesis of nanosized material in hydrothermal reaction with cadmium nitrate and L-cysteine.

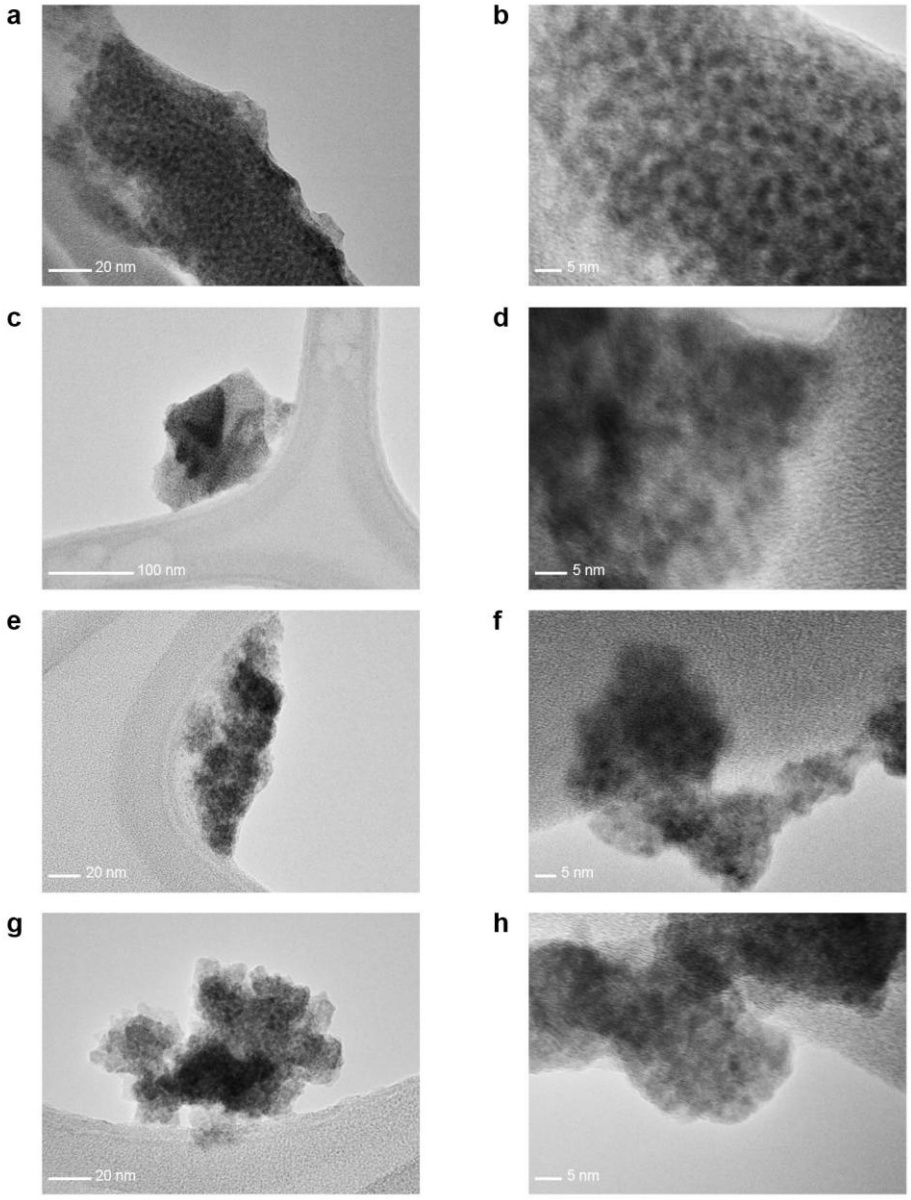

Figure 2.44, TEM images of CdS quantum dots, reaction in hydrothermal method of Cadmium Nitrate and L-cysteine, pH 8.5, for 10 min (a, b), 20 min (c, d), 30 min (e, f), and 40 min (g, h).

In summary, the study demonstrates the successful synthesis and controlled hydrothermal preparation of CdS quantum dots using Cadmium Nitrate and L-Cysteine, where L-Cysteine functions as both the sulfur source and a ligand. While the inclusion of alternative sulfur sources like thiourea or sodium thiosulfate also yielded CdS quantum dots, they resulted in diminished control over the optical properties of the reaction.

Consequently, the simplified reaction system leveraging the dual functionality of L-Cysteine is advantageous and performs effectively, as well as excluding a reactant from the system, this contributes to the bigger task of practicing green chemistry in material synthesis, such as preventing waste and improving the atom economy. Optimal control over optical properties and particle growth was achieved by adjusting the pH to 8.5, maintaining molar ratios of Cadmium Nitrate to L-Cysteine between 1:2 and 1:2.2, and modifying reaction times from 10 to 40 min. The L-Cysteine-based CdS quantum dots synthesised within this system were isolated and analysed with structural characterisation techniques of XRD and TEM.

2.11 Conclusions

From this study it was concluded that the hydrothermal method for the synthesis of CdS quantum dots is feasible, and offers a green alternative to conventional synthesis methods, without the use of organic solvents. Hydrothermal synthesis was found operational in both the conventional method with use of an autoclave and oven, as well as an adjusted approach making use of Duran tubes and a heat block, providing insight into the systems boundary between soluble/luminescence nanomaterials and the formation of bulk cadmium sulfide.

In the conventional reaction system, optimised reaction conditions were found when reacting Cadmium nitrate, thiourea, and L-cysteine (1:1.8:2.2) reacting at pH 7, whereby reaction time elongation from 100 to 180 min resulted in λ_{abs} shifts from 383 to 415 nm, and λ_{em} 616 to 709 nm. The conventional reaction system using Cadmium nitrate, thiourea and cysteamine at pH 5.6, resulted in red shift between reaction time 40 and 180 min, with λ_{abs} 347 – 393 nm and λ_{em} 506 – 701 nm.

In the adjusted reaction system, synthesis of CdS quantum dots was optimised, resulting in a suitable reaction temperature of 130 ˚C and reaction times 5 – 40 min, also the optimal pH conditions found in the conventional system were confirmed in this system by exploring different set pH values. This system addressed the green chemistry principle of the design for energy efficiency whereby this system enabled synthesis at lower temperatures and reduced time scales.

Control over the optical properties was explored and expanded by assessment of the influence of reaction time, pH, the choice of reactants, including ligand: L-cysteine and Cysteamine, cadmium source: Cadmium nitrate and cadmium chloride, and sulfur source: thiourea and sodium thiosulfate. This led to the following findings:

Sodium thiosulfate requires less decomposition energy compared with thiourea, resulting in faster nucleation and smaller initial nanocrystals, demonstrated in blue-green emission at 5-minute reactions, in contrast to yellow emission at 10-minute reactions with thiourea. Additionally, the reaction system with sodium thiosulfate provided a wider range of emission at alkaline conditions of 8.5 and 10. It was found that the reaction system with reactants Cadmium Nitrate, Sodium Thiosulfate, and Cysteamine did not yield variation in the properties of the soluble QDs, only blue emission was observed for the 5-min reaction. In conclusion, cysteamine can serve as a ligand for CdS quantum dot formation, offering good size and optical property control with reaction time variations. However, its efficacy is highly dependent on the specific reaction system, pH, and sulfur source. L-cysteine, while involving a competitive formation between a L-cysteine complex and CdS quantum dots, offers luminescence across a range of pH conditions (neutral to basic) with both sulfur sources, and provides a broader emission spectrum with reasonable control over optical properties via reaction time. Consequently, the L-cysteine system is deemed more versatile despite the competitive precipitation.

This finding was confirmed when examining a second cadmium source, which yielded good control over optical properties for optimised L-cysteine reaction with both thiourea and sodium thiosulfate, however,

using cysteamine and cadmium chloride together provided only limited control over the optical properties of the luminescence materials produced.

Crucially, validation of the reaction system revealed that omitting a dedicated sulfur source surprisingly still facilitated the synthesis of controllable CdS quantum dots. This not only demonstrates an unexpected reaction pathway but also profoundly addresses green chemistry principles by significantly reducing the precursor materials. This unexpected outcome strongly suggests that L-Cysteine exhibits unique bifunctional characteristics under hydrothermal conditions, driving reaction dynamics that are fundamentally distinct from those observed in solvothermal or hot-injection methods. Consequently, this underscores the critical importance of carefully considering the specific reaction environment and precursor properties when translating synthetic methodologies across different systems.

Further investigation revealed reaction parameters of time, pH, and molar ratios effect the optical properties of the CdS QDs greatly. Reaction conditions of pH 8.5, varying reaction time from 10 to 40 min, and using cadmium nitrate:L-cysteine in molar ration 1:2.2 yielded the broadest ranging emission spectrum, with quantum yields of 4.5%, 2.9%, 1.7%, and 1.5% for reaction times of 10, 20, 30, and 40 min, respectively. This time series was reproduced to isolate the soluble QDs for structural characterisation confirming nanoscale CdS with X-ray diffraction and transmission electron microscopy.

Overall, this chapter addressed the green chemistry of cadmium sulfide quantum dot synthesis. Exploration of the hydrothermal synthesis of cadmium sulfide semiconductive nanomaterials, offered a sustainable alternative to conventional methods, whereby water is used as solvent and a reduced reaction temperature of 130 ˚C. In the hydrothermal reaction, control over the optical properties was achieved by varying reaction time, pH, and choice of reactants. The ligand's critical role became apparent, functioning simultaneously as both the sulfur precursor and the capping agent. This simplified reaction manifold, utilising only the cadmium source and the ligand, enabled superior regulation of the absorption and emission characteristics, as well as the size, of CdS quantum dots, especially with prolonged reaction durations. Such a reaction system exemplifies the successful implementation of green chemistry principles, evidenced by a 36% reduction in molar material input, a substantially decreased reaction temperature, and the replacement of organic solvents with an aqueous medium.

2.12 References

1. K. Agarwal, H. Rai and S. Mondal, *Mater. Res. Express.*, 2023, **10**, 26.
2. C. Rengers, N. Gaponik and A. Eychmüller, in *Biological Responses to Nanoscale Particles: Molecular and Cellular Aspects and Methodological Approaches*, eds. P. Gehr and R. Zellner, 2019, DOI: 10.1007/978-3-030-12461-8_2, pp. 29-51.
3. Nobel Prize Outreach 2025, Quantum dots – seeds of nanoscience, The Nobel Prize in Chemistry 2023, <https://www.nobelprize.org/prizes/chemistry/2023/advanced-information/>, (accessed Wed. 20 Aug, 2025).
4. R. Shankar, *Principles of quantum mechanics*, Plenum Press, 2nd edn., 1994.
5. K. Momma and F. Izumi, *J. Appl. Crystallogr.*, 2011, **44**, 1272-1276.
6. J. Mao, W. Xu and S. Seo, *J. Mater. Chem. A*, 2024, **12**, 23218-23242.
7. F. Ulrich and W. Zachariasen, *Z. Kristallogr.*, 1925, **62**, 260-273.
8. W. Müller and G. Löffler, *Angew. Chem. Int. Ed*, 1933, **46**, 538-539.
9. W. Milligan, *J. Phys. Chem.*, 1934, **38**, 797-800.
10. C. Murray, D. Norris and M. Bawendi, *JACS*, 1993, **115**, 8706 - 8715.
11. P. Nagajyoti, K. Lee and T. Sreekanth, *Environ. Chem. Lett.*, 2010, **8**, 199-216.
12. J. Duruibe, M. Ogwuegbu and J. Egwurugwu, *Int. J. Phys. Sci.*, 2007, **2**, 112-118.
13. P. Vesborg and T. Jaramillo, *RSC Adv.*, 2012, **2**, 7933.
14. C. B. Murray, D. J. Norris and M. G. Bawendi, *J. Am. Chem. Soc*, 1993, **115**, 8706-8715.
15. Z. Li, W. Cai and J. Sui, *Nanotechnology*, 2008, **19**, 035602.
16. M. Hu and T. Zhu, *Nanoscale Res. Lett.*, 2015, **10**, 1-15.
17. S. Farkhani and A. Valizadeh, *IET Nanobiotechnol.*, 2014, **8**, 59-76.
18. A. Kim, J. K. Dash, P. Kumar and R. Patel, 2021, DOI: 10.1021/acsaelm.1c00783.
19. Y. Li, *J. Mater. Sci.*, 2000, **35**, 5933-5937.
20. K. Byrappa and T. Adschiri, *Prog. Cryst. Growth Charact. Mater.*, 2007, **53**, 117-166.
21. R. Judge, R. Jacobs, T. Frazier, E. Snell and M. Pusey, *Biophys. J.*, 1999, **77**, 1585-1593.
22. D. Chowdhury, N. Gogoi and G. Majumdar, *RSC Adv.*, 2012, **2**, 12156-12159.
23. A. Aboulaich, D. Billaud, M. Abyan, L. Balan, J.-J. Gaumet, G. Medjadhi, J. Ghanbaja and R. Schneider, *ACS Appl. Mater. Interfaces.*, 2012, **4**, 2561-2569.
24. N. Chen, Y. He, Y. Su, X. Li, Q. Huang, H. Wang, X. Zhang, R. Tai and C. Fan, *Biomater.*, 2012, **33**, 1238-1244.
25. C. Yao, T. Lin, Z. Lian, S. Liao, Z. Yan and S. Wu, *J. Fluoresc.*, 2020, **30**, 1601-1609.
26. D. Kumar, B. Kumar and H. Mahesh, Bikaner, INDIA, 2015.
27. K. Shirvas, S. Kailasa and H. Wu, *Rapid Commun. Mass Spectrom.*, 2009, **23**, 3603-3607.
28. M. Algarra, I. Bobos, J. Jimenez-Jiménez, R. Morento-Tost, E. Rodríguez-Castellón and J. da Silva, *J. Incl. Phenom. Macrocycl. Chem.*, 2010, **67**, 225-232.
29. C. Baslak, E. Aslan, I. Patir, M. Kus and M. Ersoz, *Int. J. Hydrogen Energy.*, 2016, **41**, 20523-20528.
30. S. Narimani, S. Saadatmand and N. Samadi, *Anal. Bioanal. Chem. Res.*, 2023, **10**, 25-32.
31. D. Sagdeev, R. Shamilov and Y. Galyametdinov, *J. Appl. Spectrosc.*, 2021, **88**, 539-545.
32. S. Watanabe, N. Tamura and M. Matsumoto, *J. Oleo Sci.*, 2012, **61**, 277-283.
33. S. Ha, H. Kim and C. Lim, *Russ. J. Phys. Chem. B.*, 2015, **9**, 141-147.
34. C. Luan, A. Vaneski, A. Susha, X. Xu, H. Wang, X. Chen, J. Xu, W. Zhang, C. Lee, A. Rogach and J. Zapien, *Nanoscale Res. Lett.*, 2011, **6**.
35. M. Satnami, S. Vaishanav, R. Nagwanshi and K. Ghosh, *J. Indian Chem. Soc.*, 2015, **92**, 1427-1435.
36. H. Wang, T. Liu, J. Xie, W. Su, A. Guo and Z. Cai, *Chin. J. Anal. Chem.*, 2010, **38**, 632-637.
37. S. Lai, X. Chang, S. Wang, J. Mao and L. Tian, *Rev. Roum. Chim.*, 2009, **54**, 815-+.
38. M. Liu, L. Xu, W. Cheng, Y. Zeng and Z. Yan, *Spectrochim. Acta A.*, 2008, **70**, 1198-1202.
39. M. Atif, W. Farooq, M. El Sadek, H. El Sheshtawy and I. Yahia, *Chalcogenide Lett.*, 2015, **12**, 91-97.
40. I. Postnova, S. Voznesenskiy, A. Sergeev, A. Galkina, Y. Kulchin and Y. Shchipunov, *Colloids Surf. A.*, 2018, **536**, 3-9.
41. C. Unni, D. Philip, S. Smitha, K. Nissamudeen and K. Gopchandran, *Spectrochim. Acta A.*, 2009, **72**, 827-832.
42. H. Wang, C. Chen, Y. Liu, Y. Wu, Y. Yuan and Q. Zhou, *Talanta*, 2019, **198**, 242-248.
43. Z. Yang, L. Lu, C. Kiely, B. Berger and S. McIntosh, *Ind. Eng. Chem. Res.*, 2016, **55**, 11235-11244.
44. J. L. Chen and C. Q. Zhu, *Anal. Chim. Acta*, 2005, **546**, 147-153.
45. S. Xiang-Ying, L. Bin, L. Hui and Y. Yan-Hua, *J. Nanosci. Nanotechnol.*, 2011, **11**, 6810-6814.
46. C. Zhou, L. Zhou, J. Xu and Y. Gan, *J. Solid State Electrochem.*, 2016, **20**, 533-540.
47. D. Sagdeev, R. Shamilov, V. Voronkova, A. Sukhanov and Y. Galyametdinov, *Russ. Chem. Bull.*, 2020, **69**, 1749-1754.

48. S. Akshya, P. Hariharan, V. Kumar and S. Anthony, *Spectrochim. Acta A.*, 2015, **135**, 335-341.
49. R. Grinyte, J. Barroso, L. Saa and V. Pavlov, *Nano Res.*, 2017, **10**, 1932-1941.
50. L. Sun, X. Fu, C. Qian, C. Liao and C. Yan, *Chem. J. Chin. Univ.*, 2001, **22**, 879-882.
51. X. Cao, C. Li, H. Bao, Q. Bao and H. Dong, *Chem. Mater.*, 2007, **19**, 3773-3779.
52. P. Chen, X. Yue, W. Dai, X. Wang, Y. Li, H. Xie, D. Jiang and Y. Jiang, *Sci. Adv. Mater.*, 2021, **13**, 864-873.
53. K. Wang, E. Dong, M. Fang, W. Zhu and C. Li, *J. Fluoresc.*, 2022, **32**, 1099-1107.
54. T. Noipa, T. Tuntulani and W. Ngeontae, *Talanta*, 2013, **105**, 320-326.
55. Y. Guo, L. Jiang, L. Wang, X. Shi, Q. Fang, L. Yang, F. Dong and C. Shan, *Mater. Lett.*, 2012, **74**, 26-29.
56. S. Kosmella, J. Venus, J. Hahn, C. Prietzel and J. Koetz, *Chem. Phys. Lett.*, 2014, **592**, 114-119.
57. A. Raevskaya, G. Grodzyuk, A. Stroyuk, S. Kuchmii and V. Dzhagan, *Theor. Exp. Chem.*, 2010, **46**, 233-238.
58. H. Mao, J. Yao, L. Wang and W. Liu, *J. Colloid Interface Sci.*, 2008, **319**, 353-356.
59. S. Chen, J. Zhang, S. Song, R. Feng, Y. Ju, C. Xiong and L. Dong, *Langmuir*, 2016, **32**, 611-618.
60. E. H. Lester, P. W. Dunne, A. S. Munn, C. L. Starkey and T. A. Huddle, 2015, DOI: 10.1098/rsta.2015.0015.
61. P. T. Anastas and J. C. Warner, *Green Chemistry: Theory and Practice*, Oxford University Press, 2000.
62. M. Bruchez, M. Moronne, P. Gin, S. Weiss and P. Alivisatos, *Science*, 1998, **281**, 2013-2016.
63. V. Bagalkot, L. Zhang, E. Levy-Nissenbaum, S. Jon, P. Kantoff, R. Langery and O. Farokhzad, *Nano Lett.*, 2007, **7**, 3065-3070.
64. S. Qi, J. Chen, X. Bai, Y. Miao, S. Yang, C. Qian, B. Wu, Y. Li and B. Xin, *RSC Adv.*, 2021, **11**, 21813-21823.
65. H. Zhu, D. Yang, G. Yu, H. Zhang and K. Yao, *Nanotechnology*, 2006, **17**, 2386-2389.
66. W. Liu, B. Guo, X. Wu, F. Zhang, C. Mak and K. Wong, *J. Mater. Chem. A*, 2013, **1**, 3182-3186.
67. M. Wei, L. Yang, Y. Yan and L. Ni, *Mater. Express*, 2019, **9**, 413-418.
68. J. Xie, *Inorg. Chem.*, 2008, **47**, 5564-5566.
69. Y. Hu, Z. Wei, B. Wu, B. Shen, Q. Dai and P. Feng, *AIP Adv.*, 2018, **8**, 7.
70. A. Ebnalwaled, M. Essai, B. Hasaneen and H. Mansour, *J. Mater. Sci.: Mater. Electron.*, 2017, **28**, 1958-1965.
71. S. Gupta, V. Kulkarni and M. Ahmaruzzaman, *J. Environ. Chem. Eng.*, 2024, **12**, 17.
72. B. Karimi, M. Afarani and A. Arabi, *Appl. Phys. A.*, 2020, **126**, 9.
73. F. Li, W. Li, S. Fu and H. Xiao, *J. Alloys Compd.*, 2015, **647**, 837-843.
74. L. Liu, Q. Peng and Y. Li, *Inorg. Chem.*, 2008, **47**.
75. N. Du, L. Ren, W. Sun, X. Jin, Q. Zhao, Y. Cheng, T. Wei and Q. Li, *J. Power Sources*, 2015, **284**, 162-169.
76. H. Bu, H. Kikunaga, K. Shimura, K. Takahasi, T. Taniguchi and D. Kim, *Phys. Chem. Chem. Phys.*, 2013, **15**, 2903-2911.
77. G. Crosby and J. Demas, *J. Phys. Chem.*, 1971, **75**, 991-1024.
78. S. Fery-Forgues and D. Lavabre, *J. Chem. Educ.*, 1999, **76**, 1260.
79. N. Katsumi, *Bull. Chem. Soc. Jpn.*, 1982, **55**, 2697-2705.
80. W. H. Melhuish, *The Journal of Physical Chemistry*, 1961, **65**, 229-235.
81. S. Narayanan and S. Pal, *J. Phys. Chem. B*, 2006, **110**, 24403-24409.
82. N. I. o. H. (NIH), *Journal*.
83. V. Argyropoulos, S. C. Boyatzis, M. Giannoulaki, E. Guilminot and A. Zacharopoulou, Springer International Publishing, 2021, DOI: 10.1007/978-3-030-69411-1_15, pp. 341-367.
84. C. Atallah, C. Charcosset and H. Greige-Gerges, *J. Pharm. Anal.*, 2020, **10**, 499-516.
85. Z.-Y. Ma, Z.-L. Yu, Z.-L. Xu, L.-F. Bu, H.-R. Liu, Y.-B. Zhu, B. Qin, T. Ma, H.-J. Zhan, L. Xu, H.-A. Wu, H. Ding and S.-H. Yu, *Matter*, 2020, **2**, 1270-1282.
86. C. H. Görbitz and B. Dalhus, *Acta Crystallographica Section C*, 1996/07/15, **52**.
87. K. Suzuki, A. Kobayashi, S. Kaneko, K. Takehira, T. Yoshihara, H. Ishida, Y. Shiina, S. Oishi and S. Tobita, *Phys. Chem. Chem. Phys.*, 2009, **11**, 9850.
88. S. Celebi, A. K. Erdamar, A. Sennaroglu, A. Kurt and H. Y. Acar, *The Journal of Physical Chemistry B*, 2007, **111**, 12668-12675.
89. A. Mandal, J. Saha and G. De, *Optical Materials*, 2011, **34**, 6-11.

Chapter 3 Hydrothermal Synthesis of Carbon Dots from Seaweed

3.1 Introduction

Introduced in Section 1.5, carbon dots are fluorescent nanomaterials primarily composed of carbon. Carbon dots are praised for their optical properties, biocompatibility, and low toxicity, making them highly attractive for life-science and environmental applications. As discussed, carbon dots encompass four types of nanomaterials which are complexly related to structure, source, luminescence properties and synthesis approach.

In this chapter the focus lies with the synthesis of amorphous carbon nanodots, gaining their photoluminescence properties primarily through the defect and surface states stemming from functional groups in the molecular structure.[1, 2] For the synthesis of carbon nanodots, the carbohydrate rich biomass of seaweed is chosen in combination with the bottom-up method of hydrothermal synthesis, to leverage sustainable chemistry practices in the process. Compared to the properties of quantum dots, carbon dots offer advantages in eco-friendliness, cost-effectiveness, and facile synthesis from biomass. Furthermore, the synthesis of carbon dots from biomass offers a sustainable approach, leveraging readily available and renewable resources such as agricultural waste, plants, and other organic biomaterials.[3] The literature extensively documents their synthesis from a wide array of biomasses, including fruits, plants, and several organic waste streams including spent tea leaves, coffee grounds, shells and peels, suggesting a broad applicability.[4-14]

This study investigates the hydrothermal synthesis of carbon dots derived from seaweed. This approach represents a significant paradigm shift from traditional linear economic models, which are characterised by a "take-make-dispose" philosophy, towards systems where waste is minimised and resources are kept in use for as long as possible.[15] This systemic transformation is crucial for addressing the escalating environmental concerns associated with plastic waste and the depletion of non-renewable resources, driving a critical need for sustainable material innovation.[16]

Besides the intrinsic properties of biomass as a renewable, cost-effective, and abundant carbon source with good biocompatibility, the synthesis of carbon dots is facilitated by green and straightforward synthetic methods, elaborated in the next section.[17]

3.1.1 Synthesis methods of carbon dots from biomass

Carbon dots can be synthesised using either top-down or bottom-up approaches. The top-down synthesis of carbon dots involves cutting and exfoliating graphene or graphite to produce graphene quantum dots.[18] The bottom-up synthesis of carbon dots utilises small organic molecules to build carbon dot structures, through chemical fusion of aromatic compounds. Bottom-up synthesis of carbon dots from biomass includes methods of pyrolysis, solvo- and hydrothermal, and microwave-assisted hydrothermal synthesis, which are elaborated below.

- Pyrolysis – carbon dots are produced through pyrolysis of organic precursors, such as citric acid, glutathione, and ethanolamine, which involves a thermal decomposition process that irreversibly alters their chemical composition and structure.[19] These "one-pot" reactions yield carbon dots after high-temperature treatment and purification.
- Solvothermal/hydrothermal[12] – carbon dots are produced from biomass using solvothermal or hydrothermal treatment. The hydrothermal method utilises water as both a solvent and a reaction medium, allowing for the hydrolysis and carbonisation of plant precursors under mild reaction conditions.
- Microwave-assisted hydrothermal – this method has emerged as an alternative to conventional hydrothermal methods, offering an expedited pathway to carbon dot production, significantly reducing reaction times.[20] This method harnesses microwave radiation to rapidly heat and carbonise plant-derived materials within a suitable solvent and catalyst system, facilitating the formation of carbon dots.

3.1.2 Formation mechanism of carbon dots from biomass

The formation of carbon dots from biomass precursors typically proceeds through a series of complex, multi-stage chemical transformations under hydrothermal conditions.[21] These include initial hydrolysis, which breaks down complex biomass macromolecules (such as polysaccharides, proteins, and lignins) into smaller monomeric units like sugars and amino acids; subsequent dehydration, involving the elimination of water molecules to form carbonyl and aromatic intermediates; polymerization (or condensation), where these fragments oligomerize via nucleophilic additions and Schiff base reactions; and final carbonization (or aromatization), yielding the sp^2-hybridized carbon core with surface functional groups responsible for fluorescence. These interconnected processes—hydrolysis, polymerization, and carbonization—are facilitated by the elevated temperature and pressure of hydrothermal synthesis, which provides a clean, cost-effective, and efficient route using sustainable biomass-derived precursors. This process is illustrated in Figure 3.1.[22-24]

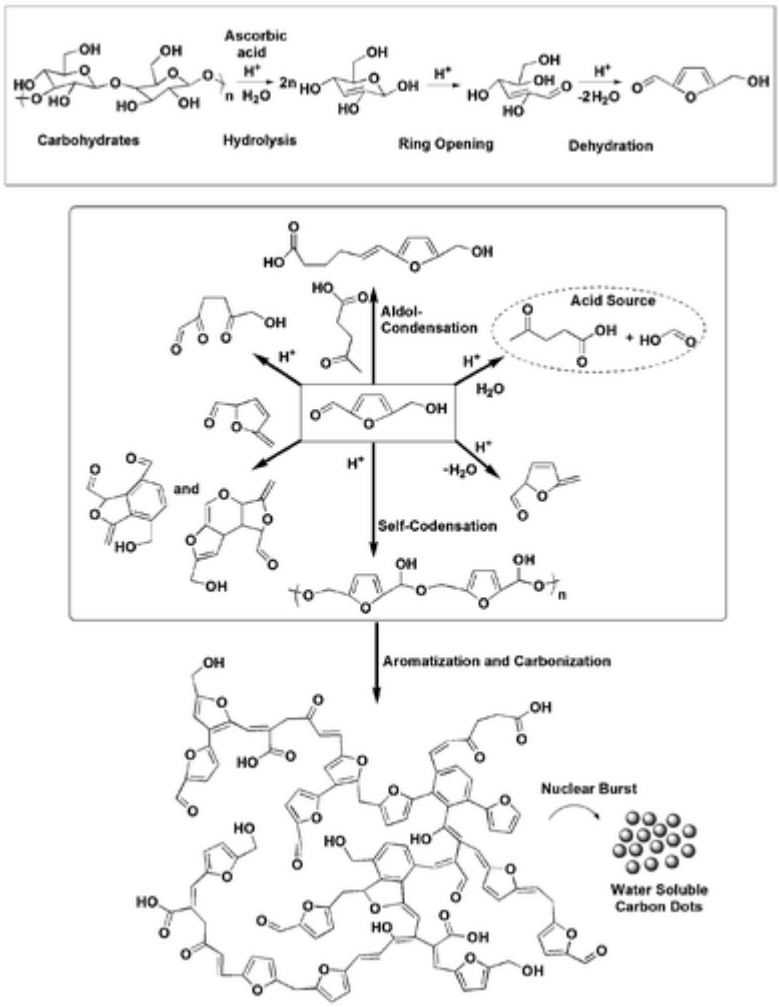

Figure 3.1, Possible mechanism for the formation of carbon dots from saccharide rich biomasses.[23]

Water's polarity and its ability to solvate small molecules facilitate the structural decomposition of biomass, making small molecular structures and saccharides readily available for conversion into carbon dots via hydrothermal treatment. Hydrothermal conversion, therefore, offers a versatile route for producing carbon dots from various carbohydrate sources.

3.1.3 Purification methods of carbon dots

The intrinsic heterogeneity and variability of biomass feedstocks frequently pose obstacles in achieving consistent product quality and high quantum yields. The reaction solution might be contaminated with unreacted feedstock, intermediate molecular structures, and other impurities that can compromise their distinct optical characteristics and impede their practical utility. Purification of carbon dots is critical for realising their full potential, especially in optical applications, for three main reasons. First, removing fluorescent byproducts from synthesis ensures the observed fluorescence originates solely from the carbon dots themselves, allowing for accurate characterisation and reliable results. Second, this ensures consistent behaviour in applications by preventing impurities from interfering with carbon dot function. Finally, it advances carbon dot technology by providing consistent and reliable samples, paving the way for their integration into next-generation materials. To address the issue, a strict purification strategy is indispensable to produce carbon dots with uniform optical properties and enhanced performance.

Table 3.1, Purification methods for carbon dots.[25]

Method	Principle	Advantage	Disadvantage
Filtration	Separates CDs by size using porous membranes	Simple and cost-effective, effective removal of larger particles	No separation between particles of similar size
Dialysis	Size-based separation using a semipermeable membrane.	Removes small impurities and salts	Slow and ineffective against large particles
Centrifugation	Separates particles through centrifugal force	Fast and effective for variation in sizes	Struggle to separate particles of similar density and could damage CDs
Solvent extraction	Separation based on solubility in various solvents	Effective separation of CDs from impurities	Requires understanding of the solubility profile of both CDs and impurities present
Chromatography	Separates materials based on different interactions with the stationary and mobile phase	High efficiency	Time consuming, specialised equipment, and parameter optimisation.
Electrophoresis	Separates charged particles in an electric field based on their charge and size	Effective separation of distinct carbon dots	Requires specialised equipment and expertise

Various purification techniques for carbon dots have been reported in the literature, each presenting unique benefits and drawbacks. The optimal method is determined by considerations such as the specific synthesis methodology, the type of impurities present, and the intended use of the purified carbon dots.[25] Common purification strategies are given in Table 3.1.

3.1.4 Biomass composition and carbohydrate content

As described in the previous section, the carbohydrate content provides the backbone in the formation of carbon dots. However, the presence of all components of the biomass may play a role in the formation of defects and surfaces states responsible for the photoluminescence properties of carbon dots. A direct relation between biomass composition and optical properties of the carbon dots derived from it is impossible to point out. However, evaluation of the carbohydrate content and all other components in the biomass might provide an educated guess on the functionality of the carbon dots it would produce.

Compared to land-based crops the chemical composition of seaweed is distinct.[26] Since seaweeds float in the water column, the need for structural parts in the seaweed are diminished, therefore they consist mostly of leaves, the carbohydrate containing parts. Due to the lack of hemicellulose and lignin, the major constituents of the structural plant cell wall, seaweeds are comparatively easy to depolymerise.[27]

Additionally, considering seaweed as a renewable feedstock compared to terrestrial crops benefits from efficient conversion of light energy, rapidly producing biomass from abundant sunlight, carbon dioxide, and nutrients, leading to higher yields per area compared to land plants. As well as marine algae do not require fertile land and can grow in various water types, including saltwater and wastewater, thereby avoiding competition with food crops for land and freshwater resources. Therefore, seaweed is recognised as an inexpensive, clean, and renewable feedstock.[28-32]

3.1.5 The seaweed revolution

Commercial seaweed cultivation originated in Asia over half a century ago.[33] The predominant cultivation in these regions has historically been driven by their intrinsic availability and geographical proximity to densely populated coastal communities. Since then, the practice has experienced substantial growth, with global commercial production of seaweed reaching over 35 million tonnes (wet weight) in 2023, depicted in Figure 3.2. While Asia currently dominates seaweed cultivation, contributing most of the global output (98%), seaweed farms are gaining traction in various regions globally.[34]

Ireland possesses a strong connection with seaweed, stemming from its extensive coastline and historical dependence on marine resources. This has fostered a deep understanding of seaweed's diverse applications, primarily within the agricultural sector, including food, feed, and fertiliser. This historical context underscores the inherent potential for expanding seaweed utilisation into emerging sectors, building upon established practices and cultural acceptance. To ensure the environmental sustainability of existing wild seaweed populations, it has been recommended to cultivate new seaweed in Irish waters to prevent depletion and ensure protection.[32] A study concerning Irish wild seaweed farming indicated that the increased demand for seaweed cultivation could present environmental concerns regarding resource use, emissions, and water quality.[35] However, the same study also highlighted that the impacts of seaweed farming were minimal or even positive on ecosystem diversity, terrestrial carbon storage, and land use, due to its non-competition with agricultural land. Key factors identified for a successful seaweed industry in Ireland include high per-hectare seaweed yields, cost-effective cultivation, optimal harvesting times, and suitable upstream and downstream processing techniques.[32]

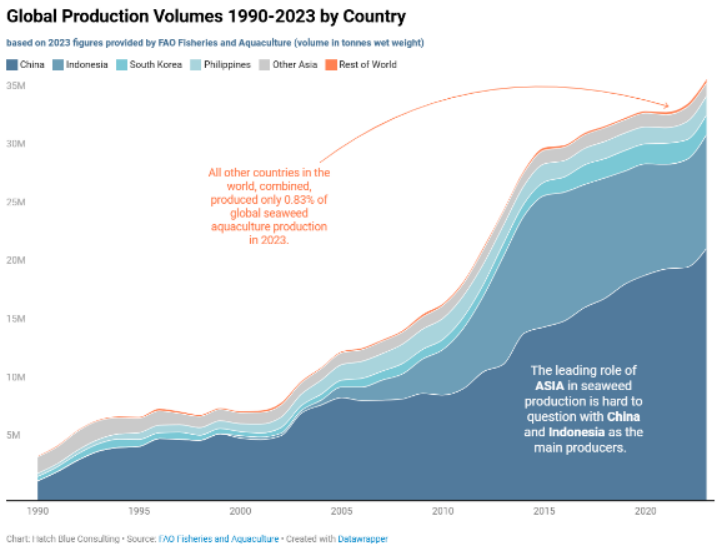

Figure 3.2, Global Seaweed Production Volumes 1990-2023 by Country (a) and by Species (b) based on 2023 figures provided by FAO Fisheries and Aquaculture (volumes in tonnes wet weight)

The newly established Irish Seaweed Association (ISA), a spin-out from the EU Horizon-funded C-FAARER project, is supported by partners such as Trinity College Dublin and Horizon Nua. The ISA aims to foster the sustainable growth of Ireland's seaweed industry by uniting stakeholders, promoting regenerative ocean farming, and addressing sector challenges. Gareth Murphy, Chair of ISA highlighted the industry's projected growth and Ireland's potential as a leader in this field, emphasising the need for government action on

licensing reviews.[36] The association will support startups and SMEs through funding, market access, and technological advancements to ensure specifically coastal communities' benefit from the industry's development.

The European Commission recently published a study on how to support the seaweed industry in the EU.[37] This initiative directly supports the ambitions outlined in the European Green Deal and the Farm to Fork Strategy, aiming to harness algae's potential for healthier diets, reduced emissions, and improved water quality.[38] The report identified opportunities in the sector that address food security, water pollution, and climate change, and found that algae cultivation can contribute to a circular economy. However, barriers identified in the study included the EU algae sector being underdeveloped within the bioeconomy, despite growing demand. Simultaneously, high costs and underutilisation of algae have been identified. Both at the producer and consumer levels, there are hurdles to overcome for widespread adoption. To establish a robust European algae sector, substantial investment in infrastructure, research and development, and market development are necessary to overcome these economic and perceptual challenges.

In the summer of 2025, Vattenfall launched an advertisement featuring Samuel L. Jackson praising wind farms and seaweed snacks, aiming to shift public perception.[39] This unusual pairing of a celebrity endorsement with sustainable energy promotion by the Swedish state-owned energy company highlights the increasingly unconventional strategies employed to boost public acceptance and awareness of renewable technologies and their associated marine permaculture, such as seaweed farming.

Figure 3.3, Vattenfall and Samuel L. Jackson present Wind Farmed Seaweed Snacks, a delicacy grown at a wind farm[39]

The private sector is also taking interest in these innovative approaches, exemplified by companies like Amazon's $100 million Right Now Climate Fund, which invests in nature-based projects globally that complement Amazon's broader operational decarbonisation and sustainability efforts.[40] This program includes support for the world's first commercial-scale seaweed farm inside an offshore wind farm in partnership with North Sea Farmers. The pioneering seaweed farm, located off the coast of the Netherlands amidst wind turbines, marks a significant milestone as its first-ever harvest was a success. This project is crucial for demonstrating the viability of commercial-scale seaweed cultivation in offshore wind farm spaces.[41, 42] The project's success validates the integration of renewable energy infrastructure with sustainable aquaculture, paving the way for scalable, environmentally beneficial solutions to climate change. This confluence of corporate investment and ecological restoration efforts demonstrates a nascent but critical shift

towards integrated sustainability initiatives that leverage both technological advancements and natural systems to achieve decarbonisation goals.

3.1.6 Development of new uses of seaweed

Seaweeds are shaped by their aquatic environment, requiring specific salinity levels and ample sunlight for photosynthesis. These conditions govern their ecology, enabling them to produce carbohydrates and lipids suitable for conversion into biofuels, chemical feedstocks, and other bioproducts. Macroalgae are broadly categorized into red, green, and brown algae, each possessing unique biochemical compositions and ecological niches. Their diverse biochemical profiles, rich in polysaccharides, proteins, and lipids, underscore their significant potential for biorefinery applications. These structural and biochemical differences among green, red, and brown algae significantly influence their suitability for various bioproduct applications, including biofuel production and the extraction of valuable polysaccharides like agar, carrageenan, and alginates.[37]

All seaweeds contain green chlorophyll for photosynthesis, with additional pigments determining their characteristic colours.

- Green algae, which are the most like land plants, utilise chlorophyll A and B for photosynthesis, storing energy in the form of starch and fats.
- Red algae, while also containing chlorophyll, appear red due to the presence of phycoerythrin and phycocyanin pigments. Their primary energy reserves are floridean starch and floridoside, and their cell walls are composed of cellulose, agar, and carrageenan.
- Brown algae are characterised by their brown pigmentation, attributed to high levels of fucoxanthin. They typically store energy as complex polysaccharides, sugars, and sugar alcohols, with laminarin serving as their primary carbohydrate reserve. Their cell walls are primarily composed of cellulose and alginic acid.

To efficiently synthesise carbon dots, the availability and carbohydrate content of seaweed are paramount. Two common Irish seaweeds, brown kelp (*Laminaria digitata*) and red Irish moss (*Chondrus crispus*), were chosen due to their high sugar content, geographical prevalence across Irish coastlines, established industrial uses, and significant historical presence in Ireland.

Kelp – *Laminaria digitata*

Kelp, also known as oarweed, tangle, or strapweed, is characterised by its broad, serrated, chocolate-coloured leaves, which appear to be composed of numerous finger-like structures.[43] This seaweed exhibits a bright sheen, reflecting the sky, and possesses a soft, slippery texture. Its stem is robust, flexible, and oval in cross-section, typically smooth and free from epiphytic growth. The size of kelp and the number of its digital extensions are directly proportional to water clarity. Kelp thrives in vigorous ocean currents along the North Atlantic coast. It demonstrates rapid growth in clear water, particularly in areas that rarely experience exposure to air. Kelp has a lifespan of up to six years. During winter, the energy reserves stored in its older leaves are translocated to the stem. With the onset of increased sunlight in spring, a new leaf develops from this stem.[44]

Historically, kelp has been utilised in various ways. In the 18th century, it was combusted to produce potash for the soap and glass manufacturing industries. In the 19th century, iodine was subsequently extracted from it. Currently, kelp serves as an organic fertilizer in agricultural and horticultural practices. When processed into alginate, it becomes a key component in toothpaste and ointments formulated for acne treatment.[36, 43]

Despite seasonal variations in chemical composition, an average analysis shows over 70% carbohydrate content by dry weight. Proteins account for 7% of the dry biomass, with minerals making up the remainder of the chemical composition. The sugar content is distributed among mannitol, laminarin, alginate, and cellulose, accounting for 19.4 ± 6.6%, 6.7 ± 6.0%, 34.6 ± 3.1%, and 11.5 ± 1.0% of the dry weight, respectively.[27]

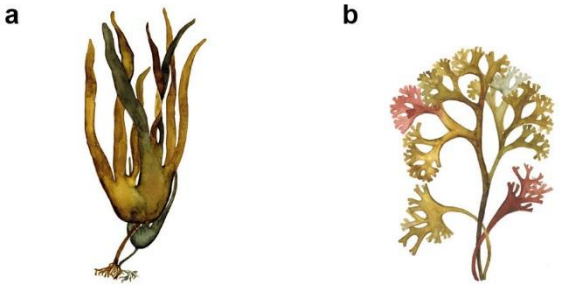

Figure 3.4, (a) Kelp and (b) Irish moss, illustrated by Miek Zwamborn[44]

Irish moss – *Crispus Chondrus*

Irish moss, also known as Carrageen, derives its name from the Irish word *carraigín*, meaning 'little rock'. It thrives on stones and rocks in tidal pools and shallow coastal waters around Ireland and Great Britain, extending along the entire European coastline. Irish moss is characterised by a basal adhesive disc from which multiple fronds emerge on flattened stems, exhibiting dichotomous branching. The fronds vary in width from millimetres to centimetres and can be either flat or curled, resembling parsley. Their coloration ranges from deep red and purple brown to yellow and green, depending on whether they are in exposed or shaded environments, respectively. Young thallus portions may display a blue iridescence, and the frond texture is membranous to coriaceous with squared tips. This perennial species can reach up to 15 cm in height, forming dense clusters that visually mimic leafless deciduous trees in winter.[44] Its chemical composition includes over 50% carbohydrate content, of which 32% is carrageenan. The protein content is around 7%, like kelp.[45]

Irish moss is a significant component in the food sector, valued for its capacity to yield carrageenan. This substance functions as a stabiliser, enhancing the texture of products such as ice cream, puddings, sausages, and ointments.[431] Historically, it was employed by beekeepers for honey clarification and by brewers to precipitate suspended solids in their brews. [44]

3.1.7 Carbon dots from kelp

A report by Zhao *et al*. details the microwave-assisted synthesis of carbon dots from seaweed.[46] Using kelp as the primary carbon source and ethylenediamine as a nitrogen dopant, the synthesised carbon dots demonstrated good water solubility and optical properties, with a UV–vis absorption peak at 282 nm and shoulder at 340 nm attributed to the π -π* transition of C=C and C=N bonds and n-π* transition of C=O, respectively.[24, 47, 48] The maximum emission was measured at 450 nm when excited at 370 nm. The study also found that the fluorescence intensity decreased with increasing pH from 3 – 8 and could be selectively quenched by Co^{2+} in a linear relationship with concentration.

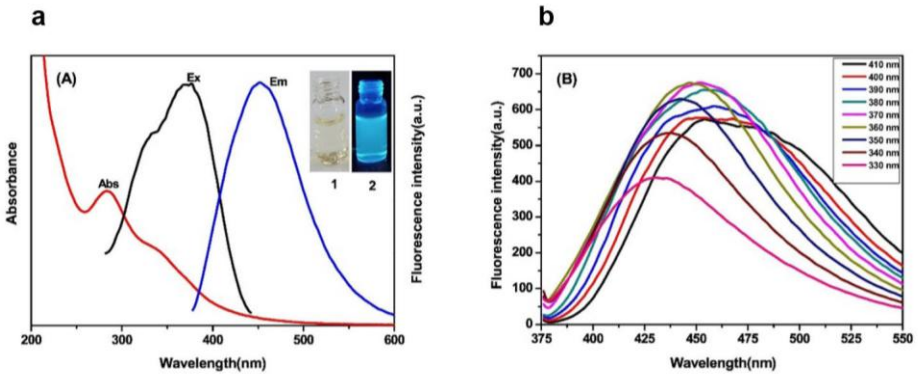

Figure 3.5, (a) UV–vis absorption (red line) and fluorescence excitation (black line) and emission (blue line) spectra of the CDs. Inset: Photographic images of CDs under (1) visible light and (2) ultraviolet light, (b) fluorescence emission spectra of CDs at different excitation wavelengths from 330 to 410 nm.[46]

The synthesis reported involved heating a mixture of kelp, ethylenediamine, and deionised water to 200 °C in 10 min using 800 W microwave irradiation. The reaction proceeded at this temperature for 1.5 h by controlling the duration of microwave irradiation. After naturally cooling to room temperature, the solution was centrifuged at 10,000 rpm, filtered through a 0.22 μm membrane, and dialysed against pure water for 12 h. It was suggested that the nutrient-rich composition of kelp including sugar, protein, fibre, mineral salts, calcium, iron, and other nutrients contributed to the favourable properties of the synthesised CDs.[46]

3.1.8 Research aims

This chapter investigates the understanding of the hydrothermal synthesis of carbon dots from biomass, with a specific focus on seaweed, a highly promising and abundant renewable resource. To comprehensively investigate the seasonal variation of the seaweed biomass and, more specifically, its saccharide content, an extensive biomass analysis was undertaken. Building upon this analysis, representative and simplified reaction systems were proposed and thoroughly evaluated to capture the intricate relations between monosaccharides, polysaccharides, and the complex biomass itself in the formation of carbon dots under hydrothermal conditions. The compelling findings derived from detailed optical and structural characterisation subsequently prompted a deeper investigation into the stability of the synthesised carbon dots in solution. The chapter culminates with a comprehensive purification and isolation study, where various separation methods are rigorously tested and optimised to significantly improve the optical properties and purity of the carbon dots in solution.

These advancements are particularly crucial given the expanding applications of carbon dots in areas such as biosensing, optoelectronic devices, and photocatalysis, where their unique properties can be fully leveraged only when characterised and isolated effectively

3.2 Experimental

3.2.1 Materials

Seaweed samples, specifically kelp and Irish moss, were harvested and supplied by Mungo Murphy's Seaweed located in Rossaveel, Galway, for this investigation. Two seasonal samples – harvested in winter and summer – of each species were collected and dried before shipping.

Standard laboratory solvents and reagents including acetonitrile D-galactose, sodium alginate, and K-carrageenan, were procured from Sigma-Aldrich, while D-glucose was obtained from Fisher Scientific. All chemical compounds were employed in their as-purchased state, without any subsequent purification. 3500 MWCO dialysis tubing, illustra NAP-10 columns, 0.22 μm nylon syringe filters, and technical grade silica (60 Å pore size, 230-400 mesh particle size, 40 – 63 μm particle size) were procured from Sigma-Aldrich. Acetonitrile was obtained through the Hazardous Materials Facility at the college.

3.2.2 Analysis of seaweed biomass

The biomass samples were submitted to Celignis for characterisation. The analysis included the process of acid-hydrolysation of the samples to measure its lignocellulosic sugar content (divided in glucan, xylan, arabinan, galactan, mannan, rhamnan). It should be noted that this process was performed on the raw sample without prior extraction, which can lead to overestimated lignin content. The samples' ash content and elemental composition (carbon, hydrogen, nitrogen, sulphur, oxygen) were also analysed, with oxygen content determined by difference.

3.2.3 Preparation of reaction mixture

Homogeneous reaction solutions were prepared by dissolving and stirring the saccharide precursors in 10 mL of distilled water, with concentrations determined by the solubility of each saccharide. This resulted in concentrations of 0.5 M D-glucose, and D-galactose, 0.05 M sodium alginate, and 0.006 M K-carrageenan. To make up the reaction mixtures for the seaweed biomasses, 1 g of ground biomass was added to distilled water, resulting in a heterogeneous mixture.

3.2.4 Hydrothermal synthesis of carbon dots

Preliminary results on the hydrothermal method with D-glucose provided suitable reaction conditions of 160 ˚C and 4 h, evaluated by the observation of photoluminescence of the sample under UV 365 nm, and no presence of precipitation formed in reaction. Higher reaction temperature and longer reaction times resulted in heterogenous samples with precipitation formed, and lower reaction temperature and shorter reaction times, yielding no or significantly reduced emissive samples.

The reaction mixtures were transferred to Teflon cups, sealed, and secured in stainless-steel autoclaves. These were then placed in a preheated oven at 160 °C for 4 h, after which the autoclaves were allowed to cool to room temperature. Subsequently, after opening the autoclaves, reactions that yielded significant solids were

centrifuged at 8000 rpm for 10 min to separate the reaction solutions from the solids before filtration with 0.22 μm nylon syringe filters. The filtered solutions, now containing the synthesised carbon dots, were stored in glass sample vials away from daylight.

3.2.5 Purification techniques

Dialysis

Following an initial 48-h dialysis using a 3500 MWCO snakeskin membrane against 800 mL of distilled water, with the water being replenished every 12 h, the retentate was kept for analysis.

Column chromatography

Column chromatography was performed using a 100 mL column packed with technical grade silica (60 Å pore size, 230-400 mesh particle size, 40 – 63 μm particle size). The mobile phase gradient was initiated with 100% acetonitrile and subsequently transitioned to an acetonitrile:water mixture of (5:1), following the methodology established by Hinterberger *et al*.[49] Fractions exhibiting fluorescence under UV light were collected, pooled, and concentrated via rotary evaporation for further characterisation.

Size exclusion chromatography

Size exclusion chromatography was conducted utilising illustra NAP-10 columns. Column preparation included removing top and bottom caps, which allowed excess liquid to drain via gravity. The column was subsequently equilibrated with 15 mL of water, allowing it to fully infiltrate the gel bed. Subsequently, 1 mL of the sample was introduced onto the column, enabling complete entry into the gel bed by gravity flow. An appropriate collection tube was positioned beneath the column, and 5 mL of water was added. The fluorescent eluent was then collected through gravity flow.

Lyophilisation

The samples underwent a freezing process at -20 °C overnight, after which they were subjected to freeze-drying under vacuum conditions (10 Pa) at -50 °C using a Labconco FreeZone Freeze Dryer for a duration of 24 h. The solid sample collected after lyophilisation was then subjected to various characterisation techniques to elucidate its physiochemical properties and structural characteristics.

3.2.6 Characterisation

The characterisation of the samples was conducted in both liquid and solid states, divided between optical and structural analyses. Optical characterisation included, UV-vis spectroscopy, and photoluminescent spectroscopy. Structural characterisation encompassed powder X-ray diffraction (XRD), Fourier transform infrared spectroscopy (FT-IR), thermogravimetric analysis (TGA), and transmission electron microscopy (TEM).

UV-vis spectroscopy

UV-Vis spectra were acquired using a Varian CARY50 UV-Vis spectrophotometer, spanning the wavelength range of 250 to 800 nm. The measurements were performed with a data interval of .5 nm, a slit width of 1

nm, and a scan speed of 240 nm/min. The instrument's lamp was changed at 326 nm, and a double-sided 10 mm quartz cuvette was utilised for the analysis.

Photoluminescent spectroscopy

Photoluminescence spectra were acquired using a HORIBA FluoroMax benchtop spectrometer. The excitation wavelengths ranged from 280 to 460 nm, and the emission wavelengths were scanned from 300 to 700 nm. To ensure a reliable signal magnitude of 10^6, the slit widths were adjusted accordingly, and measurements were conducted in a 10 mm four-sided QS High Precision Cell from Hellma Analytics.

Powder X-ray Diffraction

X-ray diffraction patterns were obtained using a Bruker D2 benchtop diffractometer, employing Cu Kα radiation and a zero-background Si sample holder. Data were collected across a 2θ range of 5 to 80°, with a step size of 0.01° and a dwell time of 0.5 seconds per step.

Fourier Transform Infrared Spectroscopy

FT-IR spectra were recorded using a Perkin Elmer Spectrum 100 instrument with Perkin Elmer Universal ATR Sampling Accessory from 4000 to 500 cm^{-1}, 25 scansin steps of 2 cm^{-1}, resolution of 10cm^{-1},

Thermogravimetric analysis

Thermogravimetric analysis was performed using a PerkinElmer Pyris 1 Thermogravimetric Analyser under a nitrogen atmosphere at 3.5 bar. Approximately 2 to 3 mg of sample was placed in a ceramic crucible and subjected to an initial hold at 30 °C for 1 min, followed by a temperature ramp to 900 °C at a rate of 10 °C/min.

Transmission electron microscopy

Transmission electron microscopy was performed by Dr. Annie Regan using a JEOL 2100 LaB TEM microscope equipped with an AMT XR50, 5k CCD camera. Samples were prepared by dispersing them in isopropyl alcohol and sonicating for 15 min. The carbon dots were then placed on lacey carbon coated copper grids and allowed to dry overnight.

3.3 Results and discussion

3.3.1 Biomass analysis

The hydrothermal synthesis of carbon dots using biomass relies on the reaction of its saccharide content. Therefore, assessing the sugar composition of the chosen biomass is essential. Four seaweed samples were analysed by Celignis for this purpose: two samples of brown seaweed, Laminaria digitata – Kelp, and two samples of Chondrus crispus – Irish moss, one sample of each collected in summer and the other in winter. The findings regarding their sugar content are presented below.

Table 3.2, Summary Biomass Content, measured in triplets

(% of total dry matter)	Kelp winter	Kelp summer	Irish moss winter	Irish moss summer
Total Sugars	47.43 ± 0.66	60.73 ± 0.50	29.88 ± 0.32	30.91 ± 0.10
Glucan	7.86 ± 0.23	21.61 ± 0.06	4.40 ± 0.03	4.28 ± 0.04
Xylan	0.51 ± 0.02	0.37 ± 0.00	0.76 ± 0.04	0.77 ± 0.00
Mannan	0.71 ± 0.03	0.44 ± 0.00	0.35 ± 0.04	0.51 ± 0.00
Galactan	0.89 ± 0.05	0.91 ± 0.04	23.87 ± 0.44	24.88 ± 0.13
Mannuronic Acid	23.12 ± 0.04	11.83 ± 0.06	-	-
Guluronic Acid	8.22 ± 0.21	4.50 ± 0.06	-	-
Mannitol	3.20 ± 0.07	17.79 ± 0.19	-	-
Fucose	2.13 ± 0.05	2.71 ± 0.04	-	-
Ash	31.37 ± 0.07	19.53 ± 0.33	18.81 ± 0.08	21.38 ± 0.54

3.3.2 Kelp biomass analysis

The brown seaweed, Kelp, demonstrated a notably high sugar content with measurements of 47% and 61% saccharides for its winter and summer harvests, which reflects the preservation and growth of the seaweed respectively. This increase in sugar content appears in tandem with a decrease in ash content, from 31.4% in winter to 19.5% in summer.

The sugar yield from kelp resulted in the preference for the summer harvest, due to its increased sugar content. The sugar composition for both harvests was primarily characterised by Glucan, Mannuronic acid, Guluronic acid, Mannitol, and Fucose, albeit with differing contributions. In the winter harvest, these components represented 16.6%, 48.8%, 17.3%, 6.7%, and 4.5% respectively, totalling 93.9% of the sugar

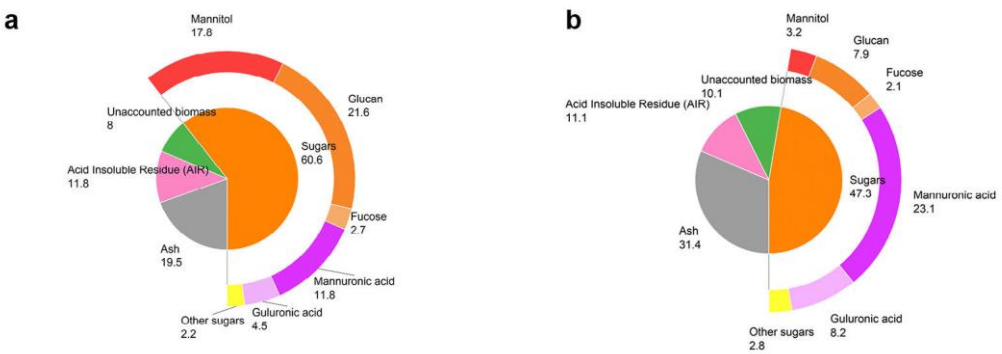

Figure 3.6, Biomass content of Kelp, harvested in summer (a), and winter (b)

content. For the summer harvest, the respective percentages were 35.6%, 19.5%, 7.4%, and 29.3%, accounting for 96.3% of the total sugar content. A decrease in Glucan was simultaneous to the increase in mannuronic and guluronic acids, the building blocks for alginate. In winter alginate makes up most of the sugar content, but in summer, more small sugars are available. The ratio of mannuronic and guluronic acids (M:G) was measured 1:2.62 and 1:2.82 in summer and winter respectively. A high guluronic acid content are stiffer and result in stronger gels, while high mannuronic content results in more flexibility and lead to softer gels.[50]

Thermal analysis revealed a C/H/N/S molar ratio of 1.00/0.11/0.09/0.04 for the winter harvest and 1.00/0.12/0.03/0.03 for the summer harvest. In comparison to the winter harvest, the summer harvest exhibited a 13% increase in elemental hydrogen, coupled with a 59% and 12% reduction in elemental nitrogen and sulfur, respectively. The same trend in big and small sugars between summer and winter is observed in the elemental ratios, where in winter higher values of nitrogen and sulfur are present, and in summer this is reduced and replaced for an increased hydrogen content.

In conclusion, the summer sample of kelp presented with a higher overall saccharide content, and more small sugars. Not only is the amount of alginate reduced compared to the winter sample, but changes in the mannuronic to guluronic acid ratio of the alginate content also render the kelp more flexible in summer. . Lastly, the elemental content of nitrogen is heavily reduced with 59% compared to the winter sample. Based on these findings it was decided to continue with the summer sample for the investigation, prioritising total saccharide content over alginate and nitrogen content.

3.3.3 Irish moss biomass analysis

The red seaweed, identified as Irish moss, exhibits a sugar content of approximately 30% of its total dry matter, with an ash content ranging from 19% to 21%. The reduced saccharide content compared to literature, ~50% could be explained by nutrient availability and habitat, or the sexual stage of harvested plants.[51] This is also reflected in the unaccounted biomass component, taking up > 33% and < 10% for the red and brown seaweed respectively. A marginal preference is observed for the summer harvest due to its slightly higher sugar content (30.9%) compared to the winter harvest (29.9%). Harvested in summer, Glucan and Galactan represent the most substantial sugar components, contributing 14% and 80% of the total sugar content, respectively. The remaining sugars comprises of other pentoses, hexoses, and uronic acids.

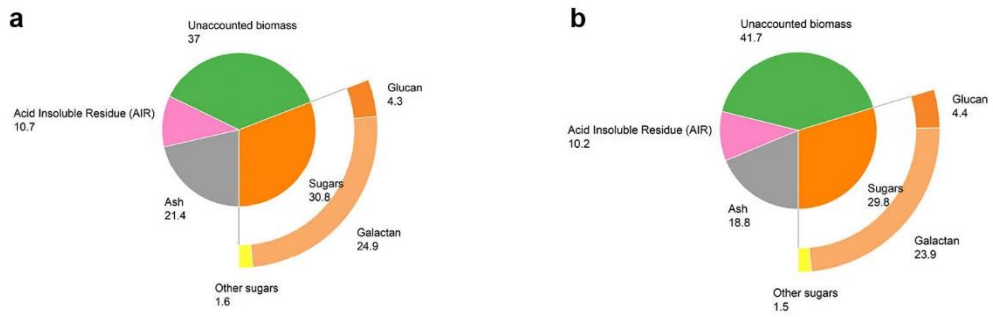

Figure 3.7, Biomass content of Irish moss, harvested in summer (a), and winter (b)

The ash content was marginally higher in the summer (21.4%) compared to the winter sample (18.8%). Regarding elemental composition, the C/H/N/S ratio of the summer sample was determined to be 1.00/0.12/0.09/0.19. This composition was the same in the winter sample, except for the nitrogen ratio, which showed an 11% increase resulting in the ratio 1.00/0.12/0.10/0.19. Overall, the summer and winter sample presented with minimal differences in biomass content, with marginally higher saccharide and ash content in the summer sample, and reduced unaccounted biomass, and nitrogen content. The summer sample was taken further into this investigation.

Comparing the findings between kelp and Irish moss, it was concluded that kelp exhibited a significantly higher sugar content, ranging from 57% to 100% more than Irish moss. Furthermore, substantial differences in biomass content were observed for kelp between summer and winter harvests, a variation not evident in Irish moss. Despite these seasonal fluctuations, the summer harvest was consistently chosen for both species for the subsequent investigation, ensuring uniformity in the experimental setup.

3.3.4 Selection of saccharides for simplified reaction systems

To gather insight into carbon dot formation from carbohydrates in seaweed biomass, it was proposed to investigate three sets of sugar precursors. The biomass, a polysaccharide, and a monosaccharide, representative of the brown and red seaweed selected. By reducing the complexity of the precursor in each system, a simplified, yet representative reaction system is investigated. First, the biomass reaction will provide a baseline of the naturally available saccharide-rich resource. Second, the most prominent polysaccharide content of the seaweed selected, based on literature and the biomass analysis. Lastly, the monosaccharide of which the selected polysaccharide is made up of will provide the most simplified yet representative reaction system for the hydrothermal synthesis of carbon dots.

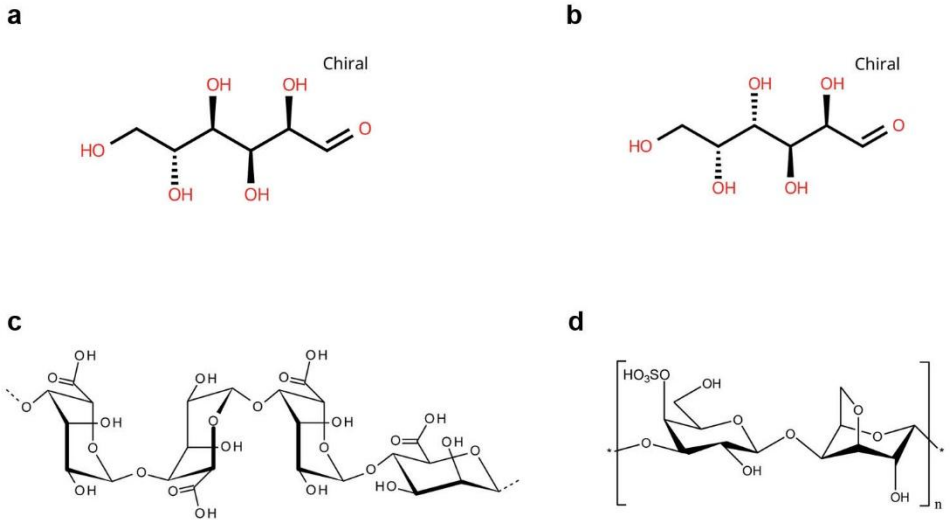

Figure 3.8, Molecular structure of D-glucose (a), D-galactose (b), alginate (c) and carrageenan (d).

From literature,[27, 45, 51] and the biomass analysis it is confirmed that alginate is most prominent polysaccharide in kelp, and carrageenan in Irish moss. Considering the reported polysaccharides are limited to Glucan and Galactan in the sugar content analysis provided by Celignis, it can be deducted that these polysaccharides of glucose and galactose, respectively, represent the presence of alginate and carrageenan.

However, it should be taken into consideration that alginate is built up by uronic acids with functional carboxyl groups, and carrageenan includes sulphated units.

Table 3.3, The six precursors selected for the representative reaction systems to investigate the hydrothermal synthesis of carbon dots from seaweed.

	Brown seaweeds	Red seaweed
Biomass	Kelp	Irish moss
Polysaccharide	Alginate	Carrageenan
Monosaccharide	D-glucose	D-galactose

3.3.5 Optical characterisation of as prepared carbon dots from brown seaweed

In the biomass analysis given in section 3.3.1, the brown seaweed Kelp proved more carbohydrate rich than the red seaweed, Irish moss. Therefor investigation started with saccharides D-glucose, Alginate, and seaweed Kelp as precursors for hydrothermal reaction.

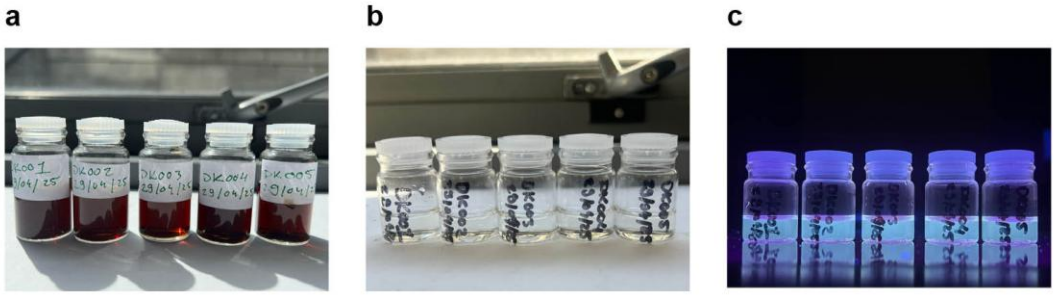

Figure 3.9, Reaction solutions of hydrothermal reaction of D-glucose, (a) as-prepared, (b) diluted to 0.1 A, and (c) under UV 365 nm

The as-prepared carbon dots from D-glucose resulted in a transparent but dark brown, amber homogeneous solution. The reaction solution was diluted to 0.1 A, suitable for photoluminescence characterisation and resulted in the following spectra. In Figure 3.10 (a), the absorbance (green), excitation (turquoise) and emission (blue) spectra are given together. The absorbance spectrum provides a strong peak at 283 nm associated with π-π∗ transition of sp^2 hybridised carbon atoms including C=C and C=N bonds.[24, 47, 48, 52] A tail is extended into the visible region up to 500 nm. To gain information into the emissive properties of the carbon dots, a systematic approach of recording the emission spectra with λ_{ex} 280 – 480 nm with 10 nm steps was taken, shown in Figure 3.10 (b). Excitation at λ_{ex} 340 nm, resulted in the highest emission intensity at $\lambda_{em,\,max}$ 414 nm. Additionally, a sharp shoulder/peak at 388 nm was recorded due to Raman scattering.[53] The excitation spectrum was recorded between $\lambda_{coll.}$ 280 – 420 nm, with emission wavelength set to $\lambda_{em,max}$ 414 nm. This resulted in $\lambda_{ex,coll.}$ 332 nm, with a Stoke's shift of 131 nm and a mirror-image observed between the excitation and emission spectra.

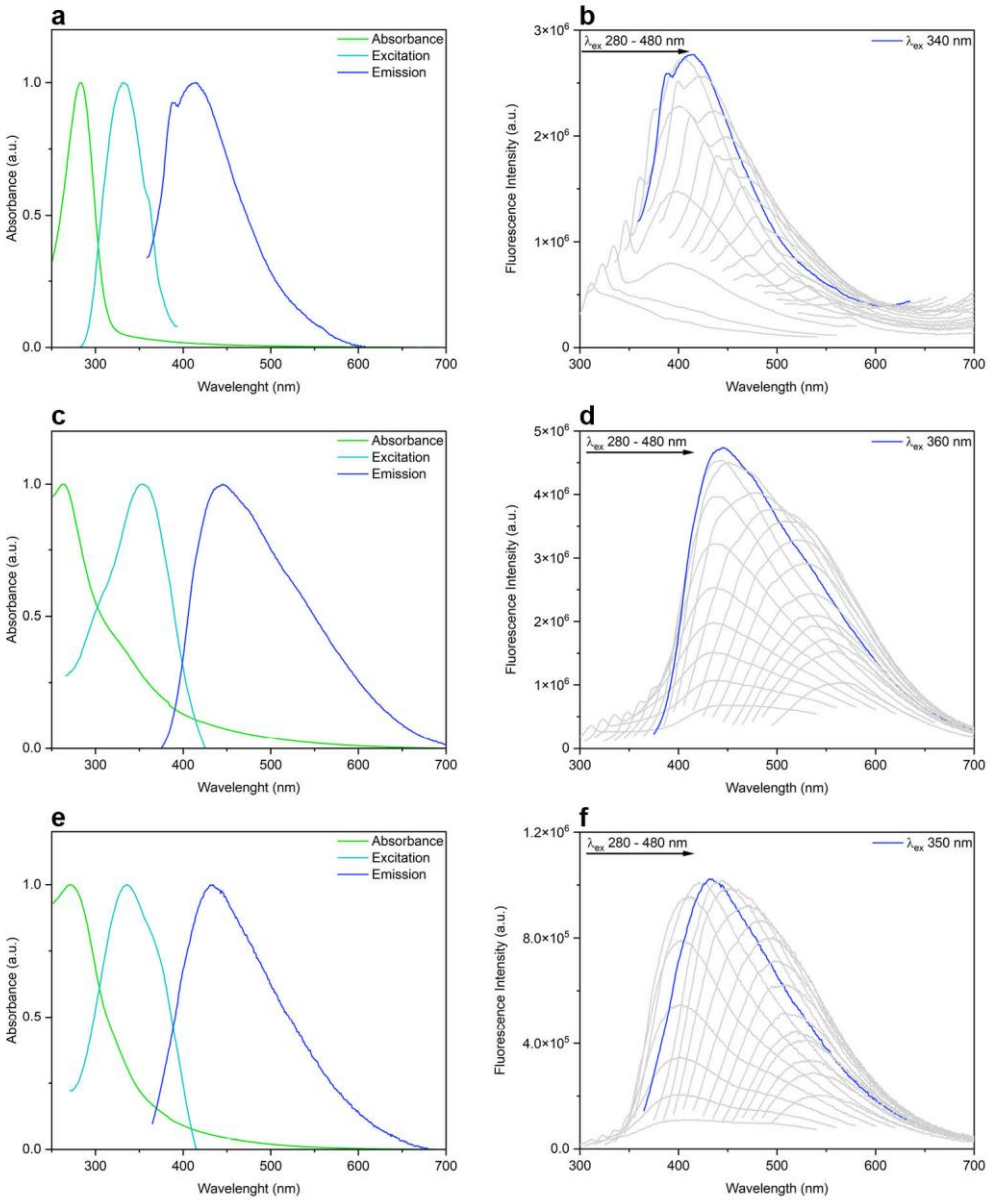

Figure 3.10, Absorbance, excitation, and emission spectra and emission spectra with λ_{ex} 280 – 480 nm with 10 nm step increase and highest emission spectrum highlighted in blue of the as-prepared carbon dots from hydrothermal synthesis with D-glucose (a) abs/ex/em, (b) λ_{ex} 280 – 480 nm, Alginate (c) abs/ex/em, (d) λ_{ex} 280 – 480 nm, and Kelp (e) abs/ex/em, (f) λ_{ex} 280 – 480 nm

Table 3.4,Overview of the optical characteristics as prepared carbon dots from D-glucose, Alginate, and Kelp

Precursor	$\lambda_{abs.}$ (nm)	$\lambda_{ex,max.}$ (nm)	$\lambda_{em,max.}$ (nm)	$\lambda_{ex,coll.}$ (nm)
D-glucose	283	340	414	332
Alginate	264/328	360	445	335
Kelp	271	350	434	336

Secondly, the optical characterisation of the carbon dots produced from polysaccharide alginate are shown in in Figure 3.10 (c). the absorbance spectrum shows rather a slope-shaped curve with a broad absorption peak, resulting in a maximum at λ_{abs} 264 nm and shoulder at 328 nm. The appearance of the second shoulder is representative for the introduction of n-π∗ transition caused by C=O bonds in the molecular structure.[52] λ_{ex} 360 nm resulted in the spectrum with the highest emission intensity, with $\lambda_{em,max}$ 445 nm highlighted in blue

in (d). The excitation and emission spectra also present with a shoulder at λ_{ex} 300 nm and λ_{em} 530 nm. This might be caused by the introduction of the carboxyl groups in the carbon dots structure. Collecting the corresponding excitation spectrum resulted in $\lambda_{ex,collected}$ 335 nm.

The optical characterisation of kelp carbon dots is shown in Figure 3.10 (e) and (f). A slope-shaped absorption curve with a peak at 271 nm is visible, with a broad peak into the visible spectra. The excitation and emission spectra of the Kelp CDs showed that using λ_{ex} 350 nm produced the $\lambda_{em,\,max}$ at 434 nm. This emission wavelength was taken to collect the excitation spectrum, resulting in $\lambda_{ex,collected}$ at 336 nm. A shoulder in the excitation spectrum was measured at 370 nm, however, when exciting at λ_{ex} 370, this resulted in no obvious changes to the emission spectrum, as can be seen in (f). Additionally, a relative strong secondary emission peak at longer wavelength is visible when using $\lambda_{ex} < 336$ nm, with λ_{em} 480.

Comparing the optical characterisation between the three reaction systems of D-glucose, alginate and kelp, the following is observed. The biggest shift in optical properties was measured between D-glucose and alginate, for $\lambda_{abs.}$, $\lambda_{ex,max.}$ and $\lambda_{em,max}$ It is theorised that using a more complicated precursor, alginate instead of glucose, has resulted in the formation of a carbonyl group in the molecular structure, expressed in a shoulder in the absorption spectrum. The presence of the carbonyl groups in the carbon dots might also explain the hypsochromic shift due to delocalisation of electrons on the oxygen atom into the π^* orbital of a neighbouring carbonyl group.[54] The spectra of alginate and kelp carbon dots present with broader excitation and emission spectra, and the Raman scattering identified in the D-glucose reaction was removed for the more complicated precursors. In addition to that, the seaweed system exhibited optical spectra with properties intermediate to those of glucose and alginate with the absorption and excitation peak directly in between the respective peaks of D-glucose and alginate. The absorption spectrum did not display a second shoulder unlike the alginate absorption spectrum. However, the absorption plot's curve exhibited a broader profile, aligning more closely with the alginate carbon dots than the distinct absorption peak and sharp decline observed in the D-glucose reaction. An explanation could involve the sugar content beyond alginate and glucose, including mannitol, as seen in the complete sugar content of kelp.

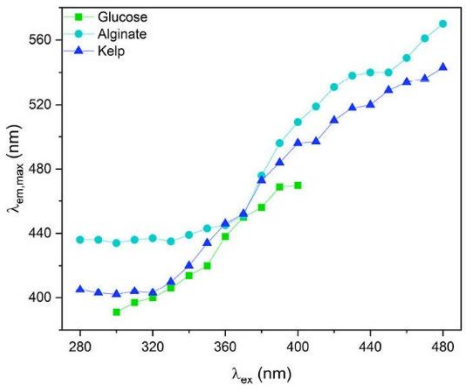

Figure 3.11, Excitation wavelength against maximum emission wavelength of as prepared carbon dots from Glucose (green), Alginate (turquoise), and Kelp (blue)

Observed in different degrees of extent between the precursors is excitation dependent and independent behaviour in the photoluminescence spectra of the carbon dots. When observing the D-glucose carbon dots only excitation dependent emission is apparent, shown in Figure 3.11 in green. However, the alginate and kelp carbon dot spectra, when exciting below the $\lambda_{ex,max}$ of 360 and 350 nm, the emission spectra appears

excitation independent emission, producing the $\lambda_{em,max}$ of 440 and 400 nm. However, when applying excitation wavelengths over the $\lambda_{ex,max}$, the emission spectrum display excitation dependent emission, increasing from 450 to 570, and 420 to 540 nm respectively. This phenomenon is captured in Figure 3.11 in turquoise and blue, whereby kelp and even more strongly alginate exhibit this excitation independent emission at low wavelengths. This observation conforms to the literature on the optical characterisation of carbon dots, introducing the threshold wavelength, or λ_{th}, whereby carbon dots exhibit excitation energy independent emission below λ_{th}, and above this threshold the emission becomes excitation dependent. Correlation between the λ_{th} and the $\lambda_{ex,max}$ is established and suggests a common origin of light emission in carbon dots. It is possible that electronic transitions associated with band-to-band transitions of the carbonic core result in emission that is independent of excitation, while transitions influenced by oxygen-related surface and edge states are responsible for excitation-dependent photoluminescence.[55]

3.3.6 Optical characterisation of as prepared carbon dots from red seaweed

The hydrothermal synthesis of carbon dots from D-galactose resulted in the following optical spectra, shown in Figure 3.12 (a) and (b). λ_{abs}, λ_{ex} and $\lambda_{em,\ max}$ were measured 284, 350, and 438 nm respectively, as can be seen in (a). The sharp peaks in the excitation and emission are caused by Raman scattering. Collecting the excitation spectrum for $\lambda_{em,max}$ $\lambda_{ex,coll.}$ 342 nm was measured. Analysis of the emission spectra collected from λ_{ex} 280 – 480 nm reveals excitation-independent emission below λ_{th}, resulting in λ_{em} 420 nm. Excitation-dependent emission is observed over λ_{th}, shifting from λ_{em} 435 – 540 nm with λ_{ex} 350 – 480 nm. A broad emission peak is present at lower excitation wavelengths, sharpening towards λ_{th} and enhancing the emission intensity at λ_{th}. The shoulder in the emission spectra for λ_{ex} 440 – 480 should not be confused with the Raman scattering of the sample, which is removed for λ_{ex} 280 – 430 nm, but included here as they present at the same wavelengths.

The hydrothermal synthesis of carbon dots from carrageenan produced the following optical properties, as seen in Figure 3.12 (c), λ_{abs} was measured 283 nm, without additional absorption events. In the excitation and emission spectrum, $\lambda_{ex,max}$ 350 nm and $\lambda_{em,max}$ 437 nm were measured. Collecting the excitation spectrum with $\lambda_{ex,max}$ was measured at 329 nm. In figure (d), the carrageenan CDs were excited from λ_{ex} 280 – 480, λ_{th} was identified at 330 nm, and exciting at this wavelength or shorter, excitation independent emission at λ_{em} 430 nm was measured. At longer excitation wavelengths, the emission max was linearly related to the excitation wavelength, depicted in Figure 3.13. Again, the Raman scattering is removed from data to increase readability of the graph for λ_{ex} 280 – 370 nm.

In Figure 3.12 (e) the optical properties of the CDs from the red seaweed Irish Moss are given. The λ_{abs} measured was 283 nm, The Raman scattering is minimal the excitation and emission spectra. The λ_{ex} 340 yielded the highest emission intensity at $\lambda_{em,max}$ 425 nm. Collecting the excitation spectrum for this wavelength produced $\lambda_{ex,max}$ 331 nm. The progression of the emission spectra from λ_{ex} 280 – 480 nm as shown in figure (f). The excitation independent emission is observed at λ_{em} 405 nm. The excitation dependent emission is minimalised below the λ_{th} but exhibits a linear red shift with λ_{ex} 340 – 480, from λ_{em} 425 – 550 nm.

To compare the optical spectra of D-galactose, carrageenan, and Irish moss, it is important to highlight the remarkable resemblance among their spectra. Both the shape and peak position of the absorption, excitation, and emission spectra exhibit close similarities, providing strong evidence of shared optical properties, and material produced in reaction.

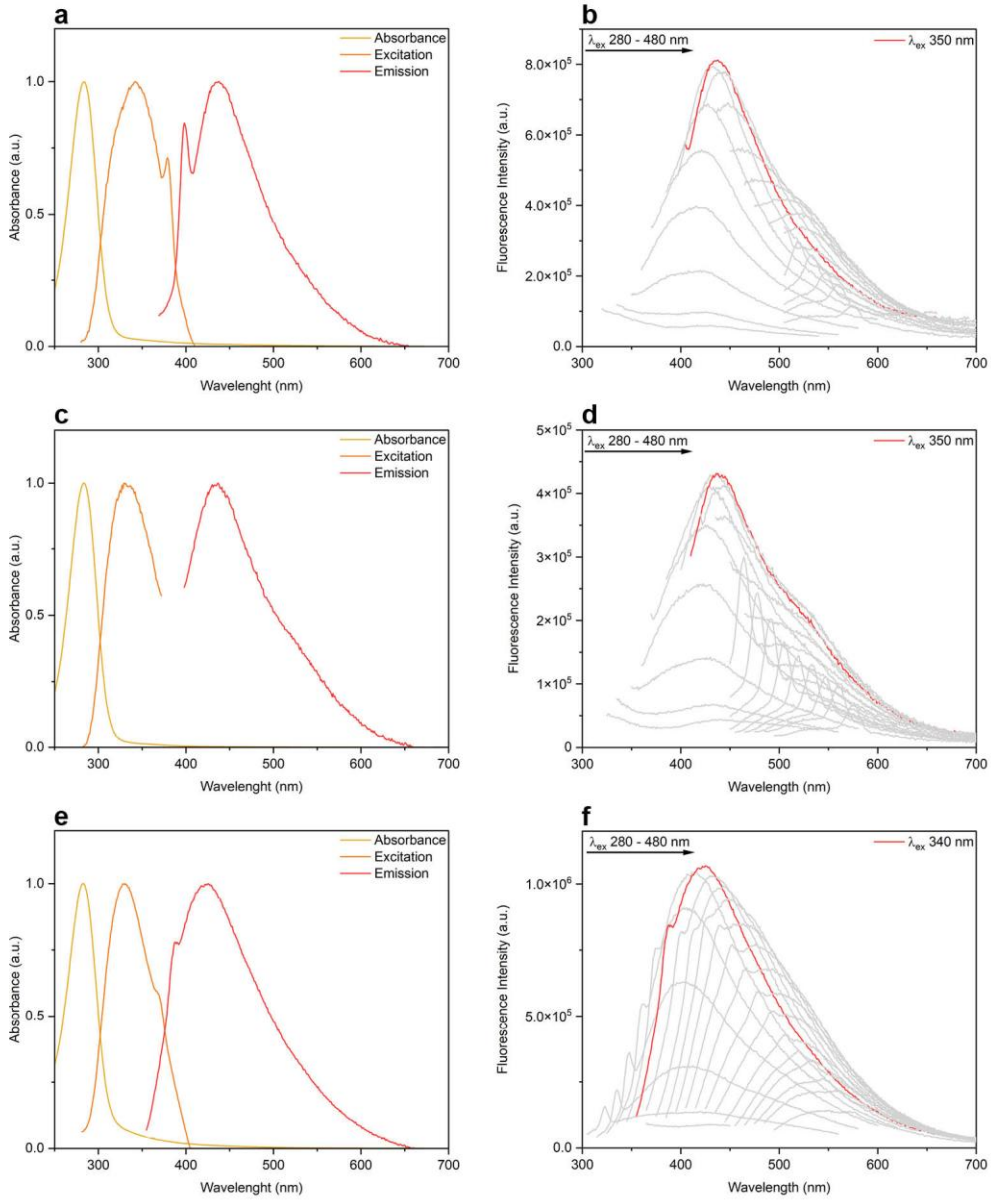

Figure 3.12, Absorbance, excitation, and emission spectra and emission spectra with λ_{ex} 280 – 480 nm with 10 nm step increase and highest emission spectrum highlighted in red of the as-prepared carbon dots from hydrothermal synthesis with D-galactose (a) abs/ex/em, (b) λ_{ex} 280 – 480 nm, Carrageenan (c) abs/ex/em, (d) λ_{ex} 280 – 480 nm, and Irish moss (e) abs/ex/em, (f) λ_{ex} 280 – 480 nm

Table 3.5, summary optical characteristics as prepared carbon dots from D-galactose, Carrageenan, and Irish moss

Precursor	$\lambda_{abs.}$ (nm)	$\lambda_{ex,max.}$ (nm)	$\lambda_{em,max.}$ (nm)	$\lambda_{ex,coll.}$ (nm)
D-galactose	284	350	438	342
Carrageenan	283	350	437	329
Irish moss	283	340	425	331

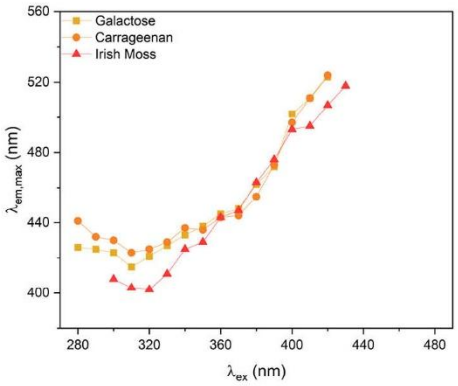

Figure 3.13, Excitation wavelength against maximum emission wavelength of as prepared carbon dots from Galactose (yellow), Carrageenan (Orange), and Irish moss (red)

3.3.7 Evaluation of the proposed reaction system

To evaluate the proposed reaction systems, the optical properties of the spectra produced within the brown and red seaweed systems are discussed below, specifically examining their relationships.

Considering the brown seaweed selected precursors, the properties of alginate CDs resemble those of kelp CDs closely with a curve sloped absorbance with a shoulder/broadness around 330 nm and presents in the wide and mirroring excitation and emission spectra. However, the optical characterisation of CDs from D-glucose resemble the more complex precursors less so. This is explained through the molecular structure of alginate, which are uronic acids, not simple sugars and not D-glucose. The presence of carboxyl groups in uronic acid provides the changes in optical properties including the n-$\pi*$ transitions presented in absorption at 330 nm. It can be concluded that alginate provides a good candidate for a precursor in a simplified reaction system for the brown seaweed Kelp, while D-glucose provides a poor candidate.

The proposed reaction system for the red seaweed, produced similar optical characteristics for all precursors investigated. This suggests polysaccharide and monosaccharides Carrageenan and D-galactose respectively provide a good reflection of the Irish moss as biomass, regardless of introduction of sulphated galactose units at the polysaccharide level. Both saccharides provide a simplification of the reaction system, while performing like the material produced from Irish Moss.

3.3.8 Stability study of carbon dots

Observations indicated a significant presence of residual free sugars in the reaction mixture following hydrothermal treatment, evidenced by the sugary/caramel aroma detected upon opening reactor autoclaves or stored samples, and the inevitable microbial proliferation in the stored samples. Furthermore, the gradual formation of precipitate at the bottom of stored samples over time suggested poor stability in aqueous solution, a phenomenon consistent with findings reported in existing literature.[56] A stability study was launched to investigate how the aqueous stability affects the carbon dots and how to remove free sugars from them. The study included three parts:

Firstly, a time study was performed in which all carbon dots in solution were monitored for two to four weeks through characterisation of UV-vis absorbance and photoluminescence emission. Secondly, the carbon dots in the solution underwent dialysis. As previously mentioned in the introduction, dialysis is a size-exclusion separation technique that employs a semipermeable membrane to eliminate small molecules. This method is frequently utilised in carbon dot isolation processes to remove minor impurities and salts, both of which are pertinent to our marine-derived precursor.[25] Finally, the dialysate was also subjected to the time study, with an investigation into the impact of dialysis on both the optical properties and the stability of the carbon dots.

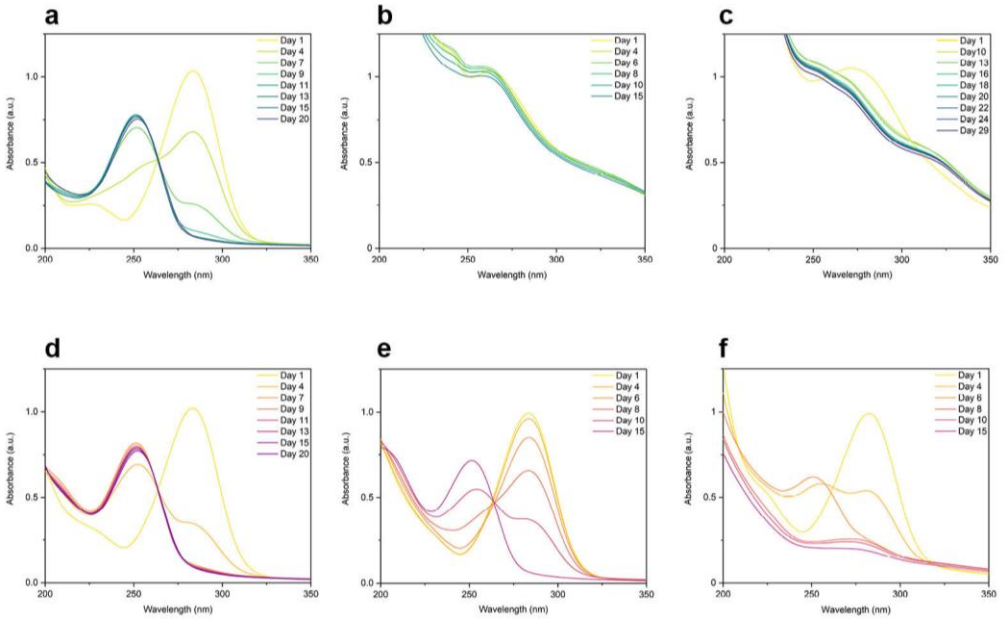

Figure 3.14, Absorbance spectra over time for as prepared carbon dots from D-glucose (a), alginate (b), kelp (c), D-galactose (d), carrageenan (e), and Irish moss (f).

Analysis of the absorbance plots for carbon dots derived from D-glucose and D-galactose, shown in Figure 3.14 (a) and (d) respectively, revealed an isosbestic point at 265 nm, indicating an equilibrium between two interconverting species.This is supplemented by the hypsochromic shift in absorbance peak over time. The peak moved from 283 nm to 250 nm, accompanied by a decrease in intensity. In the as-prepared samples, changes for D-glucose became negligible after 11 days, whereas those for D-galactose did so within 7 days , which is clarified in Figure 3.15 (a) and (d), respectively. This observed blue shift in absorbance suggests an increase in the energy of absorbed photons. In carbon dots, a blue shift can be attributed to the aggregation of particles, forming larger clusters due to van der Waals forces at high concentrations. This aggregation subsequently leads to the formation of precipitates and a reduction in CD concentration within the solution. Conversely, at lower concentrations, these clusters disperse, resulting in a decrease in particle size.[56-58]

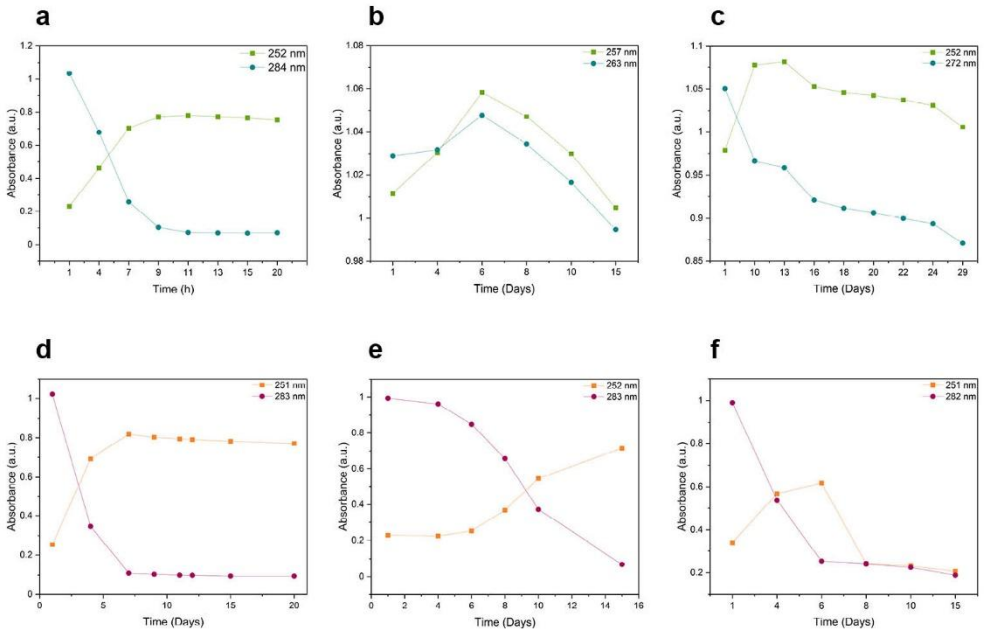

Figure 3.15, UV-vis absorption measured at distinct wavelengths over time of as prepared CDs from D-glucose (a), alginate (b), kelp (c), D-galactose (d), carrageenan (e), and Irish moss (f).

In the case of polysaccharide samples, carrageenan carbon dots mirror the temporal progression and isosbestic point observed in monosaccharides, aligning with the sugar's molecular structure. Nevertheless, the duration required to attain the shifted and diminished absorption peak is prolonged, necessitating two weeks for a complete reduction in absorption at 283 nm and its transformation into a singular absorption peak at 250 nm. Alginate carbon dots exhibit minimal alterations in UV-Vis spectra over time, displaying only a slight overall decrease in absorption across the spectrum, this can however not be compared to the change in intensities of carrageenan and the monosaccharides since the absorption spectra presents distinct to the one from alginate.

The carbon dots derived from kelp exhibited optical properties like those of the alginate sample, particularly on day 1 of measurements, where a reduction in absorption at 271 nm was observed compared to day 10. In contrast, the Irish Moss sample initially resembled the carrageenan and D-galactose samples on day 1, but over an 8-day period, its spectral characteristics progressively evolved to align with those of kelp, displaying a curve-slope with an absorption shoulder at 272 nm.

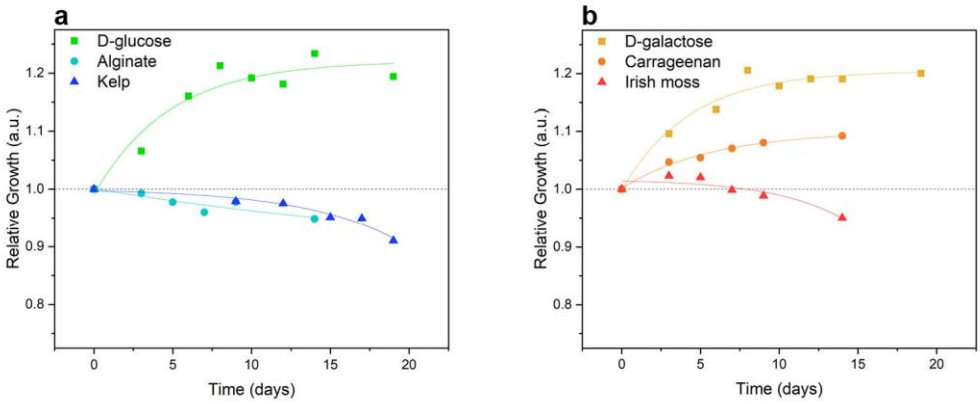

Figure 3.16, Change in photoluminescence intensity over time for as prepared carbon dots from brown seaweed and seaweed derivatives (a) and red seaweed (b), of D-glucose (green), Alginate (turquoise), Kelp (blue) D-galactose (yellow), Carrageenan (orange), and Iris

In addition to the absorption, the photoluminescence intensity was monitored over time as well, depicted in Figure 3.16. The emission intensity was monitored by exciting at the identified $\lambda_{ex,max}$. The temporal study revealed an increase in photoluminescence emission for D-glucose, D-galactose, and carrageenan. Conversely, more complex precursors such as alginate, kelp, and Irish moss exhibited a gradual decrease in fluorescence. Notably, both UV-Vis absorption has achieved stabilisation within the same timeframe, however the photoluminescence has not. The observed increase in photoluminescence intensity could be attributed to aggregation-induced emission, a phenomenon where aggregation restricts the mobility and rotation of molecules or surface functional groups within the carbon dot structure. This restriction inhibits non-radiative decay pathways, thereby promoting the emission of light from the excited state and leading to enhanced fluorescence.[59]

The temporal study of D-glucose's photoluminescence spectrum revealed an increase in intensity over the initial 7 days, after which the changes were reduced to a minimum. Concurrently, the absorption intensity at 250 nm exhibited a similar pattern, increasing until day 7 and then stabilising from day 9 onward. This trend was also observed in D-galactose and carrageenan. Conversely, alginate and kelp displayed a minor decrease in PL over time, mirroring a reduction in overall absorption. Notably, the PL over time plot for Irish moss showed an initial increase up to day 5, subsequently followed by a decrease. An analogous trend was observed in the absorption over time plot at 250 nm, where an initial intensity increase preceded a subsequent reduction.

From this temporal study, it is concluded that the colloidal carbon dots undergo post-reaction processes affecting the optical properties, suggesting aggregation and concentration effects at play. This brings into focus the critical role of concentration and interparticle interactions in governing the optical properties and colloidal stability of carbon dots over time, consistent with challenges in achieving monodispersity and sufficient zeta potential. Moreover, the direct correlation between absorption intensity at 250 nm and maximum photoluminescence intensity links these properties to the degree of carbonisation and surface functional groups formed during and after hydrothermal processing.

3.3.9 Dialysis of carbon dots from brown seaweed

Subsequently, the carbon dots, synthesised via the hydrothermal method, underwent dialysis directly after opening the autoclaves. The resulting retentate was then subjected to optical characterisation, consistent with the analysis performed on the as-prepared carbon dot solutions.

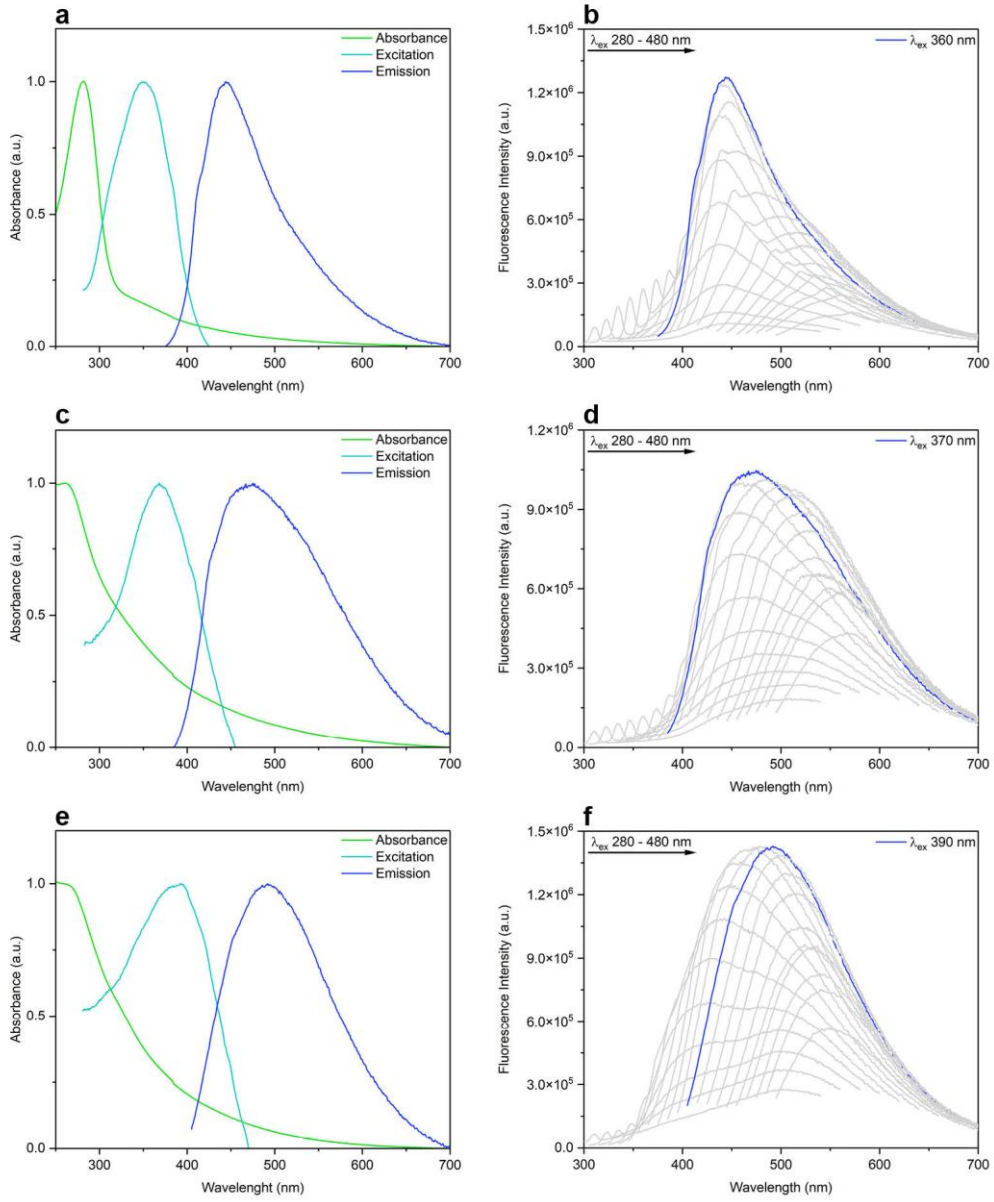

Figure 3.17, Absorbance, excitation, and emission spectra and emission spectra with λex 280 – 480 nm with 10 nm step increase and highest emission spectrum highlighted in blue of the dialysed carbon dots from hydrothermal synthesis with D-glucose (a) abs/ex/em, (b) λ_{ex} 280 – 480 nm, Alginate (c) abs/ex/em, (d) λ_{ex} 280 – 480 nm, and Kelp (e) abs/ex/em, (f) λ_{ex} 280 – 480 nm

In Figure 3.17 (a) the absorbance of the dialysed CDs shows a strong absorption peak with λ_{abs} 282 nm similar to the as-prepared sample, but the sharp profile of the absorption peak morphs into a sloped curve towards the visible region and extends up to 700 nm. In figure (b), $\lambda_{ex,max}$ 360 nm produced the highest emission intensity at $\lambda_{em,max}$ 444 nm. However, the collected excitation spectrum for λ_{em} 444 nm produced $\lambda_{ex,collected}$ at 350 nm. A second shoulder in the absorption spectrum is observed. The increase in the tail into the visible light relative to the strong absorption peak, and the presence of the shoulder at 350 nm, might be

explained by the effect of the dialysis method, in which impurities and small molecules are removed from the reaction solution, increasing the relative concentration of CDs to impurities in solution. A second explanation could be the aggregation tendency of carbon dots in aqueous solution. By creating larger clusters in solution, their absorption and emission spectra broaden and begin to overlap, leading to self-absorption and inner filter effects, through reabsorption of emitted photons or the absorption of excitation light in the aggregates, which can cause a redshift, also observed in the spectra.[60]

Table 3.6, summary overview optical characteristics dialysed carbon dots from D-glucose, Alginate, and Kelp

Precursor	$\lambda_{abs.}$ (nm)	$\lambda_{ex,max.}$ (nm)	$\lambda_{em,max.}$ (nm)	$\lambda_{ex,coll.}$ (nm)
D-glucose	282	360	444	350
Alginate	260	370	475	368
Kelp	260	390	492	393

Considering the dialysed CDs produced from alginate, shown in Figure 3.17 (c) and (d) the spectra resemble the ones from the as-prepared CDs. λ_{abs} measured 260 nm, with a sloped curve into the visible light range. The maximum emission was measured with $\lambda_{ex,max}$ 370 nm, at $\lambda_{em,max}$ 475. Collecting the excitation spectrum yielded $\lambda_{aex,coll.}$ 368, consistent with the found $\lambda_{ex,max}$. However, when compared to the as prepared optical characterisation, the purified samples show peak broadening and a red shift in excitation and emission of 10 and 30 nm, respectively.

The dialysed kelp CDs compares in UV-vis spectra with the dialysed alginate CDs in shape of the absorption curve and λ_{abs} 260 nm. However, considering the excitation and emission properties, a red shift of ~ 20 nm observed, with λ_{ex} 390 nm, $\lambda_{em,max}$ 492 nm, and $\lambda_{ex.col}$ 393 nm. The difference between the as prepared and dialysed CDs from kelp is even bigger, since the as prepared CDs were blue shifted compared to their alginate counterpart, and the dialysed CDs are red shifted compared to the alginate counterpart. This disparity arises primarily from the most pronounced differences in material composition, degree of carbonisation, and surface functional groups among the synthesised carbon dots, which are rendered more evident following purification.

3.3.10 Dialysis study of carbon dots from red seaweed

Following the hydrothermal synthesis, carbon dots derived from D-galactose, carrageenan, and Irish moss underwent dialysis and subsequent optical characterisation, shown in Figure 3.18. A significant reduction in Raman scattering within the spectra was observed across all precursors.

In Figure 3.18 (a) the absorption peak was measured at λ_{abs} 281, comparable to the spectrum of the as-prepared carbon dots. A second shoulder in absorption was measured at λ_{abs} 350 nm, and an increased tail into the visible region up to 500 nm is visible. The λ_{ex}, $\lambda_{em,max}$, and $\lambda_{ex.col}$ measured 360, 445,and 346 nm, respectively. A minimal red shift of ~ 10 nm was observed compared to the as prepared dots.

The polysaccharide carbon dots from carrageenan resemble the spectra of the as prepared carrageenan dots and both D-galactose samples closely, as depicted in Figure 3.18 (c). The λ_{ex}, λ_{ex}, $\lambda_{em,max}$, and $\lambda_{ex.col}$ measure

284, 360, 445,and 342 nm, respectively. While the carrageenan as prepared sample was slightly blue shifted compared to D-galactose, the dialysed samples' optical properties are almost identical.

The carbon dots from the Irish moss purified by dialysis provide a significant change compared to the as-prepared sample. Shown in Figure 3.18 (e) and (f), the λ_{abs} peak measures 281 nm, the strong absorption peak is replaced by a slope-curve, with shoulder at λ_{abs} 333 nm familiar from the alginate and kelp data. The tail into the visible range is extended from 450 – 620 nm. The λ_{ex}, $\lambda_{em,max}$, and $\lambda_{ex.col}$ measured 370, 459,and 362

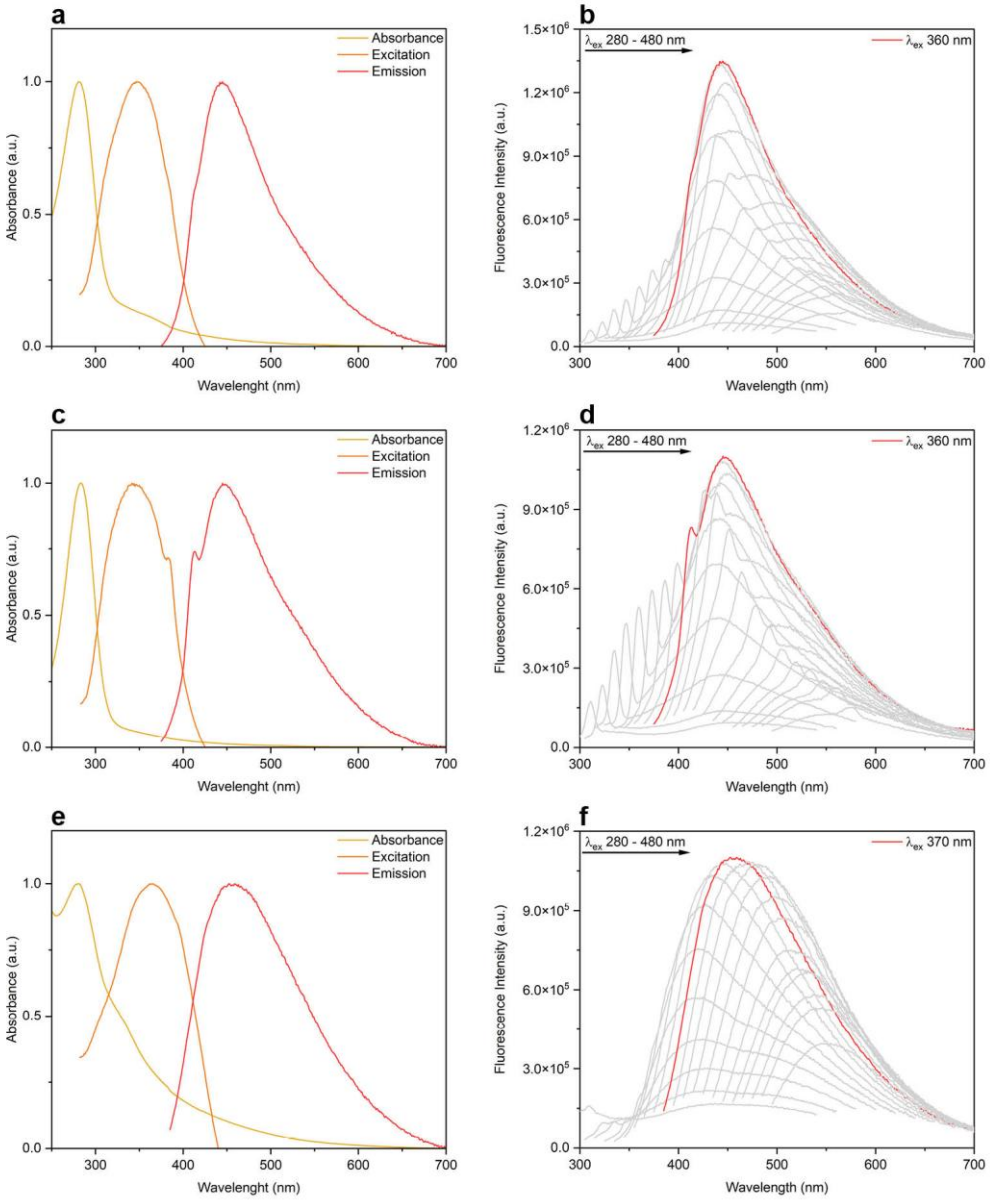

Figure 3.18, Absorbance, excitation, and emission spectra and emission spectra with λ_{ex} 280 – 480 nm with 10 nm step increase and highest emission spectrum highlighted in red of the dialysed carbon dots from hydrothermal synthesis with D-galactose (a) abs/ex/em, (b) λ_{ex} 280 – 480 nm, Carrageenan (c) abs/ex/em, (d) λ_{ex} 280 – 480 nm, and Irish moss (e) abs/ex/em, (f) λ_{ex} 280 – 480 nm

Table 3.7, summary optical characteristics dialysed carbon dots from D-galactose, Carrageenan, and Irish moss

Precursor	$\lambda_{abs.}$ (nm)	$\lambda_{ex,max.}$ (nm)	$\lambda_{em,max.}$ (nm)	$\lambda_{ex,coll.}$ (nm)
D-galactose	281/350	360	445	346
Carrageenan	284	360	445	342

Irish moss	281/333	370	459	362

nm, respectively. A notable broadening of peaks was observed in the dialysed Irish moss sample when compared to both the carrageenan sample and the as-prepared Irish moss sample. Given the minimal broadening between the as-prepared carrageenan and as-prepared Irish moss samples, this suggests that the broadening is introduced with the dialysis step. However, it remains unclear whether this effect is directly attributable to the dialysis process itself or to the inherent instability of the carbon dots in solution. This peak broadening was not observed when comparing other precursors before and after dialysis, implying that the use of a more complex precursor may lead to alterations in the optical properties of carbon dots in solution.

3.3.11 Stability study of dialysed carbon dots

To investigate the efficacy of the dialysis purification step and the impact of prolonged storage, dialysed carbon dots were monitored, with the results presented in Figure 3.19. A preliminary assessment reveals significant resemblances between the plots obtained with and without dialysis. Specifically, the absorption peak initially observed at approximately 280 nm diminishes and is subsequently replaced by a peak at around 250 nm, a phenomenon consistent with precursors such as D-glucose, D-galactose, and carrageenan. However, two key differences emerge. Firstly, the dialysed samples achieved stability within a shorter timeframe, under 5 days, in contrast to the over 7 days required for the as-prepared samples. This accelerated stabilisation can be attributed to the preceding 2-day dialysis step, rendering the timelines consistent when this factor is considered. Secondly, a sloped curve extending into the visible light spectrum is evident after dialysis. The relative enhancement of this tail into the visible light region, where optimal excitation has been identified, suggests a beneficial effect of dialysis on the samples.

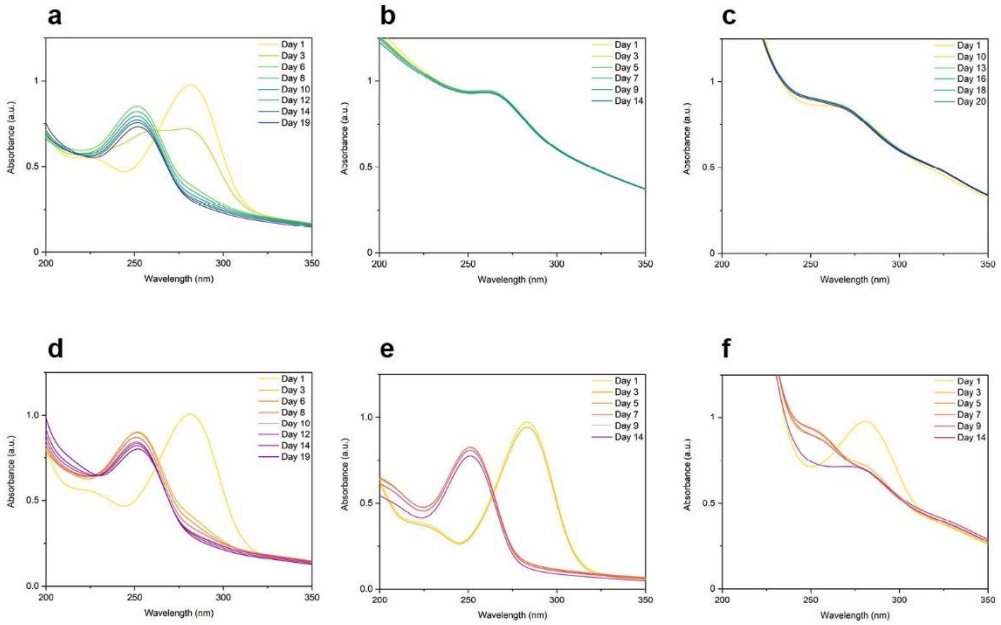

Figure 3.19, Absorbance spectra over time for dialysed carbon dots from D-glucose (a) alginate (b), Kelp (c), D-galactose (d), Carrageenan (e), and Irish moss (f).

The remaining three samples, alginate, kelp, and Irish moss, exhibit nearly identical characteristics to their as-prepared counterparts. Notably, alginate and kelp show no discernible changes. While Irish moss follows the same trend and maintains similar peak positions, the magnitude of the absorption change is diminished,

accompanied by an increased tail extending into the visible light spectrum, the changes in absorption over time are summarised in Figure 3.20.

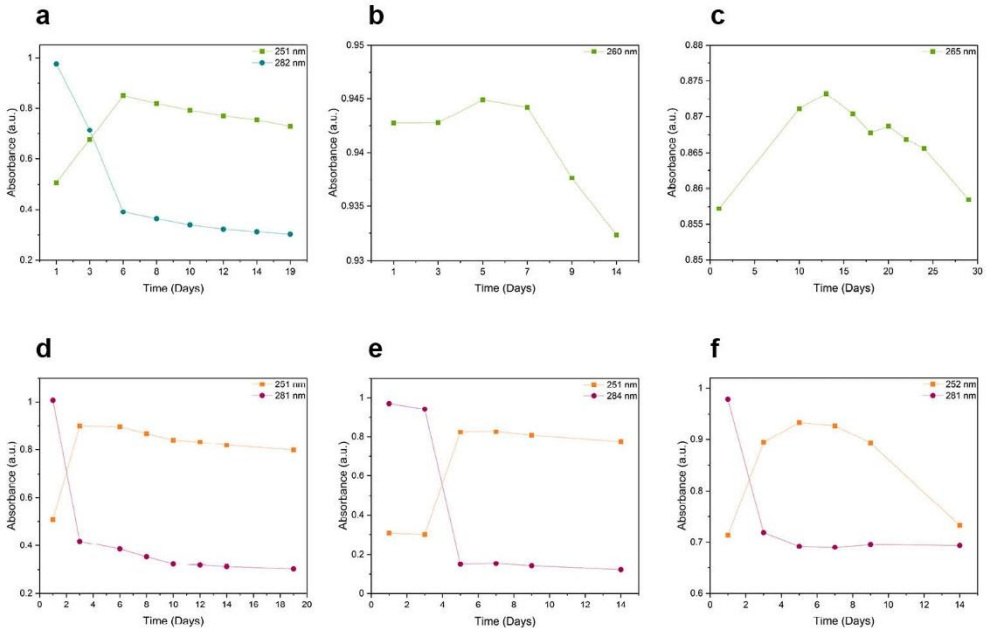

Figure 3.20, UV-vis absorption measured at distinct wavelengths over time for dialysed carbon dots from D-glucose (a), alginate (b), kelp (c), D-galactose (d), carrageenan (e), and Irish moss (f).

Photoluminescence measurements of the dialysed carbon dots over time are shown in Figure 3.21. The plots reveal comparable trends between the dialysed and as-prepared samples; however, post-dialysis, smaller intensity variations were observed. After dialysis, alginate exhibited a slight increase in photoluminescence intensity, a contrast to the minor decrease observed in the undialysed samples, depicted in Figure 3.16. Kelp displayed a similar linear decrease in PL intensity. The red seaweed precursors consistently showed an initial increase in PL intensity before stabilising after 5 days. D-galactose and carrageenan demonstrated comparable changes in intensity, narrowing the differences between the carbon dot samples derived from mono- and polysaccharides in solution. The carbon dots prepared from Irish moss exhibited a trend like the as-prepared samples, with an initial slight increase in PL followed by a subsequent decrease.

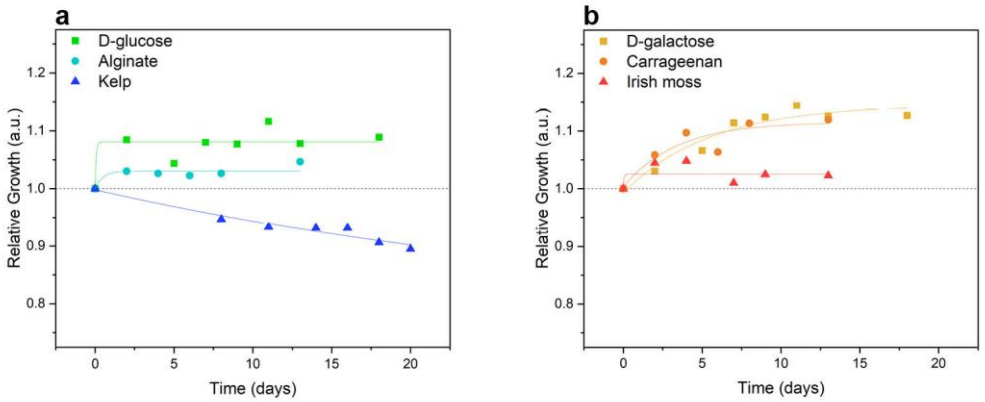

Figure 3.21, Change in photoluminescence intensity over time for as prepared and dialysed carbon dots from (a) brown and (b) red seaweed and seaweed precursors, D-glucose (green), Alginate (turquoise), Irish moss (blue), D-galactose (yellow), Carrageenan (orange), and Irish Moss (red)

The correlation between absorbance at 250 nm and photoluminescence intensity for the as-prepared CDs, was also investigated for the dialysed CDs. Upon close examination of the data, carbon dots derived from red seaweed precursors precisely adhered to this relationship. However, the situation was more intricate for brown seaweed samples; specifically, D-glucose exhibited an increase in absorption at 250 nm over 6 days, followed by stabilisation and a slight decrease. Conversely, its PL intensity demonstrated a sharp increase by day 3, after which it also stabilised. For alginate and kelp, minimal changes in absorption were observed, making it challenging to establish a direct connection with their respective PL intensities.

3.3.12 Findings on the effects of dialysis on the optical properties of carbon dots

This comparative study of as-prepared and dialysed carbon dots, utilising UV-vis absorption and photoluminescence spectroscopy monitored over time, allows for the derivation of several conclusions regarding their spectral properties.

Carbon dots derived from D-glucose, D-galactose, carrageenan, and Irish Moss consistently yield materials possessing similar spectral characteristics. These include a prominent absorption peak centred around 280 nm and a comparatively smaller tail extending into the visible light spectrum. Optimal emission, observed between 414 and 438 nm, was achieved upon excitation at wavelengths 340 or 350 nm, with the collected excitation wavelength measured between 329 and 342 nm. Further analysis revealed that varying the excitation wavelength from 280 to 480 nm resulted in excitation-independent emission below a certain threshold wavelength and excitation-dependent emission above it.

The spectral properties of alginate and kelp carbon dots also closely resemble each other. Their absorption spectra exhibit a sloped curve with a strong tail extending into the visible light region, featuring a peak between 260 and 270 nm and a shoulder at 350 nm, along with noticeable peak broadening in both excitation and emission spectra. A slight blue shift of 10 nm is observed when transitioning from alginate to kelp biomass. These distinctions are significant when compared to simple sugars and carrageenan saccharides, underscoring the critical role of molecular structures among the precursors.

From the characterisation, it is evident that carrageenan behaves and reacts similarly to monosaccharides, forming comparable materials. Therefore, it can be concluded that Irish moss readily breaks down, making carrageenan available and further fragmenting into single sugar units during the hydrothermal reaction, ultimately utilising the same reaction mechanism as D-glucose and D-galactose to form carbon dots.

Nevertheless, the disparities observed with alginate and kelp indicate that their sugar content does not align with the simpler sugar structure of D-glucose. Molecular analysis reveals that these are uronic acids—sugar acids characterised by the oxidation of the terminal methyl group to a carboxylic acid, thus possessing both carbonyl and carboxylic acid functional groups, unlike neutral sugars that contain aldehyde or ketone groups and hydroxyl groups but lack a free carboxylic acid. Characterisation studies confirmed that the carboxyl group significantly influences the photoluminescence properties of carbon dots derived from brown seaweed. In stability assessments, only carbon dots from Kelp did not exhibit aggregation-induced emission, as evidenced by consistent absorption shifts and intensity, as well as stable photoluminescence intensity.

Dialysis, intended to purify the samples by removing impurities and unreacted sugars, led to peak broadening in both excitation and emission spectra. The Irish moss sample exhibited the most significant alteration in its absorption profile, becoming more akin to alginate and kelp, and diverging from carrageenan and the monosaccharides. This transformation is attributed to the passage of time, rather than solely the effect of dialysis, a conclusion supported by the striking similarities between Figure 12f and Figure 16f.

Given the poor stability of carbon dots in aqueous solutions, which is thought to lead to particle aggregation and aggregation-induced emission, coupled with the observation that dialysis negatively impacts sample quality due to the prolonged processing time, alternative purification methods warrant consideration. Consequently, the subsequent section explores the effects of chromatographic methods on carbon dots derived from alginate and kelp, as investigated through UV-vis absorption and photoluminescence spectroscopy.

3.3.13 Expanding the purification study

Building upon the observations regarding the stability of carbon dots in aqueous solutions and the impact of dialysis, the scope of the purification investigation was refined. The decision was made to concentrate initially on a single biomass type, with kelp and alginate precursors chosen due to their closely comparable results.

Initially, the carbon dots underwent lyophilisation to yield a solid, more stable form suitable for storage and structural characterisation. The efficacy of this process was assessed by re-suspending the lyophilised carbon dots in water and re-evaluating their photoluminescence properties. This analysis, depicted in Figure 3.24 (a) and (b) for alginate and kelp carbon dots respectively, indicated no substantial alterations in photoluminescence characteristics post-lyophilisation. Furthermore, carbon dots synthesised hydrothermally from Alginate and Kelp were subsequently subjected to comprehensive structural characterisation, including FT-IR, TGA, XRD, and TEM analyses, to elucidate their surface morphology and internal structure.

The FT-IR spectrum of the alginate and kelp carbon dots in Figure 3.22 (a) and (b) show a broad O-H stretch at 3259 cm^{-1} and a small C-H sp^3 bond at 2937 cm^{-1}. The peaks at 1698 and 1588 cm^{-1} are indicators of C=O and C=C bonds., consistent with the precursor molecular structures and the presence of carboxyl groups.

The XRD pattern depicted in Figure 3.22 (c) and (d) confirm the mostly amorphous, rather than graphitic nature of the produced carbon dots and resembles the literature[23, 61] This is explained by the broad peak with the maximum at 19.8 °2θ, corresponding to the (002) peak. This is indicative of the higher interlayer spacing (*d*) of the carbon dots, 0.42 nm, compared to the graphitic interlayer spacing, 0.33 nm. This confirms the poor crystalline nature of carbon dots, which is attributed to the generation of more oxygen containing groups.

The thermogravimetric analysis plots, displayed in Figure 3.22, illustrate the degradation temperatures and profile of the carbon dots isolated. Carbon dots derived from alginate (e) show a one-third inorganic core, whereas those from kelp (f) exhibit nearly complete weight loss. For both carbon dots examined, the plot

reveals three decomposition steps. The first weight loss occurs before 200 °C, with a small 5 – 10% weight loss attributed to dehydration. The second weight loss between 200 to 400 °C is attributed to the decomposition of surface functional groups and polymer-like core. The third and last weight loss between 400 and 900 °C is explained by the slow decomposition of the graphitic core.[62, 63] The decomposition profiles clearly elucidate the distinct core structures of the carbon dots: alginate-derived variants feature a graphitic core, whereas kelp-derived ones exhibit a predominantly polymer-like core. This structural divergence indicates that kelp-derived carbon dots preserve greater polymeric character and oxygen-containing functionalities, thereby exerting a pronounced influence on their photoluminescence and thermal stability relative to the more extensive graphitic alginate counterparts.

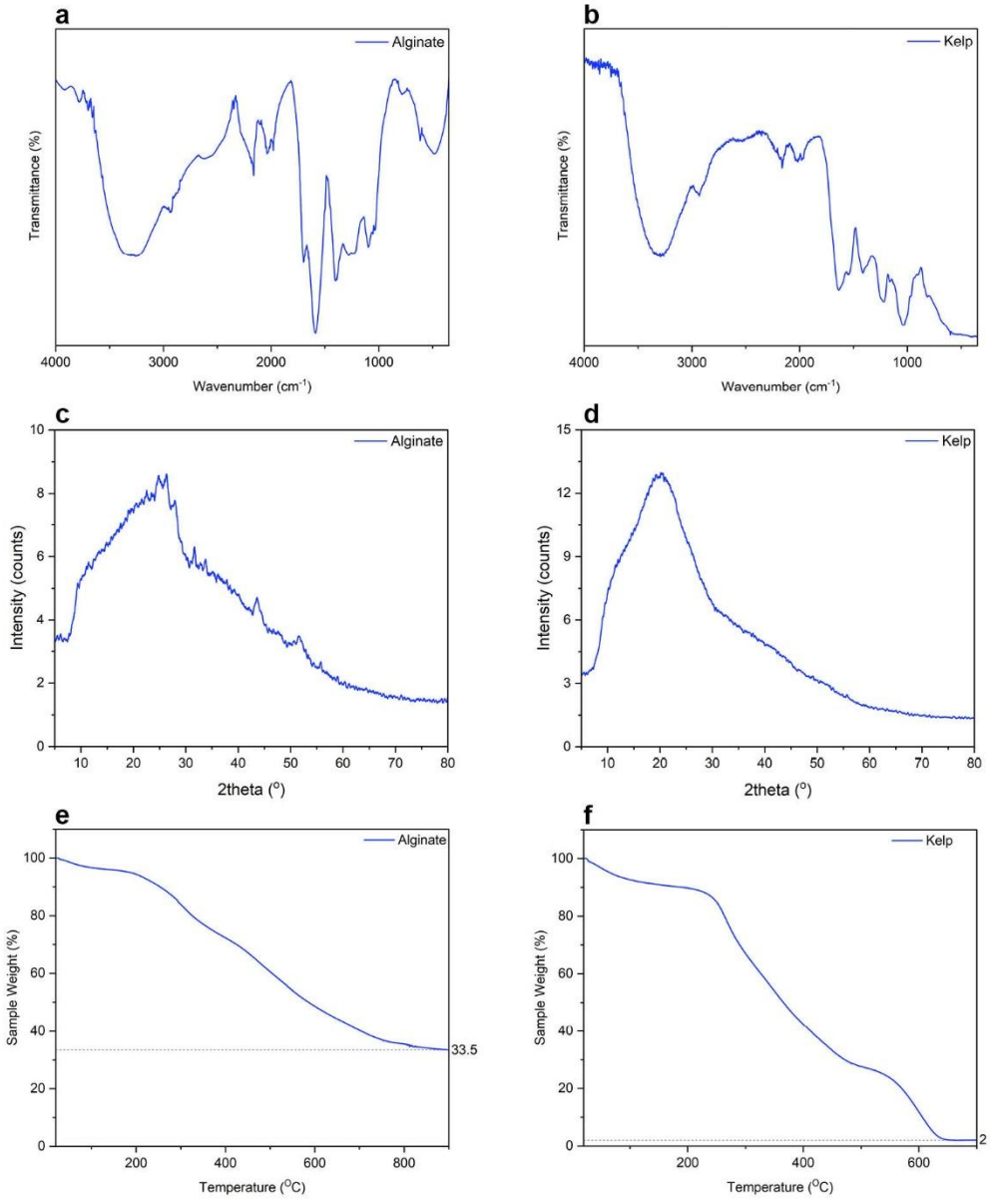

Figure 3.22, Structural characterisation of lyophilised carbon dots from hydrothermal synthesis of FT-IR (a) Alginate, (b) Kelp, XRD (c) Alginate, (d) Kelp, and TGA (e) Alginate, (f) Kelp

Additionally, transmission electron microscopy images, shown in Figure 3.23, offered visual insights into the morphology and environment of the carbon dots. The images clearly demonstrated that the hydrothermal

reactions involving alginate and kelp resulted in the formation of nanoscale semi-spherical particles, measuring around 5 nm and 20 nm, respectively. Both materials formed aggregates and were encapsulated within an organic layer. These observations provide supportive evidence for the need of an efficient purification method for carbon dots.

The focus was cast on other methods reported in literature for purification of carbon dots from biomass include chromatography methods including column chromatography and size exclusion chromatography.[64] Column chromatography with a stationary phase of silica and mobile phase of acetonitrile:water (5:1) was carried out as well as size exclusion with NAP-10 packed columns.

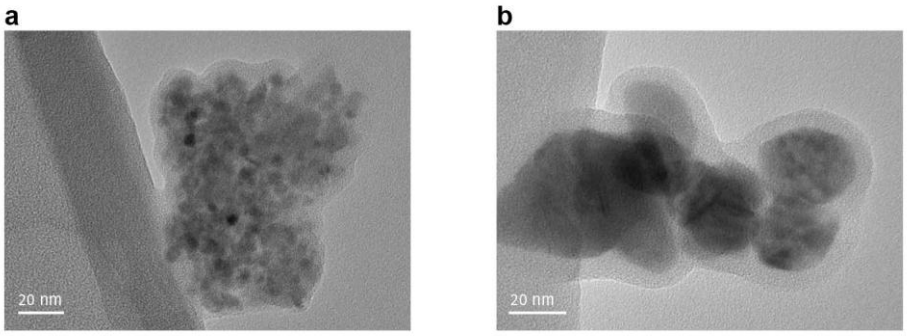

Figure 3.23, TEM images of carbon dots from (a) Alginate and (b) Kelp

Purification of the carbon dot samples from alginate and kelp through column chromatography and size exclusion chromatography resulted in the following extended emission spectra λ_{ex} 280 – 480 nm with 10 nm steps, depicted in Figure 3.24 (c), (d), (e), and (f), respectively.

The alginate carbon dot sample exhibited enhanced spectral results after column chromatography, specifically by intensifying the strongest emission and displaying a sharper emission peak for excitation wavelengths greater than 330 nm, which is characteristic of the excitation-dependent emission region. Size exclusion chromatography of the alginate CD sample, however, enhanced the secondary emission peak, present when excited at lower wavelengths (less than 350 nm), resulting in excitation-independent emission and an overall peak broadening. This technique, while enhancing the second, longer emission peak visible at low excitation wavelengths (less than 320 nm), ultimately led to the aforementioned peak broadening.

The kelp carbon dot sample did not exhibit enhanced spectral results following column chromatography. However, size exclusion chromatography of the kelp carbon dot sample intensified the secondary emission peak. While enhancing the second, longer emission peak visible at low excitation wavelengths (< 320 nm), this ultimately contributed to observed peak broadening.

This experiment unequivocally demonstrated that column chromatography is more effective in augmenting the strongest emission peak, leading to a narrower peak profile. Conversely, when requiring isolation of carbon dots with a longer emission maximum, size exclusion chromatography may present a superior

purification methodology. Nonetheless, continued exploration of carbon dot purification techniques remains essential.

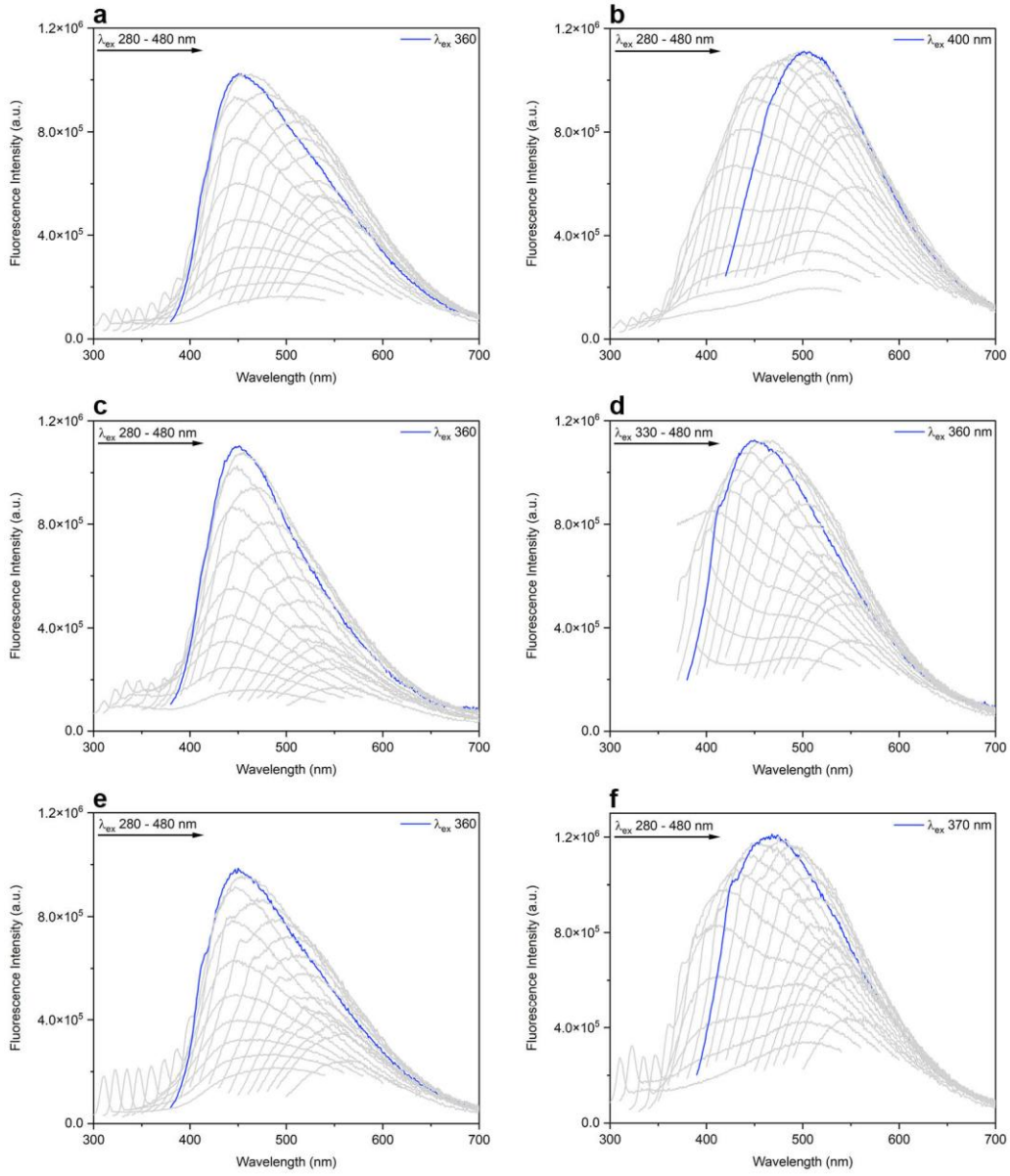

Figure 3.24, Emission spectra with λ_{ex} 280 – 480 nm with 10 nm step increase and highest emission spectrum highlighted in blue of the dialysed carbon dots from freeze dried CDs from (a) Alginate, (b) Kelp, CDs purified by column chromatography from (c) Alginate, (d) Kelp, and CDs purified by Size exclusion chromatography from (e) Alginate and (f) Kelp.

3.4 Conclusions

Hydrothermal synthesis of seaweed and seaweed saccharide content will yield blue emissive carbon dots. Both brown and red seaweed, of kelp and Irish moss are suitable biomasses for the hydrothermal synthesis of CDs, due to their varied and extensive saccharide content.

From this study, it becomes clear that alginate is a good precursor to investigate a simplified reaction system regarding kelp. This is consistent with the literature reported biomass composition as well as the saccharide analysis from the seaweed in our study. The carboxyl group in alginate and kelp significantly contribute the optical properties of the carbon dots produced. However, to further simplify the reaction system, it is not recommended to use D-glucose, as it is not representative for the kelp biomass, due to the lack of the functional carboxyl group. It would be advisable to consider the use of isolated uronic acids; however, this approach would concurrently increase the experimental cost.

Designing a simplified reaction system for the red seaweed Irish moss, Carrageenan, and D-galactose provide each a good precursor with representative optical features. Especially the similarities between D-galactose and Carrageenan are strong and are believed to react in the same mechanism to form carbon dots. When considering the biomass, Irish moss itself, it shows an increased complexity in the optical properties, like the alginate and kelp carbon dots. From the literature and the biomass analysis, it is known that more saccharides are present in the red seaweed and will contribute to the reaction, and complex molecular structures.

The stability of carbon dots in aqueous solution was investigated through UV-vis absorption and PL spectroscopy analysis and revealed change in absorption and peak shifts, both suspected to be caused by aggregation and concentration effects. This suspicion is strengthened by the intensity change in photoluminescence emission, which shows either an increase or decrease before stabilising after 5 – 7 days.

Purification of carbon dots through dialysis generally resulted in increase of the tail into visible light spectrum and peak broadening in excitation and emission spectra. Together with the time study of the dialysed carbon dots, it was concluded that the extended time it takes to purify the dots, and the effects of aggregation and concentration effects outweigh the benefits of dialysis. It was concluded alternative methods for purification should be considered. Purification through chromatography methods did improve certain properties of the carbon dot emissive spectra. Column chromatography resulted in peak narrowing, at the most emissive wavelength. While size exclusion resulted in the enhancement of secondary emissive peaks, introducing a certain degree of control and variation.

Based on structural and surface characterisation of dried carbon dots from Alginate and Kelp, the purification of carbon dots needs to be explored further. Additionally, optimisation of the reaction system, including reaction parameters, might enhance the optical properties of the materials, as well as introduce a form of control. While the first is investigated within our research group, this research will focus on the latter by investigating the reaction optimisation of hydrothermal synthesis of carbon dots from seaweed in the last chapter.

3.5 References

1. A. Rasal, T. Subrahmanya, S. Kizhepat, G. Getachew, A. Ghule, R. Devan, W.-S. Hung, M. Fahmi, A. Wibrianto and J.-Y. Chang, *Coord. Chem. Rev.*, 2025, **533**, 216510.
2. S. Zhu, Y. Song, X. Zhao, J. Shao, J. Zhang and B. Yang, *Nano Res.*, 2015, **8**, 355-381.
3. C. Kang, Y. Huang, H. Yang, X. Yan and Z. Chen, *Nanomaterials*, 2020, **10**, 2316.
4. A. Su, D. Wang, X. Shu, Q. Zhong, Y. Chen, J. Liu and Y. Wang, *Chem. Res. Chin. Univ.*, 2018, **34**, 164-168.
5. A. Kumar, A. Chowdhuri, D. Laha, T. Mahto, P. Karmakar and S. Sahu, *Sens. Actuators B-Chem.*, 2017, **242**, 679-686.
6. H. Huang, J.-J. Lv, D.-L. Zhou, N. Bao, Y. Xu, A.-J. Wang and J.-J. Feng, *RSC Adv.*, 2013, **3**, 21691.
7. N. Irmania, K. Dehvari, G. Gedda, P. J. Tseng and J. Y. Chang, *J. Biomed. Mater. Res. B Appl. Biomater.*, 2020, **108**, 1616-1625.
8. G. Wang, Q. Guo, D. Chen, Z. Liu, X. Zheng, A. Xu, S. Yang and G. Ding, *ACS Appl. Mater. Interfaces.*, January 31, 2018, **10**.
9. W. Chen, J. Shen, G. Lv, D. Li, Y. Hu, C. Zhou, X. Liu and Z. Dai, *ChemistrySelect*, 2019, **4**, 2898-2902.
10. T. John, P. Yadav, D. Kumar, S. Singh and S. Hasan, *J. Lumin.*, 2020, **35**, 913-923.
11. S. Liu, J. Tian, L. Wang, Y. Zhang, X. Qin, Y. Luo, A. Asiri, A. Al-Youbi and X. Sun, *Adv. Mater.*, 2012, **24**, 2037-2041.
12. J. Shen, S. Shang, X. Chen, D. Wang and Y. Cai, *Mater. Sci. Eng. C.*, 2017, **76**, 856-864.
13. H. Zhang, S. Kang, G. Wang, Y. Zhang and H. Zhao, *ACS Sens.*, 2016, **1**, 875-881.
14. G. Arora, N. Sabran, C.-W. Liew, C. Ng, F. Low, P. Singh and H. Jun, *Chem. Phys. Impact.*, 2024, **9**, 100767.
15. S. Goyal, M. Esposito and A. Kapoor, *Thund. Int. B. Rev.*, 2018, **60**, 729-740.
16. *Supply chain analysis and material demand forecast in strategic technologies and sectors in the EU – A foresight study*, Report ISBN: 978-92-68-00339-8, European Union, https://single-market-economy.ec.europa.eu/, 2023.
17. W. Meng, X. Bai, B. Wang, Z. Liu, S. Lu and B. Yang, *Energy Environ. Mater.*, 2019, **2**, 172-192.
18. S. Chung, R. A. Revia and M. Zhang, *Journal*, 2021, **33**.
19. J. P. Naik, P. Sutradhar and M. Saha, *J. Nanostruct. Chem.*, 2017, **7**, 85-89.
20. L. Tang, R. Ji, X. Cao, J. Lin, H. Jiang, X. Li, K. S. Teng, C. M. Luk, S. Zeng, J. Hao and S. P. Lau, *ACS Nano*, 2012, **6**, 5102-5110.
21. Z. Wang, R. Changotra, M. Dasog, G. S. Selopal, J. Yang and Q. S. He, *SM&T*, 2025/07/01, **44**.
22. M. Liu, B. Chen, C. Li and C. Huang, *Green Chem.*, 2019, **21**, 449-471.
23. B. De and N. Karak, *RSC Adv.*, 2013, **3**, 8286-8290.
24. A. Barati, M. Shamsipur, E. Arkan, L. Hosseinzadeh and H. Abdollahi, *Mater. Sci. Eng. C.*, 2015, **47**, 325-332.
25. N. Ullal, R. Mehta and D. Sunil, *Anal.*, 2024, **149**, 1680-1700.
26. W. N, Q. J and J. Y, *Trends Biotechnol.*, 2013 Feb, **31**.
27. P. Schiener, K. Black, M. Stanley, D. Green, P. Schiener, K. Black, M. Stanley and D. Green, *J. Appl. Phycol.*, 2014-05-10, **27**.
28. BIM, *Scoping a seaweed biorefinery concept for Ireland*, CyberColloids, 2020.
29. L. Allahgholi, M. Jönsson, M. Christensen, A. Jasilionis, M. Nouri, S. Lavasani, J. Linares-Pastén, G. Hreggviðsson and E. Karlsson, *Fermentation*, 2023, **9**.
30. B. Salehi, J. Sharifi-Rad, A. Seca, D. Pinto, I. Michalak, A. Trincone, A. Mishra, M. Nigam, W. Zam and N. Martins, *Journal*, 2019, **24**, 4182-4182.
31. M. Seghetta, D. Romeo, M. D'Este, M. Alvarado-Morales, I. Angelidaki, S. Bastianoni and M. Thomsen, *J. Clean. Prod.*, 2017, **150**, 1-15.
32. M. Tabassum, A. Xia and J. Murphy, *Journal*, 2017, **68**, 136-146.
33. V. Dhargalkar and X. Verlecar, *Aquac.*, 2009/02/18, **287**.
34. H. Blue, *Journal*, 2025.
35. G. Bishop, C. Girón-Domínguez, J. Gaffey, M. Henchion, R. Fealy, J. Zimmermann, W. Kargupta and D. Styles, *Resour. Environ. Sustain.*, 2025, DOI: 10.1016/j.resenv.2025.100201, 100201.
36. A. Cox, *Journal*, 2025.
37. *Study to support a Sustainable EU Algae Industry*, European Maritime, Aquaculture and Fisheries Fund (EMFAF), 2025.
38. The European Green Deal, European Commission, 2019, https://eur-lex.europa.eu/legal-content/EN/ALL/?uri=CELEX:52019DC0640).
39. Vattenfall, Vattenfall and Samuel L. Jackson present Wind Farmed Seaweed Snacks, a delicacy grown at a wind farm, https://group.vattenfall.com/press-and-media/pressreleases/2025/vattenfall-and-samuel-l.-jackson-present-wind-farmed-seaweed-snacks-a-delicacy-grown-at-a-wind-farm).

40. Sustainability Report, https://sustainability.aboutamazon.com/reports).
41. First-ever harvest at pioneering North Sea seaweed farm, funded by Amazon's Right Now Climate Fund, https://www.northseafarmers.org/news/first-ever-harvest-at-pioneering-north-sea-seaweed-farm-funded-by-amazons-right-now-climate-fund).
42. Harvest time at world's first co-located seaweed farm and offshore windfarm, Plymouth Marine Laboratory, https://pml.ac.uk/news/harvest-time-at-worlds-first-co-located-seaweed-and-offshore-wind-farm/).
43. A. Soler-Vila, Edwards, M., Whelan, S., Hanniffy, D., Heesch, S., Hernández-Kantún, J., Moniz, M., Quéguineur, B., Ratcliff, J., Wan, A.H.L., and M.D. Guiry 2022, 66 pp.
44. M. Zwamborn, *Wieren*, Uitgeverij Van Oorschot, Amsterdam, 2018.
45. A. Mathieson and E. Tveter, *Aquat. Bot.*, 1975/01/01, **1**.
46. C. Zhao, X. Li, C. Cheng and Y. Yang, *Microchem J.*, 2019, **147**, 183-190.
47. M. I. S. Dela Cruz, N. Thongsai, M. D. G. de Luna, I. In and P. Paoprasert, *Colloids and Surfaces a-Physicochemical and Engineering Aspects*, 2019, **568**, 184-194.
48. C. Kang, Y. Huang, H. Yang, X. F. Yan and Z. P. Chen, *Nanomaterials*, 2020, **10**, 2316.
49. V. Hinterberger, C. Damm, P. Haines, D. Guldi and W. Peukert, *Nanoscale*, 2019, **11**, 8464-8474.
50. A. Trincone, *Enzymatic Technologies for Marine Polysaccharides*, CRC Press, Boca Raton, 1st edn., 2019.
51. T. Chopin, *Can. Tech. Rep. Fish. Aquat. Sci.*, 1986, **1514**, v+ 69.
52. H.-L. Yang, L.-F. Bai, Z.-R. Geng, H. Chen, L.-T. Xu, Y.-C. Xie, D.-J. Wang, H.-W. Gu and X.-M. Wang, *Mater. Today Adv.*, 2023, **18**, 100376.
53. D. A. Long, *Journal*, 1977, 0-3.
54. S. Singh and A. Das, *Phys. Chem. Chem. Phys.*, 2015, **17**, 9596-9612.
55. A. Siddique, S. Hossain, A. Pramanick and M. Ray, *Nanoscale*, 2021, **13**, 16662-16671.
56. L. Yang, L. Li, R. Liu, C. Xie, J. Zhao, W. Chang, L. Chen, Y. Yan, N. Zhang, W. Zhang, B. Liu and L. Yang, *Talanta*, 2024, **267**, 125137.
57. X.-D. Tang, H.-M. Yu, W. Nguyen, E. Amador, S.-P. Cui, K. Ma, M.-L. Chen, S.-Y. Wang, Z.-Z. Hu and W. Chen, *Adv. Photonics Res.*, 2023, **4**, 2200314.
58. N. Javed and D. M. O'Carroll, *Nanoscale Advances*, 2021, **3**, 182-189.
59. L. Fu, C. Zhang, H. Li, K. Jian, Y. Han and X. Zhao, *Microchem J.*, 2024, **202**, 110765.
60. C. Devan, M. Bijeesh, S. Subhamoy and B. Jayeeta, *Spectrochim. Acta A.*, 2025, **342**, 126392.
61. A. Shaikh, *J. Nanosci. Nanotechnol.*, 2019, **19**, 2339–2345.
62. S. Dua, P. Kumar, B. Pani, A. Kaur, M. Khanna and G. Bhatt, *RSC Advances*, 2023, **13**, 13845-13861.
63. O. Zaca-Moran, F. Díaz-Monge, A. Rodríguez-Juárez, C. L. Gómez-Muñoz, P. Zaca-Moran, O. Secundino-Sánchez and J. Díaz-Reyes, *Results Chem.*, 2024, **11**, 101788.
64. V. Hinterberger, C. Damm, P. Haines, D. Guldi and W. Peukert, *Nanoscale*, 2019/04/25, **11**.

Chapter 4 Reaction Optimisation of the Hydrothermal Synthesis of Carbon Dots from Seaweed and Seaweed Derivatives

4.1 Introduction

This chapter investigates the absence of a consistent approach in the experimental methodologies employed for the hydrothermal synthesis of carbon dots derived from biomass. The literature acknowledges notable inconsistencies in the selection of critical variables, including reaction temperature, duration, and precursor concentration, as well as challenges in purification, all of which substantially affect the quantum yield and physicochemical characteristics of the produced carbon dots.[1] Additionally, the inherent variability in the chemical composition of natural feedstocks leads to poor reproducibility and batch-to-batch variations.[2] The properties of biomass sources can vary significantly depending on geographic origin, seasonal changes, storage conditions, and extraction techniques. This variability hinders the development of standardised synthesis protocols and a thorough understanding of the structure-property correlations in biomass derived carbon dots.[2, 3] To address these issues, understanding biomass compositions, implementing standardised protocols, pre-treating raw materials, and real-time monitoring of synthesis parameters are crucial to ensure the reproducibility and scalability of green CQDs synthesis.[4]

This chapter addresses part of this problem – the variation in reaction parameters – with a literature review of fifty publications involving the synthesis of carbon dots from biomass through the hydrothermal method. Subsequently, a standardised method is proposed and tested on six precursors, including two seaweed species. This approach directly tackles the identified inconsistencies in the literature, providing a system to optimise the performance of the produced carbon dots while also managing the formation of waste and byproducts. This systematic approach not only aims to enhance the consistency and predictability of carbon dot synthesis but also contributes to the sustainable utilisation of biomass resources by minimising environmental impact.

4.1.1 Literature review on the hydrothermal synthesis of carbon dots from biomass

The hydrothermal synthesis of carbon dots from biomass exhibits considerable divergence in its reaction parameters, lacking a standardised methodology for production and optimisation. Current approaches frequently rely on previous publications without adequately assessing the influence of these varied parameters. Consequently, a literature review encompassing fifty studies on the hydrothermal synthesis of carbon dots from biomass was conducted to collate and analyse information on reaction parameters and optical properties, with the findings presented in Table 4.1

Among the fifty reviewed publications, four investigated reaction parameters and its effect on the properties of the carbon dots produced. Three of those studies speficically varied reaction parameters in time and temperature.[12, 39, 43]A fourth study examined reaction temperatures ranging from 150–250 °C while maintaining a constant reaction time of 10 h, also investigating the influence of pH.[5] The findings of these studies are summarised below.

Table 4.1, Literature review data: collection of fifty publication on the hydrothermal synthesis of carbon dots from biomass, * size determined through TEM imaging.

Biomass	Conc. (g/ml)	ff	Temp (˚C)	Time (h)	λ_{abs} π -π* (nm)	λ_{abs} n-π* (nm)	λ_{ex} (nm)	λ_{em} (nm)	QY %	Size* (nm)
Lime juice[6]	-	-	180	7	-	332	340	443	40	7.6
Collagen[7]	0.05	0.2	240	3	265	320	350	435	8	1.3
Tulsi leaves[8]	0.33	0.6	180	4	280	330	450	500	-	3
Orange peels[9]	0.08	-	180	12	268	-	340	431	36	4.8
Lemon peels[10]	0.01	0.8	200	6	-	-	425	505	11	9.5
Lemon peels[11]	-	-	200	12	270	320	358	441	14	-
Cabbage[12]	-	-	140	5	276	320	345	432	16.5	-
Aqua mesophase pitch[13]	0.0003	0.9	120 – 180	12 – 48	280	-	340	420	27.6	2.8
Latex[14]	-	0.4	180	3	250	320	360	450	39.2	3.4
Ocimum tenuiflorum[15]	-	-	200	12	254	315	320	405	11.5	-
Strawberry juice[16]	-	0.7	180	12	283	-	344	427	6.3	5.2
Corn powder[17]	0.01	-	180	8	250	350	360	450	-	-
Aloe[18]	0.20	0.5	180	11	278	-	441	503	10.4	5
Prawn-shell[19]	0.25	0.6	180	12	265	345	345	417	-	3
Cow milk[20]	-	0.55	200	4.5	275	333	340	415	8	2.8
Sweet potato[21]	0.29	-	180	18	266	-	360	442	8.6	3.4
Tea[22]	0.03	0.6	200	4	-	-	325	410	-	-
Peanut shell[22]	0.05	0.6	200	4	-	-	335	430	-	-
Coconut husk[23]	0.02	0.5	200	3	278	-	360	440	-	3.3
Gelatin[24]	0.02	0.8	300	3	265	320	350	430	31.6	1.7
Cane molasses[25]	0.06	0.67	190	24	260	-	376	440	21.3	2.5
Lemon juice[26]	-	-	120	3	283	-	410	482	16.7	3.1
Wheat straw[27]	0.02	0.2	250	10	247	334	360	467	9.2	-
Palm oil[28]	0.04	0.75	200	3	282	-	360	440	24.6	7
Waste green tea[29]	0.04	-	200	10	280	-	350	420	-	5
Papaya[30]	0.04	0.4	200	5	250-290	-	370	450	-	3.4
Neem leaf[31]	0.03	-	300	8	300	-	365	440	41.2	5
Fenugreek seed extract[31]	0.01	-	300	8	-	-	-	-		5.6
Orange waste peel[32]	0.06	-	200	6	235	332	330	426	11.4	2.9
Eichhornia crassipes[33]	0.004	0.7	140	6	280	325	400	459	-	-
Grass[34]	-	-	180	3	-	-	-	-	-	-
Wheat bran[35]	0.02	-	180	3	288	320	410	500	-	4.9
Pomelo[36]	-	-	200	7	284	-	370	452	-	3
Beetroot[37]	-	-	150	16	282	-	370	450	6	5
Rice husk[5]	0.003	-	150 – 250	10	-	-	-	-	19.1	-
Cotton cellulose[38]	0.001	0.6	180	8	282	-	480	551	19.4	-
Orange pericarp[39]	0.08	0.6	160 – 220	6 – 168	282	-	428	528	2 - 9	2.9
Rose-heart radish[40]	0.20	0.4	180	3	282	-	330	420	13.6	3.6
Pomelo peel[41]	-	-	200	3	-	-	-	-	-	-
Durian[42]	0.30	0.67	150	12	256	445	447	601	79	4
Waste paper[43]	0.03	-	180 – 200	12 – 20	280	-	365	420	-	-
Sugarcane bagasse[44]	0.20	-	170	3	280	320	390	461	-	2.26
Larch wood[45]	-	-	180	12	267	-	350	434	-	3.28
Cyanobacteria[46]	0.01	0.4	180	12	270	-	360	439	9.2	2.48
Hair[47]	0.02	-	200	24	275	330	330	415	10.7	4.56
Bamboo leaves[48]	0.08	-	200	6	279	320	365	440	7.1	3.6
Roasted fish[49]	-	-	200	.83	-	-	-	348	-	2.73
Honey[50]	0.20	0.4	100	2	278	-	320	435	19.8	2

Chen *et al*.[13] concluded that hydrothermal synthesis with aqua mesophase pitch at a temperature of 120 °C and a holding time of 24 h yielded carbon quantum dots with small and homogeneous size with QY 27.6% compared to other conditions (e.g., 150°C/48h or 180°C/48h), which result in slightly larger particles with a wider size distribution.

Du *et al*.[39] reported the hydrothermal synthesis using orange pericarp and found carbon dots with an increase in quantum yield 1.8 – 9.0% with increase of reaction temperature (at set reaction time of 6 h), and with increase in reaction time (at set reaction temperature of 220 °C) shown in Figure 4.1.

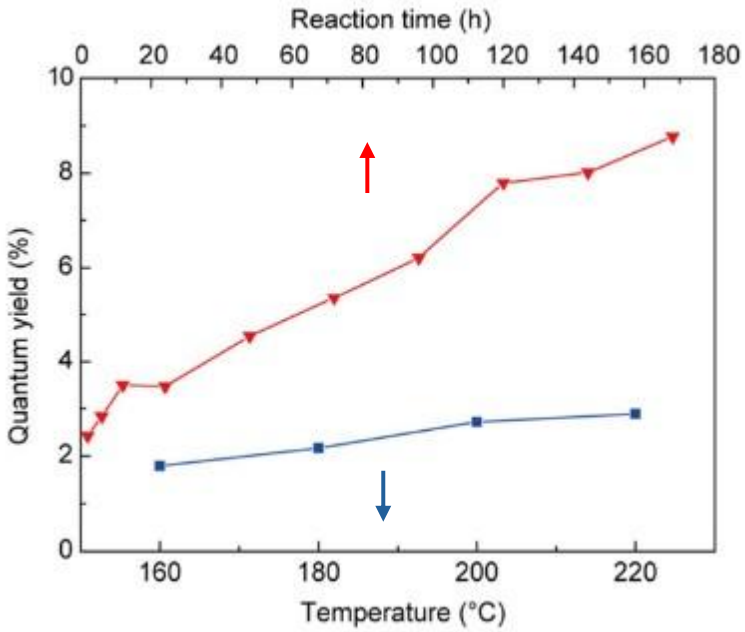

Figure 4.1, quantum yields of the CQDs prepared at different reaction temperatures for 6 h (blue line) and at 220 °C for different reaction times (red line).[39]

Wang e*t al.*[43] used waste paper in hydrothermal method to produce carbon dots and found increasing the reaction time from 12 to 20 h (at set reaction temperature of 180 °C) increased the photoluminescence intensity with 40%, and increasing the reaction temperature from 180 to 200 °C (at set reaction time 15 h) increased the photoluminescence response with 50%, depicted in Figure 4.3.

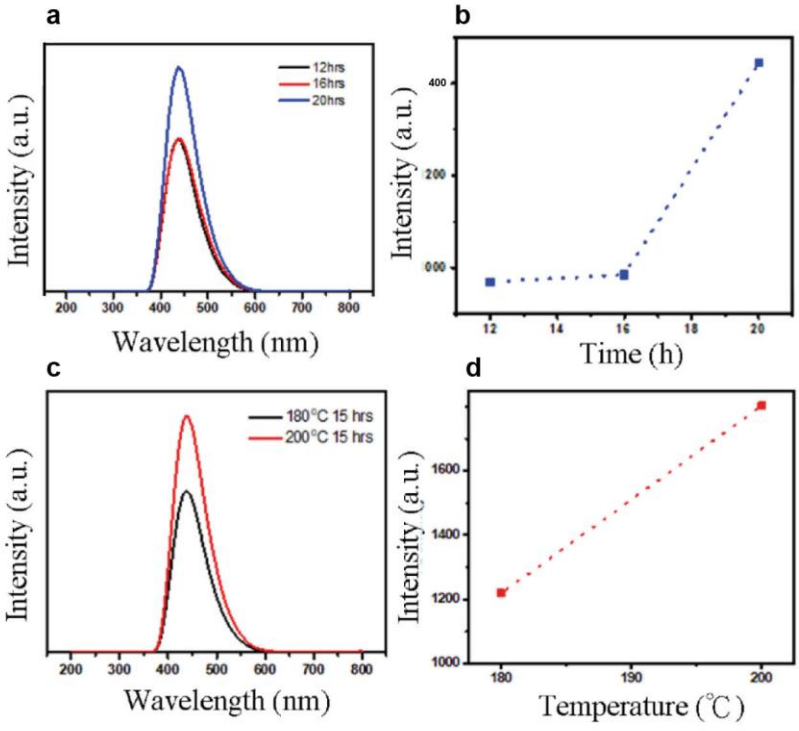

Figure 4.2, PL spectra of carbon dots prepared from waste paper, at 180 °C for different reaction times (a), dependence of PL intensity on reaction time (b), at different temperatures for 15 h using a urea concentration of 0.05 M (c), and dependence of PL intensity on temperature (d).[51]

Wongso *et al.*[5] investigated the hydrothermal synthesis of carbon dots making use of rice husk. They investigated the reaction temperature between 150 and 250 °C (at set time of 10 h and pH 4), and the pH

between 4 – 12 (at set temperature 200 °C and time 10 h). They found the optimum reaction temperature for the reaction at pH 4 and reaction time 10 h, was 225 °C. Additionally, they found the emission wavelength shifted hypsochromic 550 to 470 nm, by increasing the reaction temperature from 150 to 225 °C. However, reaction at 250 °C resulted in emission wavelength at 550 nm again, illustrated in Figure 4.3.

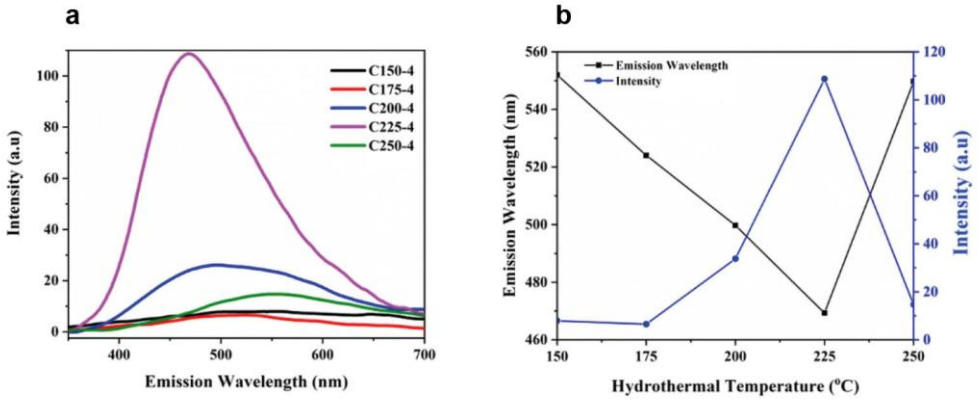

Figure 4.3, PL spectra (a) and properties (b) of carbon dots from rise husk at various hydrothermal temperatures with excitation wavelength of 325 nm.[5]

From these individual studies, the relevance of the reaction parameters is highlighted, especially the influence of reaction time and temperature on the photoluminescence intensity and quantum yield.

4.1.2 The variation in reaction parameters

Against the complete literature review, quantitative variations were observed in reaction time, temperature, concentration, and fill fraction, alongside qualitative differences in biomass pretreatment and the inclusion of additives were found relevant. In Table 4.2 a summary of the descriptive statistics of the reaction parameters is given.

Table 4.2, Descriptive Statistics of Reaction Parameters of Hydrothermal Synthesis of Carbon Dots from Biomass

	N total	Mean	SD	Minimum	Median	Maximum
concentration (g/ml)	35	0.08	0.10	0.0003	0.04	0.33
fill fraction	25	0.57	0.18	0.20	0.60	0.90
reaction temperature (˚C)	45	192.22	39.02	100.00	190.00	300.00
reaction time (h)	45	8.19	5.30	2.00	7.00	24.00

The statistical analysis of the provided data reveals that the concentration exhibits considerable variability, ranging from a minimum of 0.0003 g/mL to a maximum of 0.33 g/mL, spanning three orders of magnitude. However, 63% of the data point measure between 0.01 – 0.1 g/mL, as is depicted in Figure 4.4 (a). The fill fraction presents a mean of 0.57 and standard deviation of 0.18, together with a median of 0.60, indicate a relatively symmetrical and well-centred distribution, shown in Figure 4.4 (b). Consequently, drawing from a tightly clustered distribution of the reaction temperature around a mean of 192 ˚C (standard deviation of 39 ˚C) and observed values spanning 100.00 to 300.00 ˚C, illustrated in Figure 4.4 (c), this narrow and consistent temperature range is effective for the synthesis of high-quality carbon dots. Controverse of the reaction temperature, the reaction time, provided a wide distribution with values ranging from 2 – 24 h, resulting in the mean of 8.2 h and a standard deviation of 5.3 h, shown in Figure 4.4 (d). This suggests a less

consistent optimisation or a varied understanding of its optimal parameters. This variability underscores the critical need for further systematic investigation into the formation of carbon dots, particularly how reaction time influences their structural and optical properties.

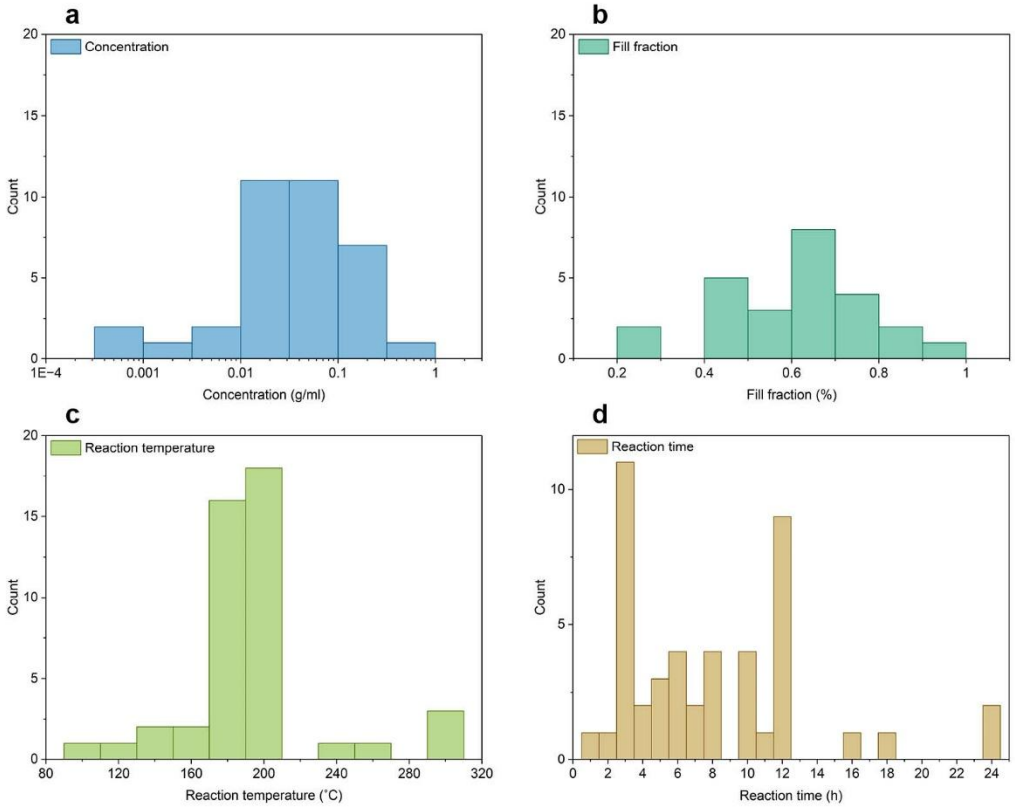

Figure 4.4, Histograms of the reaction parameters of hydrothermal synthesis of carbon dots from biomass, (a) concentration (g/ml), (b) fill fraction (%), (c) reaction temperature (°C), and (d) reaction time (h)

Biomass typically undergoes pre-treatment steps, such as drying and grinding into a powder, prior to synthesis.[10, 31, 43, 46] An alternative method involves thermal treatment to facilitate its breakdown before the primary hydrothermal synthesis.[28, 32, 51] Often, the prepared biomass is then dispersed and agitated in water before being introduced into a Teflon-lined autoclave.[7, 17, 31, 50, 52] For specific feedstocks like citrus fruits, the common practice is to juice them, followed by centrifugation to isolate the supernatant for use as the reaction solution.[6, 26, 36] Some protocols, such as one involving Tulsi leaves, have also reported sterilisation with ethanol before grinding.[15]

A variety of additives are commonly employed in these hydrothermal reactions, including acetic acid, citric acid, hydrogen peroxide, ammonium bicarbonate, urea, ammonia, and manganese chloride.[6, 13, 22, 29, 32, 43, 50] These additives often serve various roles, such as pH adjustment, promoting carbonisation, or acting as passivating agents to enhance the quantum yield and stability of the resulting carbon dots.

4.1.3 Optical properties – literature review

This review also included the optical properties of the produced carbon dots to identify and analyse cause-and-effect relationships between the reaction parameters and the optical properties. This analysis incorporates UV-Vis spectroscopy, as the absorption peaks of carbon dots are fundamentally attributed to the electronic

transitions between bonding and antibonding orbitals. Specifically, the prominent absorption features observed under 300 nm are typically assigned to π-π* transitions of sp^2 hybridised carbon atoms including C=C and C=N bonds. Absorption in the 300 – 350 nm range often correspond to n-π* transitions involving C=O and C-O bonds.[6, 53-56] When an absorption peak extends this region, this is typically assigned to the transition of functional groups on the surfaces of C-dots.[42] This was observed for one study in the literature review wherein the hydrothermal synthesis of carbon dots from durian biomass resulted in a second absorbance peak that shifted to 445 nm. This shift was attributed to the use of a platinum sheet as a catalyst at the bottom of the Teflon-lined autoclave. This study was considered an outlier in the statistical analysis and not considered for the descriptive statistics of the optical properties which are tabulated in Table 4.3, and visualised in Figure 4.5.

Table 4.3, Descriptive Statistics of Optical Properties of the Carbon Dots synthesised through the Hydrothermal Method from Biomass

	N total	Mean	SD	Minimum	Median	Maximum
λ_{abs} π – π* (nm)	39	273	13	235	278	300
λ_{abs} n – π* (nm)	19	328	11	315	325	350
λ_{ex} (nm)	45	366	39	310	360	480
λ_{em} (nm)	45	448	42	348	440	601
QY %	31	17	11	6	14	41
size (nm)	35	3.9	1.7	1.3	3.4	9.5

For the lower wavelength absorption λ_{abs} π -π*, statistical analysis indicates a mean absorption of 273 nm, with a standard deviation of 13 nm. The observed values range from a minimum of 235 nm to a maximum of 300 nm, with a median value of 278 nm, suggesting a distribution that is tightly clustered around the mean, indicating a robust and consistent absorption characteristic for this parameter. For the longer wavelength absorption λ_{abs} n-π*, the analysis indicates a mean value of 328 nm, with a standard deviation of 11. The observed range spans from a minimum of 315 to a maximum of 350, and the median value is 325 nm. This consistent clustering around a specific absorption wavelength suggests that the primary light-absorbing groups responsible for this electronic transition are robustly formed under typical synthesis conditions.

Compared to the absorption wavelength, the excitation wavelength is more broadly distributed, reflecting a wider range of optimal excitation energies for different luminescent species. The mean of the excitation wavelength (λ_{ex}) was found 366 nm with a standard deviation of 39, with a minimum of 310, a median of 360, and a maximum of 480. The excitation wavelength overlays the λ_{abs} n-π* transition, typically red shifted around 30 nm. Conversely, the photoluminescence emission (λ_{em}) exhibits a mean of 448 nm and a standard deviation of 42 nm, with values ranging from 348 to 601 nm, and a median of 440 nm, further emphasising the variability in emission characteristics.

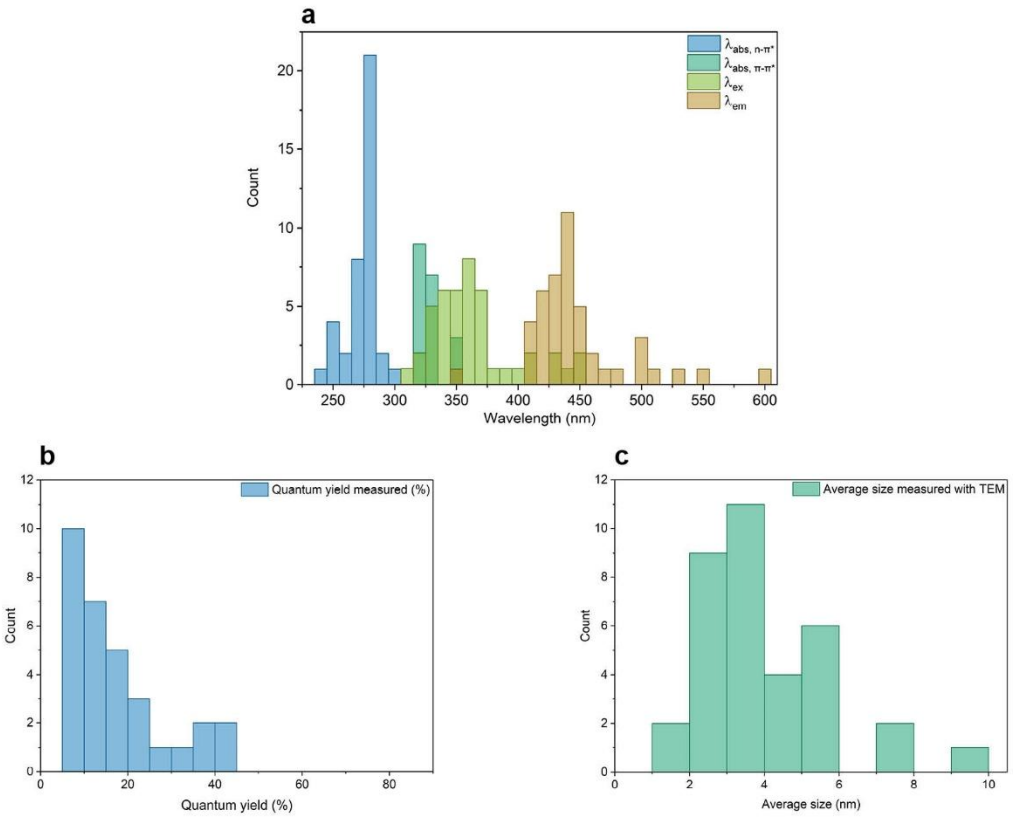

Figure 4.5, Distribution of the optical characteristics of the carbon dots synthesised in hydrothermal method from biomass (a), including: λ_{abs} $\pi - \pi^*$ (blue), λ_{abs} n – π^* (turquoise), λ_{ex} (green), and λ_{em} (orange), quantum yield (b), and size (c).

For the quantum yield, the mean is 17 with a standard deviation of 11, a minimum of 6, a median of 14, and a maximum of 41. This data suggests a distribution that is skewed towards higher values, as the median is lower than the mean, indicating a consistent trend in quantum yield across the experiments. Nonetheless, the observed quantum yields, ranging from 6% to 40% (excluding outliers), indicate a substantial potential for biomass-derived carbon dots in various optical applications, particularly when optimised synthesis parameters are employed.

For the recorded size, the method of transmission electron microscopy was applied to measure and count the size of the carbon dots for 35 publications. A mean of 3.9 nm was found with a standard deviation of 1.7, a minimum of 1.3, a median of 3.4, and a maximum of 9.5, indicating a distribution that is relatively well-centred around the mean, suggesting consistency in this parameter's selection. The broad range of carbon dot sizes observed across different studies, reflects methodology variations, and underscores the influence of specific synthesis conditions on nanoscale morphology and quantum yield.

4.1.4 Introduction to the Response Surface Method

In the literature review concerning the hydrothermal synthesis of carbon dots from biomass, Dela Cruz *et al.*[53] proposed the use of Response Surface Method for reaction optimisation.

The response surface method utilises regression models to describe the relationship between independent variables and a response variable. Two common types of regression models, differing significantly in the complexity of relationships they can capture, are linear and second-order regression models.
A linear regression model assumes a straight-line relationship between the dependent variable (response) and the independent variables (factors). This model is suitable when the effect of each independent variable on the response is constant, regardless of the values of other variables, and there are no curvature or interaction effects. In contrast, a second-order regression model (also known as a quadratic model) is employed when the relationship between the response and the independent variables is nonlinear, exhibiting curvature or interaction effects. It includes linear terms, quadratic terms, and interaction terms. This model is more flexible than linear regression and can capture more complex relationships, such as optimal points (maximum or minimum) within the experimental region, which is particularly useful in optimisation studies like those conducted using the response surface method, a technique frequently employed in analytical chemistry to identify conditions that yield the best possible outcome for a given procedure, for example with the desirability function, initially proposed by Derringer and Suich in 1980.[56-58]

This multivariate statistical technique systematically investigates the relationships between multiple independent variables and one or more response variables, providing a robust framework for process enhancement and discovery. While traditional optimisation often involves a one-variable-at-a-time approach, which can be inefficient and fail to capture interaction effects, RSM employs multivariate techniques to simultaneously assess the influence of several factors on a response. This approach minimises the number of experiments required while maximising the information gained regarding optimal conditions and interactions among independent variables.[59]

In the study of Dela Cruz *et al.*[53] highly photoluminescent carbon dots from polyurethane were synthesised. They employed RSM's Box-Behnken design to model and optimise three parameters for carbon dot synthesis.[57, 60] They included the reaction parameters of reaction time, temperature, and the introduction of a catalyst, aimed to maximise the quantum yield of the carbon dots through reaction. The resultant carbon dots, suspended in an aqueous solution, displayed blue-green emission under UV light irradiation and achieved a quantum yield of 33%, a finding consistent with the RSM model's prediction.[53]

Based on the review of existing literature, four parameters are frequently reported in the hydrothermal reaction and offer avenues for control: precursor concentration, autoclave fill fraction, reaction time, and reaction temperature. This study concentrates on the latter two parameters, as they are both controllable and monitorable within the reaction process. Although precursor concentration and fill fraction can also be managed, the sugar content concentration of the chosen biomass is often unknown and varies with location, season, and agricultural practices. A similar issue arises with fill fraction, as it is directly associated with the autogenous pressure generated within the reactor, as a function of temperature, which remains unmonitored in this reaction system. Consequently, this research will prioritise control via reaction temperature and time.

4.1.5 Design of Experiment

The integrity of experimental conclusions is fundamentally reliant on the chosen experimental design and the robustness of the data acquisition strategy. Therefore, the right approach must be selected, in this case, the choice between a first or second-order regression model. The selection between these models often hinges on the anticipated complexity of the response surface and the necessity to capture potential non-linear relationships and interaction effects among variables. A first-order regression model employs a factorial design to fit a linear model and identify the path of steepest ascent. This model includes linear terms, represented by the equation

$$y = \beta_0 + \beta_1 x_1 + \beta_2 x_2 + \varepsilon \quad (4.1)$$

With y as the response,
β_0 as the intercept,
$\beta_1 x_1$ as the linear effect of factor 1,
$\beta_2 x_2$ as the linear effect of factor 2, and
ε as the error term.

For more intricate relationships where curvature is observable, a second-order polynomial model is frequently utilised. This model incorporates quadratic terms and interaction effects to provide a more precise approximation of the response surface, capturing non-linear relationships and enabling the identification of optimal experimental conditions. This allows for a more flexible data fit than first-order models. The equation for the second-order model is

$$y = \beta_0 + \beta_1 x_1 + \beta_2 x_2 + \beta_{12} x_1 x_2 + \beta_{11} x_1^2 + \beta_{22} x_2^2 + \varepsilon \quad (4.2)$$

With y as the response,
β_0 as the intercept,
$\beta_1 x_1$ as the linear effect of factor 1,
$\beta_2 x_2$ as the linear effect of factor 2,
$\beta_{12} x_1 x_2$, as the interaction effect between factor 1 and 2,
$\beta_{11} x_1^2$ as pure quadratic interaction of factor 1,
$\beta_{22} x_2^2$ as pure quadratic interaction of factor 2, and
ε as the error term.

The central composite design (CCD), a common type of Response Surface Methodology, are particularly adept at fitting second-order polynomial models. These designs efficiently explore the experimental domain with fewer runs compared to full factorial designs while still estimating all coefficients, making them an efficient strategy for optimising processes. For instance, a CCD for two factors comprises a two-level factorial design, supplemented with axial points and one centre point shown in Figure 4.6. Highlighted in green is the central point (n_C). For statistical significance and ensuring reproducibility, the central point reaction is often carried out in multitude since a minimum of 12 data points are required for a reliable CCD analysis. The CCD is a spherical design in which all points are at the same distance from the centre point. Based on Pythagoras theorem, the distance to the centre point (0,0) would be $\alpha = \sqrt{2} \cong 1.414$ for all points. The number of data points is determined by the number of factors (k) resulting in axial points $n_A = 2k = 4$, shown in red, and factorial points $n_F = 2^k = 4$, shown in blue. This structure allows for rotatability and

robust estimation of linear, quadratic, and interaction effects, which are crucial for capturing curvature and interaction effects in process optimisation.

To investigate a second-order regression model, a Central Composite Design must be established, natural variables identified, and quantifiable performance metrics defined. This experimental design allows for the generation of tridimensionality response surfaces or bidimensional contour plots, which are invaluable for describing datasets and predicting optimal response values.

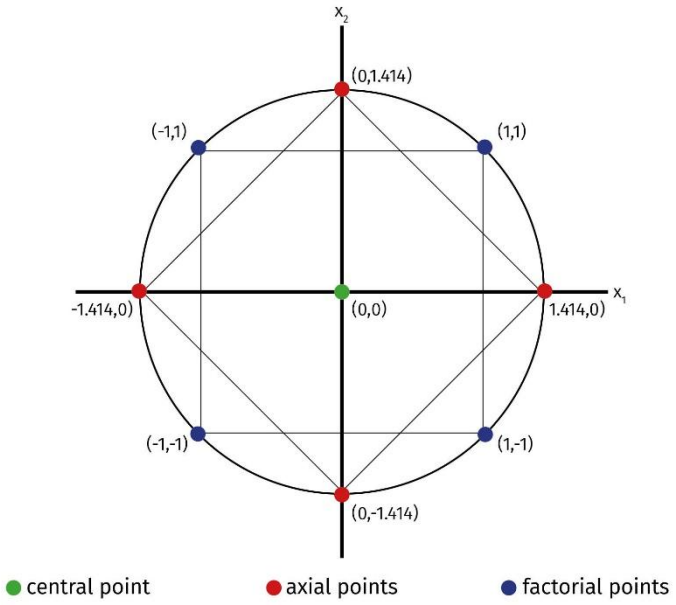

Figure 4.6, Visualisation of the Central Composite Design, with the axial and factorial points at 1.414 from the central point (0,0), resulting in a circle shape

To elucidate the principles of Response Surface Methodology, this study presents an illustrative example focused on reaction optimisation, based on the dataset provided by Dr. R. Rech.[61] The Central Composite Design will be employed to fit a quadratic model, thereby identifying the experimental parameters that yield the maximum response. Furthermore, the methodology for analysing multiple responses concurrently will be demonstrated. The data analysis will be conducted Utilising R-Studio. This statistical software provides comprehensive tools for model fitting, graphical representation, and optimisation, ensuring a thorough exploration of the experimental design space.

4.1.6 Building the central composite design

The example study investigates the reaction parameters of reaction time and temperature, and evaluates its performance based on three specified responses, including the quantum yield (%), turbidity (NTU), and the λ_{max} (nm) of the product. The goal of the study is to find the reaction parameters that will result in a quantum yield of 49% or more, a turbidity between 10 – 15 NTU, and a λ_{max} of 460 nm or lower. These goals are critical when designing and investigating system parameters and will be revisited during the multi-objective optimisation phase to balance competing objectives in this example including maximising the quantum yield while minimising λ_{max} or maintaining turbidity within a specific target.

In this example, the central point of the reaction was 60 min, 150 ˚C, with a variation of 5 min or 5 ˚C for the factorial points, respectively. To find the values for the experimental matrix of x_1 and x_2, the following relations are established:

$$x_1 = \frac{Time - 60}{5} \tag{4.3}$$

$$x_2 = \frac{Temperature - 150}{5} \tag{4.4}$$

Based on the central composite design, the reaction matrix was constructed to systematically explore the influence of these two factors on the measured responses, the populated reaction matrix is detailed in Table 4.4.

Table 4.4, Central Composite Design of example Design of Example Model

Reaction nr.	x1	x2	Time (min)	Temperature (˚C)	QY (%)	Turbidity (NTU)	L_{max} (nm)
1	-1	-1	55	145	47.6	19.4	393
2	-1	1	55	155	47.9	23.3	463.9
3	1	-1	65	145	48.6	11.7	491.9
4	1	1	65	155	49.5	25.3	520
5	0	0	60	150	50	5.8	427.8
6	0	0	60	150	49.8	7.8	455.8
7	0	0	60	150	49.6	3.9	439.8
8	0	0	60	150	49.7	1.9	467.9
9	1.414	0	67.07	150	48.8	7.8	449.2
10	-1.414	0	52.93	150	47.1	1.9	403.7
11	0	1.414	60	157.07	48.9	27.2	485.2
12	0	-1.414	60	142.93	47.9	29.2	421.1

4.1.7 The Second-Order Regression Model

Following the generation of the design matrix, the model is iteratively run and optimised to identify the best fit for the output data. This process involves running the model within R and scrutinising the analysis of variance, paying close attention to metrics such as the multiple R-squared, adjusted R-squared, p-value, and lack of fit. The optimal values for multiple R-squared and adjusted R-squared approach 1, indicating a strong fit, while the p-value and lack of fit should ideally be close to 0 or statistically insignificant. Model adjustments are made by systematically removing non-significant quadratic terms and interaction effects of the factors, which in turn modifies the fit of the experimental data to the model. Through this iterative evaluation of model fit, it is possible to discern which factors, and their interrelationships most effectively describe the underlying data model. Each response, in this case yield, viscosity, and molecular weight, is analysed independently using a second-order polynomial model to determine the optimal fit for each output.

The models for the quantum yield and the turbidity response were found optimal including all second order regression factors. The model for the λ_{max} fit the model best by excluding the quadratic interactions. Relying on the linear relation of both factors and their two-way interactions. This resulted in the following models:

$$Quantum\ yield\ = \beta_0 + \beta_1 x_1\ + \beta_2 x_2\ + \beta_{12}\, x_1 x_{\,2} + \beta_{11}\, x_1^2 + \beta_{22}\, x_2^2 \quad (4.5)$$

$$Turbidity\ = \beta_0 + \beta_1 x_1\ + \beta_2 x_2\ + \beta_{12}\, x_1 x_{\,2} + \beta_{11}\, x_1^2 + \beta_{22}\, x_2^2 \quad (4.6)$$

$$\lambda_{max}\ = \beta_0 + \beta_1 x_1\ + \beta_2 x_2\ + \beta_{12}\, x_1 x_{\,2} \quad (4.7)$$

Analysis of variance shows the quantum yield provides a very good fit for the second order model. The turbidity produces lower R-squared values but a reduction in lack of fit, compared to the quantum yield. The λ_{max} model fit the data poorly with the multiple R-squared value of 0.72 and increased p-value and lack of fit compared to the turbidity. However, the model could not be further improved by in- or excluding more terms in the model.

Table 4.5, Analysis of variance of the three responses, Yield, Viscosity, and Molecular Weight

	Quantum yield	Turbidity	λ_{max}
Multiple R-squared	0.9808	0.9005	0.7199
Adjusted R-squared	0.9647	0.8177	0.6148
p-value	$4.575*10^{-5}$	0.005749	0.01334
Lack of fit	0.42152	0.1051	0.2811

4.1.8 Residual plots

After determining the optimal model fit, residual plots are constructed to verify the randomness of residuals or to identify any patterns not captured by the model. In our example study, the residual plots of each model (quantum yield, turbidity, λ_{max}) include the response against the residual, as well as x1 (time) and x2 (temperature) versus the residual. Should these residual plots suggest a lack of randomness, a re-evaluation of the model and data is necessary, potentially involving the identification and management of outliers or model refinements, before new residual plots are generated and evaluated prior to proceeding with the generation of contour plots.

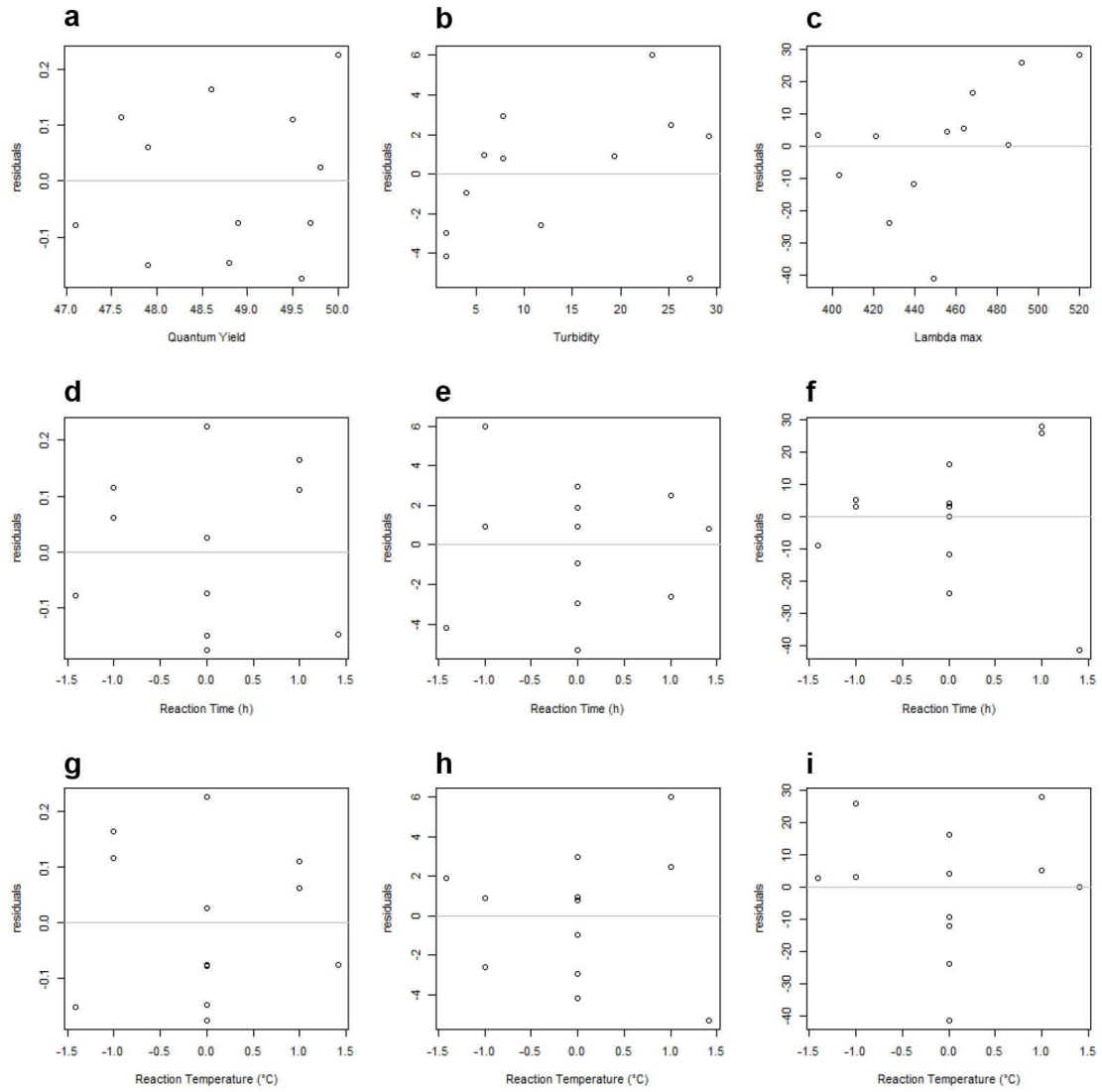

Figure 4.7, Residual plots of, (a) quantum yield against residuals, (b) turbidity against residuals, (c) λ_{max} against residuals, residuals against reaction time for the model of (d) quantum yield, (e) turbidity, and (f) λ_{max}. Residuals against reaction temperature for the model of (g) quantum yield, (h) turbidity, and (i) λ_{max}. * Note: residual plot (i) shows a mirror image on the x-axis, however since this is an example data set purposed to demonstrate the method of RSM, this is disregarded and not further investigated.

4.1.9 Contour plots

Following the validation of the model and residual plots, contour plots can be generated. These visualisations display the individual responses of quantum yield, turbidity, and λ_{max} , by plotting x1 and x2 on the respective axes, with the response represented as a heatmap, Alternatively, a three-dimensional plot can be created with the response depicted on the z-axis, both options shown in Figure 4.8. Various relationships between the reaction conditions and the observed output can be established and visualised.

In this example study, the objectives include maximising quantum yield, maintaining turbidity within a specific target, and minimising the λ_{max} of the product. This provides guidance on interpreting contour and three-dimensional plots for individual responses, thereby assisting in the determination of optimal operational zones within the experimental design space. For example, the contour plot of the yield in Figure 4.8 (a),

shows response of 49.5% in a circular shape centred around a maximum of reaction temperature 152 ˚C and 62 min. In the contour plot of the turbidity Figure 4.8 (b) a clear minimum is also visible; however, a range of acceptable responses was identified between 10 – 15 NTU. This results in optimised conditions between 146 – 147.5 and 153 – 155 ˚C approximately across all reaction times. Lastly, the acceptable response for the λ_{max} was identified as lower than 460 nm. This results in an acceptable response for the green and yellow area, under the curve from x-axis at 65 min to the y-axis at 156 ˚C on the contour plot in Figure 4.8 (c).

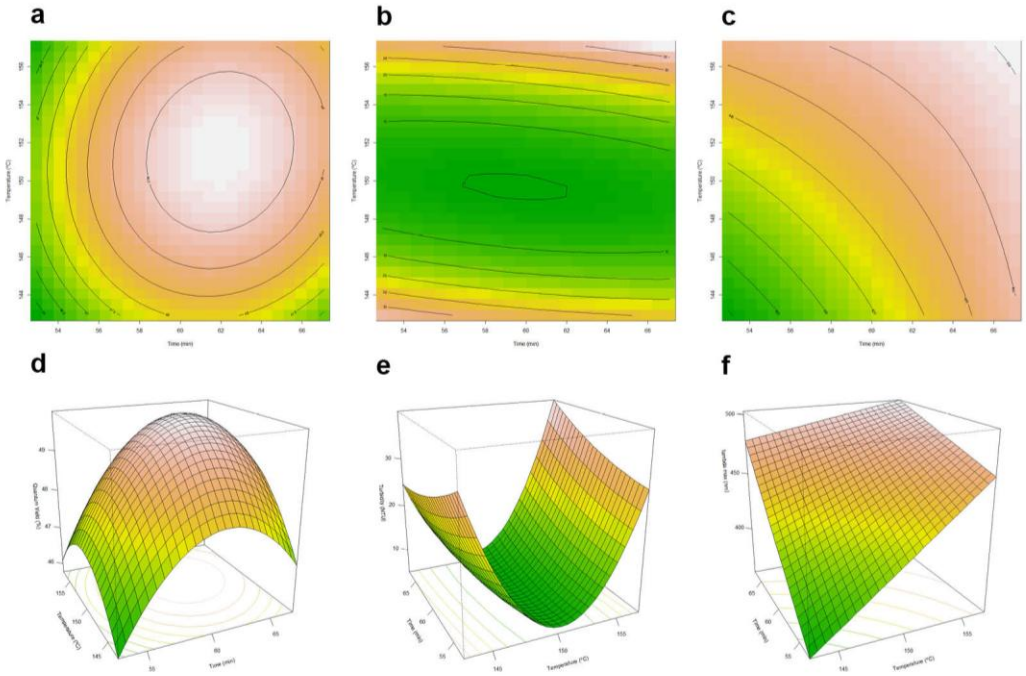

Figure 4.8, Contour plot of the model for quantum yield (a), turbidity (b), and λ_{max} (c), 3D-plot of the model for the quantum yield (d), turbidity (e), and λ_{max} (f).

4.1.10 Optimisation of the multi-objective problem

To optimise any multi-objective problem, careful consideration of trade-offs is necessary, often visualised through overlaying contour plots or desirability functions to identify optimal operating regions where all objectives are met or appropriately balanced. In our example study the acceptable responses for yield are set to be over 49.0%, turbidity between 10 – 15 NTU, and λ_{max} below 460 nm. These specific target ranges define the boundaries within which a satisfactory compromise among competing objectives can be achieved. The outcome of this multi-problem objective optimisation resulted in the following overlay plot, show in Figure 4.9. The overlay plot shows two areas which satisfy the boundaries of all responses, highlighted in green.

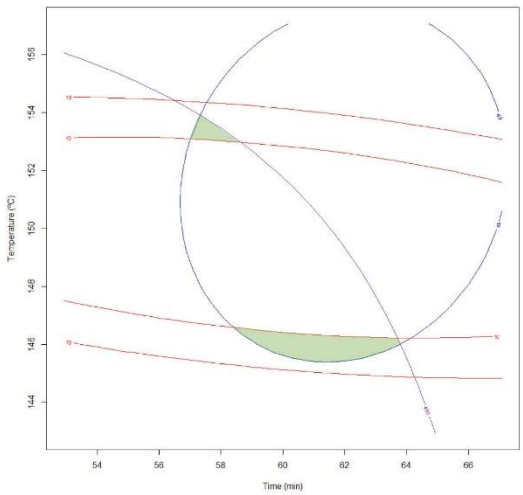

Figure 4.9, Overlay plot of the desirable reaction conditions for satisfactory responses for the quantum yield, turbidity, and λ_{max}.

Additionally, the desirability function, serves as a robust tool to combine multiple responses into a single metric, allowing for a comprehensive evaluation of overall process performance and the identification of optimal parameter settings that simultaneously satisfy all established criteria. This function transforms each response into a desirability value ranging from 0 to 1, where 1 signifies the most desirable outcome and 0 indicates an undesirable result. The individual desirability values are then aggregated into an overall desirability score, which facilitates the identification of optimal factor settings that simultaneously maximise the desired responses and minimise undesired outcomes. This aggregated desirability score is then maximised to pinpoint the optimal experimental conditions that achieve the best compromise across all specified objectives. Such an approach facilitates the identification of robust operating windows where process parameters can be varied slightly without significantly compromising the overall desirability, offering practical flexibility.

$$y_i \rightarrow 0 \leq d_i \leq 1 \tag{4.8}$$

y_i is at its goal or target $\rightarrow d_i = 1$, and

y_i is outside an acceptable region $\rightarrow d_i = 0$,

$$D = (d_1 * d_2 * \dots * d_m)^{\frac{1}{m}} \tag{4.9}$$

With D is overall desirability, and

m is the number of responses.

The overall desirability will be zero if any of the individual responses is undesirable.

The function to maximise a response includes:

$$d_{max} = \begin{cases} 0, & y < L \\ \left(\dfrac{y-L}{T-L}\right)^r, & L \leq y \leq T \\ 1, & y > T \end{cases} \tag{4.10}$$

The function to target a range of responses includes:

$$d_{target} = \begin{cases} 0, & y < L \\ \left(\dfrac{y-L}{T-L}\right)^{r_1}, & L \leq y \leq T \\ \left(\dfrac{U-y}{U-T}\right)^{r_2}, & T \leq y \leq U \\ 1, & y > U \end{cases} \tag{4.11}$$

The function to minimise the response includes:

$$d_{min} = \begin{cases} 1, & y < T \\ \left(\frac{U-y}{U-T}\right)^r, & T \leq y \leq U \\ 0, & y > U \end{cases} \quad (4.12)$$

In Table 4.6 the set values for the lower and upper limit, target and weight are given together with the desirability functions suitable for the optimisation of the reaction parameters for the response.

Table 4.6, overview values used for the desirability functions for the multiple response example model

	Quantum yield	**Turbidity**	λ_{max}
function	d_{max}	d_{target}	d_{min}
L (lower limit)	49.0	10	-
U (upper limit)	51.0	15	460
T (target)	-	12.5	300
r (weight)	1	$r_1 = r_2 = 1$	1

Following the establishment of the mathematical functions, a grid is constructed to determine desirability. Natural values are incorporated alongside the predicted responses, after which the desirability is computed for each data point. Finally, the desirability function is graphically represented and shown in Figure 4.10. The desirability plot delineates the operational space in blue where all individual response objectives are achieved, pinpointing the optimal parameter settings that yield the highest overall desirability, with increased saturation. For the example model, the highest overall desirability is achieved when using reaction parameters temperature 146.5 ˚C and time 61 min.

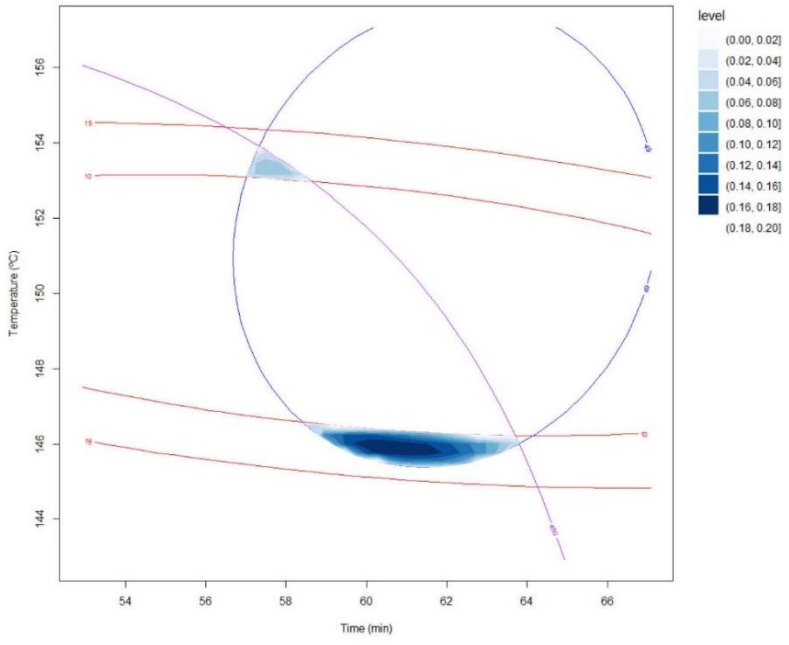

Figure 4.10, The desirability plot of the satisfactory responses for the quantum yield, turbidity, and λ_{max} of the example model.

4.2 Experimental

4.2.1 Materials

Seaweed specimens, comprising kelp and Irish moss, were sourced from Mungo Murphy's Seaweed. Prior to dispatch, the seaweed was subjected to a drying procedure whereby the seaweed was left to dry at 30 ˚C until it has lost all it flexibility.

Essential laboratory reagents, such as D-galactose, sodium alginate, K-carrageenan, and quinine sulfate were acquired from Sigma-Aldrich, whereas D-glucose was procured from Fisher Scientific. All chemical compounds were utilised in their as-received condition without further purification.

4.2.2 Methods

Preparation of reaction mixture

Homogeneous reaction solutions were prepared by dissolving and stirring saccharide precursors in 250 mL of distilled water, with concentrations adjusted to the solubility of each saccharide. This yielded solutions of 1.0 M D-glucose and D-galactose, 0.05 M sodium alginate, and 0.006 M K-carrageenan, providing sufficient stock for reactions involving each precursor.

Table 4.7, Precursor properties including solubility and monosaccharide content. *Calculated based on saccharide analysis in previous chapter

	Molecular weight (g/mol)	**Monosaccharide (units /mol)**	**Soluble saccharide content (g/l)**	**Conc. (mol/l)**	**Monosaccharide conc. (mol/l)**	**Conc. (g/mL)**
D-glucose	180.2	1.0	909	5.0	5.0	0.18
D-galactose	180.2	1.0	180	1.0	1.0	0.18
Sodium alginate	12000 – 40000	67 – 222	10	$2.5 – 8.3 * 10^{-4}$	$5.6 * 10^{-2}$	0.01
K-carrageenan	400000	2220	5	$1.25 * 10^{-5}$	$2.8 * 10^{-2}$	0.005
Kelp			49.8*			0.050
Irish moss			24.9*			0.025

For the seaweed-based reactions, the biomass was processed using a Nutribullet 900 pro and subsequently fractionated by particle size. A two-sieve system, comprising a 100 µm mesh below a 500 µm mesh, with a collection tray, separated the ground seaweed into three size fractions. For the hydrothermal synthesis of carbon dots, the intermediate fraction, particles retained on the 100 µm sieve and passing through the 500 µm sieve, was Utilised. Smaller particles were excluded due to excessive salt content integrated during drying, while larger particles were re-ground to achieve a uniform sample size. This iterative process continued until 100 grams of ground biomass were collected. To prepare the seaweed reaction mixtures, each reaction was individually formulated by combining 1 g of ground biomass with 12 mL of distilled water, resulting in a heterogeneous suspension.

Hydrothermal synthesis of carbon dots

Subsequently, 12 mL of this reaction mixture was transferred into Teflon cups, sealed, and secured within stainless-steel autoclaves. These autoclaves were then placed in a preheated oven for a duration and temperature determined by the Central Composite Design. Following the reaction period, the autoclaves were cooled to room temperature.

Following the reaction period, the autoclaves were dismantled, and the resulting soluble samples underwent filtration using 0.22 µm nylon syringe filters. For reactions involving biomass that produced substantial solid material, an initial centrifugation step at 8000 rpm for 10 min was performed to separate the solid components from the reaction solutions prior to filtration. The processed samples were subsequently stored in glass vials, protected from light. The recovered solid residues were dried in an oven at 50°C overnight, or until complete moisture removal was achieved. For reactions Utilising kelp and Irish moss, the mass of the solid precipitate post-reaction was quantified and recorded.

Design of experiment – Central Composite Design

The experimental design for carbon dot synthesis will be centred around a previously established reaction protocol, as detailed in the preceding chapter, the central point of the central composite design was chosen 4 h and 160 ˚C. The independent variables, designated as x1 and x2, were systematically varied by ±2 h and ±40 °C, respectively. The following relations are established:

$$x_1 = \frac{Time - 4}{2} \tag{4.12}$$

$$x_2 = \frac{Temperature - 160}{40} \tag{4.13}$$

This methodology, which considers temperature and reaction time as critical variables, was designed with the primary goal of identifying the sample with the highest emission after hydrothermal synthesis.
Simultaneously, the study aimed to reduce waste generation and reduce post-reaction processing. To measure these objectives, the following quantifiable metrics were defined: the dilution factor (DF) and the integrated area of the photoluminescence intensity (IA). The dilution factor was defined as following:

$$Dilution\ Factor = \frac{\left(\frac{Volume\ sample\ (0.1\ A)}{Volume\ sample + water\ (0.1\ A)}\right)}{Volume\ supernatant\ from\ reaction} \tag{4.14}$$

$Volume\ sample\ (0.1\ A)$ = the volume of the sample used to dilute to 0.1 absorption (µL) in cuvette.
$Volume\ sample + water\ (0.1\ A)$ = the total volume of water and sample to dilute to 0.1 absorption (µL) in cuvette.
$Volume\ supernatant\ from\ reaction$ = volume supernatant produced in hydrothermal reaction (mL).

The synthesised carbon dots were diluted with water to achieve an absorbance of 0.1 at their respective excitation maxima. Both the specific absorbance value and the corresponding dilution factor (DF) were meticulously documented, serving as the foundational quantitative data for the subsequent response surface methodology analysis.

The integrated area of the photoluminescence intensity was systematically quantified through the following: A representative sample from the central point of the experimental design was analysed using three distinct excitation wavelengths: 345 nm, 360 nm, and 375 nm, chosen based on their prevalence in the relevant literature. Subsequently, the sample that demonstrated the highest emission intensity at its optimal excitation wavelength (λ_{ex}) was further analysed by acquiring an excitation spectrum at its emission maximum ($\lambda_{em,max}$). This identified excitation wavelength ($\lambda_{ex,coll.}$) was then employed to generate an emission spectrum, which was subsequently compared against spectra obtained at the three standard excitation wavelengths. To ensure the comparability of emission intensities, all measurement parameters were maintained consistently. Following this comparative analysis, the excitation wavelength ($\lambda_{ex,\ opti}$) that elicited the greatest emission intensity was selected for subsequent investigation of the emission profile across all reactions employing the identical precursor.

For all reactions utilising the same precursor, excitation wavelengths, emission collection ranges, and slit widths were kept constant. The emission response was documented as a corrected spectrum against the corrected lamp intensity (S1c/R1c). Following the refinement of emission spectra through the exclusion of Raman scattering the absolute integrated area (IA) within the designated emission wavelength range was computed. This computation provided not only the integrated area of the photoluminescence response but also generated values for maximum intensity, the excitation wavelength at maximum intensity, and the full width at half maximum, thereby offering a more profound understanding of how parameter variations influenced the outcomes.
Subsequently, two quantitative metrics, the Integrated Area and the Dilution Factor, were established, thereby enabling the population of the Central Composite Design. Following the formulation of the Central Composite Design, the experimental outcomes were methodically documented, with the R script utilised for this approach elaborated upon in the appendices.

4.2.3 Characterisation

UV-vis absorption

UV-Vis spectra were acquired using a Varian CARY50 UV-Vis spectrophotometer, spanning the wavelength range of 250 to 800 nm. The measurements were performed with a data interval of 1 nm, a slit width of 1 nm, and a scan speed of 240 nm/min. The instrument's lamp was changed at 326 nm, and a double-sided 10 mm quartz cuvette was Utilised for the analysis.

Photoluminescent spectroscopy

Photoluminescence spectra were acquired using a HORIBA FluoroMax benchtop spectrometer. The excitation wavelengths ranged from 280 to 460 nm, and the emission wavelengths were scanned from 300 to 700 nm. To ensure a reliable signal magnitude of 10^6, the slit widths were adjusted accordingly, and measurements were conducted in a 10 mm four-sided QS High Precision Cell from Hellma.Analytics.

Quantum Yield Measurements

Emission quantum yields were determined using the optically dilute method.[62, 63] Stock solutions of absorbance values of *ca.* 0.3 at λ_{ex} = 350 nm were prepared and diluted to yield solutions with absorbances of *ca.* 0.1, 0.075, 0.05 and 0.025. The Beer-Lambert Law was found to be linear at these concentrations. Emission spectra were obtained in aerated conditions. Linear regression analysis between the absorption and emission intensity verified the relationship with R^2 values surpassing 0.99 in all cases. Individual relative quantum yield values were calculated for each solution and reported values represent the slope value:

$$\varphi_s = \varphi_r \left(\frac{A_r}{A_s}\right)\left(\frac{I_s}{I_r}\right)\left(\frac{n_s}{n_r}\right)^2 \quad (4.15)$$

φ_r is the absolute quantum yield of the reference

n is the refractive index of the solvent and assumes $n \approx 1.33$ for water.

A and *I* describe the absorbance values at the excitation wavelength and integrated area under the emission curves, respectively,

while *r* and *s* subscripts denote the reference and sample values, respectively

A solution of quinine sulfate in 0.1 M H_2SO_4 (φ_r = 57.7% with λ_{ex} 350 nm) was used as the external reference.[64]

4.3 Results and Discussion

The optimisation results for the hydrothermal synthesis of carbon dots are presented below, focusing on six precursors: monosaccharides, polysaccharides, and biomass derived from the brown seaweed Kelp and the red seaweed Irish moss. The experimental design for the hydrothermal synthesis of carbon dots mirrored that of the preceding chapter, focusing on precursor selection. To elucidate the formation mechanisms of carbon dots from carbohydrate sources within seaweed biomass, three categories of sugar precursors were examined. The first category comprised the raw seaweed biomass, establishing a baseline reflective of its natural saccharide composition. The second category included alginate and carrageenan, the predominant polysaccharides in kelp and Irish moss, respectively. Finally, the study investigated monosaccharides, specifically glucose and galactose, to establish a simplified yet pertinent reaction system for hydrothermal carbon dot synthesis. Although prior research indicated that D-glucose is not an ideal proxy for the sugar content in kelp, it was included in this investigation to leverage the findings from the previous chapter.

4.3.1 D-Glucose

Given that D-glucose was found to be the least representative sugar in seaweed's composition, this precursor was initially employed as a preliminary test. This allowed for subsequent adjustments to the experimental parameters before proceeding with the analysis of other precursors.

Table 4.8, Populated CCD of D-glucose reactions

Reaction nr.	x1	x2	Time (h)	Temperature (°C)	Type of data point	IA ($\times 10^8$)	DF	ABS (A)	Solids Y/N
1	0	0	4	160	central	1.39	0.0005	0.10	N
2	0	0	4	160	central	1.44	0.0005	0.09	N
3	0	0	4	160	central	1.36	0.0006	0.09	N
4	0	0	4	160	central	1.39	0.0006	0.10	N
5	0	0	4	160	central	1.40	0.0006	0.09	N
6	-1.414	0	1.17	160	axial	2.08	0.0460	0.09	N
7	1.414	0	6.83	160	axial	1.47	0.0005	0.09	N
8	-1	-1	2	120	factorial	0.84	0.0909	0.09	N
9	1	-1	6	120	factorial	2.34	0.0204	0.11	N
10	-1	1	2	200	factorial	2.53	0.0004	0.10	Y
11	1	1	6	200	factorial	3.19	0.0006	0.09	Y
12	0	-1.5	4	100	axial	0.24	0.0909	0.01	N
13	0	1.5	4	220	axial	3.83	0.0008	0.10	Y

Shown in Table 4.8 is the D-glucose CCD. The central composite design indicated that conducting the central point reaction at a reaction time of 4 h and a reaction temperature of 160 °C multiple times yielded five data entries. Combined with four axial points and four factorial points, this experiment generated a total of thirteen data points. The populated CCD of D-glucose is given in Table 4.8. The initial selection for axial points used α of 1.414, which led to reaction times of 1.17 and 6.83 h. To simplify the process, α was adjusted to 1.5, yielding reaction times of 1 and 7 h, and reaction temperatures of 100 and 220 °C, instead of the previously determined 103.44 and 216.56 °C. This modification streamlined the experimental design

without compromising the statistical integrity of the central composite methodology, facilitating a more manageable yet robust exploration of the parameter space. This data was used to gather information on the linear, quadratic, and interaction effects between reaction time and temperature.

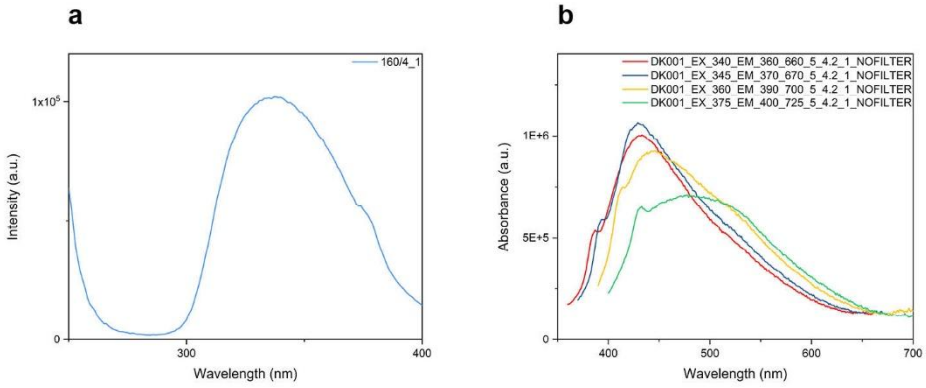

Figure 4.11, Excitation spectrum with λ_{em} 429 nm (a), and emission spectra with λ_{ex} 345, 360 and 375 nm (b) of the sample from hydrothermal synthesis of D-glucose at the central point (160 ˚C/4 h)

After synthesising D-glucose via the hydrothermal method described in the experimental section, and with reaction variables set according to the CCD, minimal precipitate was produced. Therefore, filtration with a 0.22 µm nylon filter was sufficient to collect the supernatant The samples were diluted to 0.1 A at 365 nm. The diluted samples were screened to find the optimum λ_{ex} by exciting at 345, 360 and 375 nm, and slit widths of 5 and 4.2, respectively into and out of the chamber. Exciting at λ_{ex} 345 nm resulted in the highest emission intensity at λ_{em} 429 nm and an excitation spectrum was run with λ_{em} set to 429 nm, shown in Figure 4.11 (a) This resulted in maximum excitation intensity at 340 nm. A fourth emission spectrum with λ_{ex} 340 nm was produced. All examined emission spectra are shown in Figure 4.11 (b), and it concluded that exciting at 340 nm does not increase the photoluminescence emission intensity, therefore λ_{ex} 345 nm with slit widths 5/4.2 will be used for all D-glucose samples to record the emission spectra in this study.

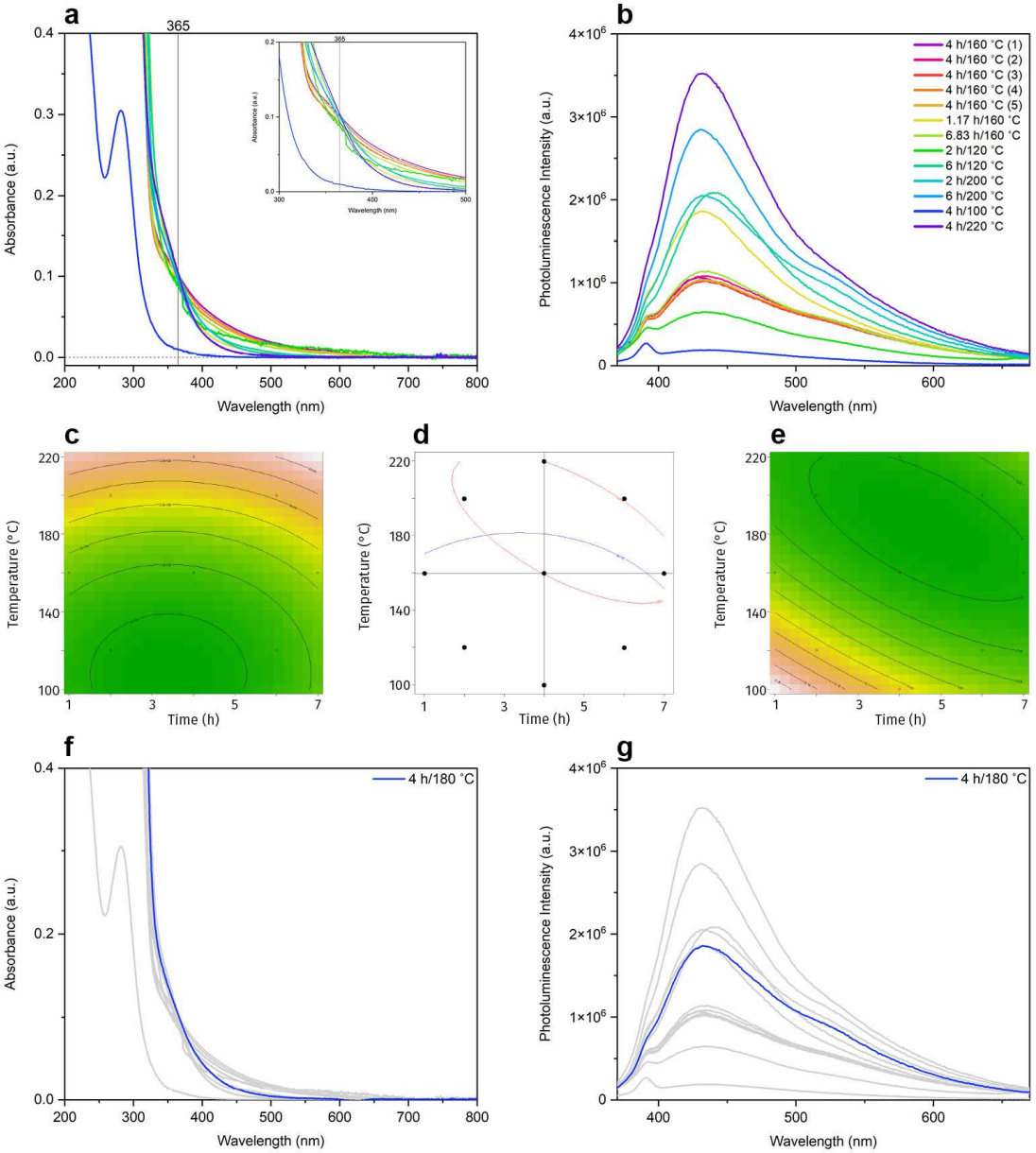

Figure 4.12, Optical characterisation of D-glucose carbon dots, (a) absorption diluted to 0.1 A at 365 nm, (b) emission spectra, at λex 345 nm, λcollect 370 – 670 nm, and slits 5/4.2, (c) contour plot of the IA response, (d) overlay plot of IA and DF responses, (e) contour plot of the DF response, (f) absorption spectra with optimised reaction condition highlighted, (g) photoluminescence spectra with reaction conditions highlighted

Diluting all D-glucose samples to 0.1 A at 365 nm resulted in the spectra shown in Figure 4.12. In (a) the absorption of all samples is shown, in the graph the absorption spectra follow the same trend, with slight differences in the absorption curve, with changes in the onset of the absorption and variations from smooth transitions to stronger changes presenting shoulders. All but one sample, (100 ˚C/4 h) measured closely to 0.01 A at 365 nm. The one outlier was measured 0.0094 A undiluted. This is a magnitude lower than intended, however, since this sample is undiluted, this is indicative of a very poor response because of the reaction conditions. This will be taken into consideration in the analysis that follows.

Secondly the emission spectra of the D-glucose samples are shown in Figure 4.12 (b), the data was gathered with λ_{ex} 345 nm, slits 5/4.2, recording the S1c signal. The emission peak was found around the same wavelengths of 429 – 443 nm. A second emission peak around 520 nm is present in the spectra, most prominent at central point 160 ˚C/4 h and least prominent at high temperature conditions of 220 ˚C/4 h. From these spectra gathered, the five central points, show minimal variation between them with $\lambda_{em,max}$ 435 nm, and 1 * 10^6 intensity. Three reaction parameter combinations produced a doubled intensity around 2 * 10^6 intensity, including the combinations of 120 ˚C/6 h, 160 ˚C/6.83 h, and 200 ˚C/ 2 h. The reaction combinations of 200 ˚C /6 h performed even better with 2.8 * 10^6, and 220 ˚C/ 4 h produced the highest measured intensity of 3.5 * 10^6. Additionally, three reaction combinations resulted in the formation of solids in reaction, including 200 ˚C/ 2 h, 200 ˚C /6 h, and 220 ˚C/ 4 h.

It is anticipated that more rigorous conditions, characterised by extended reaction durations and elevated temperatures, will augment the reaction dynamics and kinetics and consequently the synthesis of materials. A clear system boundary for the formation of solids during the reaction has been identified, establishing an upper limit for the reaction temperature at 200 °C, independent of the reaction time. When comparing the photoluminescence spectra at a constant reaction temperature of 160 °C, the shorter reaction time of 1.17 h yields a sample with significantly greater photoluminescence than the 4-hour reactions, whereas the 6.83-hour reaction exhibits similar luminescence intensity. This suggests that shorter reaction times are favourable, or that increasing reaction time does not enhance luminescence when employing D-glucose in the reaction.

Lowering the reaction temperature leads to a reduction in luminescence intensity, with a reaction time of 2 h at 120 °C producing significantly less luminescence compared to the central point, while a 6-hour reaction time at the same temperature yields similar results. These findings underscore the significant influence of both reaction temperature and time on the properties of the synthesised carbon dots. It is hypothesised that extending the reaction time and increasing the reaction temperature enhance the synthesis of photoluminescent carbon dots. However, this also leads to an increase in solid formation, presenting a trade-off between material performance and by-product generation. Furthermore, the experimental data suggest an optimal reaction time beyond which further extensions result in a decline in optical properties. The spectrum generated at 100 °C for 4 h was excluded from this analysis due to its diminished absorption at 365 nm.

The excitation spectra were acquired at the emission wavelength exhibiting maximum intensity, spanning a range of 280–400 nm, Utilising consistent slit widths. The observed intensities were comparable to those in the emission spectra. The peak excitation wavelengths ranged from 329 nm at 100 °C for 4 h to 354 nm at 120 °C for 6 h. To populate the CCD, the S1c signal was integrated over the range of 400–670 nm, effectively excluding the Raman peak from the spectra, thereby yielding the IA response. The dilution factor was determined according to the methodology outlined in this chapter. The populated CCD data can be referenced in Table 4.8. The second-order regression model was optimised by omitting two-way interactions for the Integrated Area. The absence of two-way interaction terms in the model indicates that the individual effects of reaction time and temperature on the integrated area are largely independent within the studied range. The complete second-order regression model, incorporating all interaction terms, effectively elucidates the collective influence of these synthesis parameters on the dilution factor. Yielding the following models:

$$IA(glucose) = \beta_0 + \beta_1 x_1 + \beta_2 x_2 + \beta_{11} x_1^2 + \beta_{22} x_2^2 \quad (4.17)$$

$$DF(glucose) = \beta_0 + \beta_1 x_1 + \beta_2 x_2 + \beta_{12} x_1 x_2 + \beta_{11} x_1^2 + \beta_{22} x_2^2 \quad (4.18)$$

Table 4.9, Analysis of variance of the integrated area and dilution factor of D-glucose reactions

	Integrated Area	**Dilution Factor**
multiple R-squared	0.792	0.9971
adjusted R-squared	0.688	0.995
p-value	0.007799	1.059e-08
Lack of Fit	7.547e-06	6.920e-08

The multiple R-squared value for the integrated area model was determined to be 0.792, indicating a suboptimal fit. In contrast, the dilution factor model demonstrated a strong fit. Despite this being the initial application of this model, it was retained for further investigation, with the understanding that future iterations, particularly for other precursors within this study, could benefit from enhancements. A key potential improvement involves acquiring the S1c/R1c signal rather than solely the S1c signal, which is expected to elevate the data quality. This improved signal acquisition strategy would directly address the limitations observed in the integrated area model, potentially leading to a higher R-squared value and more robust predictive capabilities for future precursor analyses.

The residual plots, presented in the appendix, Figure A 1, exhibited random distributions. Contour plots for the integrated area and dilution factor, generated by the model, are in Figure 4.12 (c) and (e) respectively. Analysis of the integrated area revealed an optimal reaction time of 3.5 h, independent of temperature, consistent with observations from optical characterisation spectra. The reaction temperature demonstrated a positive linear correlation. For the dilution factor, an optimum was identified concerning both reaction time and temperature, characterised by a linear relationship at lower reaction times and temperatures. However, when considering the combined effect of reaction time and temperature, a minimum was observed, beyond which the dilution factor increased. A third critical factor, solid formation, becomes prominent at reaction temperatures of 200 °C and above. Given the established objective of minimising side product formation, reaction temperatures below 200 °C are advisable. Integration of the contour plots yielded an overlay plot, shown in Figure 4.12 (d). Based on these model outputs, the optimised reaction conditions for the D-glucose reaction were determined to be 180 °C for 3.5 h. However, it is unknows at what temperature in the range of 160–200 °C precipitate is formed. By selecting a reaction time of 4 h, consistent with the central and vertical axial points, any potential solid formation can be attributed to the interplay between temperature and solid generation, independent of reaction time variations. Therefore, the optimised reaction conditions tested were 180 °C for 4h.

The optimised reaction parameters of 180 °C for 4 h yielded a homogeneous sample, free from solid by-products. The absorption and emission spectra corresponding to this condition are presented in blue in Figure 4.12 (f) and (g), respectively. Notably, the absorption spectrum closely resembled those obtained under all other tested conditions. The photoluminescence spectrum and intensity for this optimised condition were nearly double that of the central experimental point, with a maximum emission wavelength $\lambda_{em,max}$ of 432 nm and an intensity of $1.9 * 10^6$, although these parameters did not correspond to the highest observed emission intensity.

The model's prediction for the integrated area under optimised reaction conditions (180 °C for 4 h) was $1.8*10^8$, however, the experimentally measured integrated area response was $2.3*10^8$, representing a deviation of over 25% from the predicted value. The calculated dilution factor was 0.0005, which is among the lowest observed dilution factors within the experimental design. Notably, the reaction parameter combination of 200 °C for 2 h yielded a lower dilution factor of 0.0004 and a higher integrated area of $2.5*10^8$ compared to the optimised conditions, even though solid by-products were formed during this reaction. This suggests that while a low dilution factor is achievable, it must be balanced against the propensity for solid byproduct formation at higher temperatures, indicating a critical trade-off in the optimisation process. Further investigation into the interplay between temperature, reaction time, and byproduct formation is crucial to fully understand and mitigate this challenge.

After the initial precursor's analysis within the experimental design, several modifications were instituted.

1. Primarily, the number of central data points was reduced to four, deemed adequate for demonstrating reproducibility, as twelve total data points had already furnished sufficient information for the analysis.
2. Concurrently, the axial points were adjusted to x = 1.5 from the previous value of 1.41. This adjustment corresponded to reaction times of 1 and 7 h, and reaction temperatures of 100 and 220 °C. The adoption of rounded numerical values, rather than the precise 1.41 from the circular design, was rationalised by the consideration that minor variations of a few degrees Celsius or min might not substantially impact the outcomes.
3. Finally, the recorded emission spectrum was changed from the S1c signal to the S1c/R1c signal. This change was implemented to improve data quality by mitigating the variability linked to lamp performance. This enhanced signal acquisition method was expected to yield a more stable and accurate representation of the luminescence, thereby improving the reliability of the quantitative analysis of subsequent precursors

These adjustments are anticipated to provide a more robust and accurate model for optimising reaction conditions for the other precursors, leading to a more precise understanding of the factors influencing reaction outcomes, similar to how design of experiments approaches have accelerated optimisation in other chemical processes.

4.3.2 D-Galactose

Subsequently, the D-galactose reaction was analysed following the aforementioned modifications. The central point of the D-galactose reaction was initially evaluated through screening, and 350 nm was identified as the optimal excitation wavelength. The sample diluted to an absorbance of 0.1 at 350 nm, mirroring the procedure for D-glucose. With slit widths configured at 3.7/3.7, the emission spectrum was recorded from 370–680 nm, revealing a peak emission at 432 nm, with a discernible secondary shoulder at 525 nm. Once these parameters were established, the remaining D-galactose reactions were executed using the same methodology, culminating in the subsequent CCD in Table 4.10 and optical characterisation findings in Figure 4.13.

Table 4.10, Populated CCD of D-galactose reactions

Reaction nr.	x1	x2	Time (h)	Temperature (°C)	Type of data point	IA ($\times 10^7$)	DF	ABS (A)	Solids Y/N
1	0	0	4	160	central	1.31	0.0005	0.10	N
2	0	0	4	160	central	1.35	0.0005	0.10	N
3	0	0	4	160	central	1.29	0.0005	0.10	N
4	0	0	4	160	central	1.42	0.0005	0.10	N
5	-1.5	0	1	160	axial	0.74	0.0215	0.10	N
6	1.5	0	7	160	axial	1.50	0.0005	0.11	N
7	-1	-1	2	120	factorial	0.84	0.0606	0.10	N
8	1	-1	6	120	factorial	1.13	0.0115	0.11	N
9	-1	1	2	200	factorial	1.75	0.0005	0.10	N
10	1	1	6	200	factorial	2.44	0.0008	0.10	Y
11	0	-1.5	4	100	axial	0.90	0.0010	0.08	N
12	0	1.5	4	220	axial	3.70	0.0909	0.10	N

The absorption spectra, depicted in the Figure 4.13, indicate that two samples exhibited weak absorption and did not reach the target absorbance of 0.1 even when undiluted. These conditions were 100 °C/4 h and 120 °C/2 h, with undiluted absorbance readings of 0.034 and 0.052, respectively. Subsequently the lowest emission intensity was recorded for the 120 °C/2 h parameters. The highest emission intensity was observed under the reaction conditions of 220 °C/4 h, closely followed by 200 °C/6 h, with intensities of $2.2 * 10^5$ and $2.1 * 10^5$, respectively, as shown in the figure. Solid formation occurred in the same high emitting samples, as well as in 200 °C/2 h and one of the central points. This trend aligns with the findings from the D-glucose analysis. An energetic threshold for precipitate formation exists, which can be surpassed by increasing the reaction temperature. While the central point reactions, repeated four times, displayed greater variation in emission spectra compared to the D-glucose spectra (ranging between $7.8 * 10^4$ and $1.2 * 10^5$), this variability did not impede the subsequent model development.

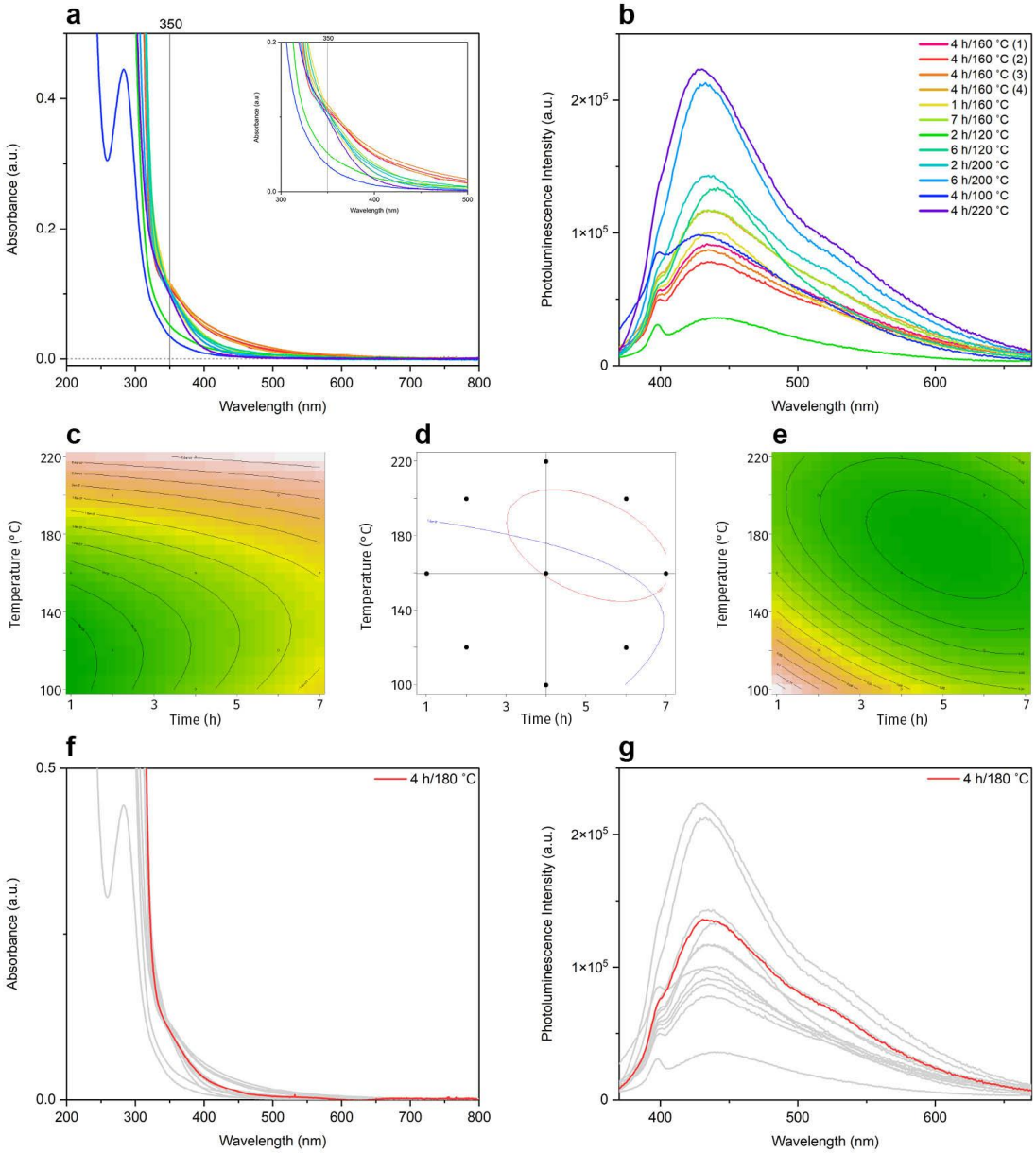

Figure 4.13, Optical characterisation of D-galactose carbon dots, (a) absorption diluted to 0.1 A at 365 nm, (b) emission spectra, at λ_{ex} 345 nm, $\lambda_{collect}$ 370 – 670 nm, and slits 5/4.2, (c) contour plot of the IA response, (d) overlay plot of IA and DF responses, (e) contour plot of the DF response, (f) absorption spectra with optimised reaction condition highlighted, (g) photoluminescence spectra with reaction conditions highlighted

Shown in Figure 4.13 (a), the absorption spectra are displayed. It is shown that two samples were weakly absorbing, and undiluted did not reach the 0.1 A. This included reaction conditions 100 ˚C/4 h and 120 ˚C/2, respectively measuring 0.034 and 0.052 A undiluted. Displayed in Figure 4.13 (b), the highest emission intensity was recorded for reaction conditions 220 ˚C/4 h with a close runner up of 200 ˚C/6 h., at 2.2 * 10^5 and 2.1 * 10^5 intensity, respectively. Four samples formed solids in reaction, this included one of the central points, 160 ˚C/4 h, 200 ˚C/2 h, 200 ˚C/6 h, and 220 ˚C/4 h. This provides a comparable trend to the D-glucose analysis. The lowest emission intensity was measured for parameters 120 ˚C/2 h, however since the corresponding absorption does not reach to 0.1 A, this should be considered with care. The central point reactions repeated four times showed some variation in the emission spectra, more than the D-glucose

spectra, between 7.8 * 10^4 and 1.2 * 10^5, however this variation proved not an issue in the model produced next.

The central composite design was constructed by quantifying the integrated area of the photoluminescence spectra within the 405 – 680 nm range. A modification from the D-glucose study involved Utilising the S1c/R1c signal instead of the S1c signal to enhance the comparative analysis of the integrated area.

Regarding the integrated area, the optimal fit was determined by excluding the quadratic interaction of x1. This exclusion suggests that within the studied parameter range, the influence of time on the integrated area is predominantly linear. All interactions were incorporated into the second-order regression model for the dilution factor. Subsequently, the optimisation of this second-order regression model resulted in the following formula:

$$IA(galactose) = \beta_0 + \beta_1 x_1 + \beta_2 x_2 + \beta_{12} x_1 x_2 + \beta_{22} x_2^2 \quad (4.19)$$

$$DF(galactose) = \beta_0 + \beta_1 x_1 + \beta_2 x_2 + \beta_{12} x_1 x_2 + \beta_{11} x_1^2 + \beta_{22} x_2^2 \quad (4.20)$$

Table 4.11, Analysis of variance of the integrated area and dilution factor of D-galactose reactions

	Integrated Area	**Dilution factor**
multiple R-squared	0.9051	0.9591
adjusted R-squared	0.8509	0.9251
p-value	0.001098	0.0004279
Lack of Fit	0.40023	1.798e-06

The regression model demonstrated a superior fit for the integrated area when contrasted with the D-glucose model, achieving a multiple R-squared value of 0.9. However, the lack of fit was statistically significant at 0.4. Both models exhibited good fits for the dilution factor, with R-squared values exceeding 0.9, though not to the same extent as observed in the D-glucose system. Residual plots indicated a random distribution, as visually represented in the appendix, Figure A 2.

The contour plot illustrated in Figure 4.13 (d) reveals the integrated area is profoundly dependent on reaction temperature. Nevertheless, a more significant linear correlation is evident between reaction time and integrated area, indicating that an extended reaction duration corresponds to an augmented integrated area. In contrast, the D-glucose analysis identified an optimal reaction time within the range of 3.5 to 4 h. The contour plot for the dilution factor as depicted in Figure 4.13 (f), exhibits similarities to that obtained for D-glucose. This indicates a consistent influence of experimental parameters on the dilution factor across different monosaccharide precursors.

Specifically, higher temperatures and longer reaction times generally necessitate greater dilution to achieve the target absorbance, implying increased product concentration under these conditions. Considering the potential for undesirable side products at elevated temperatures, an overlay of the contour plots was performed, shown in Figure 4.13 (e). Drawing upon these graphical representations and prior findings from glucose experiments, the reaction condition of 180°C for 4 h was identified as optimal for the subsequent processing of D-galactose.

Under the optimised conditions of 180°C for 4 h, no precipitate was observed. Subsequent optical characterisation of this sample yielded the provided absorption and photoluminescence spectra in Figure 4.13 (g) and (h), respectively. The absorption spectrum revealed a shoulder at 350 nm, aligning with the identified excitation wavelength. The emission spectrum demonstrated a peak emission at 431 nm, with an intensity measuring $1.4 * 10^5$. This intensity signifies a 46% enhancement relative to the mean intensity recorded at the central points within the experimental design. The integrated area model had forecasted a value of $1.4 * 10^7$, whereas the experimentally measured integrated area was $1.7 * 10^7$, indicating a 20% deviation from the predicted value.

The calculated dilution factor for the reaction at 180 °C for 4 h was $2.8 * 10^{-4}$, which is comparable to the lowest dilution factor of $2.5 * 10^{-4}$ observed at 200 °C for 2 h. The integrated areas for these conditions were $1.69 * 10^7$ and $1.75 * 10^7$, respectively. Consequently, the reaction conditions of 200 °C for 2 h yielded marginally superior results for both responses. Although this outcome was not fully represented in the developed model, it indicates a slight advantage for the shorter reaction time at the higher temperature.

4.3.3 Alginate

Transitioning to the examination of polysaccharides, specifically alginate carbon dots, the study encountered challenges in obtaining consistent absorption spectra and identifying an optimal excitation wavelength. Analysis of the absorption spectra, revealed in Figure 4.14 (a), showed distinct peaks and shoulders across various wavelengths predominantly around 250 nm, 325 nm, and 357 nm. Drawing upon existing literature that indicates hydrothermally synthesised carbon dots are typically excited within the 340-370 nm range; the longest observed wavelength of 357 nm was selected as the optimal excitation wavelength. This selection was further validated through preliminary characterisation. Consequently, all alginate samples were prepared to an absorbance of 0.1 at 357 nm and subsequently excited at this determined wavelength. The collected emission spectra, recorded between 390 nm and 670 nm with slit widths of 5/3.7, displayed a maximum emission wavelength ($\lambda_{em,max}$) at 442 nm, accompanied by a secondary shoulder at 535 nm in select samples. The CCD was populated according to these findings, shown in Table 4.12, followed by the optical characterisation in Figure 4.14.

Table 4.12, Populated CCD of Alginate reactions

Reaction nr.	x1	x2	Time (h)	Temperature (°C)	Type of data point	IA ($\times 10^7$)	DF	ABS (A)	Solids Y/N
1	0	0	4	160	central	1.22	0.0006	0.11	N
2	0	0	4	160	central	1.06	0.0005	0.11	N
3	0	0	4	160	central	1.14	0.0006	0.11	N
4	0	0	4	160	central	1.52	0.0007	0.12	N
5	-1.5	0	1	160	axial	1.18	0.0478	0.11	N
6	1.5	0	7	160	axial	1.49	0.0004	0.11	N
7	-1	-1	2	120	factorial	0.44	0.0606	0.05	N
8	1	-1	6	120	factorial	1.45	0.0202	0.11	N
9	-1	1	2	200	factorial	1.75	0.0002	0.10	N
10	1	1	6	200	factorial	2.35	0.0010	0.11	Y
11	0	-1.5	4	100	axial	1.19	0.0636	0.04	N
12	0	1.5	4	220	axial	2.59	0.0183	0.10	N

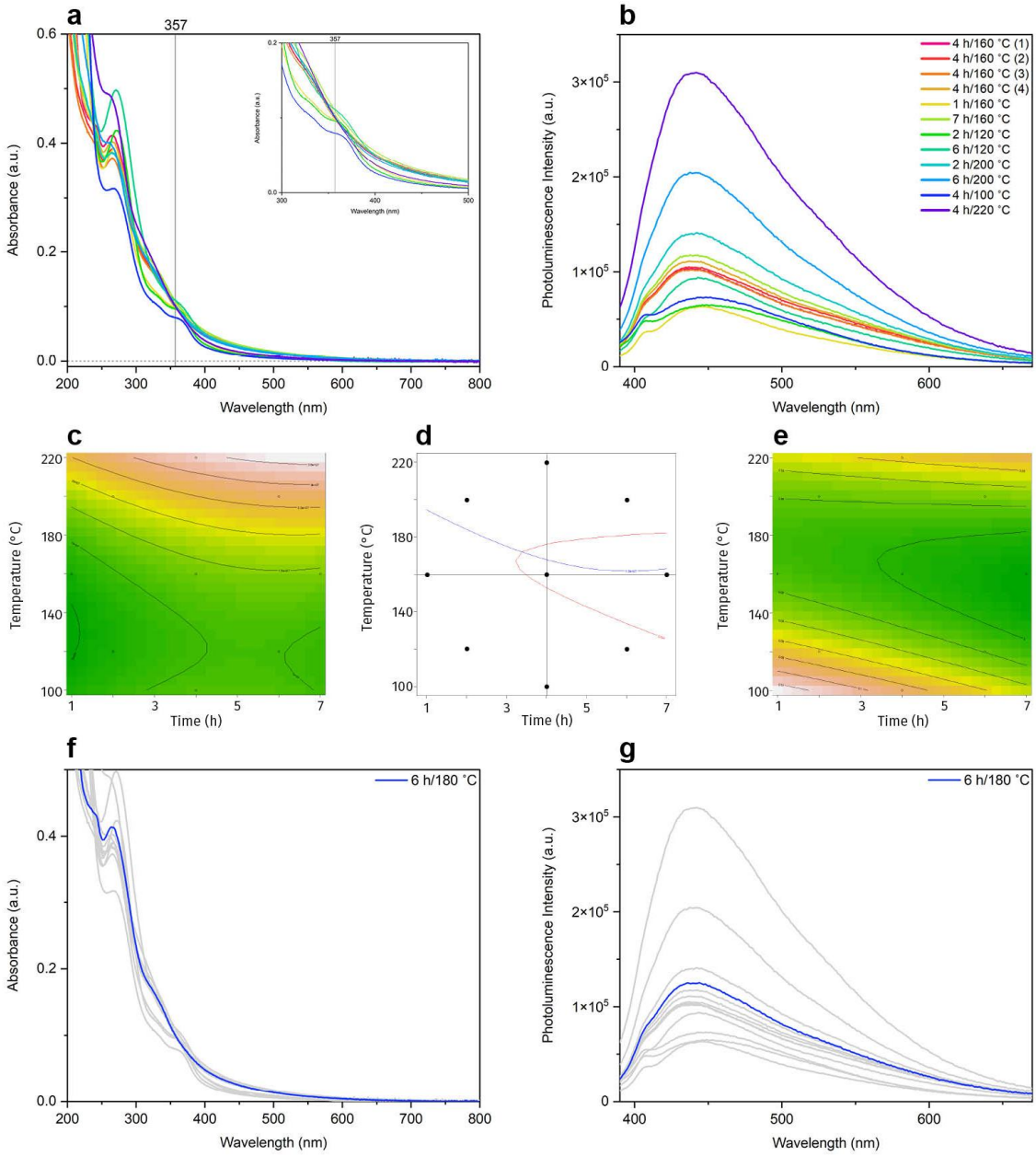

Figure 4.14, Optical characterisation of Alginate carbon dots, (a) absorption diluted to 0.1 A at 365 nm, (b) emission spectra, at λ_{ex} 345 nm, $\lambda_{collect}$ 370 – 670 nm, and slits 5/4.2, (c) contour plot of the IA response, (d) overlay plot of IA and DF responses, (e) contour plot of the DF response, (f) absorption spectra with optimised reaction condition highlighted, (g) photoluminescence spectra with reaction conditions highlighted

Under the synthesis parameters of 100 °C for 4 h, the reaction yielded an absorbance of 0.08 A without the need for dilution. This observation suggests a relatively low concentration of light-absorbing species, potentially indicative of suboptimal carbonisation or a limited formation of chromophores under these less severe reaction conditions.

Photoluminescence emission intensity was maximised under the synthesis conditions of 200 °C for 2 h, 200 °C for 6 h, and 220 °C for 4 h. The integrated area was subsequently determined from the S1c/R1c signal within the spectral range of 415 – 670 nm, a region chosen to circumvent interference from Raman scattering present in the low-intensity emission spectra.

Only one set of parameters, specifically 200 °C for 6 h, yielded solid formation. This contrasts with monosaccharide reactions, where temperatures exceeding 200 °C combined with reaction times shorter than 6 h result in solid formation. This phenomenon may be attributed to the molecular structure of the precursor, necessitating the hydrolysis of alginate into individual sugar units before carbon dot formation can occur,[65] or the absolute carbon concentration difference between the monosaccharides and alginate in solution, as outlined in Table 4.7.

The second-order regression model was optimised, yielding the following formula. For the integrated area, a second-order regression model incorporating all linear, two-way, and quadratic interactions provided the optimal fit. In the case of the dilution factor, the quadratic interaction of x1 (reaction time) was excluded from the regression model, along with the data point corresponding to reaction number 11, which was identified as an outlier in the residual plot and further confirmed in the absorbance plot.

$$IA(alginate) = \beta_0 + \beta_1 x_1 + \beta_2 x_2 + \beta_{12} x_1 x_2 + \beta_{11} x_1^2 + \beta_{22} x_2^2 \quad (4.21)$$

$$DF(alginate) = \beta_0 + \beta_1 x_1 + \beta_2 x_2 + \beta_{12} x_1 x_2 + \beta_{22} x_2^2 \quad (4.22)$$

Table 4.13, Analysis of variance of the integrated area and dilution factor of D-alginate reactions

	Integrated Area	**Dilution factor**
multiple R-squared	0 .9529	0.7413
adjusted R-squared	0.9137	0.5343
p-value	0.000649	0.09713
Lack of Fit	0.0075912	1.191e-07

The regression model demonstrated a strong correlation with the integrated area, evidenced by a multiple R-squared value of 0.95, a statistically significant low p-value, and no significant lack of fit. However, the model's fit for the dilution factor was less robust, achieving a multiple R-squared of 0.74, even after implementing model adjustments and excluding an outlier data point. Analysis of the residuals, shown in the appendix, Figure A 3, indicated a random distribution, suggesting the absence of systematic bias in the model.

The contour plots of the alginate model are shown in Figure 4.14 (c) and (e), respectively for the integrated area and the dilution factor. The integrated area contour plot indicates an optimal reaction time, with photoluminescence intensity peaking at 6 h of reaction compared to reactions at the same temperature but varying durations. Furthermore, a direct correlation was observed between reaction temperature and photoluminescence intensity. Analysing the dilution factor contour plot of the model, a minimum reaction temperature is identified. The minimum dilution factor is observed at 180 °C. Employing reaction temperatures higher than this threshold promotes the formation of solids, as evidenced by reaction conditions of 200 °C/6 h. Conversely, Utilising reaction temperatures below this optimum leads to augmented dilution factors, which is also disadvantageous. The overlay plot Figure 4.14 (d), derived from the contour plots, was generated to establish the optimised reaction conditions, identified as 180 °C for a 6-hour duration.

The hydrothermal reaction of alginate into carbon dots at 180 °C for 6 h yielded no solid byproducts and resulted in the optical characterisation plots shown in Figure 4.14, with the absorption (f) and photoluminescence (g) spectra highlighted in blue. The absorption spectra exhibited a shoulder at 325 nm, rather than at 357 nm (the excitation wavelength), and a minor peak at 265 nm was also present.

The photoluminescence spectrum exhibited a maximum emission wavelength ($\lambda_{em,max}$) of 442 nm with an intensity of $1.25 * 10^5$, representing a 20% enhancement relative to the average of the central point experimental conditions. This finding underscores the substantial improvement in photoluminescence characteristics achieved through the optimised reaction parameters.

The model predicted an integrated area of $1.9 * 10^7$ for these specific reaction conditions. Experimentally, the IA was measured at $1.6 * 10^7$, indicating a slight deviation from the model's prediction. The quantum yield for the optimised alginate reaction was determined to be 1.0%. Notably, the dilution factor was found to be $4.86 * 10^{-5}$, which is significantly lower than the minimum DF recorded across all reaction conditions tested within the central composite design. This reduced dilution factor demonstrates the efficiency of the optimised conditions in producing a concentrated product, one of the goals of the study.

4.3.4 Carrageenan

The investigation into carrageenan followed a previously established protocol. Carrageenan samples were diluted to an absorbance of 0.1 at 332 nm. However, the excitation wavelength (λ_{ex}) was set to 345 nm to achieve enhanced photoluminescence intensity. Emission spectra were recorded from 370 nm to 670 nm using slit widths of 3 nm for excitation and 2.5 nm for emission. The resulting emission spectra exhibited a maximum emission wavelength ($\lambda_{em,max}$) at 435 nm, with an additional shoulder observed at 525 nm. The corresponding CCD and optical characterisation are presented in Table 4.14 and Figure 4.15, respectively. The presence of a shoulder at 525 nm suggests the existence of multiple emissive species or surface traps within the synthesised carbon dots.

Table 4.14, Populated CCD of Carrageenan reactions

Reaction nr.	x1	x2	Time (h)	Temperature (˚C)	Type of data point	IA (× 10^7)	DF	ABS (A)	Solids Y/N
1	0	0	4	160	central	0.55	0.005	0.10	N
2	0	0	4	160	central	0.60	0.005	0.10	N
3	0	0	4	160	central	0.50	0.005	0.09	N
4	0	0	4	160	central	0.56	0.006	0.10	N
5	-1.5	0	1	160	axial	0.50	0.111	0.07	N
6	1.5	0	7	160	axial	0.68	0.004	0.10	N
7	-1	-1	2	120	factorial	0.29	0.067	0.02	N
8	1	-1	6	120	factorial	0.60	0.064	0.08	N
9	-1	1	2	200	factorial	0.72	0.004	0.11	N
10	1	1	6	200	factorial	1.5	0.003	0.10	N
11	0	-1.5	4	100	axial	0.26	0.061	0.03	N
12	0	1.5	4	220	axial	0.20	0.002	0.10	N

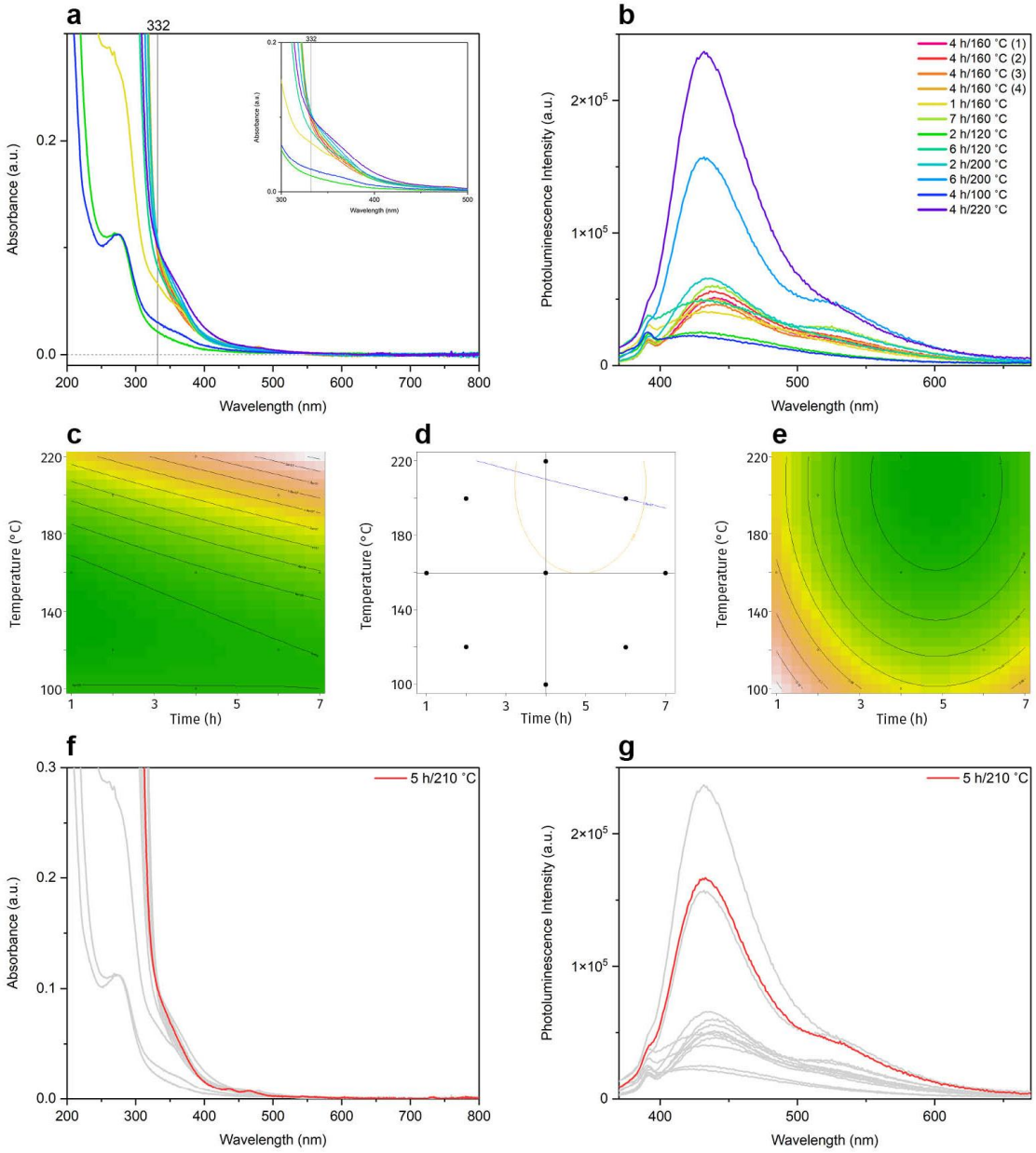

Figure 4.15, Optical characterisation of Carrageenan carbon dots, (a) absorption diluted to 0.1 A at 365 nm, (b) emission spectra, at λ_{ex} 345 nm, $\lambda_{collect}$ 370 – 670 nm, and slits 5/4.2, (c) contour plot of the IA response, (d) overlay plot of IA and DF responses, (e) contour plot of the DF response, (f) absorption spectra with optimised reaction condition highlighted, (g) photoluminescence spectra with reaction conditions highlighted

The absorption spectrum displayed two distinct peaks or shoulders, located at 365 nm and 275 nm. The samples were diluted to an absorbance of 0.1 at 332 nm. For the conditions of 100 °C/4 h, 120 °C/2 h, and 160 °C/1 h, the resulting samples exhibited low undiluted absorbances of 0.30, 0.21, and 0.66, respectively. The subsequent analysis of the model addresses this particular aspect.

The emission spectra revealed in Figure 4.15 (b) that the highest emission intensities occurred at 220 °C/4 h and 200 °C/6 h. The secondary emission at 525 nm varied in prominence depending on the reaction conditions. This secondary emission was most apparent under conditions of 200 °C/2 h and 160 °C/7 h, whereas it was not observed in the low temperature, short time reactions.[66] To demonstrate the difference is spectra, two of the emission spectra's peak fitting are shown below in Figure 4.16 (b) and (c), however the

peak fitting for all spectra can be referenced in the appendix, Figure A 7. The study further investigated the relationship between the emission intensities of the 432 nm and 525 nm peaks across various reaction conditions, shown in Figure 4.16 (a). The long emission peak is most visible at the central point reaction conditions of 160 °C and 4 h. The secondary peak is reduced yet visible when increasing reaction temperature to 200, 210, and 220 °C. However, the peak disappears at low reaction temperatures of 100 and 120 °C. This suggests that the underlying mechanisms for these two emission features are distinct, potentially indicating intermediate structures contributing to the overall luminescence profile. Such variations in emission spectra, particularly the emergence and modulation of secondary peaks, are commonly attributed to the formation of diverse surface defects and functional groups, in this case involving the sulfur group of carrageenan, also illustrated in Figure 3.8.[67] This offers the possibility to optimise the model to favour the production of materials emitting at 525 nm.

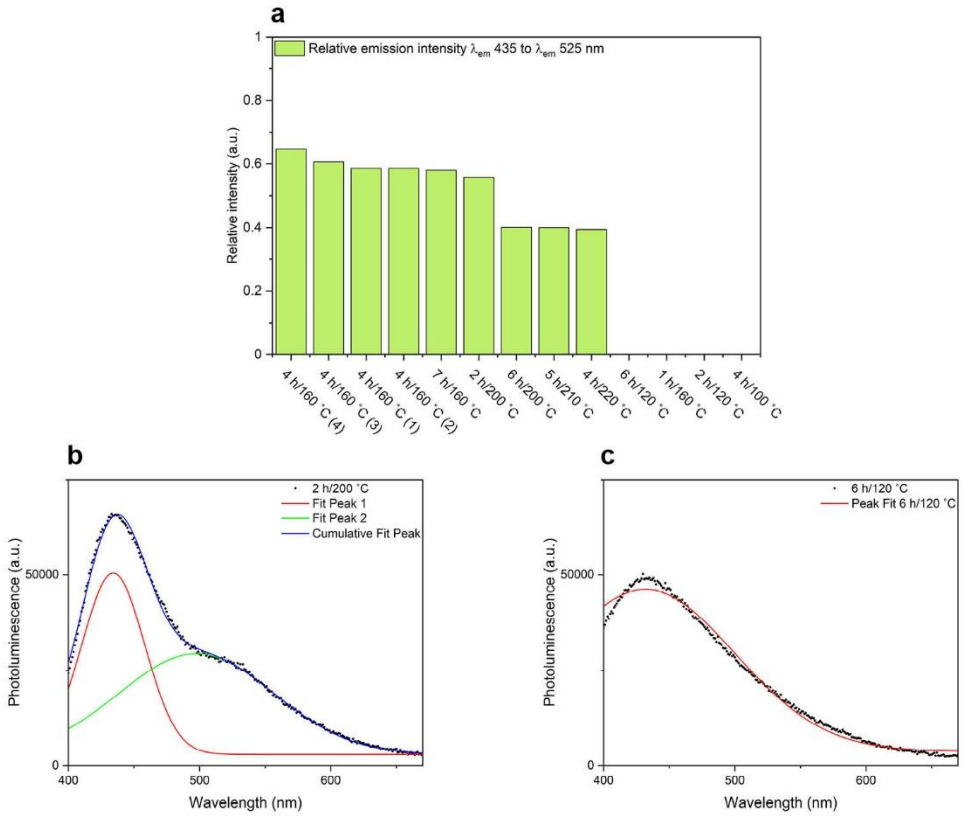

Figure 4.16, Relative emission intensity of λ_{em} 435 to λ_{em} 525 nm (a), peak fit at 200 °C/2 h (b), and 120 °C/6 h (c) of the photoluminescence spectra of carbon dots from hydrothermal synthesis of carrageenan.

However, the primary analytical focus remained on the comprehensive photoluminescence, particularly the integrated area of the S1c/R1c signal spanning the 400 – 670 nm range. A second-order regression model underwent optimisation, resulting in the subsequent formula. For the integrated area, the most effective fit was achieved by excluding the quadratic interaction of reaction time from the regression model. Conversely, concerning the dilution factor, the two-way interaction term was removed from its respective regression model. Initially, data points with dilution factors below 0.1 A were omitted from the dilution factor model; however, this led to an inferior model fit. Consequently, all data points were subsequently incorporated.

$$IA(carrageenan) = \beta_0 + \beta_1 x_1 + \beta_2 x_2 + \beta_{12}\, x_1 x_{\,2} + \beta_{22}\, x_2^2 \quad (4.23)$$

$$DF(carrageenan) = \beta_0 + \beta_1 x_1 + \beta_2 x_2 + \beta_{11}\, x_1^2 + \beta_{22}\, x_2^2 \quad (4.24)$$

Table 4.15, Analysis of variance of the integrated area and dilution factor of Carrageenan reactions

	Integrated Area	Dilution factor
multiple R-squared	0.9136	0.8107
adjusted R-squared	0.8642	0.7025
p-value	0.0007957	0.01133
Lack of Fit	0.0086538	4.341e-06

The model demonstrated a strong fit for the integrated area, evidenced by a multiple R-squared value of 0.91, a low p-value, and an acceptable lack of fit. While the dilution factor fit was deemed acceptable, it was not optimal, yielding a multiple R-squared greater than 0.8 and necessitating the exclusion of the two-way interaction term. Residual plots confirmed randomness, as detailed in the appendix, Figure A 4.

The contour plots for the carrageenan model are presented in Figure 4.15 (c) and (e), illustrating the integrated area and the dilution factor, respectively. The integrated area contour plot demonstrates that at lower reaction temperatures (100 – 120 ˚C), changes in photoluminescence are minimal when the reaction time is varied. However, at elevated reaction temperatures, an increase in photoluminescence is observed, which is linearly correlated with an increase in reaction time, leading to a higher integrated area. This plot highlights a lower limit in reaction temperature for carrageenan, which is suspected to be necessary for the breakdown of the polysaccharide into monosaccharide units, facilitating carbon dot formation. The model shows the interaction between temperature and time is non-linear and complex, indicating that a balance must be achieved to maximise both the breakdown of the polysaccharide and the subsequent formation of luminescent carbon dots. Analysis of the dilution factor contour plot reveals a minimum sample dilution occurring at 210 °C/5 h. Based on this plot and the favourable outcome indicated by the integrated area, optimal reaction conditions were selected for these conditions. This selection balances the need for high photoluminescence with a manageable dilution factor, satisfying both objectives of this study.

These optimal conditions were subsequently employed in a validation experiment to assess the reproducibility and tunability of the synthesised carbon dots. The optical absorption and photoluminescence spectra are presented in Figure 4.15 (f) and (g) respectively. The absorption spectrum closely mirrored those observed under the Central Composite Design conditions, exhibiting a shoulder at 345 nm. The emission spectrum was comparable to that obtained from the 200 °C/6 h reaction, displaying an intensity of 1.57 x 10^5, while the 210 °C/5 h condition yielded an intensity of 1.67 x 10^5. The integrated area response predicted by the model was 1.8 x 10^7. The integrated area was empirically determined to be 1.5 x 10^7, which was slightly lower than the predicted value. The measured dilution factor was 0.003, identical to that of the 200 °C/6 h reaction. Consequently, the 210 °C/5 h condition represents the truly optimised reaction parameter set.

4.3.5 Kelp

Subsequently, the biomass-based methodology underwent investigation. The kelp study followed previously established methods, with some modifications. The reaction mixture was prepared by suspending 1 gram of kelp in 12 ml of water, rather than forming a solution, which allowed for the accurate determination of biomass consumed during the reaction. This involved an additional step of quantifying the solid residue post-reaction, which was reflected in the CCD, shown in Table 4.16

Furthermore, modifications were implemented in the optical characterisation procedure to optimise efficiency. Initially, all samples underwent dilution and subsequent characterisation via UV-vis spectroscopy. Following this, the optimal excitation wavelength was determined, preceding the collection of emission spectra. Given that the absorption spectra of the central point kelp reactions lacked a distinct absorption feature at the optimised excitation wavelength, an elevated absorption value was employed to adequately capture the emissive properties of the carbon dots within the presumed excitation wavelength range. This approach ensured sufficient photon absorption to elicit measurable photoluminescence, even in the absence of sharply defined absorption bands.

With an excitation wavelength (λ_{ex}) maintained at 370 nm, emission spectra were recorded across the range of 390–720 nm, Utilising slit widths of 2.5/2 nm. The emission spectra revealed a maximum emission wavelength ($\lambda_{em,max}$) between 445 and 470 nm, alongside a secondary shoulder observed at 520 nm. This shoulder was particularly pronounced in reactions conducted at lower temperatures and shorter durations, specifically 100 °C for 4 h and 120 °C for 2 h, as opposed to the spectra from carrageenan derived carbon dots. This indicates that while certain conditions might not yield a prominent absorption peak at the excitation wavelength, the formation of light-absorbing species, including carbon dots, still occurs.
The comprehensive optical characterisation is depicted in Figure 4.17 (a) and (b).

Table 4.16, Populated CCD for kelp study

Reaction nr.	x1	x2	Time (h)	Temperature (˚C)	Type of data point	IA (× 10^7)	DF	ABS (A)	Solids (g)
1	0	0	4	160	central	2.90	0.001	0.29	0.16
2	0	0	4	160	central	3.20	0.001	0.31	0.32
3	0	0	4	160	central	3.20	0.001	0.31	0.37
4	0	0	4	160	central	3.40	0.001	0.29	0.35
5	-1.5	0	1	160	axial	2.10	0.02	0.29	0.30
6	1.5	0	7	160	axial	3.80	0.001	0.27	0.07
7	-1	-1	2	120	factorial	2.20	0.509	0.34	0.42
8	1	-1	6	120	factorial	2.30	0.011	0.27	0.29
9	-1	1	2	200	factorial	4.30	0.001	0.26	0.11
10	1	1	6	200	factorial	7.80	0.001	0.24	0.22
11	0	-1.5	4	100	axial	1.90	0.063	0.27	0.71
12	0	1.5	4	220	axial	8.00	0.001	0.23	0.31

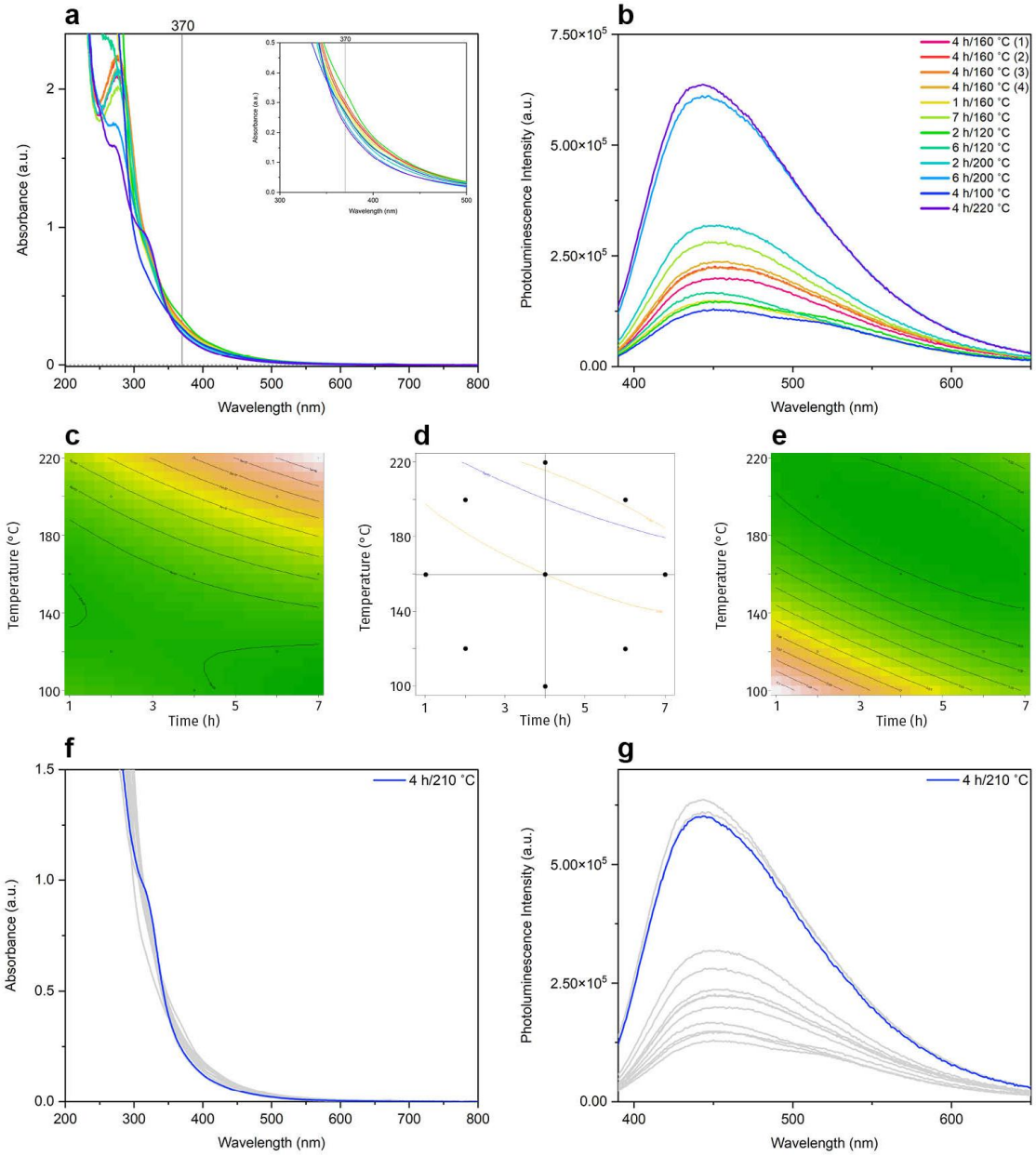

Figure 4.17, Optical characterisation of Kelp carbon dots, (a) absorption diluted to 0.1 A at 365 nm, (b) emission spectra, at λ_{ex} 345 nm, $\lambda_{collect}$ 370 – 670 nm, and slits 5/4.2, (c) contour plot of the IA response, (d) overlay plot of IA and DF responses, (e) contour plot of the DF response, (f) absorption spectra with optimised reaction condition highlighted, (g) photoluminescence spectra with reaction conditions highlighted

The absorption spectra shown in depict a shoulder or peak at 270 nm across all samples, with a secondary feature appearing at either 315 nm or 370 nm in some. However, absorption values at 370 nm ranged from 0.23 to 0.31 A for most samples, except for the 120 °C/2 h reaction, which exhibited the most prominent shoulder at 370 nm, yielding a value of 0.34 A. The shoulder at 315 nm was most pronounced under reaction conditions of 220 °C/4 h. This observation may indicate the influence of reaction temperature on the structure and optical properties of the synthesised carbon dots. The presence of distinct absorption features at 270 nm and shoulders at 315 nm or 370 nm suggests the formation of diverse carbon dot structures, which could be attributed to varying degrees of carbonisation and surface functionalisation. Such spectral characteristics, particularly the shoulder around 270 nm, are consistent with $\pi \rightarrow \pi^*$ electronic transitions of C=C bonds

within the carbon dot core, while features at longer wavelengths, such as 315 nm and 370 nm, are often ascribed to n → π* transitions involving C=O and C-N bonds from surface functional groups.

The excitation spectra, Figure 4.17 (a) revealed a shoulder at 305 nm in several instances, specifically for reactions conducted at 100 °C for 4 h, 120 °C for 2 h, 120 °C for 6 h, and 160 °C for 1 hour. This shoulder aligns with previous findings attributing such spectral characteristics to n-π* transitions of C=O and C=N bonds, highlighting the presence of surface functionalisation, also noted in the absorption spectra. The highest emission intensities were observed under two reaction conditions: 220 °C for 4 h and 200 °C for 6 h. To populate the Central Composite Design for the kelp study, the integrated area was calculated across the range of 390–650 nm.

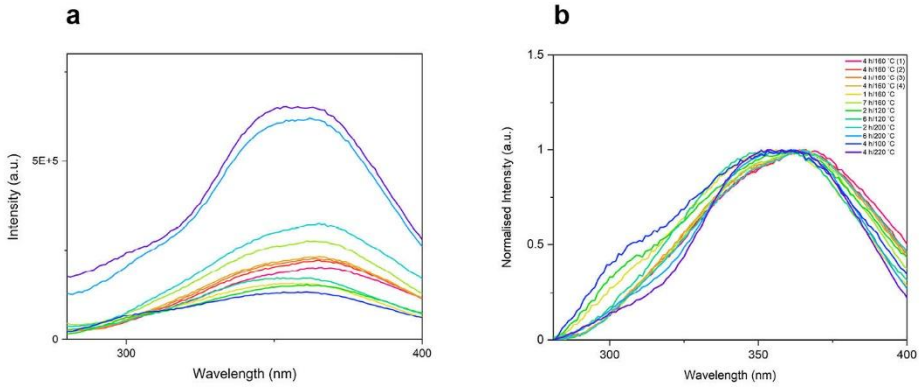

Figure 4.18, Excitation spectra of hydrothermal synthesis of carbon dots from kelp (a) absolute numbers and (b) normalised.

The second-order regression model underwent optimisation. For the integrated area, the optimal fit was achieved by excluding the quadratic interaction of x1 (reaction time) from the regression model. Conversely, the complete model demonstrated the best fit for the dilution factor. An outlier, identified as the data point 120 °C/2 h with 0.34 A, was removed from the dataset prior to model generation due to its prominence in the residual plot.

$$IA(kelp) = \beta_0 + \beta_1 x_1 + \beta_2 x_2 + \beta_{12}\, x_1 x_{\,2} + \beta_{22}\, x_2^2 \quad (4.25)$$

$$DF(kelp) = \beta_0 + \beta_1 x_1 + \beta_2 x_2 + \beta_{12}\, x_1 x_{\,2} + \beta_{11}\, x_1^2 + \beta_{22}\, x_2^2 \quad (4.26)$$

Table 4.17 Analysis of variance of the integrated area and dilution factor of kelp reactions

	Integrated Area	Dilution factor
multiple R-squared	0.9888	0.9736
adjusted R-squared	0.9824	0.9472
p-value	6.594e-07	0.0005969
Lack of Fit	0.2434377	1.349e-06

The developed model exhibited an excellent fit for both the integrated area and dilution factor, evidenced by multiple R-squared values of 0.99 and 0.97, respectively. Residual plots demonstrated randomness, as depicted in the appendix, Figure A 5. Contour plots illustrating the integrated area and dilution factor in Figure 4.17 (c) and (e) respectively, to reveal their specific relationships. At lower reaction temperatures (< 140 ˚C), minimal variations in photoluminescence are observed with increasing reaction time. Conversely, at

elevated temperatures (> 160 ˚C), photoluminescence intensity escalates with prolonged reaction times. Similarly, for shorter reaction durations (< 2 h), incremental changes in reaction temperature yield negligible effects on photoluminescence; however, longer reaction times (> 2 h) demonstrate an enhancement in photoluminescence with increasing reaction temperature. The two-way interaction between time and temperature exhibits a positive linear correlation with photoluminescence intensity. Regarding the second response, the dilution factor, the contour plot illustrates a similar trend, albeit inverse, with a minimum optimal point identified at 210 °C/4 h, beyond which the dilution factor begins to increase.

Based on the overlay plot Figure 4.17 (d), the optimised reaction condition was determined to be 210 °C/4 h. Optical characterisation of the absorption spectrum (f) revealed a sloped absorption curve with a shoulder at 320 nm. The emission spectrum (g) demonstrated excellent photoluminescence properties, with a maximum emission wavelength ($\lambda_{em,max}$) at 443 nm and an intensity of 6.0 * 10^5. This intensity is comparable to the two highest-emitting reaction conditions recorded in the Central Composite Design, which yielded 6.1 * 10^5 and 6.5 * 10^5 for conditions 200 °C/6 h and 220 °C/4 h, respectively.

The model predicted an integrated area value of 7.0 * 10^7 and the measured integrated area was 7.6 * 10^7, nearly 10% higher than the model's prediction, while the dilution factor matched the lowest recorded in the CCD, which can be consulted in Table 4.16Table 4.16, Populated CCD for kelp study. The optimised reaction produced 0.09 g of solids, making it the second lowest yield; the lowest was 0.07 g from conditions 160 °C/7 h, although these conditions did not exhibit competitive optical properties. While both 220 °C/4 h and 200 °C/6 h produced slightly higher IA values with the same dilution factor, they generated two to three times more solids, respectively, compared to the optimal conditions. Therefore, the chosen optimised conditions are considered truly optimal.

4.3.6 Irish Moss

The methodology employed for the Irish moss investigation mirrored that of the Kelp analysis, encompassing the measurement of the formed precipitate reflected in Table 4.18 and subsequent optical characterisation in Figure 4.19. This characterisation involved an initial dilution of the samples, followed by the acquisition of absorption spectra, determination of the optimal excitation wavelength, and finally, the collection of emission spectra. Due to the absence of discernible features in the absorption spectrum for the central point reaction conditions of the Irish moss, samples were diluted to achieve an absorbance of 0.165 A at 360 nm, the lowest wavelength for which all spectra resemble each other. The excitation wavelength was optimised to 345 nm, and emission spectra were recorded between 360 nm and 670 nm using slit widths of 2/2 nm.

Table 4.18, Populated CCD of Irish moss study

Reaction nr.	x1	x2	Time (h)	Temperature (°C)	Type of data point	IA ($\times 10^7$)	DF	ABS (A)	Solids (g)
1	0	0	4	160	central	2.90	0.001	0.16	0.08
2	0	0	4	160	central	3.10	0.001	0.17	0.02
3	0	0	4	160	central	3.10	0.001	0.17	0.10
4	0	0	4	160	central	3.10	0.001	0.16	0.02
5	-1.5	0	1	160	axial	1.30	0.023	0.17	0.37
6	1.5	0	7	160	axial	3.60	0.001	0.17	0.05
7	-1	-1	2	120	factorial	0.99	0.056	0.14	0.75
8	1	-1	6	120	factorial	2.20	0.009	0.17	0.28
9	-1	1	2	200	factorial	3.90	0.001	0.16	0.09
10	1	1	6	200	factorial	7.20	0.001	0.16	0.33
11	0	-1.5	4	100	axial	0.72	0.003	0.17	0.54
12	0	1.5	4	220	axial	8.50	0.001	0.17	0.12

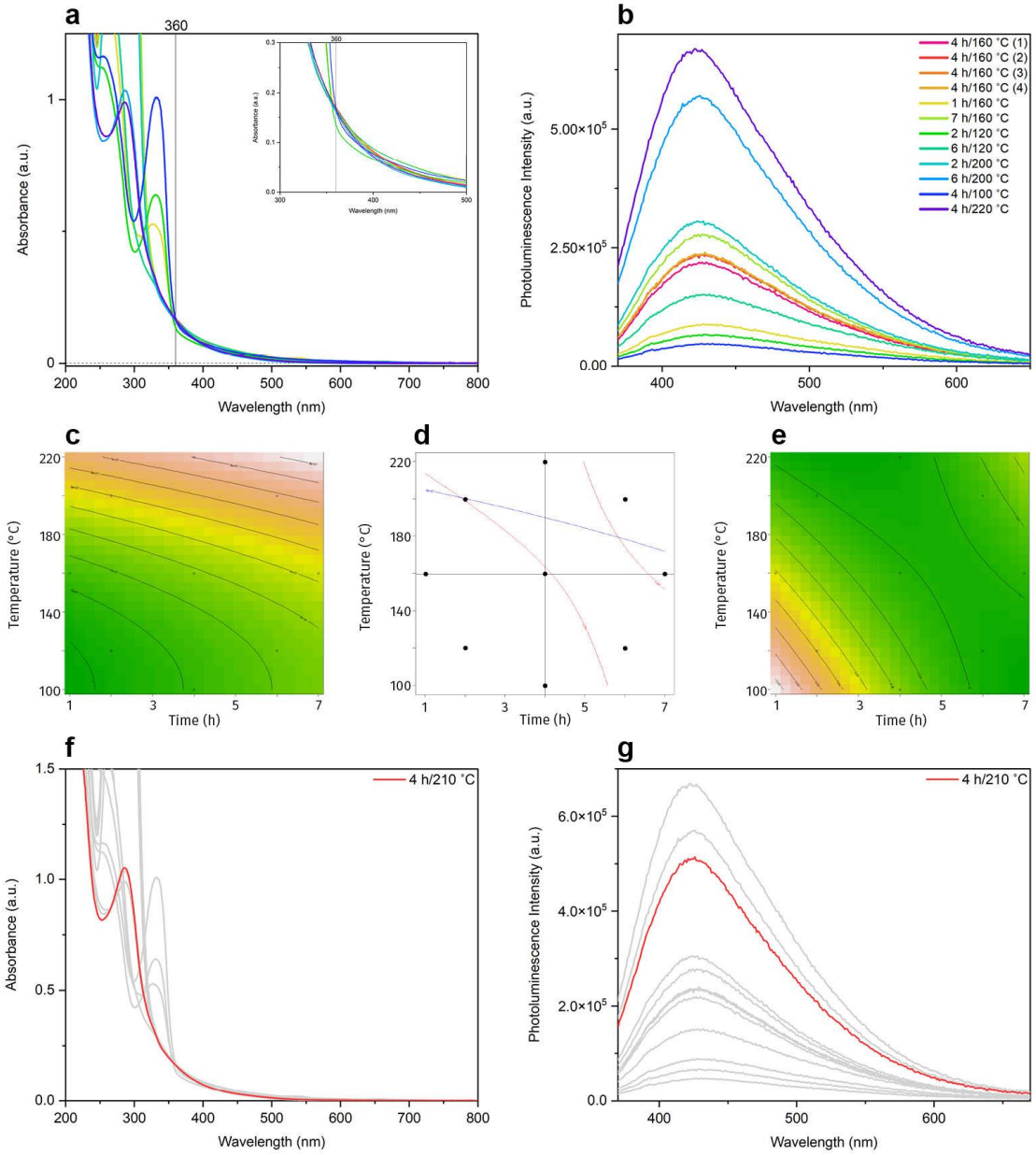

Figure 4.19, Optical characterisation of Irish Moss carbon dots, (a) absorption diluted to 0.1 A at 365 nm, (b) emission spectra, at λ_{ex} 345 nm, $\lambda_{collect}$ 370 – 670 nm, and slits 5/4.2, (c) contour plot of the IA response, (d) overlay plot of IA and DF responses, (e) contour plot of the DF response, (f) absorption spectra with optimised reaction condition highlighted, (g) photoluminescence spectra with reaction conditions highlighted

The absorption spectrum of Irish moss samples exhibited in Figure 4.19 (a) variations in shoulder and peak characteristics. A prominent peak at 332 nm was observed under reaction conditions of 100 °C for 4 h, 120 °C for 2 h, and 160 °C for 1 hour. These conditions, along with 120 °C for 6 h, also displayed a shoulder feature at 255 nm. This suggests the formation of specific structures at both short and low reaction temperatures at these wavelengths.

However, the 255 nm feature was absent when the reaction time at 120 °C was extended from 2 to 6 h. Reaction conditions of 160 °C with durations of 4 h or longer, as well as higher temperatures, resulted in the loss of both the 332 nm peak and the 255 nm shoulder. Instead, these extended reaction times and higher temperatures revealed a peak at 285 nm, which was particularly strong for 160 °C at 4 and 7 h, and for 200

°C at 2 h. The same 285 nm peak was also present, albeit with reduced intensity, under conditions of 220 °C for 4 h and 200 °C for 6 h. This observation suggests a dynamic evolution of carbonaceous structures with increasing thermal treatment, potentially indicating the formation of distinct chromophores including molecular fluorophores or nanoscale carbon domains by isolating the sulfur containing groups and forming a molecular fluorophore or graphitisation and growth of sp^2 hybridised structures typically found in GQD.[66] This shift in spectral features from 332 nm and 255 nm to 285 nm with increased thermal processing aligns with observations in other carbon-based materials, where more aggressive thermal conditions lead to enhanced carbonisation and changes in optical properties.[68]

Shown in Figure 4.19 (b) the central point exhibited an emission maximum ($\lambda_{em,max}$) at 425 nm, with an intensity of 2.29 * 10^5. Across the various reaction conditions, minimal variation was observed in the overall shape of the emission spectra. The lowest photoluminescence intensity at $\lambda_{em,max}$425 nm was recorded at 4.7 * 10^4 for the 100 °C/4 h reaction condition. In contrast, the two highest emissions were measured at 6.65 * 10^5 and 5.70 * 10^5, corresponding to reaction conditions of 220 °C/6 h and 200 °C/6 h, respectively.

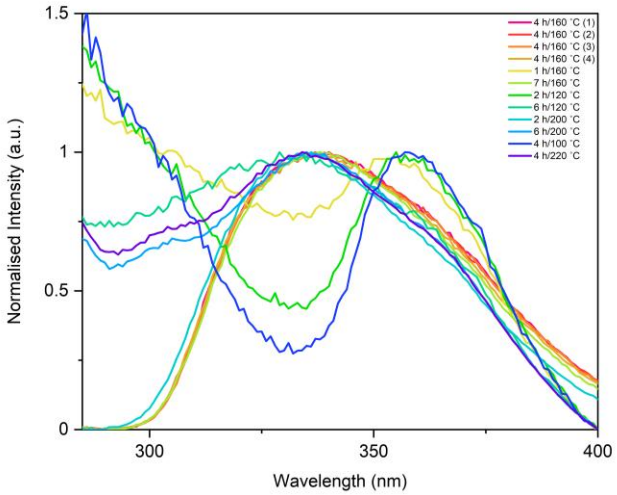

Figure 4.20, Normalised excitation spectrum of Irish moss reactions

In contrast to carbon dots derived from other precursors, the excitation spectra of the Irish moss carbon dots displayed distinct characteristics, as illustrated in an appended figure. The normalised excitation spectra highlight two observed excitation wavelengths: 340 nm and 355 nm. The red-shifted excitation wavelengths were recorded under the same conditions that led to increased absorbance at 345 nm: 100 °C for 4 h, 120 °C for 2 h, and 160 °C for 1 hour. This bimodal excitation behaviour suggests the presence of distinct populations of fluorophores within the carbon dot ensemble, possibly related to surface passivation or the formation of different conjugated domains caused by dynamic evolution of the carbone

The second-order regression model underwent optimisation, yielding a specific formula, shown below. For the integrated area, the optimal fit was achieved by excluding the two-way interaction between x1 and x2 from the regression model. Conversely, for the dilution factor, the complete model demonstrated the best fit.

$$IA(Irish\ moss) = \beta_0 + \beta_1 x_1 + \beta_2 x_2 + \beta_{11}\, x_1^2 + \beta_{22}\, x_2^2 \quad (4.27)$$

$$\boldsymbol{DF(Irish\ moss) = \beta_0 + \beta_1 x_1 + \beta_2 x_2 + \beta_{12}\, x_1 x_2 + \beta_{11}\, x_1^2 + \beta_{22}\, x_2^2} \quad \boldsymbol{(4.28)}$$

Table 4.19, Analysis of variance of the integrated area and dilution factor of Irish moss reactions

	Integrated Area	Dilution factor
multiple R-squared	0.963	0.742
adjusted R-squared	0.9419	0.527
p-value	4.243e-05	0.08174
Lack of Fit	0.003892	8.267e-08

The model demonstrated a strong fit for the integrated area with a multiple R-squared value of 0.963; however, the dilution factor model exhibited a less robust fit, evidenced by a multiple R-squared value of 0.74. This discrepancy could potentially be attributed to the variability observed in absorption at the excitation wavelength. Residual plots, presented in the appendix, Figure A 6, confirmed the random distribution of errors, indicating model validity.

The model generated the contour plots for the integrated area and the dilution factor and are displayed in Figure 4.19 (c) and (e), respectively. In the contour plot of the IA response, a strong linear relation between the reaction temperature and photoluminescence intensity is observed. Overall, a higher reaction temperature and/or reaction time generally correlated with an increased photoluminescence intensity, which conforms to the trends observed by Du *et al.* and Wang *et al*.[39, 43] A linear relation between the reaction time and photoluminescence intensity is also established, however at a smaller slope. The contour plot of the dilution factor, shows a minimum area around 160 ˚C/5.5 h. If you would draw a straight line through 120 ˚C/7 h and 220 ˚C/3.5 h, all reaction condition on this line would result in the minimal DF. Combining the information from both contour plots, into the overlay plot shown in Figure 4.19 (d), the optimum condition was decided 210 ˚C/4 h, like the optimised conditions for kelp.

The absorption and emission spectra for the optimised conditions are presented in Figure 4.19 (f) and (g) respectively, with the optimised conditions highlighted in red. The 210 °C/4 h condition exhibited a sloped absorption curve featuring a shoulder at 286 nm. The photoluminescence spectrum indicated that the optimised conditions yielded the third-highest intensity at 426 nm, measuring $5.1 * 10^5$. This was preceded by the 220 °C/4 h and 200 °C/6 h conditions, which recorded intensities of $6.6 * 10^5$ and $5.7 * 10^5$, respectively. The model's prediction for the integrated area response was $7.0 * 10^7$, while the experimentally measured value was $6.5 * 10^7$, representing a deviation of 10%. The dilution factor for the optimised conditions was lower (0.008) compared to both higher-emitting reaction conditions. The sole instance of a lower dilution factor was observed for the 200 °C/2 h sample, which, however, generated only half of the integrated area. Consequently, 210 °C/4 h is considered the genuinely optimised reaction condition.

4.3.7 Consideration on the Response Surface Method

The hydrothermal synthesis of carbon dots from various seaweed and seaweed derivatives underwent comprehensive optimisation for all reaction systems. This section outlines the observed differences and similarities in the results obtained from distinct precursors. A consistent methodology was applied across all precursors, employing a central composite design centred around a 160 °C/4 h reaction condition. However, the efficacy of the developed models varied, as summarised in Table 4.20.

Table 4.20, Tabulated results of the CCD models for the Integrated Area of the Photoluminescence Intensity, and the Dilution Factor

Precursor	Change in IA (%)	Change in DF (%)	Model IA Multiple R squared	Model DF Multiple R squared	Model IA Lack of fit	Model DF Lack of fit
D-Glucose	+ 155	+ 387	0.792	0.9971	7.547e-06	6.920e-08
D-Galactose	+ 76	+ 108	0.9051	0.9591	0.40023	1.798e-06
Alginate	+ 15	- 90	0 .9529	0.7413	0.0075912	1.191e-07
Carrageenan	+ 171	- 43	0.9136	0.8107	0.0086538	4.341e-06
Kelp	+ 139	No change	0.9888	0.9736	0.2434377	1.349e-06
Irish Moss	+ 26	- 26	0.963	0.742	0.003892	8.267e-08

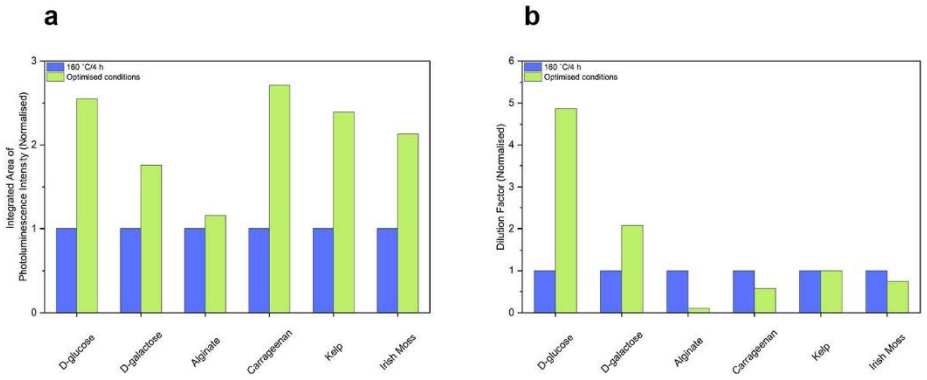

Figure 4.21, Tabulated data of the responses of the CCD, in blue the central point (160 ˚C/4 h) and in green the optimised reaction conditions, (a) the Integrated Area of the photoluminescence intensity and (b) the Dilution Factors

Figure 4.21 (a) illustrates a comparison between the optimised reaction conditions to the average of the standard reaction conditions, with the data normalised against the latter. All optimised reaction conditions resulted in a notable increase in intensity, ranging from 15% to 170%.

Regarding the dilution factor shown in Figure 4.21 (b), a decrease was observed for Alginate, Carrageenan, and Irish Moss, while it remained unchanged for Kelp and increased for D-glucose and D-galactose. Although an increase in the dilution factor is generally undesirable, it represents a trade-off between maximising photoluminescence intensity and minimising solid formation. The only viable approach to mitigate solid formation was to select optimal conditions that prioritise enhanced photoluminescence, thereby compromising the dilution factor. This trade-off is further evident when considering the responses for the Alginate precursor before and after optimisation. While optimisation yielded a modest 15% improvement in photoluminescence, it also led to a substantial 90% reduction in the dilution factor, indicating a significant overall enhancement.

The prioritisation of one response over another presents a challenge in balancing the two responses in this study. For Carrageenan, Kelp, and Irish Moss precursors, both models yielded comparable contour plots for the integrated area and dilution factor responses, resulting in improvements in both aspects.

The experimental data-driven model generally exhibited a strong fit for the integrated area, apart from a diminished R-squared value for the D-glucose sample, which was considered a testbed for this study, and

after which adjustments were made to improve the model. Furthermore, a significant Lack of Fit was observed for the D-galactose and Kelp precursors, indicating that the model did not adequately capture the relationship between the experimental factors and the integrated area for these specific samples. This could be mitigated by including more data points in the model, as well as revisited sample dilutions, as now the optimal absorption and excitation wavelengths are clear from the complete model.

In contrast, the dilution factor model provided reliable results for approximately half of the precursors, as indicated by multiple R-squared values exceeding 0.95 and an insignificant Lack of Fit for D-glucose, D-galactose, and Kelp. However, the models developed for Alginate, Carrageenan, and Irish moss exhibited lower R-squared values, ranging from 0.74 to 0.81, despite maintaining an insignificant Lack of Fit. This response does not fully capture the relevant properties of the carbon dots produced. To enhance the system, it is proposed that the dilution factor response be divided into two distinct responses: a simplified dilution factor and the quantity of solids produced, allowing for an additional contour plot to be generated.

$$DF\ 2 = \frac{sample\ volume}{total\ volume\ in\ cuvette} \tag{4.29}$$

4.3.8 Quantum yields measurements and deductions

The final phase of this study involved assessing the quantum yields of carbon dots synthesised under optimised reaction conditions. As depicted in Figure 4.22, D-glucose and D-galactose exhibited comparable QY values of 1.5% and 1.5%, respectively, for their optimised conditions. The polysaccharide Alginate yielded a lower QY of 1.1%, whereas Carrageenan measured a QY of 2.6%. This observed disparity between the quantum yields of the carbon dots derived from these polysaccharides can again be attributed to their distinct molecular structures: Alginate is composed of uronic acids, while Carrageenan consists of galactose units. Carbon dots produced from seaweed demonstrated QY values of 6.1% and 6.0% for kelp and Irish moss respectively. This represents more than a two-fold increase compared to the highest emitting saccharide.

The quantum yields measured were comparatively low to the literature, a phenomenon that can be attributed to several factors, including pretreatment steps such as washing of the biomass with water or acids,[9, 14, 15] or more advanced treatments including boiling the biomass, [31] oven drying the biomass > 100 ˚C for > 10 h.[9, 28] and/or pyrolysis at 700 ˚C.[5, 28] Additionally, various additives are reported to enhance the hydrothermal reaction step, including ammonia,[6, 13] hydrogen peroxide,[50] hydrochloride,[9] and acids.[22, 32, 51, 52] A correlation was observed between high quantum yield carbon dots, and high temperature reactions (300 ˚C),[31] and long reaction times (12 h).[9]

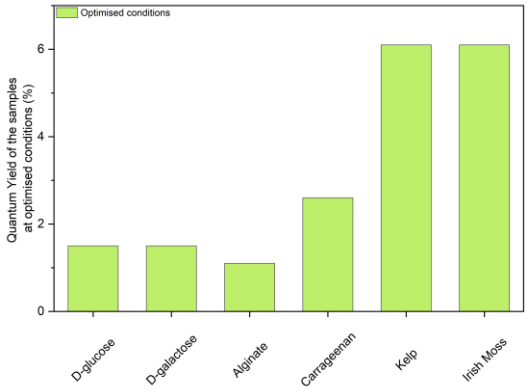

Figure 4.22, Quantum yields of the carbon dots produced in hydrothermal synthesis by six precursors for their optimised reaction conditions.

The enhanced quantum yield observed in carbon dots derived from biomasses compared to saccharides suggests that not only saccharide content, but also other biomass constituents play a crucial role in carbon dot formation. This observation suggests a correlation with the elevated nitrogen concentration prevalent in biomass, potentially leading to the formation of nitrogen-doped or surface-passivated carbon dots. This phenomenon has been documented in existing literature concerning carbon dots synthesised from citric acid, glucose, and natural amino acids, particularly when employing the microwave assisted method[69-73]

4.4 Conclusions

In this chapter the design of experiment's approach of the Response Surface Method was successfully applied to the hydrothermal synthesis of carbon dots from seaweed and seaweed derivatives. The general trend showed an increase in photoluminescence intensity with the increase of reaction time and reaction temperature.

The analysis of the experimental data revealed several significant findings. Firstly, all optimised reaction conditions consistently involved an increase in reaction temperature with or without an increase in reaction time, relative to the standard conditions of 160 °C/4 h. Specifically, the optimal reaction temperatures across all precursors ranged from 180 °C to 210 °C, while optimal reaction times varied between 4 and 6 h.

Table 4.21, Summarised results of the optimised conditions

	Reaction temperature (˚C)	**Reaction time (h)**	**λ_{abs} (nm)**	**λ_{ex} (nm)**	**λ_{em} (nm)**	**QY (%)**	**Change IA (%)**	**Change DF (%)**
Glucose	180	4	365	345	429	1.4	+ 155	+ 387
Galactose	180	4	350	350	432	1.5	+ 76	+ 108
Alginate	200	6	357	357	442	1.0	+ 16	- 90
Carrageenan	210	5	332	345	435	2.5	+ 171	- 43
Kelp	210	4	370	370	450	5.8	+ 139	No change
Irish Moss	210	4	360	345	425	5.7	+ 114	- 26

The selected reaction conditions, consistent with established literature, align with the reported reaction temperature range of 170 – 210 ˚C, which accounts for 76% of previously documented studies. This observation substantiates the present study's findings. Nevertheless, a mere 20% of the reviewed literature exhibited comparable reaction times, ranging from 4 to 6 h, while a substantial 53% reported reaction durations exceeding 6 h. Reaction times of 3 and 12 h accounted for 24% and 20% of the examined literature, respectively. The disparities noted between the current findings and previous research can be primarily ascribed to this study's explicit focus on precipitate formation, a consideration often overlooked in other investigations and subsequently addressed through post-reaction processing.

Optimisation of the reaction system with the selected monosaccharides has led to the optimised conditions of 180 ˚C/4 h, leading to an increase of 155 and 76% in measured integrated area of the photoluminescence spectrum, and resulted in a QY of 1.4 and 1.5% for D-glucose and D-galactose respectively, without the formation of solids. An upper limit in reaction temperature was identified because of the formation of solids ≥ 200 ˚C. The observed positive relationship between the reaction time and the photoluminescence intensity suggests there is potential for an even higher luminescence with an increase in reaction time without the formation of solids.

The optimised polysaccharide reaction system with alginate demonstrated a 15% enhancement in photoluminescence intensity, registering the lowest quantum yield at 1.0% within this investigation. Nonetheless, the optimised conditions for alginate, while yielding a modest quantum yield, significantly improved process efficiency by facilitating a 90% reduction in the dilution factor. Furthermore, optimising the carrageenan reaction system led to a 170% surge in photoluminescence intensity by integrated area and a 43% decrease in dilution factor under optimal conditions of 210 °C/5 h, yielding the highest quantum yield among saccharide precursors at 2.5%. The elevated reaction time and temperature, in contrast to the

monosaccharide system, are necessary to overcome provide the energy required to depolymerise polysaccharides, thereby making their saccharide constituents accessible for carbon dot formation. This suggests that the molecular structure and complexity of the carbon precursor significantly influence the optimal synthesis parameters and the resulting quantum yield of the carbon dots, supported by the research of Chen *et al.*[74]

Optimising the reaction conditions for the seaweed reaction system resulted in optimal parameters of 210 °C/4 h for both kelp and Irish moss. This optimisation led to improved quantum yields of 5.8% and 5.7% for the resulting carbon dots, representing increases of 139% and 114%, respectively. While no change in the dilution factor was observed for the kelp biomass, a 26% reduction was achieved for Irish moss, with minimal byproducts after the reaction. Although saccharides are the primary constituents for carbon dot formation, the remaining biomass likely contributes to the optical properties of the formed carbon dots, potentially through an increased nitrogen content leading to structural defects. This elemental doping can significantly influence the emission properties of carbon dots.[70]

The response surface methodology proved suitable for designing experiments for the hydrothermal synthesis of carbon dots from saccharide precursors. For quantitative analysis, careful consideration is advised regarding the identification of relevant responses and the methods used to capture them. While the integrated area of the photoluminescence spectra served as an excellent optical characterisation metric, the secondary metric—the dilution factor, intended to reflect carbon dot concentration and byproduct formation—was not entirely effective. It is recommended to separate this metric into two distinct responses, with solid formation assigned its own dedicated response.

4.5 References

1. C. Xia, S. Zhu, T. Feng, M. Yang and B. Yang, *Adv. Sci.*, 2019, **6**, 1901316.
2. M. Tavan, Z. Yousefian, Z. Bakhtiar, M. Rahmandoust and M. H. Mirjalili, *Ind. Crop. Prod.*, 2025, **231**, 121207.
3. Y. Zhou, W. Zhang and R. Leblanc, *J. Phys. Chem. B*, 2022, **126**, 10777-10796.
4. S. Varadharajan, K. S. Vasanthan, V. Mathur, N. Hariperumal and N. Mazumder, *Discov. Nano*, 2024, **19**.
5. V. Wongso, N. Sambudi, S. Sufian and Isnaeni, *Biomass Convers. Biorefin.*, 2021, **11**, 2641-2654.
6. A. Barati, M. Shamsipur, E. Arkan, L. Hosseinzadeh and H. Abdollahi, *Mater. Sci. Eng. C.*, 2015, **47**, 325-332.
7. A. Dehghani, S. M. Ardekani, M. Hassan and V. Gomes, *Carbon*, 2018, **131**, 238-245.
8. A. Kumar, A. Chowdhuri, D. Laha, T. Mahto, P. Karmakar and S. Sahu, *Sens. Actuators B-Chem.*, 2017, **242**, 679-686.
9. A. Prasannan and T. Imae, *Ind. Eng. Chem. Res.*, 2013, **52**, 15673-15678.
10. A. Su, D. Wang, X. Shu, Q. Zhong, Y. Chen, J. Liu and Y. Wang, *Chem. Res. Chin. Univ.*, 2018, **34**, 164-168.
11. A. Tyagi, K. M. Tripathi, N. Singh, S. Choudhary and R. K. Gupta, *RSC Adv.*, 2016, **6**, 72423-72432.
12. A.-M. Alam, B.-Y. Park, Z. K. Ghouri, M. Park and H.-Y. Kim, *Green Chem.*, 2015, **17**, 3791-3797.
13. Y. Cheng, M. Bai, J. Su, C. Fang, H. Li, J. Chen and J. Jiao, *J. Mater. Sci. Technol.*, 2019/08/01, **35**.
14. D. Bano, V. Kumar, V. Singh, S. Chandra, D. Singh, P. Yadav, M. Talat and S. H. Hasan, *ACS Sustain. Chem. Eng.*, 2019, **7**, 1923-1932.
15. D. Shukla, F. P. Pandey, P. Kumari, N. Basu, M. K. Tiwari, J. Lahiri, R. N. Kharwar and A. S. Parmar, *ChemistrySelect*, 2019, **4**, 4839-4847.
16. H. Huang, J.-J. Lv, D.-L. Zhou, N. Bao, Y. Xu, A.-J. Wang and J.-J. Feng, *RSC Adv.*, 2013, **3**, 21691.
17. H. Teymourinia, M. Salavati-Niasari, O. Amiri and H. Safardoust-Hojaghan, *J. Mol. Liq.*, 2017, **242**, 447-455.
18. H. Xu, X. Yang, G. Li, C. Zhao and X. Liao, *J. Agric. Food Chem.*, 2015, **63**, 6707-6714.
19. H. Zhang, S. Kang, G. Wang, Y. Zhang and H. Zhao, *ACS Sens.*, 2016, **1**, 875-881.
20. S. He, M. Turnbull, Y. Nie, X. Sun and Z. Ding, *Surf. Sci.*, 2018/10/01, **676**.
21. J. Shen, S. Shang, X. Chen, D. Wang and Y. Cai, *Mater. Sci. Eng. C.*, 2017, **76**, 856-864.
22. J. Zhu, F. Zhu, X. Yue, P. Chen, Y. Sun, L. Zhang, D. Mu and F. Ke, *J. Nanomater.*, 2019, **2019**, 1-7.
23. A. Chunduri, A. Kurdekar, S. Patnaik, V. Dev, T. Rattan and V. Kamisetti, *Mater. Focus.*, 2016, **5**, 55-61.
24. Q. Liang, W. Ma, Y. Shi, Z. Li and X. Yang, *Carbon*, 2013/08/01, **60**.
25. Y. Lou, J. Ji, A. Qin, L. Liao, Z. Li, S. Chen, K. Zhang and J. Ou, *ACS Omega*, March 3, 2020, **5**.
26. M. He, J. Zhang, H. Wang, Y. Kong, Y. Xiao and W. Xu, *Nanoscale Res. Lett.*, 2018, **13**.
27. M. Yuan, R. Zhong, H. Gao, W. Li, X. Yun, J. Liu, X. Zhao, G. Zhao and F. Zhang, *Appl. Surf. Sci.*, 2015, **355**, 1136-1144.
28. N. Mahat and S. Shamsudin, *Diam. Relat. Mater.*, 2020, **102**, 107660.
29. N. Irmania, K. Dehvari, G. Gedda, P. J. Tseng and J. Y. Chang, *J. Biomed. Mater. Res. B Appl. Biomater.*, 2020, **108**, 1616-1625.
30. N. Wang, Y. Wang, T. Guo, T. Yang, M. Chen and J. Wang, *Biosens. Bioelectron.*, 2016, **85**, 68-75.
31. P. Roy, A. P. Periasamy, C. Chuang, Y.-R. Liou, Y.-F. Chen, J. Joly, C.-T. Liang and H.-T. Chang, *New J. Chem.*, 2014, **38**, 4946-4951.
32. P. Surendran, A. Lakshmanan, G. Vinitha, G. Ramalingam and P. Rameshkumar, *J. Lumin.*, 2020, **35**, 196-202.
33. Q. Yang, J. Duan, W. Yang, X. Li, J. Mo, P. Yang and Q. Tang, *Appl. Surf. Sci.*, 2018, **434**, 1079-1085.
34. S. Liu, J. Tian, L. Wang, Y. Zhang, X. Qin, Y. Luo, A. Asiri, A. Al-Youbi and X. Sun, *Adv. Mater.*, 2012, **24**, 2037-2041.
35. T. John, P. Yadav, D. Kumar, S. Singh and S. Hasan, *J. Lumin.*, 2020, **35**, 913-923.
36. V. Ramar, S. Moothattu and K. Balasubramanian, *Sol. Energy*, 2018, **169**, 120-127.
37. V. Singh, K. Rawat, S. Mishra, T. Baghel, S. Fatima, A. John, N. Kalleti, D. Singh, A. Nazir, S. Rath and A. Goel, *J. Mater. Chem. B.*, 2018, **6**, 3366-3371.
38. W. Chen, J. Shen, G. Lv, D. Li, Y. Hu, C. Zhou, X. Liu and Z. Dai, *ChemistrySelect*, 2019, **4**, 2898-2902.
39. W. Du, X. Xu, H. Hao, R. Liu, D. Zhang, F. Gao and Q. Lu, *Sci. China Chem.*, 2015, **58**, 863-870.
40. W. Liu, H. Diao, H. Chang, H. Wang, T. Li and W. Wei, *Sens. Actuators B-Chem.*, 2017, **241**, 190-198.

41. W. Lu, X. Qin, S. Liu, G. Chang, Y. Zhang, Y. Luo, A. Asiri, A. Al-Youbi and X. Sun, *Anal. Chem.*, 2012, **84**, 5351-5357.
42. G. Wang, Q. Guo, D. Chen, Z. Liu, X. Zheng, A. Xu, S. Yang and G. Ding, *ACS Appl. Mater. Interfaces.*, January 31, 2018, **10**.
43. R.-C. Wang, J.-T. Lu and Y.-C. Lin, *J. Alloys Compd.*, 2020/01/15, **813**.
44. X. Chai, H. He, H. Fan, X. Kang and X. Song, *Bioresour. Technol.*, 2019, **282**, 142-147.
45. X. Gao, X. Ji, T. Nguyen, X. Gong, R. Chai and M. Guo, *Vacuum*, 2019, **164**, 256-264.
46. X. Wang, P. Yang, Q. Feng, T. Meng, J. Wei, C. Xu and J. Han, *Polymers*, 2019, **11**, 616.
47. Y. Guo, L. Zhang, F. Cao, Y. Leng, Y. Guo, L. Zhang, F. Cao and Y. Leng, *Sci. Rep.*, 2016-10-20, **6**.
48. Y. Liu, Y. Zhao and Y. Zhang, *Sens. Actuators B-Chem.*, 2014, **196**, 647-652.
49. Y. Song, L. Cao, J. Li, S. Cong, D. Li, Z. Bao and M. Tan, *J. Funct. Foods*, 2019, **10**, 3706-3716.
50. X. Yang, Y. Zhuo, S. Zhu, Y. Luo, Y. Feng and Y. Dou, *Biosens. Bioelectron.*, 2014/10/15, **60**.
51. Z. Wang, J. Yu, X. Zhang, N. Li, B. Liu, Y. Li, Y. Wang, W. Wang, Y. Li, L. Zhang, S. Dissanayake, S. Suib and L. Sun, *ACS Appl. Mater. Interfaces.*, 2016, **8**, 1434-1439.
52. Z. Ding, F. Li, J. Wen, X. Wang and R. Sun, *Green Chem.*, 2018, **20**, 1383-1390.
53. M. Dela Cruz, N. Thongsai, M. de Luna, I. In and P. Paoprasert, *Colloids Surf. A.*, 2019, **568**, 184-194.
54. H.-L. Yang, L.-F. Bai, Z.-R. Geng, H. Chen, L.-T. Xu, Y.-C. Xie, D.-J. Wang, H.-W. Gu and X.-M. Wang, *Mater. Today Adv.*, 2023, **18**, 100376.
55. C. Kang, Y. Huang, H. Yang, X. Yan and Z. Chen, *Nanomaterials*, 2020, **10**, 2316.
56. P. Araujo and R. Brereton, *Trends Anal. Chem.*, 1996, **15**, 156-163.
57. G. Derringer and R. Suich, *J. Qual. Technol.*, 1980, **12**, 214-219.
58. M. A. Bezerra, R. E. Santelli, E. P. Oliveira, L. S. Villar and L. A. Escaleira, *Talanta*, 2008, **76**, 965-977.
59. M. Carabajal, C. Teglia, S. Cerutti, M. Culzoni and H. Goicoechea, *Microchem. J.*, 2020, **152**, 104436.
60. S. Ferreira, R. Bruns, H. Ferreira, G. Matos, J. David, G. Brandão, E. Da Silva, L. Portugal, P. Dos Reis, A. Souza and W. Dos Santos, *Anal. Chim. Acta.*, 2007, **597**, 179-186.
61. R. Rech, Design of Experiments for Optimisation., 2025).
62. G. Crosby and J. Demas, *J. Phys. Chem.*, 1971, **75**, 991-1024.
63. S. Fery-Forgues and D. Lavabre, *J. Chem. Educ.*, 1999, **76**, 1260.
64. J. W. Eastman, *Photochemistry and Photobiology*, 1967, **6**, 55-72.
65. Z. Wang, R. Changotra, M. Dasog, G. S. Selopal, J. Yang and Q. S. He, *SM&T*, 2025/07/01, **44**.
66. H. Luo, L. Lari, H. Kim, S. Hérou, L. C. Tanase, V. K. Lazarov and M.-M. Titirici, *Nanoscale*, 2022/01/20, **14**.
67. J. Schneider, C. Reckmeier, Y. Xiong, M. Von Seckendorff, A. Susha, P. Kasák and A. Rogach, *J. Phys. Chem. C.*, 2017, **121**, 2014-2022.
68. W. Liang, P. Wang, M. Meziani, L. Ge, L. Yang, A. Patel, S. Morgan and Y.-P. Sun, *Nanoscale Adv.*, 2021, **3**, 4186-4195.
69. W. Wei, C. Xu, L. Wu, J. Wang, J. Ren and X. Qu, *Sci. Rep.*, 2014, **4**.
70. C. Deeney, S. Wang, S. Belhout, A. Gowen, B. Rodriguez, G. Redmond and S. Quinn, *RSC Adv.*, 2018, **8**, 12907-12917.
71. J. Liu, X. Liu, H. Luo and Y. Gao, *RSC Adv.*, 2014, **4**, 7648.
72. X. Zhai, P. Zhang, C. Liu, T. Bai, W. Li, L. Dai and W. Liu, *Chem. Commun.*, 2012, **48**, 7955.
73. Y. Dong, R. Wang, H. Li, J. Shao, Y. Chi, X. Lin and G. Chen, *Carbon*, 2012, **50**, 2810-2815.
74. C.-S. Chen, A. S. Yokokawa, K.-H. Tseng, M.-H. Wang, K. S.-K. Ma and C.-F. Wan, *RSC Adv.*, 2023, **13**, 28250-28261.

Chapter 5 Conclusions & Future Work

5.1 Conclusions

This thesis comprehensively explored the hydrothermal synthesis of energy materials, specifically quantum dots and carbon dots, with a strong emphasis on sustainable green chemistry approaches, as originally introduced in Chapter 1.

Chapter 2 specifically focused on the green chemistry aspects pertinent to the synthesis of cadmium sulfide quantum dots. This investigation concluded that the hydrothermal method serves as a feasible and sustainable alternative to conventional synthesis techniques. Key achievements included the successful avoidance of organic solvents by utilising water as the primary solvent and the employment of significantly reduced reaction temperatures through both conventional and adjusted approaches (using Duran tubes and a heat block). This work also elucidated the system's boundary between soluble/luminescent nanomaterials and the formation of bulk cadmium sulfide. Within this hydrothermal reaction system, precise control over the optical properties of the CdS QDs was achieved through systematic variations in reaction time, pH, and the selection of reactants.

A critical dual role was identified for the ligand, functioning simultaneously as both the sulfur precursor and the capping agent. This simplified reaction, requiring only the cadmium source and the ligand, allowed for superior regulation of the absorption and emission characteristics, as well as the size of CdS QDs, particularly with prolonged reaction durations. Optimal reaction conditions were determined to be pH 8.5, reaction times varying from 10 to 40 min, and a cadmium nitrate:L-cysteine molar ratio of 1:2.2, which collectively yielded the broadest emission spectrum. Corresponding quantum yields observed were 4.5%, 2.9%, 1.7%, and 1.5% for reaction times of 10, 20, 30, and 40 min, respectively. The success of this reaction system in embodying green chemistry principles was unequivocally demonstrated by a 36% reduction in molar material input, a substantially decreased reaction temperature, and the crucial replacement of organic solvents with an aqueous medium.

Building upon the principles of green chemistry, Chapter 3 identified seaweed as a highly promising renewable precursor for nanomaterial synthesis. Its abundant saccharide content, independence from traditional agricultural land use, and notable Irish historical connection position seaweed as an attractive and sustainable feedstock for the hydrothermal synthesis of carbon dots, offering a viable alternative to conventional inorganic quantum dots in Ireland. Both brown and red seaweed varieties, specifically kelp and Irish moss, were found to be suitable biomasses for CD synthesis due to their varied and extensive saccharide content. Hydrothermal synthesis at 160 °C for 4 h consistently yielded blue emissive carbon dots. Investigations into simplified reaction systems of prevalent polysaccharide and monosaccharide content found in kelp and Irish moss further enhanced the understanding of CD formation from saccharide content in biomass. However, this chapter also identified inherent challenges in purification and stability due to side product formation during the reaction and subsequent aggregation.

Addressing the limitations highlighted in Chapter 3, Chapter 4 delved into the optimisation of reaction parameters, specifically temperature and time, for the synthesis of carbon dots from seaweed and seaweed saccharides. This optimisation was crucial for improving purification and stability. The Response Surface Method was effectively utilised to optimise hydrothermal reaction parameters for six distinct seaweed precursors. This process identified optimal reaction temperatures ranging from 180 °C to 210 °C and reaction times from 4 to 6 h. These optimised conditions led to significantly enhanced quantum yields and photoluminescence compared to the previously established standard conditions of 160 °C/4 h. Notably, kelp and Irish moss processed at 210 °C/4 h demonstrated substantial enhancements of 139% and 114%, respectively.

Collectively, this thesis rigorously demonstrates the successful application of green chemistry principles across the synthesis of both quantum and carbon dots. This success is underpinned by the consistent utilisation of water as a solvent, the reduction of reaction temperatures, and the innovative leveraging of renewable biomass significantly mitigating the environmental impact typically associated with the synthesis of traditional inorganic quantum dots. Furthermore, a standardised reaction optimisation method for carbon dots is proposed, offering a pathway to enhance their optical properties and facilitate more efficient post-synthesis processing. This comprehensive work significantly contributes to the development of eco-friendly nanomaterials, which are crucial for driving advancements in renewable energy technologies.

5.2 Future Work

The green synthesis of CdS quantum dots whereby the dedicated sulfur source is eliminated can be expanded to investigate the reaction kinetics and mechanics through more granular time series experiments. The addition of a shell for the quantum dots in this reaction system can be assessed to narrow the emission peaks and improve stability of the dots in water. In the interest of reducing the environmental cost of quantum dot synthesis even further, the emerging I-III-VI QDs including copper indium sulfide and copper tin sulfide, could be investigated in this reaction systems as well by avoiding the use of heavy metals.

The green synthesis of carbon dots from seaweed identified two bottlenecks, namely a standard procedure to optimise the hydrothermal reaction from biomasses in general, and the isolation and purification of the dots in water. The first issue was addressed in this work, however, to enhance the performance and quality of the carbon dots even further, isolation methods should be further investigated. Additionally, the synthesis can be enhanced by considering additives in reaction, as identified in the literature review on the hydrothermal synthesis of carbon dots from biomass. The research can be expanded to other seaweed species, identified with high carbohydrate content. To bring carbon dots from biomass to the next level, research into carbon dot applications is important and recognised by the C-dots project in the Dunne group.

The response surface method, a statistical approach to design of experiment and analysis was applied to the optimisation of the reaction parameters of the hydrothermal synthesis of carbon dots. To enhance the method further, a third reaction parameter of choice could be included, leading to a three level and Box-Benken design, providing a more complete yet complex understanding of the relations between variables in reaction. Lastly this method could be applied more broadly to any materials synthesis reaction system.

Appendix

Script for reaction optimisation of the hydrothermal synthesis of carbon dots in R

```
# Loading the Response Surface Methodology package
Install.packages("rsm")
library(rsm)

# Build a central composite design for 2 factors
dsg <- ccd(2, alpha = "spherical")
dsg

# add the natural variables
dsg$Time <- dsg$x1*2 + 4
dsg$Temp <- dsg$x2*40 + 160
dsg

# saves the design in a file
dsg <- as.data.frame(dsg)
write.csv(dsg, "design_precursor.csv")

# Populate CCD with experimental data

# Open populated data file: design_precursor.csv
# x1: Time (h)
# x2: Temp (˚C)
# IA: Integrated area of photoluminescence spectrum (a.u.)
# DF: Dilution Factor (a.u.)

# setting the relationship between the coded and the natural variables and check the structure of the file
design_precursor <- as.coded.data(design_precursor,
                    x1 ~ (Time - 4)/2,
                    x2 ~ (Temp - 160)/40)

str(design_precursor)

###
##
# regression model Integrated Area
model_IA <- rsm(IA ~ FO(x1,x2) + TWI(x1,x2) + PQ(x1,x2), data = design_precursor)
summary(model_IA)
```

```
# regression model Dilution Factor
model_DF <- rsm(DF ~ FO(x1,x2) + TWI(x1,x2) + PQ(x1,x2), data = design_precursor)
summary(model_DF)

# residuals plots
par(mfrow=c(3,2))
plot(design_precursor$IA, model_IA$residuals,
    xlab="Integrated Area",ylab ="residuals") +
  abline(h=0, col="grey")
plot(design_precursor$DF, model_DF$residuals,
    xlab = "Dilution Factor", ylab = "residuals") +
  abline(h=0, col="grey")
plot(design_precursor$x1, model_IA$residuals,
    xlab = "Reaction Time (h)", ylab = "residuals") +
  abline(h=0, col="grey")
plot(design_precursor$x1, model_DF$residuals,
    xlab = "Reaction Time (h)", ylab = "residuals") +
  abline(h=0, col="grey")
plot(design_precursor$x2, model_IA$residuals,
    xlab = "Reaction Temperature (˚C)", ylab = "residuals") +
  abline(h=0, col="grey")
plot(design_precursor$x2, model_DF$residuals,
    xlab = "Reaction Temperature (˚C)", ylab = "residuals") +
  abline(h=0, col="grey")

# contour plots of the Integrated Area
contour(model_IA, ~ x1+x2,
       image = TRUE,
       xlabs=c("Time (h)", "Temperature (ºC)"))
points(design_precursor$Time, design_precursor$Temp)

persp(model_IA, ~ x1+x2, col = terrain.colors(50), contours = "colors",
     zlab = "Integrated Area (a.u.)",
     xlabs=c("Time (min)", "Temperature (ºC)"))

# predicting the Integrated Area at the stationary point
max <- data.frame(x1 = 0, x2 = 1.25)
predict(model_IA, max)

# contour plots of the Dilution Factor
contour(model_DF, ~ x1+x2,
       image = TRUE,
```

```
      xlabs=c("Time (h)", "Temperature (ºC)"))
points(design_precursor$Time, design_precursor$Temp)

persp(model_DF, ~ x1+x2, col = terrain.colors(50), contours = "colors",
    zlab = "Dilution Factor (a.u.)",
    xlabs=c("Time (min)", "Temperature (ºC)"))

###
##
# Contour plots for overlay
# Integrated Area higher than 2.5*10^7
contour(model_IA, ~ x1+x2,
      levels = c(1.8e+07), col = "blue",
      xlabs=c("Time (min)", "Temperature (ºC)"))


# Dilution Factor lower than 0.001
contour(model_DF, ~ x1+x2,
      levels = c(0.001), col = "red",
      xlabs=c("Time (min)", "Temperature (ºC)"),
      add = TRUE)

### Functions for desirability
# y = response
# L = unacceptability boundary
# T = target acceptability boundary T
# U = upper unacceptability boundary
# r, r1, r2 = exponent 1 for L and U
# d = desirability function

# Maximum
maxD <- function(y, L, T, r) {
 if (y < L){d <- 0}
 else if (y > T){d <- 1 }
 else{d <- ((y - L) / (T - L))^r}
 return(d) }

# Minimum
minD <- function(y, U, T, r) {
 if (y < T){d <- 1}
 else if (y > U){d <- 0}
 else{d <- ((U - y) / (U - T))^r}
```

```
  return(d) }

# create a grid for the desirability determination
dataD_precursor <- expand.grid(seq(-2, 2, by=0.05), seq(-2, 2, by=0.05))
colnames(dataD_precursor) <- c("x1", "x2")
View(dataD_precursor)

# add the natural variables
dataD_precursor$Time <- dataD_precursor$x1*2 + 4
dataD_precursor$Temp <- dataD_precursor$x2*40 + 160

# add the predicted responses
dataD_precursor$IA <- predict(model_IA, newdata = dataD_precursor)
dataD_precursor$DF <- predict(model_DF, newdata = dataD_precursor)

# For each data value, calculate desirability
for (i in 1:nrow(dataD_precursor)) {
  d1 <- maxD(dataD_precursor$IA[i]
          , L = 5e7, T = 8e+7, r = 1)
  d2 <- minD(dataD_precursor$DF[i]
          , U = 0.001, T = -0.01, r = 1)
  D <- (d1 * d2)^(1/2)
  dataD_precursor[i, c("d1", "d2", "D")] <- c(d1, d2, D)}

# plot the desirability results
library(ggplot2)


ggplot(data = dataD_precursor, aes(x=Time, y=Temp, z = D)) +
geom_contour_filled() +
scale_fill_brewer() +
scale_x_continuous(limits=c(1,7), breaks=seq(1,7,2)) +
scale_y_continuous(limits=c(100,220), breaks=seq(100,220,20)) +
theme_bw() +
theme(panel.grid.major = element_blank(), panel.grid.minor = element_blank()) +
labs(subtitle="Desirability function")
ggsave("desirability_precursor.png", width = 4.1, height = 2.5, dpi = 1000)
```

Residual plots Response Surface Method

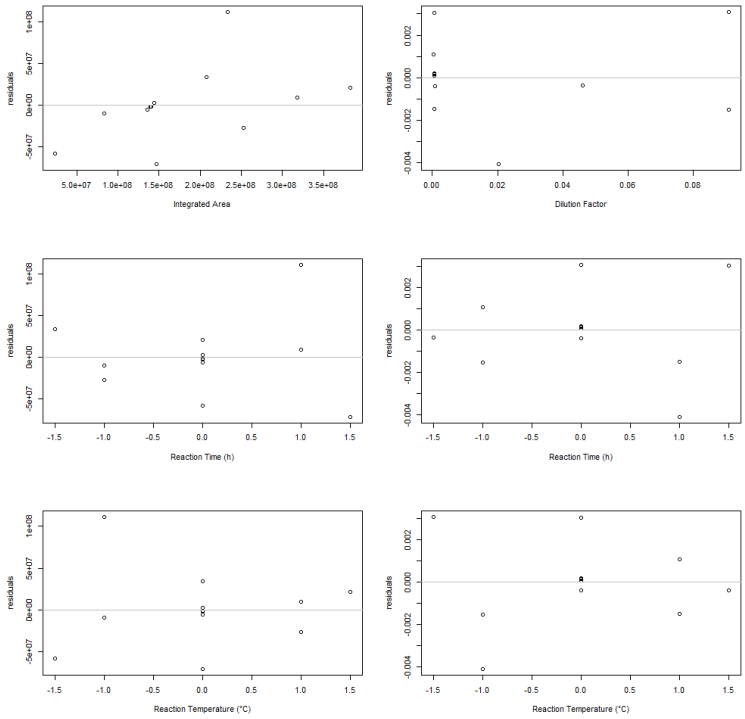

Figure A 2, Residual plots D-glucose, (a) Integrated Area response against Residuals, (b) Dilution Factor against Residuals, (c) Reaction Time against Residuals, IA model, (d) Reaction Time against Residuals, DF model, (e) Reaction Temperature against Residuals, IA model, (f) Reaction Temperature against Residuals, DF model.

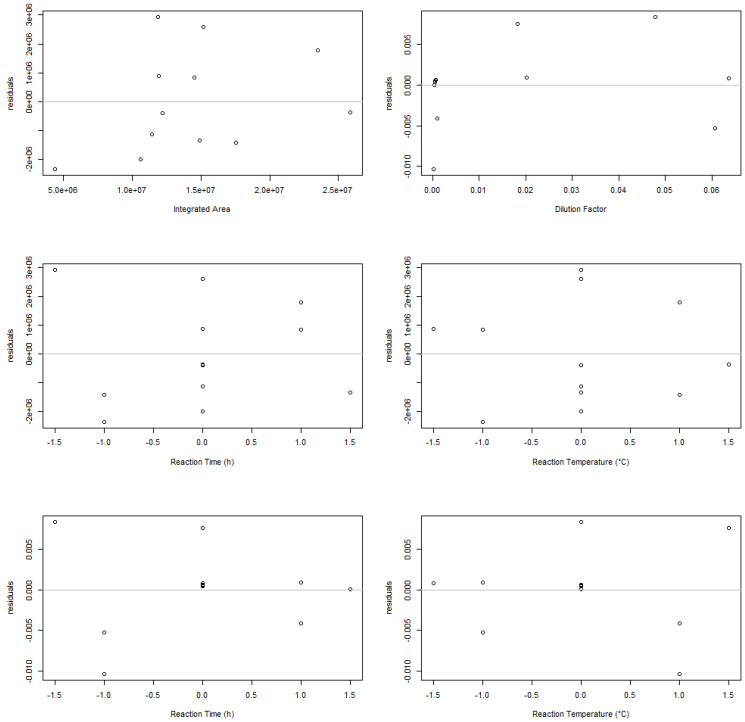

Figure A 3, Residual plots D-galactose, (a) Integrated Area response against Residuals, (b) Dilution Factor against Residuals, (c) Reaction Time against Residuals, IA model, (d) Reaction Time against Residuals, DF model, (e) Reaction Temperature against Residuals, IA model, (f) Reaction Temperature against Residuals, DF model.

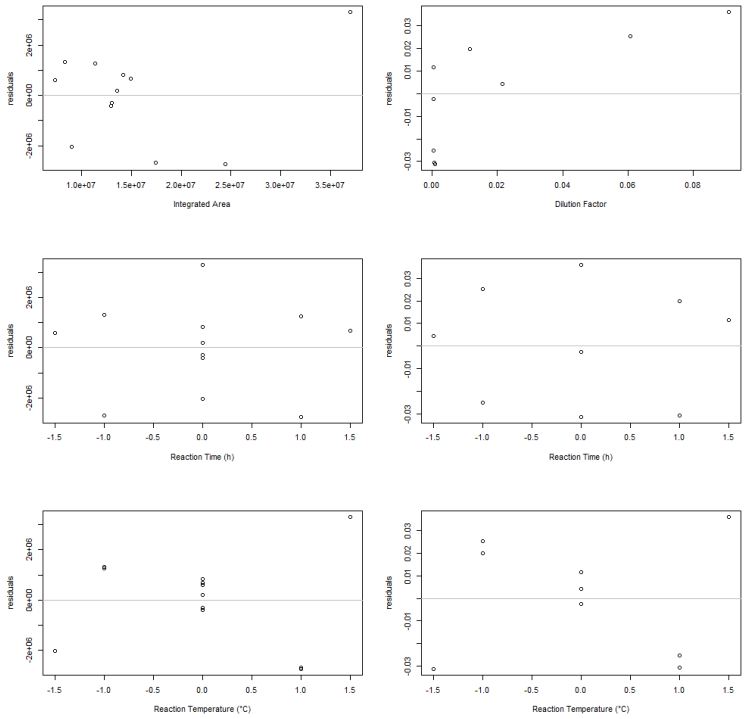

Figure A 4, Residual plots Alginate, (a) Integrated Area response against Residuals, (b) Dilution Factor against Residuals, (c) Reaction Time against Residuals, IA model, (d) Reaction Time against Residuals, DF model, (e) Reaction Temperature against Residuals, IA model, (f) Reaction Temperature against Residuals, DF model.

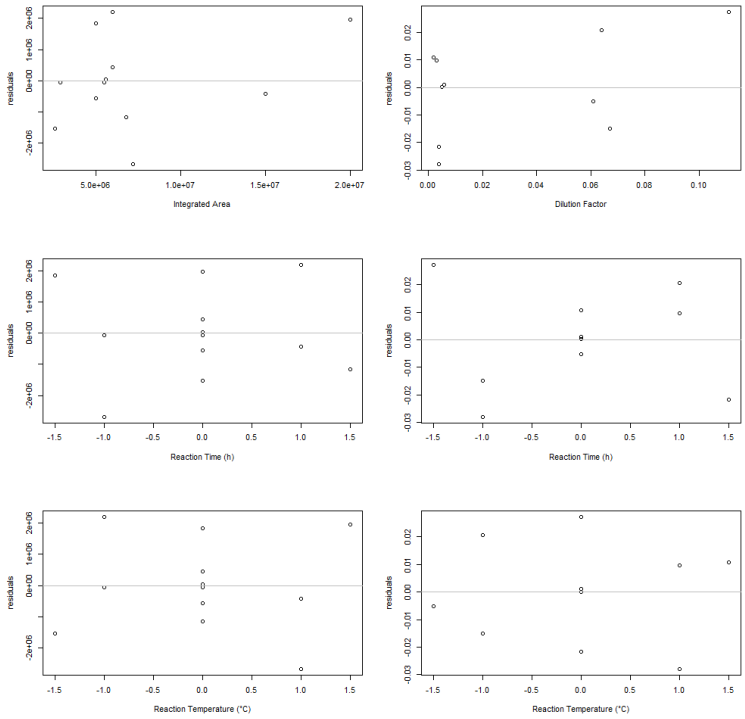

Figure A 5, Residual plots Carrageenan, (a) Integrated Area response against Residuals, (b) Dilution Factor against Residuals, (c) Reaction Time against Residuals, IA model, (d) Reaction Time against Residuals, DF model, (e) Reaction Temperature against Residuals, IA model, (f) Reaction Temperature against Residuals, DF model.

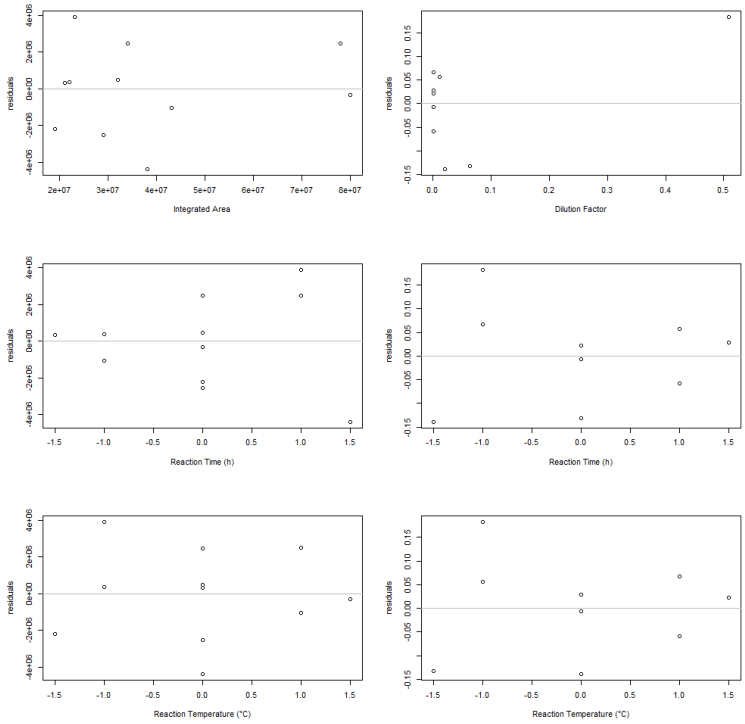

Figure A 6, Residual plotsKelp (a) Integrated Area response against Residuals, (b) Dilution Factor against Residuals, (c) Reaction Time against Residuals, IA model, (d) Reaction Time against Residuals, DF model, (e) Reaction Temperature against Residuals, IA model, (f) Reaction Temperature against Residuals, DF model.

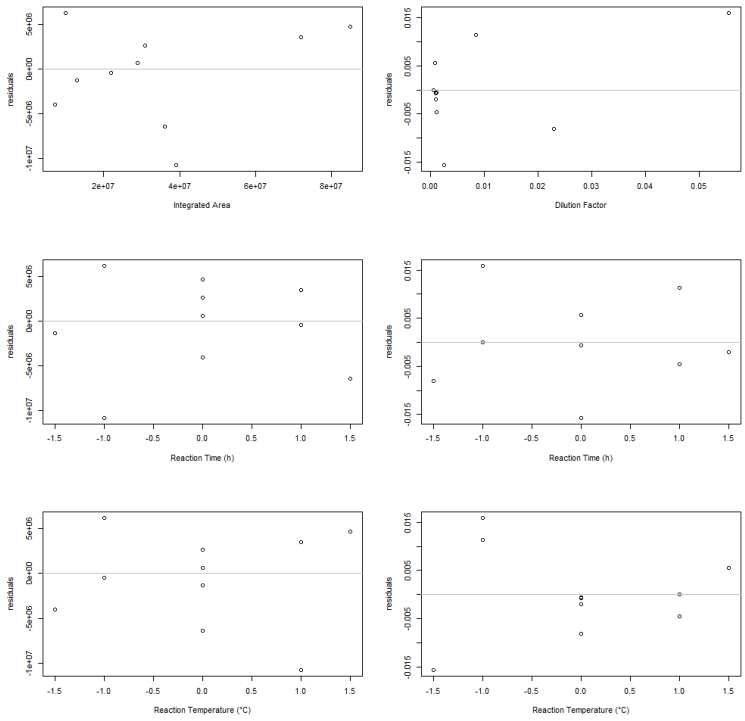

Figure A 7, Residual plots Irish moss, (a) Integrated Area response against Residuals, (b) Dilution Factor against Residuals, (c) Reaction Time against Residuals, IA model, (d) Reaction Time against Residuals, DF model, (e) Reaction Temperature against Residuals, IA model, (f) Reaction Temperature against Residuals, DF model.

Peak fit photoluminescence spectra – Carrageenan reactions RSM

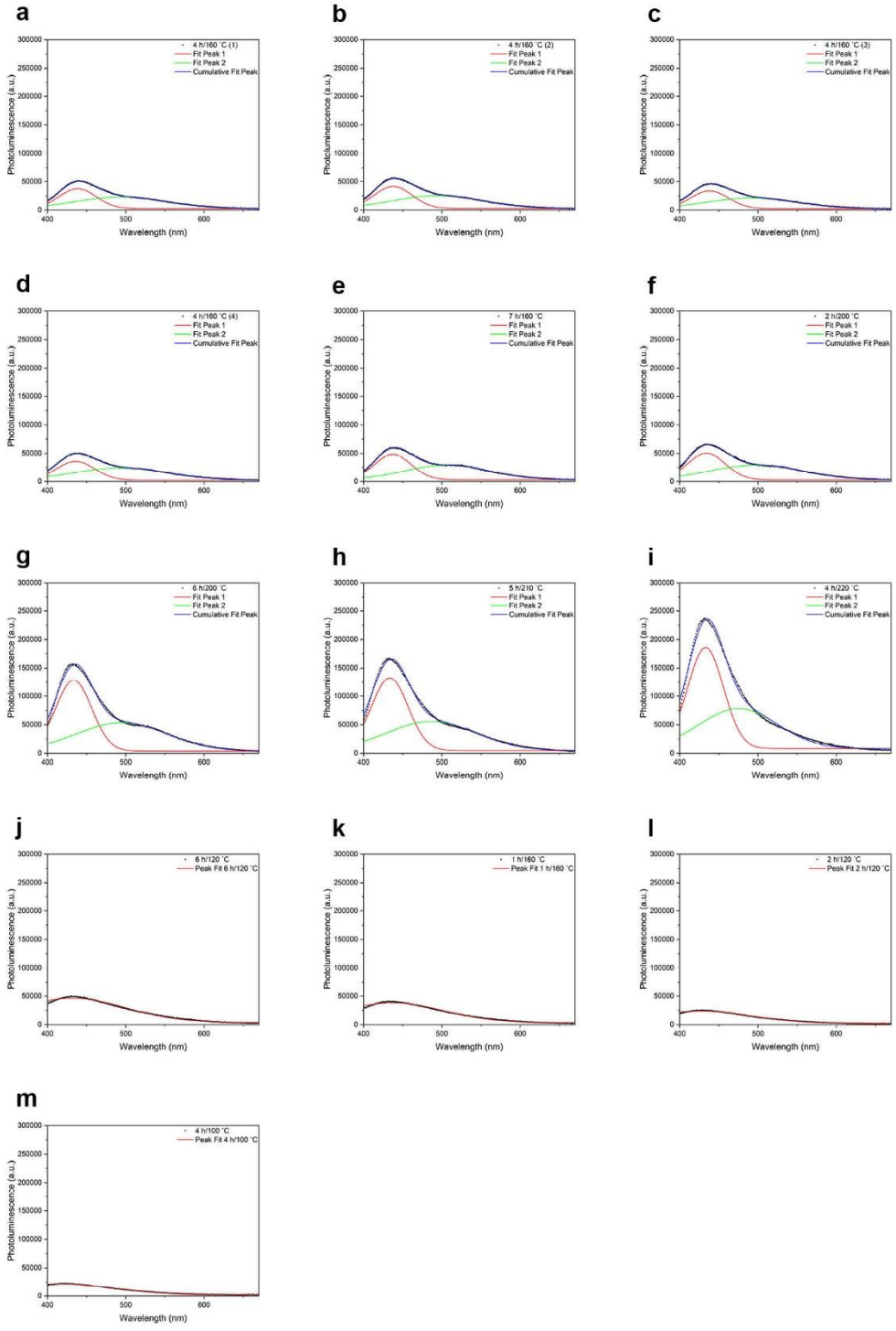

Figure A 8, Peak fit of the photoluminescence spectra of the carbon dots from hydrothermal synthesis of carrageenan with the following reaction conditions; (a) 160 ˚C, 4 h (1), (b) 160 ˚C, 4 h (2), (c) 160 ˚C, 4 h (3), (d) 160 ˚C, 4 h (4), (e) 160 ˚C, 7 h (f) 200 ˚C, 2 h (g) 200 ˚C, 6 h (h) 210 ˚C, 5 h (i) 220 ˚C, 4 h (j) 120 ˚C, 6 h (k) 160 ˚C, 1 h (l) 120 ˚C, 2 h (m) 100 ˚C, 4 h.